Analysis of time series of solar-like oscillations –

Applications to the Sun and HD 52265

Dissertation
zur Erlangung des Doktorgrades
der Mathematisch-Naturwissenschaftlichen Fakultäten
der Georg-August-Universität zu Göttingen

vorgelegt von
Thorsten Stahn
aus Göttingen

Göttingen 2010

Printed in Germany

Summary

The study of stellar oscillations allows one to constrain the structure and dynamics of stellar interiors to a precision that cannot be achieved with other methods. This dissertation focusses on the measurements of the parameters (frequencies, amplitudes, linewidths, and rotational splitting) of the global modes of solar-like oscillations observed in the Sun and in the Sun-like star HD 52265. The thesis is organized in three main parts: (i) an implementation and validation of a global fit of stellar oscillation power spectra using solar observations, (ii) an application of this method to original 4-month-long CoRoT observations of the solar-like star HD 52265, and (iii) an extension of the fitting method to time series with gaps. My main results concern HD 52265: the mode frequencies of the radial, dipole and quadrupole modes are measured with the highest precision achieved so far for a solar-type star and, for the first time, I measure unambiguously the effect of rotation on oscillations in a solar-type star.

Analysis of 14 years of disk-integrated solar observations with SoHO/VIRGO: This data set spans more than a full sunspot cycle. Based on the maximum likelihood method I perform global fits of the solar oscillation power spectra using 4 months of observations at a time. The global parametric model prescribes smooth variations of the parameters with radial order. I determine the parameters of solar p modes with degrees $\ell \leq 2$ ranging over 14 consecutive radial orders. The model parameters include rotation and the inclination angle of the rotation axis to the line of sight. By comparison with published mode frequencies, I find that my measurements are essentially unbiased and have errors that are consistent with expectations, hence validating my global fit for application to Sun-like stars other than the Sun.

Analysis of 4 months of CoRoT observations of HD 52265: This star is particularly interesting as it is a Sun-like star and it hosts a planet. At the time of writing, the observations of HD 52265 provide the best oscillation power spectrum which is currently available for a distant solar-like star. In particular, the radial, dipole, and quadrupole modes of oscillation are well resolved over a range of 10 consecutive radial orders. The derived large and small separations, $\Delta\nu = 98.84 \pm 0.12\,\mu\text{Hz}$ and $\delta\nu = 8.14 \pm 0.20\,\mu\text{Hz}$, provide strong constraints on the density, mass, and age of the star. For example, the precision on the mean stellar density is 0.4% and the precision on the mass is about 2%. Even though the azimuthal components of the non-radial modes of oscillation are not resolved there is direct evidence for rotational broadening of the peaks in the power spectrum, which allows to measure the stellar angular velocity Ω and the inclination angle i of the rotation axis. Combined with estimates of rotation derived from the modulation of the light curve by the passage of starspots, I find $2.1 \leq \Omega/\Omega_\odot \leq 2.5$ and $27° \leq i \leq 55°$. Assuming

the stellar rotation axis and the normal to the orbital plane of the companion are aligned, $i = i_p$, the radial velocity measurement of $M_p \sin i_p$ can be turned into a constraint on the mass of the companion: $1.3 \leq M_p/M_{Jup} \leq 2.4$. This strongly suggests that HD 52265b is a planet and not a brown dwarf, while it also illustrates the connections between astero-seismology and exoplanet science.

Fitting method for the analysis of gapped time series: I implement a new MLE method to determine the mode parameters of solar-like oscillations with higher precision and less bias compared to a standard fitting method. In the case of a 2 week observation of one single mode of solar-like oscillation with a signal-to-noise ratio $\mathcal{S}/\mathcal{N} = 6$, and using a typical single-site observation window (duty cycle of 30%), the frequency estimate of the new method is by a factor of two more precise than the estimate obtained with the old method. The analysis of ground-based observations of stellar oscillations should benefit from the application of the new fitting method.

Contents

List of Figures

List of Tables

1   Introduction

1.1   General purpose of helio- and asteroseismology

Helio- and asteroseismology are tools to investigate the interior structure and the evolution of the Sun and distant stars. Many stars of various types and evolutionary stages undergo global oscillations, which can be observed at the stellar surface in brightness or velocity. These oscillations, in particular their frequencies, contain precious information on stellar interiors, e.g. the sound speed. See, e.g., Cox (1980), Unno et al. (1989), and Aerts et al. (2010) for general presentations of the theory of stellar oscillations and, e.g., Christensen-Dalsgaard (2002) for a review of helioseismology.

The theory of stellar structure is a well-established branch in astrophysics (e.g. Kippenhahn and Weigert 1990, Hansen et al. 2004). Until only recently, tests of the theory of stellar structure and evolution relied mostly on the study of stellar clusters where stars are assumed to have the same age and chemical composition (e.g. VandenBerg and Stetson 2004). However, helio- and asteroseismology make possible the study of the structure of isolated stars and offer independent methods to test and refine the theory of stellar evolution. The confrontation of the measured oscillation frequencies and those calculated from models provide stringent constraints on the input physics of the models.

Thanks to our ability to make images of the solar surface, about 10^7 modes of oscillations have been measured in the Sun. This provides a very detailed model of the sound speed, temperature, density, and internal rotation of the Sun (e.g. Gough et al. 1996, Christensen-Dalsgaard et al. 1996, Thompson et al. 2003). The detection of oscillations in distant stars is a lot more challenging. Asteroseismology is becoming a reality thanks to advanced ground-based spectrographs (e.g., CORALIE, VLT/UVES, AAT/UCLES, HARPS) and the space missions MOST (Microvariability and Oscillations of STars, Walker et al. 2003), CoRoT (Convection, Rotation, and planetary Transits, Baglin et al. 2006) and Kepler (Borucki et al. 2010). A few tens of modes of global oscillations (radial, dipole, and quadrupole modes) have been detected at once in several solar-like pulsators: for example, α Cen A, B (Bouchy and Carrier 2002, Kjeldsen et al. 2005), Procyon (e.g., Arentoft et al. 2008), η Boo (Kjeldsen et al. 2003), 70 Oph A (Carrier and Eggenberger 2006), HD 49933 (Michel et al. 2008, Appourchaux et al. 2008), HD 181420 (Michel et al. 2008, Barban et al. 2009), HD 181906 (Michel et al. 2008, García et al. 2009), KIC 6603624, KIC 3656476, KIC 11026764 (Chaplin et al. 2010), and HAT-P-11 (Christensen-Dalsgaard et al. 2010). In the future, the asteroseismology of many thousands of stars in various stages of their evolution will enable us to tackle several long-standing problems, such as stellar dynamos, stellar convection, and the rotational history of stars.

The main outcome of asteroseismic studies are precise estimates of the fundamental stellar parameters, e.g. stellar radii, masses, ages, and initial chemical compositions. These are required in several fields of astrophysics. For instance, Prantzos (2009) argues that the age-metallicity distribution, which is an indicator for the chemical evolution of the Milky Way, is difficult to interpret due to uncertainties in the stellar ages. While classical age estimates, e.g. from isochrones, have typically uncertainties of $\sim 50\%$ (Saffe et al. 2005), seismic mass constraints are expected to be much more precise. For a star of solar age, the uncertainty on the seismic age may be as low as a few hundred million years as we shall see in this thesis.

Another potential application of asteroseismology is the study of solar and stellar magnetism, and stellar activity cycles in particular (e.g. Rempel 2008, Lanza 2010). This requires the study of the internal rotation, convection, and magnetic activity of many stars. The latitudinal differential rotation or the depth of the convection zone can potentially be measured by means of asteroseismology, as demonstrated by Verner et al. (2006), using disk-integrated observations of solar oscillations.

The detection and characterization of exoplanets have become one of the most vibrant fields in astrophysics. Stello et al. (2007) emphasized the importance of asteroseismology to supplement planetary transit measurements. Transit measurements and follow-up spectroscopy must be supplemented by the asteroseismology of planet-host stars in order to constrain the fundamental parameters of the planets within a few percent, especially their masses and ages. Space missions like Kepler and especially PLATO (if selected) plan to exploit this exciting possibility.

1.2 Observations of solar-like oscillations

Oscillations in stars like the Sun are excited by turbulent convection in the near surface layers (e.g. Goldreich and Keeley 1977, Stein et al. 2004). In addition to Sun-like stars, solar-like oscillations can also be observed in K and G giants, e.g. ξ Hya (Frandsen et al. 2002), or ε Oph (De Ridder et al. 2006). Solar-like stellar oscillations can be measured both by photometry and spectroscopy. Photometric observations of stellar oscillations measure the brightness variations of the star. Periodic expansion and contraction lead to temperature variations which cause a change in the light flux. The oscillations in the Sun have very low intensity amplitudes of a few ppm. In addition the displacement of the stellar surface caused by the oscillations can be measured spectroscopically in terms of Doppler shifts of the absorption lines in the spectrum of the star. In the Sun, the line-of-sight doppler velocities are of the order of a few cm/s, which is small compared to surface convective motions or the 2 km/s rotation. The mode amplitudes result from the complicated interplay of mode excitation and damping (e.g. Houdek et al. 1999). Kjeldsen and Bedding (1995) found that the velocity amplitude, v_{osc}, of solar-like oscillations scales like $v_{osc} \propto (L/M)^{\alpha}$ where L and M are the luminosity and the mass of the star, and $\alpha \sim 0.7$ Samadi et al. (2007b). The oscillation amplitude increases as a star evolves on the main sequence towards the red giant branch.

Photometric observations are technically less demanding than spectroscopic observations. On the other hand, velocity measurements have a significantly lower level of background noise relative to the oscillation signal (e.g. Harvey 1988, and compare Figure 1.1 and Figure 2.2 in this work).

Figure 1.1 shows an observation of the Sun with the GOLF instrument (Global Oscillations at Low Frequencies, Gabriel et al. 1997, Gelly et al. 2002) aboard the SoHO spacecraft (Solar and Heliospheric Observatory). This instrument measures disk-integrated radial velocities as a function of time, $v(t)$. The top panel of the figure shows a two-hour section of a time series with a cadence of 20 seconds. The five-minute oscillations of the Sun which were first detected by Leighton et al. (1962) are evident. Information on the modes of individual oscillations may be recovered in Fourier space. For this purpose, the bottom panel of Figure 1.1 shows a power spectrum, P, of a one-year GOLF time series. Only the radial, dipole, and quadrupole modes ($\ell \leq 2$) are clearly visible. Modes of higher spherical-harmonic degrees have much lower amplitudes in disk-integrated sunlight. The comb-like structure in Figure 1.1 is the characteristic signature of high overtone, low-degree ($n >> \ell$) solar-like oscillations. This pattern of solar-like oscillations is discussed in Section 1.3.

In the case of the Sun it is also possible to record spatially resolved images of the solar surface as a function of time. This is realized for instance by the MDI instrument (Michelson Doppler Imager, Scherrer et al. 1995) aboard SoHO. Such observations allow one to study modes of much higher degree (ℓ up to about 3000). The study of the high-degree modes enables us to investigate the subsurface layers of the Sun in three-dimensions. For reviews of the field of local helioseismology see Gizon and Birch (2005) and Gizon et al. (2010b).

The precision on asteroseismic inferences, e.g. stellar mass and age, depends on the precision of the determined mode frequencies. This requires long and uninterrupted time series with high signal-to-noise ratio. The total length T of a time series determines the frequency resolution, $1/T$, in Fourier space. Gaps in the time series result in the convolution of the Fourier spectrum with the Fourier transform of the observation window. Due to this convolution the power in a frequency bin is spread over some frequency range. Furthermore, the Fourier amplitudes at different frequencies become correlated. These two effects make the data analysis significantly more complicated (see Chapter 4 of this work).

Long and uninterrupted time series can only be achieved by setting up ground-based networks of telescopes or by observing from space. There are two main ground-based observation networks dedicated to helioseismology, BiSON (Birmingham Solar Oscillations Network, e.g. Chaplin et al. 1996) and GONG (Global Oscillation Network Group, e.g. Harvey et al. 1996). Both networks consist of six stations located at different longitudes to guarantee a high duty cycle of the data. BiSON data for instance extend now over three decades and accomplish a duty cycle of $\sim 80\%$ in long-term on a yearly basis (Chaplin et al. 1996). Asteroseismic observations on the ground rely on collaborations organizing multi-site campaigns, e.g. WET (Whole Earth Telescope, Nather et al. 1990) and the Delta Scuti Network[1]. In the near future the SONG network (Stellar Observations Network Group, e.g. Grundahl et al. 2008) is expected to provide long-term (~4 month) radial-velocity measurements of distant stars with a duty cycle comparable to the BiSON data.

Observations from space guarantee long time series and high duty cycles ($\gtrsim 90\%$). These observations are also not affected by perturbations of the earth atmosphere. SoHO

---

[1]http://www.univie.ac.at/tops/dsn/intro.html
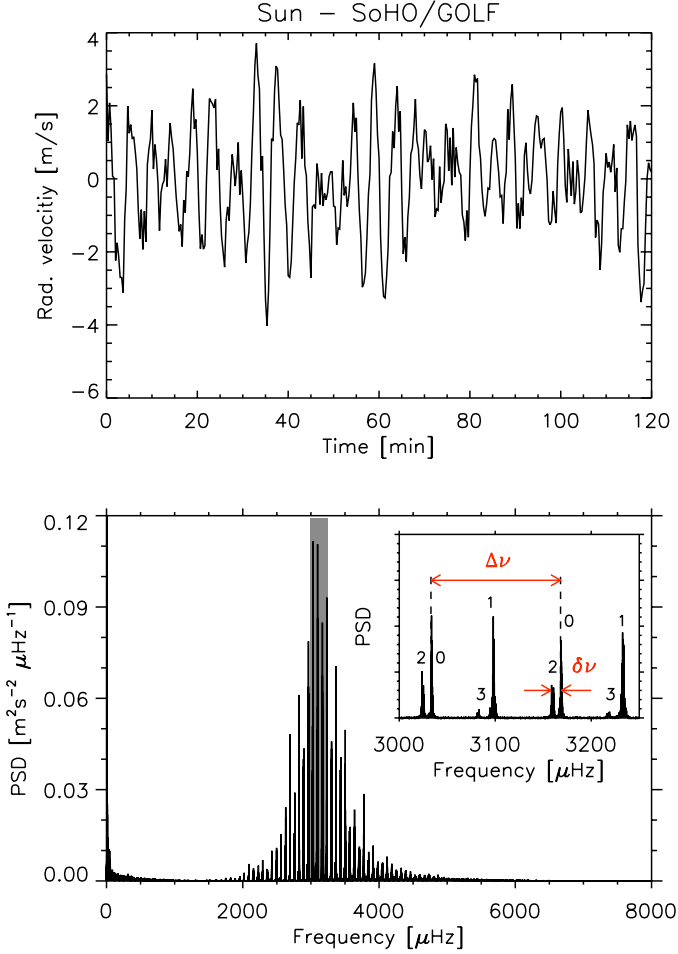
Figure 1.1: Disk-integrated observation of solar acoustic oscillations. The *top panel* shows a 2-hour section of a time series of the Sun observed with the GOLF instrument aboard the SoHO spacecraft. The time series shows radial velocity measurements of the disk-integrated light of the Sun. The five-minute oscillations are clearly visible. The *bottom panel* presents the solar power spectrum of a 1 year observation with GOLF. The comb-like structure of the solar oscillations is evident. The power in the *grey-shaded section* is shown in the inset. The Sun-as-a star power spectrum is composed of low-degree modes as indicated by the numbers labeling each peak. The *red arrows* define the regular spacing of the individual modes in terms of the large separation, $\Delta\nu = \nu_{n+1\,\ell} - \nu_{n\ell}$, and the small separation, $\delta\nu = \nu_{n\ell} - \nu_{n-1\,\ell+2}$.

for instance is operating since 1996 and carries three experiments suited for helioseismic studies: GOLF, MDI, and VIRGO. The VIRGO instruments (Variability and solar IRadiance and Gravity Oscillations, Fröhlich et al. 1995, 1997) measure irradiance fluctuations, which will be used in this thesis. This year the Solar Dynamics Observatory (SDO) was launched to replace the SOHO/MDI instrument. For asteroseismology, the CoRoT and Kepler space telescopes provide time series with a total length of 4-6 months and a duty cycle of about ∼ 90%.

1.3 Basic properties of solar-like oscillations

Here I provide a brief outline of the main properties of solar-like stellar oscillations. Solar-like oscillations are caused by acoustic waves trapped in spherical-shell cavities. They are also known as p modes, for pressure modes. Acoustic waves propagate with the speed of sound $c = \sqrt{\gamma p/\rho}$ where γ is the first adiabatic exponent, p is pressure and ρ is density. Assuming an ideal gas law, we have $p/\rho = \mathcal{R}T/\mu$, where T is temperature, $\mathcal{R}$ is a constant, and μ is the mean molecular weight. The sound speed, $c \propto \sqrt{T/\mu}$, increases towards the center of the star as does the temperature. For the Sun $c \sim 10$ km/s at the surface and $c \sim 500$ km/s at the center.

For a spherical, non-rotating star, stellar oscillations can be expressed as a superposition of spheroidal eigenmodes. In a spherical-polar coordinate system with radius r, colatitude θ, and longitude ϕ, a scalar quantity, like pressure, can be written as

$$p(r, \theta, \phi, t) = \text{Re} \sum_{n\ell} \sum_{m=-\ell}^{\ell} A_{n\ell m} p_{n\ell}(r) Y_{\ell}^{m}(\theta, \phi) \exp(\text{i}2\pi\nu_{n\ell m}t). \tag{1.1}$$

where Y_{ℓ}^{m} is a spherical harmonics, $A_{n\ell m}$ is a complex mode amplitude, and $p_{n\ell}(r)$ is the eigenfunction of the mode with frequency $\nu_{n\ell m}$. For a spherical-symmetric star the mode frequencies of the individual azimuthal components of a multiplet are $2\ell + 1$-fold degenerate. Each mode of oscillation is labeled by a set of three integers $\{n\ell m\}$: the radial order n denotes the number of nodes in the radial direction, the spherical harmonics degree ℓ corresponds to the total number of lines of node on the sphere, and the azimuthal order $m = -\ell, -\ell+1, \ldots, \ell$ corresponds to the number of node lines that cross the equator. Modes with $\ell = 0$ are called radial modes. Modes with $\ell \geq 1$ are non-radial modes. At fixed frequency, the penetration depth of a particular mode depends on degree ℓ: modes with low ℓ penetrate deeper into the stellar interior than modes with higher ℓ. At fixed ℓ, modes with large values of n penetrate deeper than modes with low n. Thus, different modes probe different regions of a star.

Tassoul (1980) derived a very useful asymptotic expression for the p-mode frequencies in the limit $n >> \ell$. The result may be written as (see also Gough 1986)

$$\nu_{n\ell} \simeq \left(n + \frac{\ell}{2} + \epsilon\right)\Delta\nu - [A\ell(\ell + 1) - B]\frac{\Delta\nu^2}{\nu_{n\ell}}, \tag{1.2}$$

where

$$A = \frac{1}{4\pi^2\Delta\nu}\left[\frac{c(R)}{R} - \int_0^R \frac{1}{r}\frac{dc}{dr}dr\right]. \tag{1.3}$$

In Equation (1.2) $\epsilon = \epsilon(\nu)$ and B are determined by the reflection properties near the surface (e.g., Gough 1986) and the *large separation* is

$$\Delta\nu = \left[2 \int_0^R \frac{dr}{c(r)}\right]^{-1}.$$
(1.4)

The large separation is the inverse of the sound travel time through the stellar diameter. It scales like the dynamical time scale and is proportional to the square root of the mean stellar density: $\Delta\nu \propto \bar{\rho}^{1/2}$. Equation (1.2) describes a uniform spacing of modes with constant angular degree ℓ and consecutive radial order n:

$$\Delta\nu_{n\ell} \simeq \nu_{n+1\,\ell} - \nu_{n\ell}.$$
(1.5)

The large separation is easy to measure in the solar power spectrum in Figure 1.1.

Neglecting the term in the surface sound speed in Equation (1.3) and assuming B to be small (Gough 1986) the second term of Equation (1.2) gives rise to the *small frequency separation* between adjacent $\ell = 0$ and $\ell = 2$ modes:

$$\delta\nu_{n\ell} = \nu_{n\ell} - \nu_{n-1\,\ell+2} \simeq -(4\ell + 6)\frac{\Delta\nu}{4\pi^2\nu_{n\ell}} \int_0^R \frac{1}{r}\frac{dc}{dr}dr.$$
(1.6)

The small separation is illustrated in Figure 1.1.

Deviations from spherical symmetry lift the degeneracy and cause a splitting of the azimuthal components. For example, magnetic fields and stellar rotation. Rotation lifts entirely the azimuthal degeneracy of the frequencies. For a star that rotates slowly with angular velocity $\Omega(r, \theta)$ around the polar axis $\theta = 0$, the mode frequencies can be written to first order as

$$\nu_{n\ell m} = \nu_{n\ell 0} + \frac{m}{2\pi}\langle\Omega\rangle$$
(1.7)

with

$$\langle\Omega\rangle = \int_0^R dr \int_0^\pi d\theta \, K_{n\ell m}(r, \theta)\Omega(r, \theta).$$
(1.8)

The kernel function $K_{n\ell m}$ gives the spatial sensitivity of the mode's frequency perturbation to rotation; it depends solely on the eigenfunctions of the unperturbed spherically-symmetric stellar model (e.g., Christensen-Dalsgaard 2002). The rotational frequency splitting is defined as

$$\delta\nu_{n\ell m}^{(\text{rot})} = \nu_{n\ell m} - \nu_{n\ell 0}.$$
(1.9)

For the Sun, the rotational splitting can be measured for thousands of modes using spatially resolved observations of oscillations. The above equation can be inverted by solving a linear system of equations. This gives the internal angular velocity as a function of latitude and depth down to about half the solar radius (e.g., Howe 2009). A major achievement of helioseismology has been the discovery that the latitudinal differential rotation of the Sun persists throughout the entire convection zone, until it transitions to rigid body rotation in the radiative zone.

For uniform rotation, i.e. $\Omega = \text{const.}$, Ledoux (1951) derived an expression for the rotational splitting:

$$\delta\nu_{n\ell m}^{(\text{rot})} = \frac{m}{2\pi}(1 - C_{n\ell})\Omega \simeq \frac{m}{2\pi}\Omega$$
(1.10)

Here, $C_{n\ell}$ is the Ledoux constant, which is $\ll 1$ for a slowly rotating star.

1.3.1 Other types of stellar oscillations

This work is focused on solar-like oscillations, i.e. randomly excited and damped p modes. For the sake of completeness I note that there are also other types of oscillations and excitation mechanisms.

For gravity, or g modes, the restoring force is buoyancy. G modes are expected in the Sun but have not been unambiguously confirmed so far. They have great potential to probe the central regions of the Sun since their amplitudes are at maximum there. For a recent review on the quest for solar g modes, see e.g. Appourchaux et al. (2010). In other types of stars g modes have been observed, e.g. in evolved stars like subdwarf B (sdB) stars and white dwarfs (e.g. Green et al. 2003, Winget and Kepler 2008).

Concerning the excitation mechanism, the oscillations in many stars are driven by a heat engine, the $\kappa-$mechanism (see e.g. Cox 1980). A κ-mechanism may sustain oscillations in certain regions of a star where the opacity $\kappa = \kappa(\rho, T)$ increases with density and temperature. This condition is satisfied for some stars in partial ionization zones of particular elements. Oscillations which are excited by a κ-mechanism are long-lived with respect to the length of the observation ($\tau >> T$) and are commonly described in terms of sine functions. A κ-mechanism acts in a large variety of oscillating stars, e.g. Cepheids, β Cepheids, δ Scuti stars, sdBs, and white dwarfs (e.g. Aerts et al. 2010).

1.4 Interpretation of stellar oscillation frequencies

The goal of asteroseismology is to deduce stellar fundamental parameters, in particular the radius, mass, and age, from the frequency measurements. For distant stars the seismic measurements are restricted to a few tens of modes only. For solar-like stars the frequency separations $\Delta\nu$ and $\delta\nu$ have particular high diagnostic potential. As discussed in Section 1.3 the large separation is linked to the mean density of the star, $\Delta\nu \propto \overline{\rho}^{1/2}$, and is thus directly related to its mass and radius.

The small separation $\delta\nu$ is sensitive to the age of the star. The integral in Equation (1.6) is sensitive to the sound speed gradient dc/dr near the stellar core. Nuclear burning leads to an increase of the helium fraction in the core while the hydrogen content goes down. Thus, the mean molecular weight μ increases. Assuming that the core temperature does not change much while the star remains on the main sequence, the sound speed decreases in the core and dc/dr gives a positive contribution to the integral in Equation (1.6). Thus, $\delta\nu$ decreases as the star evolves.

Figure 1.2 shows an asteroseismic Hertzsprung-Russell diagram (HRD, Christensen-Dalsgaard 1984, 1988), i.e. a representation of the small separation versus the large separation. Here the asteroseismic HRD shows stellar evolutionary tracks for models with solar initial chemical composition and various stellar masses. The asteroseismic HRD illustrates how measurements of the large and small frequency separation can be related to the stellar mass and the core hydrogen abundance, i.e. the evolutionary state of the star. Thus accurate measurements of $\Delta\nu$ and $\delta\nu$ translate into precise estimates on the stellar mass and age within a few percent. The prospects of deducing the stellar mass and age from measurements of $\Delta\nu$ and $\delta\nu$ strongly depend on proper modeling. For instance, Christensen-Dalsgaard (1993), and Monteiro et al. (2002) pointed out that the stellar models are sensitive to several parameters, e.g. the heavy-element abundance, the
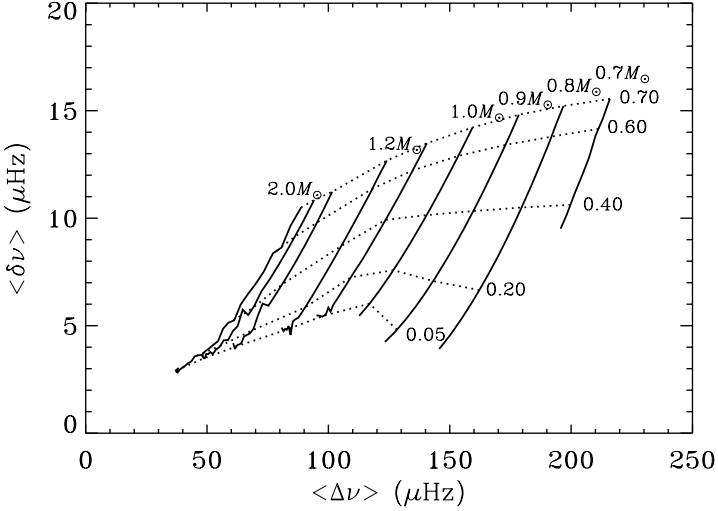
Figure 1.2: Asteroseismic Hertzsprung-Russell diagram, i.e. a representation of the small separation $\delta\nu$ versus the large separation $\Delta\nu$. The *solid lines* show stellar evolutionary tracks for stars with various masses and solar chemical composition. The *dotted lines* correspond to isopleths of constant central hydrogen abundance. The fraction of hydrogen at the star's center is indicated by the numbers at the right end of each dotted line. Estimates of the large and the small separations derived from the data analysis of stellar time series allow to constrain the mass and the evolutionary state of a particular object. Figure courtesy of J. Christensen-Dalsgaard.

initial hydrogen abundance, and the mixing length parameter of convection in the stellar models.

In addition to the determination of stellar fundamental parameters seismic measurements may also be used as diagnostics of several internal properties of the star. Sharp features in the sound speed profile of the star can give oscillations in the regular pattern of the mode frequencies of solar-like oscillations. These *acoustic glitches* may be analyzed in terms of the second difference, $\Delta_2\nu_{n\ell} = \nu_{n-1,\ell} - 2\nu_{n\ell} + \nu_{n+1,\ell}$, and have a high diagnostic potential even for low-degree modes with $\ell \leq 3$. By means of the second difference it is possible to measure the envelope helium abundance (e.g. Basu et al. 2004), the location of the near-surface helium ionization zones (e.g. Verner et al. 2006, Houdek and Gough 2007), and the depth of the base of the convection zone (e.g. Monteiro et al. 2000, Ballot et al. 2004, Verner et al. 2006, Houdek and Gough 2007). The asteroseismic inference of stellar structure requires very precise estimates on the mode frequencies. Monteiro et al. (2000) pointed out that the precision of the mode frequencies must be better than $0.1\,\mu$Hz to determine the depth of the convection zone. Such high precision is only achieved if

long and continuous time series and oscillation spectra with high signal-to-noise ratio are available. Verner et al. (2006) predicted the required length of a time series to detect the signatures of the helium ionization zones ($T = 3$ months), the depth of the convection zone ($T = 6$ months), and the envelope helium abundance ($T = 10$ months). Now that time series of such lengths are made available by CoRoT and Kepler, the measurement of such interior properties may become feasible even for distant stars.

1.5 Maximum likelihood estimation of stellar oscillation parameters

Helio- and asteroseismology rely on accurate mode frequencies. Maximum Likelihood Estimation (MLE) is a well established method in helioseismology to extract the solar p-mode parameters from the power spectrum (e.g. Anderson et al. 1990, Schou 1992, Toutain and Appourchaux 1994, Appourchaux et al. 1998, 2000, Gizon and Solanki 2003). The standard MLE is based on the assumption that the frequency bins in the power spectrum are uncorrelated. Thus, uninterrupted time series are required. MLE has been applied recently to analyze time series of solar-like oscillations (e.g. Appourchaux et al. 2008, Barban et al. 2009, García et al. 2009, Deheuvels et al. 2010). I will use MLE to analyze Sun-as-a-star data and the CoRoT observation of HD 52265.

The maximum likelihood method allows to estimate the parameters of a particular model based on the statistics of the power spectrum of an observed signal. Let $\tilde{y}_i = \tilde{y}(t_i)$ be the signal in the time domain sampled at times $t_i = i\Delta t$, where $i = 0, 1, \ldots, N - 1$ is an integer and Δt is the sampling time. The total length of the observation is $T = (N - 1)\Delta t$. The discrete Fourier transform of the observed signal is defined as

$$\hat{y}_j = \frac{1}{N} \sum_{i=0}^{N-1} \tilde{y}_i \, \mathrm{e}^{-\mathrm{i}2\pi \nu_j t_i} \quad \text{for } j \in \mathbb{N}, \tag{1.11}$$

with the frequency $\nu_j = j/T$ and the frequency resolution $1/T$. The power spectrum is the squared magnitude of the discrete Fourier transform, i.e. $P(\nu_i) = |y(\nu_i)|^2$. Woodard (1984) showed that the solar power spectrum is distributed as a χ^2 with two degrees of freedom. The probability density for the power at frequency ν_i is thus an exponential distribution

$$f(P_i) = \frac{1}{\overline{P_i}} \exp\left(-\frac{P_i}{\overline{P_i}}\right), \tag{1.12}$$

where $P_i = P(\nu_i)$ is the observed power and $\overline{P_i}$ is the expectation value of P_i. For solar-like oscillations the expectation value of the power near a mode frequency ν_0 can be modeled by a Lorentzian function (power of an exponentially damped harmonic oscillator, Anderson et al. 1990).

$$\overline{P_i}(\boldsymbol{\mu}) = HL(\nu) = H\left[1 + \left(\frac{\nu - \nu_0}{\Gamma/2}\right)^2\right]^{-1}. \tag{1.13}$$

Here, H is the peak amplitude of the Lorentzian and Γ is the the full width at half maximum (FWHM) which is related to the lifetime τ of the mode by $\tau = 1/\pi\Gamma$. In the Sun,

the mode linewidth of the low-degree five-minute oscillations is about $\Gamma \sim 1\,\mu$Hz corresponding to a lifetime of $\tau \sim 4$ days. I introduced the notation $\overline{P}_i = \overline{P}_i(\boldsymbol{\mu})$ to point out that the expectation value of the power is modeled by a set of parameters

$$\boldsymbol{\mu} = \{\nu_0, \Gamma, H\}. \tag{1.14}$$

If the section of interest of the power spectrum contains more than one mode (and modes with $\ell \geq 1$) the power spectrum can be modeled as a sum of Lorentzians. In that case $\boldsymbol{\mu}$ contains the mode parameters (ν_0, Γ, H) of each mode and possible additional parameters, e.g. the stellar angular velocity Ω. The vector $\boldsymbol{\mu}$ may also contain the parameters which describe the stellar and instrumental background in the power spectrum.

Because the frequency bins are independent, the joint probability density function (joint PDF) of the power spectrum is given by the product of probabilities

$$F(\boldsymbol{\mu}) = \prod_i f(P_i, \boldsymbol{\mu}). \tag{1.15}$$

In practice one minimizes the likelihood function

$$\mathcal{L}(\boldsymbol{\mu}) = -\ln F(\boldsymbol{\mu}) = \sum_i \left(\ln \overline{P}_i(\boldsymbol{\mu}) + \frac{P_i}{\overline{P}_i(\boldsymbol{\mu})} \right). \tag{1.16}$$

The ultimate goal of the MLE is to find the maximum likelihood estimates, $\boldsymbol{\mu}_\star$, that maximize the probability of observing the sample data:

$$\boldsymbol{\mu}_\star = \arg \min_{\boldsymbol{\mu}} \mathcal{L}(\boldsymbol{\mu}). \tag{1.17}$$

There are several methods to minimize $\mathcal{L}(\boldsymbol{\mu})$. I applied the downhill simplex method (Chapter 2 and 3 of this thesis) and the direction set method (Chapter 4 and 5 of this thesis, e.g. Press et al. 1992).

I note that the assumption of independent frequency bins in Equation (1.15) is valid only if the observed time series is continuous and does not contain gaps. Gabriel (1994) derived a joint PDF for the Fourier line of a gapped time series. In Chapter 4, maximum likelihood estimators of gapped time series are implemented for the first time and tested for solar-like oscillations and long-lived oscillations.

2 Implementation and validation of a global fit of stellar oscillation power spectra using solar observations

The main objective of this work is the analysis of time series of Sun-like stars. My intention is to implement a global fit of stellar oscillation power spectra. For global fits, the complete oscillation power spectrum is fitted at once including all identified low-degree modes ($\ell \leq 2$). I will further assume that the mode parameters frequency, linewidth, and amplitude vary smoothly with the radial order n so that a simplified parameterization can be used. I will calibrate and check it with Sun-as-a-star data from the VIRGO instrument onboard SoHO. The SPM data from the VIRGO instrument measure irradiance variations of the disk-integrated sunlight. In Section 2.1, I will describe the data that I use for the analysis. The parameterization of the solar power spectrum for the global fit is presented in Section 2.2, and finally, the results of the analysis are discussed in Section 2.3.

2.1 Solar observations with SoHO/VIRGO

The objective of the VIRGO instrument is the investigation of the solar interior using p modes measured from spectral irradiance and radiance variations. A detailed description of the VIRGO-instrument is given by Fröhlich et al. (1995). Two sunphotometers (SPM) are part of the VIRGO-instrument and measure the disk-integrated spectral irradiance at three different wavelengths (blue at $\lambda = 395$ nm, green at $\lambda = 500$ nm, and red at $\lambda = 865$ nm) with a cadence $\Delta t = 1$ min. SoHO has observed the Sun since 1996 allowing the measurement of solar p-mode parameters over more than a full sunspot cycle. For the global fit of the solar data I will split the VIRGO data into blocks of about 4 month according to the length of a typical CoRoT long run. This allows us to study many blocks of nearly uninterrupted time series of the Sun. The SPM data of the VIRGO instrument is well suited to test the global fit and to explore its performance for asteroseismic application.

The Level 2 data of VIRGO/SPM was downloaded from the public SoHO science archive at ESAC (European Space Astronomy Centre). The data set contains in total 4916 days of observation covering almost 14 years (1/1/1996 - 19/11/2009). For this analysis, I use the data of the green filter. The data reduction of the raw lightcurves was carried out year by year. The time series of each year was detrended using a two-day triangular filter. Missing data and outliers bigger than 7 σ were replaced by zeros. The full time series is shown in Figure 2.1. Next, the full time series was divided into sections
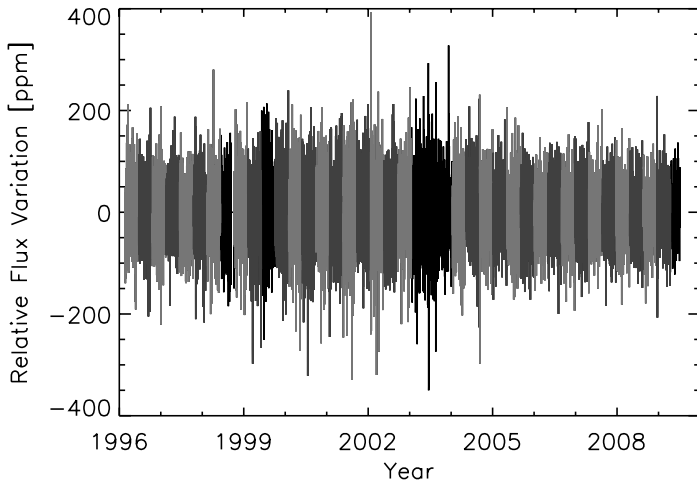
Figure 2.1: Fourteen years of Sun-as-a-star data obtained with SoHO/VIRGO (SPM-instrument, green channel). For practical reasons only one data point every 1000 points is shown. The *grey shaded regions* are 35 sections with a length of 120 days each and a duty cycle $\geq 97\%$. The *black regions* are sections of the data set which does not have a duty cycle $\geq 97\%$ for a block of 120 days. Details on the data reduction are given in the text.

with a length of $T = 120$ days. For the data analysis I only chose sections with a duty cycle higher than 97 %. The constraint on the duty cycle ensures a time coverage comparable to CoRoT observations and allows us to apply the standard maximum likelihood estimation as described in Section 1.5. In this way the full VIRGO data set was divided into 41 blocks of 120 days with 35 blocks fulfilling the condition on the duty cycle. These "good" 4-month blocks data are displayed in Figure 2.1.

Figure 2.2 shows the power spectrum of a 120 day VIRGO time series. The comb-like structure of low-degree p modes is evident in the frequency region $2200\,\mu Hz < \nu < 4100\,\mu Hz$. The power of the solar p modes peaks around $\nu \sim 3000\,\mu Hz$ corresponding to a period of $\sim 5\,min$ on top of a frequency-dependent background. The background increases at low frequencies. The background noise in the VIRGO irradiance observations is much higher than the background in velocity data (cf. Figure 1.1). The noise background is due to convection and photon noise. There is clear evidence for modes with $\ell \leq 2$ as shown in the inset. The large separation $\Delta\nu$ and the small separation $\delta\nu_{02}$ between modes with $\ell = 0, 2$ are easy to see.

A common representation of solar-like oscillations is the echelle diagram (Grec et al. 1983) where the power at a given frequency is plotted against the frequency modulo a folding frequency $\widetilde{\Delta\nu}$. In other words, the power spectrum is divided into $\widetilde{\Delta\nu}$-wide inter-
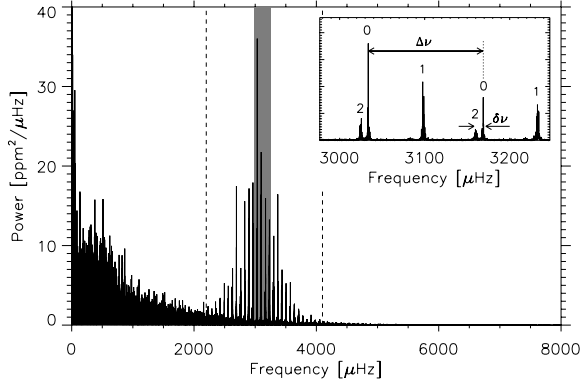
Figure 2.2: Oscillation power spectrum of a 120 day time series observed with SoHO/VIRGO. The solar-like oscillations are evident between $\nu = 2000 - 4000$ μHz. The *vertical dashed lines* mark the frequency range of the global fit. The power in the *grey shaded region* is amplified in the inset. It shows two series of modes with $\ell \leq 2$ corresponding to the sections $n^* = 23 - 24$ in Figure 2.3. The large separation $\Delta\nu$ and the small separation $\delta\nu$ are indicated by horizontal arrows.
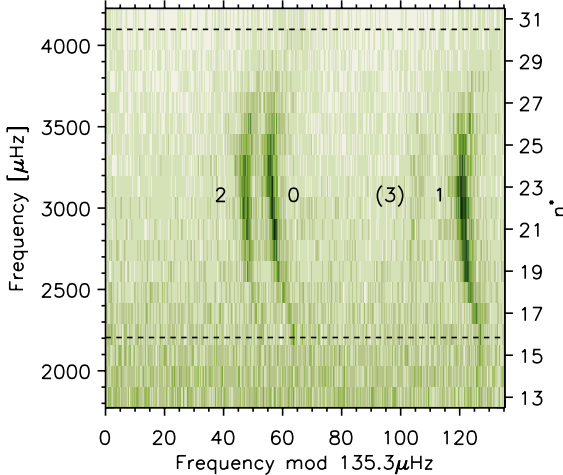
Figure 2.3: Echelle spectrum of the oscillation power spectrum from Figure 2.2. The frequency resolution is reduced by a factor of three for clarity. The folding frequency is $\widetilde{\Delta\nu} = 135.3$ μHz. Three distinct ridges corresponding to modes with $\ell = 0, 1$, and 2 are clearly visible. The distance between the ridges for modes with $\ell = 0$ and $\ell = 2$ is the small separation $\delta\nu$. In this particular realization, there is a very weak signature of $\ell = 3$ modes. The *horizontal dashed lines* mark the frequency range of the global fit. The right y-axis is an integer which denotes the $n^\star$'s section of width $\widetilde{\Delta\nu}$.

13

vals which are plotted section by section. The folding frequency $\widetilde{\Delta\nu}$ is chosen to be close to the large separation $\Delta\nu$. For a proper choice of $\widetilde{\Delta\nu}$ all modes with the same angular degree ℓ are arranged along individual ridges. As an example, Figure 2.3 shows the echelle diagram of the power spectrum in Figure 2.2. For $\widetilde{\Delta\nu} = 135.3\ \mu$Hz the echelle diagram shows three individual ridges corresponding again to modes with angular degree $\ell = 0, 1$, and 2. The small separation $\delta\nu_{02}$ between the ridges $\ell = 0$ and $\ell = 2$ is evident. Modes of oscillation with $\ell = 3$ are expected at lower frequencies with respect to the $\ell = 1$ ridge. In this particular example, there is only a weak indication for $\ell = 3$ modes. For some of the 35 blocks the $\ell = 3$ modes are in the noise. I consider only modes with $\ell = 0, 1$, and 2 in the global fit.

2.2   Parameterization of the global fit

Here I describe the parameterization of the expectation value of the solar oscillation power spectrum for the global fit. The expectation value of the power of a mode of solar-like oscillation is commonly modeled by a Lorentzian line profile (e.g. Anderson et al. 1990). This corresponds to the power of an exponentially damped harmonic oscillator. Thus, the expectation value of the power of the full solar power spectrum, $\overline{P}(\nu)$, is given as the sum of Lorentzians $L_{n\ell m}(\nu)$ on top of a global background model, $\mathcal{B}(\nu)$:

$$\overline{P}(\nu) = \sum_{n\ell m} L_{n\ell m}(\nu) + \mathcal{B}(\nu), \tag{2.1}$$

where, each mode of oscillation is characterized by a set of mode numbers $\{n\ell m\}$. The Lorentzian line profile of each mode is given by

$$L_{n\ell m}(\nu) = H_{n\ell m}(i)\left[1 + \left(\frac{\nu - \nu_{n\ell m}}{\Gamma_{n\ell m}/2}\right)^2\right]^{-1}, \tag{2.2}$$

where $H_{n\ell m}(i)$ is the mode height. The mode height for each mode depends on the inclination angle i of the rotation axis with respect to the line of sight. The parameters $\nu_{n\ell m}$ and $\Gamma_{n\ell m}$ are the mode frequency and the mode linewidth. Mode frequencies, linewidths, and amplitudes can be described in terms of smooth functions of the radial order n or the frequency ν. I will describe the specific functional form of these parameters in the following sections.

For the global fit itself, I will apply a two-step fitting strategy. In the first step, I will do a fit of the full power spectrum to determine the solar background noise. In the second step, I will derive maximum likelihood estimates of the oscillation parameters from a global fit of the oscillation power spectrum.

2.2.1   Fit of the solar background noise

Figure 2.4 shows the power spectrum of a 120 day VIRGO time series on a double-logarithmic scale. The frequency-dependent background consists of solar and non-solar contributions. The solar contribution to the background includes convection, e.g. granulation, mesogranulation, and supergranulation (e.g. Fröhlich et al. 1997). The non-solar contribution to the background is photon noise. The fit of the solar background noise is
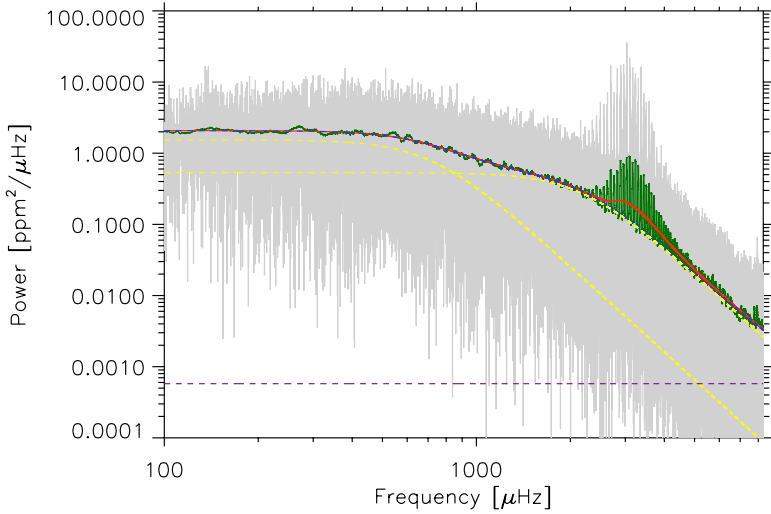
Figure 2.4: Fit of the solar background noise. The *grey* power spectrum corresponds to a 120 day time series observed with SoHO/VIRGO. The *green* spectrum is smoothed with a 25 μHz-boxcar. The *red line* is the fit of the smoothed power spectrum including the oscillation signal and the background noise. The *blue dashed line* represents the background noise alone composed of two Harvey models (*yellow dashed lines*) and a flat photon noise background (*purple dashed line*).

Table 2.1: Results of the fit of the solar background noise [Eq. (2.3)-(2.6)]. The values correspond to the mean and the 1σ standard deviation derived from fits of 35 blocks of 120 day time series of obtained from observations with SoHO/VIRGO.

Convection terms	$A_1 = (1.607 \pm 0.082)\,\mathrm{ppm}^2\,\mu\mathrm{Hz}^{-1}$
	$A_2 = (0.542 \pm 0.030)\,\mathrm{ppm}^2\,\mu\mathrm{Hz}^{-1}$
	$\tau_1 = (1390 \pm 30)\,\mathrm{s}$
	$\tau_2 = (455 \pm 10)\,\mathrm{s}$
Photon noise	$P_{\mathrm{WN}} < 0.004\,\mathrm{ppm}^2\,\mu\mathrm{Hz}^{-1}$
P-mode signal	$P_{\mathrm{S}} = (0.081 \pm 0.008)\,\mathrm{ppm}^2\,\mu\mathrm{Hz}^{-1}$
	$\nu_c = (3036 \pm 48)\,\mu\mathrm{Hz}$
	$\sigma_1 = (625 \pm 107)\,\mu\mathrm{Hz}$
	$\sigma_2 = (942 \pm 62)\,\mu\mathrm{Hz}$

performed in the frequency range between $100\,\mu\text{Hz} \leq \nu \leq 8300\ \mu\text{Hz}$. The upper limit is set by the Nyquist frequency $\nu_{\text{Ny}} = 1/(2\Delta t) \approx 8300\ \mu\text{Hz}$. I perform a least-square fit of a smoothed power spectrum to suppress large point-to-point variations and the fine structure of the solar p modes. For the smoothing I applied a $25\,\mu\text{Hz}$ boxcar. The expectation value of the smoothed power spectrum, $\overline{P}_{\text{smooth}}$, is modeled by two terms, one which describes the p-mode signal, P_{osc}, and one describing the background noise, N:

$$\overline{P}_{\text{smooth}}(\nu) = P_{\text{osc}}(\nu) + N(\nu). \tag{2.3}$$

I model the background noise, $N(\nu)$, by three components. Two components describe the solar contribution to the background, e.g. granulation, meso- and supergranulation. The third component is a flat photon noise, P_{WN}:

$$N(\nu) = \sum_{i=1}^{2} \frac{A_i}{1 + (\tau_i \nu)^4} + P_{\text{WN}}. \tag{2.4}$$

Here, A_i and τ_i denote the amplitude and the time scale of the i-th component. The two terms describing the solar background are similar to a Harvey model (Harvey 1985) except that the exponent is different (Harvey used an exponent of 2). I found an exponent of 4 fits the smoothed power spectrum better. This confirms the study of Michel et al. (2009) who found that the exponent for the green channel of VIRGO/SPM is close to 4. According to Harvey (1985) the expected time scales are $\tau \sim 5\,\text{min}$ for granulation, $\tau \sim 3\,\text{h}$ for mesogranulation and $\tau \sim 1\,\text{day}$ for supergranulation.

The power excess caused by the p modes of the Sun is modeled with an empirical envelope. Kallinger et al. (2010) for example used a Gaussian to model the p-mode envelope of Red Giants. In this study I found that a better fit of the envelope of the p-mode spectrum may be achieved by a function which is defined as

$$P_{\text{osc}} = P_{\text{S}} F(\nu, \nu_c, \sigma_1, \sigma_2), \tag{2.5}$$

where P_{S} is the amplitude of the envelope and F is a function of the form

$$F(\nu, \nu_c, \sigma_1, \sigma_2) = \begin{cases} \left[1 + \left(\frac{\nu - \nu_c}{\sigma_1}\right)^2\right]^{-2}, & \nu \leq \nu_c \\ \left[1 + \left(\frac{\nu - \nu_c}{\sigma_2}\right)^2\right]^{-2}, & \nu > \nu_c \end{cases}. \tag{2.6}$$

The function F is composed of two halves of squared Lorentzians with central frequency ν_c and widths σ_i ($i = 1, 2$) for frequencies below and above ν_c respectively. I emphasize that the function F describes the envelope of the full oscillation spectrum (for the Sun in the frequency range $2\,\text{mHz} \lesssim \nu \lesssim 4\,\text{mHz}$) and not the envelope of one single p mode.

Figure 2.4 shows the result of the fit of the smoothed power spectrum, P_{smooth}, and the solar background noise, $N(\nu)$. Table 2.1 lists the results of the least-square fit of the solar background noise including the parameters of the p-mode envelope. The numbers correspond to the mean and the 1σ standard deviation derived from fits of all 35 blocks of VIRGO data. The characteristic time scale $\tau_2 \approx 7.5\,\text{min}$ corresponds well to the typical time scale of solar granulation. The time scale $\tau_1 \approx 23\,\text{min}$ is short compared to the mesogranulation time scale given by Harvey (1985). However, Michel et al. (2009) note that the mesogranulation peak in the power spectrum may range up to $\sim 1\,\mu\text{Hz}$

corresponding to a time scale of 1000 s. This is consistent with the time scale τ_1 measured in this work. Supergranulation cannot be detected here since it peaks at frequencies $10\,\mu\text{Hz} \leq \nu \leq 100\,\mu\text{Hz}$, i.e. outside of the fitting region. For the photon noise I only give an upper limit since it is extremely low in 80% of all VIRGO power spectra which I analyze here. As expected, the power excess caused by the p modes is centered around 3 mHz.

For the estimation of the oscillation parameters the functional form and the parameters of the model for the background noise $N(\nu)$ are fixed. For the estimation of the oscillation parameters the background is only considered by a free scaling parameter, c_{bg}. I assume that the non-smoothed background noise can be written as

$$\mathcal{B}(\nu) = c_{\text{bg}} \cdot N(\nu). \tag{2.7}$$

2.2.2 Mode frequencies and rotational splitting

The estimates of the oscillation parameters are determined by a global fit, i.e. a simultaneous fit of the identified modes in the oscillation power spectrum. The frequency range of the global fit is constrained between $2200\,\mu\text{Hz} \leq \nu \leq 4100\,\mu\text{Hz}$, i.e. the frequency range where p modes are easily identified in the power and echelle spectra (Figure 2.2 and Figure 2.3). I only include those modes in the fit which can be easily identified and which are clearly above the noise level. At $\nu < 2200\,\mu\text{Hz}$ and $\nu > 4100\,\mu\text{Hz}$ the modes are in the noise.

The model of the oscillation power spectrum takes into account the regular pattern of solar-like oscillations. In terms of frequencies, this pattern is defined by the large and small separation, $\Delta\nu$ and $\delta\nu$. Here, the the mode frequencies of the p modes, $\nu_{n\ell 0} = \nu_{n\ell}$, are parameterized by a low-order polynomial of the radial order n.

Figure 2.5 shows an echelle spectrum according to Broomhall et al. (2009). These measurements are based on 23 years of BiSON-data. In the frequency range which is considered for the global fit, the frequencies can be fitted quite well with a 2nd-order polynomial:

$$\nu_{n\ell} = \sum_{i=0}^{2} c_i^{(\ell)} (n - n_0)^i \qquad \ell = 0, 1. \tag{2.8}$$

where the $c_i^{(\ell)}$ are free parameters of the fit. The parameter n_0 is an integer and denotes an arbitrarily chosen "central" radial order. Here, I chose $n_0 = 21$, i.e. near the maximum signal-to-noise of the solar p modes and close to the center of the frequency range of the global fit. In Equation (2.8), the $c_i^{(\ell)}$ can be interpreted as follows: for a particular ℓ, $c_0^{(\ell)}$ is the central mode frequency of the mode with radial order n_0, $c_1^{(\ell)}$ is an "average" large separation, and $c_2^{(\ell)}$ is the first-order deviation from a constant large separation, i.e. the curvature of the $\ell = 0$ and $\ell = 1$ frequency ridges in the echelle spectrum. Note that the modeling of the central frequencies with $\ell = 0$ and $\ell = 1$ using a simple parabola is applicable only in the frequency range $2200\,\mu\text{Hz} \leq \nu \leq 4100\,\mu\text{Hz}$. If a larger frequency range is used, one would need a higher order polynomial.

Figure 2.6 shows the small separation δ_{02} and δ_{13} as a function of the radial order n. The small separations were determined from the frequency measurements of Broomhall
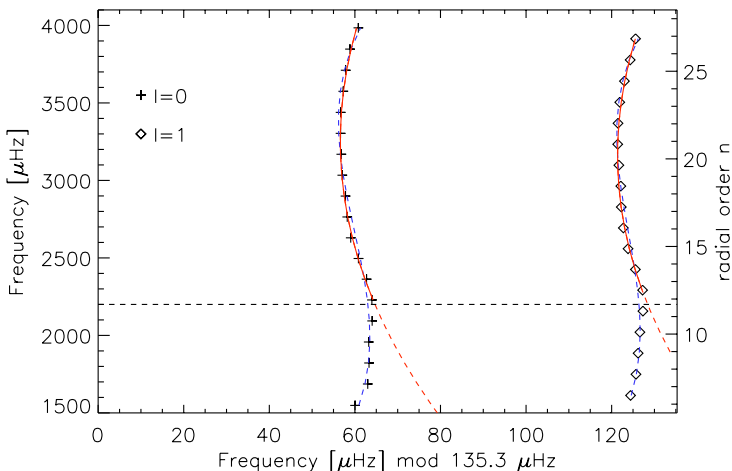
Figure 2.5: Solar p-mode frequencies of modes with $\ell = 0, 1$ in echelle format. The frequencies are derived from 23 years of BiSON observations (Broomhall et al. 2009). The 1σ error bars are smaller than the size of the symbols. The *red lines* show a 2nd order polynomial fit in the frequency range $2200\,\mu\text{Hz} \leq \nu \leq 4100\,\mu\text{Hz}$, i.e. the frequency range of the global fit (indicated by the *horizontal dashed line*). The *red dashed extended line* is the continuation of the 2nd order polynomial to frequencies $\nu \leq 2200\,\mu\text{Hz}$. The *blue dashed lines* represent a 3rd order polynomial fit for frequencies $1500\,\mu\text{Hz} \leq \nu \leq 4100\,\mu\text{Hz}$

et al. (2009). Figure 2.6 demonstrates that the small separation can be approximated well by a linear function of n. Given the small separation, $\delta\nu_{n\ell} = \nu_{n\ell} - \nu_{n-1\ell+2}$, the central frequencies of modes with angular degree $\ell = 2$ are

$$\nu_{n-1,2} = \nu_{n0} - \delta\nu_{02},$$ (2.9)

where the small separation is described as

$$\delta\nu_{02} = c_0^{(2)} + c_1^{(2)}(n - n_0).$$ (2.10)

The coefficients $c_i^{(2)}$ are free parameters and can again be interpreted as follows: $c_0^{(2)}$ is the small separation between the $\ell = 0$ mode with $n = n_0$ and the nearby $\ell = 2$ mode with $n = n_0 - 1$. The coefficient $c_1^{(2)}$ is the first-order deviation from a constant small separation. Note that the small separation δ_{13} could be modeled in the same way but $\ell = 3$ modes are not considered in this analysis.

The individual azimuthal components of the multiplets of non-radial modes ($\ell \geq 1$) are split due to the rotation of the Sun. For a mode of angular degree ℓ there are $2\ell + 1$ az-
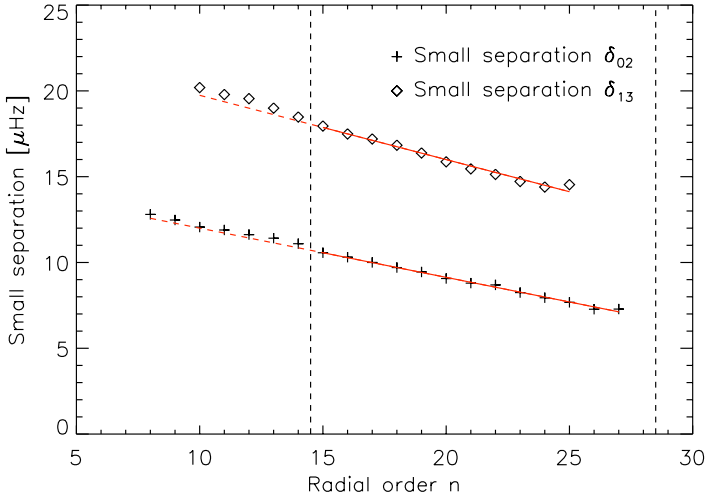
Figure 2.6: Small separation δ_{02} and δ_{13} as a function of radial order n. The small separation is determined based on the frequency measurements of Broomhall et al. (2009). The *solid red lines* are linear fits to the measured small separations within the frequency range of the global fit, i.e. $2200\,\mu$Hz $\leq \nu \leq 4100\,\mu$Hz or $15 \leq n \leq 28$ (indicated by the *vertical dashed lines*). The *red dashed extended lines* show the continuation of the linear fit to lower frequencies and lower radial orders respectively.

imuthal components denoted by m. Here, I assume slow rigid body rotation with angular velocity Ω. Thus, the splitting of the azimuthal components does neither depend on the radial order n nor on the azimuthal component m. Under these simplifying assumptions I write [cf. Equation (1.10)]

$$\nu_{n\ell m} = \nu_{n\ell} + m\Omega/2\pi \qquad \text{for } -\ell \leq m \leq \ell. \tag{2.11}$$

The rotational splitting $\Omega/2\pi$ of the azimuthal components of the non-radial modes is a free parameter of the global fit.

2.2.3 Mode linewidths

For the Sun, the linewidths of the p modes in the power spectrum depend on frequency. Overall, the linewidth increases with frequency and reaches a plateau of $\Gamma \sim 1\,\mu$Hz (or $\tau = 1/\pi\Gamma \sim 4$ days) at frequencies between $2500\,\mu$Hz $\leq \nu \leq 3000\,\mu$Hz. This particular frequency dependence of the mode linewidth can be observed for low- to medium-degree modes (e.g. Chaplin et al. 1998, Libbrecht 1988, Komm et al. 2000). Figure 2.7 shows the mode linewidth of solar radial p modes ($\ell = 0$) as a function of the radial order n.
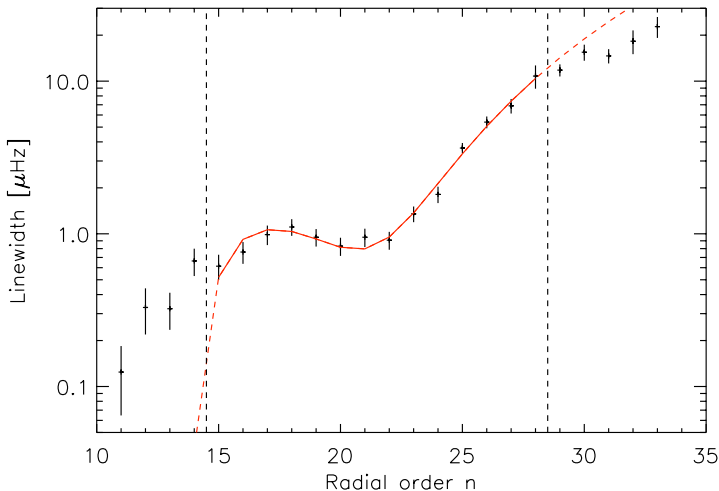
Figure 2.7: Mode linewidth (FWHM) of the radial modes ($\ell = 0$) of the Sun determined from about 4.5 years of BiSON-data (Chaplin et al. 1998). The mode linewidth is shown as a function of radial order n. The range of the global fit is indicated by the *vertical dashed lines*. The *solid red line* represents a 3$^{\text{rd}}$ order polynomial fit to the linewidth in the frequency range of the global fit, i.e. between $2200\,\mu\text{Hz} \leq \nu \leq 4100\,\mu\text{Hz}$ or $15 \leq n \leq 28$. The *dashed red extended lines* show the continuation of the fit beyond the range of the global fit.

The mode linewidths were determined from about 4.5 years of BiSON-data by Chaplin et al. (1998). For $18 \lesssim n \lesssim 23$, there is a slight dip of the linewidth. The physics of the frequency dependence of the p-mode linewidths is complicated. It is determined by the interplay of mode damping and excitation (e.g. Houdek 2006). As demonstrated in Figure 2.7 the linewidth of the radial modes can be well approximated by a simple 3$^{\text{rd}}$-order polynomial within the range of the global fit. Thus, I parameterize the mode linewidth of the radial modes, $\Gamma_{n\ell} = \Gamma_{n0}$, as

$$\Gamma_{n0} = \sum_{i=0}^{3} g_i (n - n_0)^i, \tag{2.12}$$

where the coefficients g_i are free parameters and n_0 is defined as in Section 2.2.2. Note that this empirical model may have to be modified if modes outside the chosen frequency range are included in the analysis. I note again that the particular choice of the frequency range for the global fit is solely based on the visibility of p modes in the solar power spectrum and is not motivated by having a simple dependence of Γ on n (or on ν). Chaplin et al. (1998) also showed that the linewidth of modes with $0 \leq \ell \leq 3$ obey the same frequency

dependence, i.e. at a given frequency the linewidth depends very little on the angular degree. Therefore, I assume that:

$$\Gamma_{n1} = \Gamma_{n0}, \qquad \Gamma_{n-1,2} = \Gamma_{n0}. \qquad (2.13)$$

I further assume that the mode linewidth does not depend on the azimuthal order m, i.e. $\Gamma_{n\ell m} = \Gamma_{n\ell}$.

2.2.4   Mode amplitudes and mode visibility

Solar oscillations show a characteristic distribution of mode amplitudes with a maximum at $\nu \sim 3000\ \mu$Hz. This amplitude distribution is the result of the interaction of modes excitation and damping (for details, see e.g. Goldreich et al. 1994, Houdek 2006).

For the global fit the amplitude envelope is modeled by a simple parameterized function. In Section 2.2.1 the envelope of the power of the solar p modes is modeled quite well by Equations (2.5)-(2.6). This functional form is adopted to determine the mode height $H_{n\ell m}(i)$ of a mode at frequency $\nu_{n\ell m}$:

$$H_{n\ell m}(i) = \frac{\mathcal{A}_\ell^2}{\pi \Gamma_{n\ell m}}\ \mathcal{E}_{\ell m}(i)\ F(\nu_{n\ell m}, \nu_0, \widetilde{\sigma}_2, \widetilde{\sigma}_2). \qquad (2.14)$$

In the equation above, $\mathcal{A}_\ell$ is the maximum of the amplitude envelope for modes with a particular angular degree ℓ. The envelope $F(\nu_{n\ell m}, \nu_0, \widetilde{\sigma}_1, \widetilde{\sigma}_2)$ is given by Equation (2.6). The center of the amplitude envelope is denoted by ν_0 and $\widetilde{\sigma}_i$ ($i = 1, 2$) are the widths of the envelope below and above ν_0. Assuming energy equipartition of the azimuthal components of the non-radial modes, Gizon and Solanki (2003) showed that the visibility of the individual m-components depend on the inclination angle, i, of the rotation axis with respect to the line of sight. The mode visibility, denoted by $\mathcal{E}_{\ell m}(i)$ in Equation (2.14), is given by

$$\mathcal{E}_{\ell m}(i) = \frac{(\ell - |m|)!}{(\ell + |m|)!} \left[P_\ell^{|m|}(\cos i) \right]^2 . \qquad (2.15)$$

Here, $P_\ell^m(\cos i)$ denotes the associate Legendre function of degree ℓ and order m (e.g. Abramowitz and Stegun 1965). Thus the model of the mode heights, $H_{n\ell m}(i)$, includes seven free parameters: three parameters (ν_0, $\sigma_{1,2}$) for the amplitude envelope, three parameters ($\mathcal{A}_\ell$) for the maximum of the envelope for a particular ℓ, and the inclination of the rotation axis which defines the height ratio of the azimuthal components.

The mode height, $H_{n\ell m}$, is measured in ppm^2/μHz. In the literature (e.g. Appourchaux et al. 2008, Barban et al. 2009), one often finds the mode amplitude, $A_{n\ell m}$, measured in ppm which is related to the mode height and the mode linewidth according to

$$A_{n\ell m} = \sqrt{\pi H_{n\ell m} \Gamma_{n\ell m}}. \qquad (2.16)$$

2.2.5   Asteroseismic constraints on Ω and i

Basic stellar oscillation parameters, e.g. mode frequencies, linewidths and amplitudes, may be determined with a fit of a suitable line profile to a peak in the Power spectrum of

a star. Furthermore, it is possible to infer the rotation of a star and the inclination angle of its rotation axis from the analysis of the time series. The inclination angle of the rotation axis may be inferred from the height ratios of the azimuthal components of the non-radial modes (see Section 2.2.4). Gizon and Solanki (2003) investigated the estimation of rotation and inclination by means of Monte Carlo simulations of long and uninterrupted time series. They demonstrated that for a star rotating at least twice as fast as the Sun and for an inclination angle $i \geq 30°$ both parameters may be estimated with high precision. Gizon and Solanki (2003) and Ballot et al. (2006, 2008) pointed out that a simultaneous fit of the rotational splitting and inclination angle of the rotation axis may be difficult to achieve for slowly rotating stars. In this context, a slow rotator is a star for which the mode linewidth Γ is of the same order or larger than the rotational splitting, i.e. $2\pi\Gamma/\Omega \gtrsim 1$. In such a case the inclination angle i cannot be inferred correctly. However, the so-called projected splitting $\Omega \sin i$ can still be estimated accurately. The difficulties of measuring $\Omega/2\pi$ and i independently for slow rotators should be kept in mind when interpreting the results of the global fit of the VIRGO data of the Sun and the HD 52265-data in the next chapter.

2.3   Global fit of the VIRGO data

In this section, I present the results of the global fit of 35 120-day blocks of VIRGO data. The determination of the solar p-mode parameters is performed with the maximum like-lihood estimation method (Section 1.5). I applied many random guesses to minimize the log-likelihood function [Equation (1.16)]. This allows us to test the stability of the fitting procedure by comparing the distributions of the initial guesses with the results of the fit. A high number of random initial guesses also improves the chance to recover the global minimum of the log-likelihood function instead of being confined to a local minimum. For the analysis of the VIRGO data in this work, I used 100 random guesses for each of the 35 realizations. The guesses are uniformly distributed around reasonable initial values for each parameter. For the frequencies and linewidths, these initial parameters are taken from Broomhall et al. (2009) and Chaplin et al. (1998) respectively. The initial values for the parameters of the amplitude envelope are taken from Table 2.1. The guesses of the rotational splitting and the inclination angle of the rotation axis are uniformly distributed in the range $0.1\,\mu\text{Hz} \leq \Omega/2\pi \leq 1.3\,\mu\text{Hz}$ and $0° \leq i \leq 90°$ respectively.

Figure 2.8 shows an example of the global fit to one block of a 120 day VIRGO time series. The figure shows the observed power spectrum and the expectation value of the power obtained with the global fit. The global fit covers a total of 14 radial orders of modes with $\ell \leq 2$. At first sight, the result of the fit looks reasonably good over the full range of the fit. An alternative representation of the result of the global fit is given in Figure 2.9. The figure shows small sections of the observed power spectrum around the fitted p modes, and the corresponding expectation value of the power deduced from the global fit. The sections are ordered according to their angular degree ℓ and their radial order n. At the bottom of Figure 2.9, there are average line profiles of modes with $\ell \leq 2$. These average line profiles are simply averages from the sections above. The averaging over several radial orders allows us to inspect the results of the global fit. It is evident, that the average line profile of the non-radial modes ($\ell = 1, 2$) is slightly broader than the
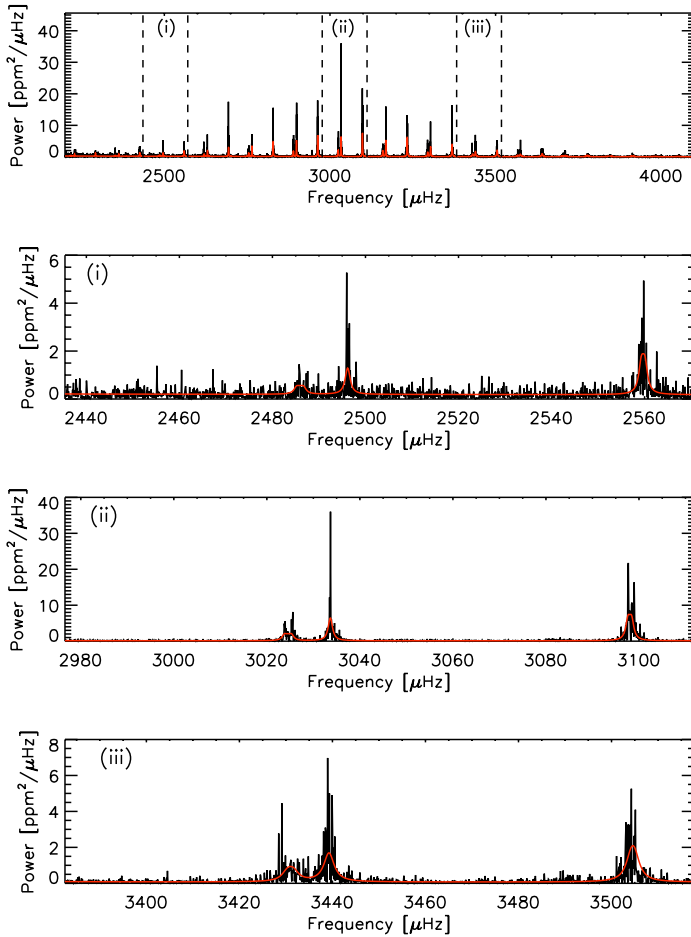
Figure 2.8: Global fit of the solar oscillation power spectrum. *Top panel:* Power spectrum of a 120 day time series of SoHO/VIRGO data (*black*) in the frequency range covered by the global fit performed in this work. The expectation value of the power determined with the fit is drawn as a *red line*. The three frequency regions *(i)-(iii)* indicated by the vertical dashed lines are shown enhanced in the panels below. Any of the panels *(i)-(iii)* shows one mode with $\ell = 2$, $\ell = 0$, and $\ell = 1$ (from left to right).
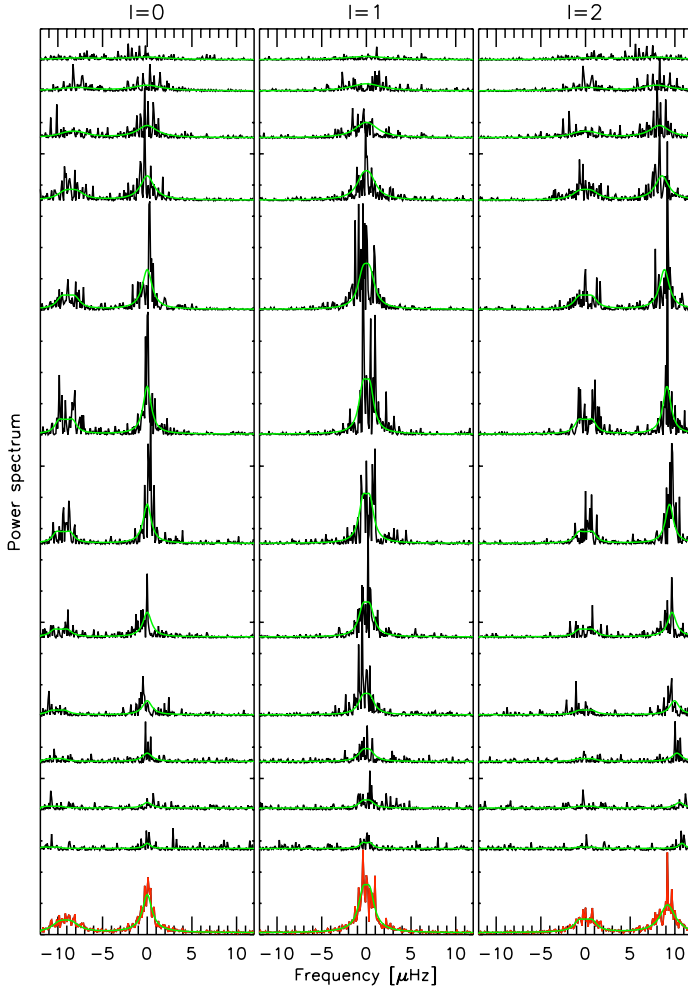
Figure 2.9: Global fit of the solar power spectrum of a 120 day time series of SoHO/VIRGO-data. The figure shows small sections of the observed power spectrum (*black*) centered around the mode frequencies. The modes are ordered by their angular degree ℓ (increasing from left to right) for 12 consecutive radial orders (n increasing from top to bottom). The *green* line represents the fit, i.e. the expectation value of the power. At the bottom the *red line* is an average over the radial orders shown above with an average fit in *green*. Note that the average $\ell = 0$ mode is slightly more narrow than the non-radial modes ($\ell = 1, 2$) but the azimuthal components are not resolved (for a detailed discussion, see Section 2.3.4).

average line profile of the radial $\ell = 0$ modes. This can be interpreted as the signature of rotational splitting of the azimuthal components of the non-radial modes. The splitting $\Omega/2\pi$ is small compared to the mode linewidth Γ, i.e. $2\pi\Gamma/\Omega \sim 2$, so that the individual azimuthal components are not resolved.

Figure 2.8 and Figure 2.9 demonstrate that the global fit of the solar oscillation power spectrum leads to a qualitatively reasonable results. For a quantitative evaluation, I performed a global fit for all 35 blocks of VIRGO power spectra. In the following sections, I discuss the results of the estimation of the solar p-mode parameters in detail.

2.3.1   Mode frequencies

Figure 2.10 shows the distributions of the 100 initial guesses and the corresponding fit results of the frequency parameters for one block of a 120 day time series of VIRGO data. The panels in Figure 2.10 show the distributions of the coefficients $c_i^{(\ell)}$ from Equation (2.8) and (2.10. The result of the global fit for each coefficient shows a single peaked distribution compared to the uniformly distributed set of initial guesses. The parameters of the best fit, i.e. those which minimize the log-likelihood function are all located close to the maximum of the distribution. The distributions of the individual parameters of all 35 blocks of VIRGO data show similar characteristics as those shown in Figure 2.10. Thus, the global fit of the mode frequencies is stable and does not show a significant bias for any of the parameters. The estimates of the coefficients $c_i^{(\ell)}$ allow us to calculate the mode frequencies of the $m = 0$ components according to Equations (2.8)-(2.10).

The VIRGO-observations analyzed here span over roughly 14 years. They cover the full solar cycle 23 and the onset of solar cycle 24. It is known that solar p-mode frequencies vary with solar magnetic activity (e.g. Woodard and Noyes 1985, Chaplin et al. 2001, Gelly et al. 2002). Recent studies (e.g. Howe et al. 2002, Chaplin et al. 2007, Salabert et al. 2009, 2010) investigated frequency shifts of low-degree solar p modes. Figure 2.11 shows the variation of the mode frequencies between 1996-2008 as determined in this work. The frequency shift is defined as the difference of a particular mode frequency measured at a certain time and the mean frequency averaged over the full time span. Each point in Figure 2.11 is a yearly average, i.e. the frequency shift is averaged over 2-3 blocks of VIRGO data. In 1998 and 1999, there are only two blocks with duty cycles higher than 97%, in 2003 no data set fulfills this requirement (cf. Section 2.1, Figure 2.1). The frequency shifts are furthermore averaged over modes in the frequency range 2500 μHz $\leq \nu \leq$ 3300 μHz. In this frequency range the considered modes have both a high signal-to-noise ratio and a rather small mode linewidth of $\Gamma \leq 2$ μHz ensuring a small frequency uncertainty of the individual frequency estimates. In this way, frequency shifts for modes with angular degree $\ell = 0, 1,$ and 2 are determined. Figure 2.11 shows a clear correlation between the frequency shift of the solar p modes and the solar surface activity during cycle 23 between 1996-2007. The mode frequencies increase during solar maximum ($\sim$1999-2002) and decrease again with decreasing surface activity. Note that the extended minimum with very low surface activity beyond 2007 is also recovered in the frequency shifts as the frequencies remain small. Interestingly, the frequencies for the $\ell = 0$ and $\ell = 2$ modes tend to increase slightly in 2007 and more significant in 2008 while the $\ell = 1$ mode frequencies keep decreasing. This is in agreement with the studies of Salabert et al. (2009, 2010) who interpret the ℓ-dependent changes of the frequency variations in terms of different
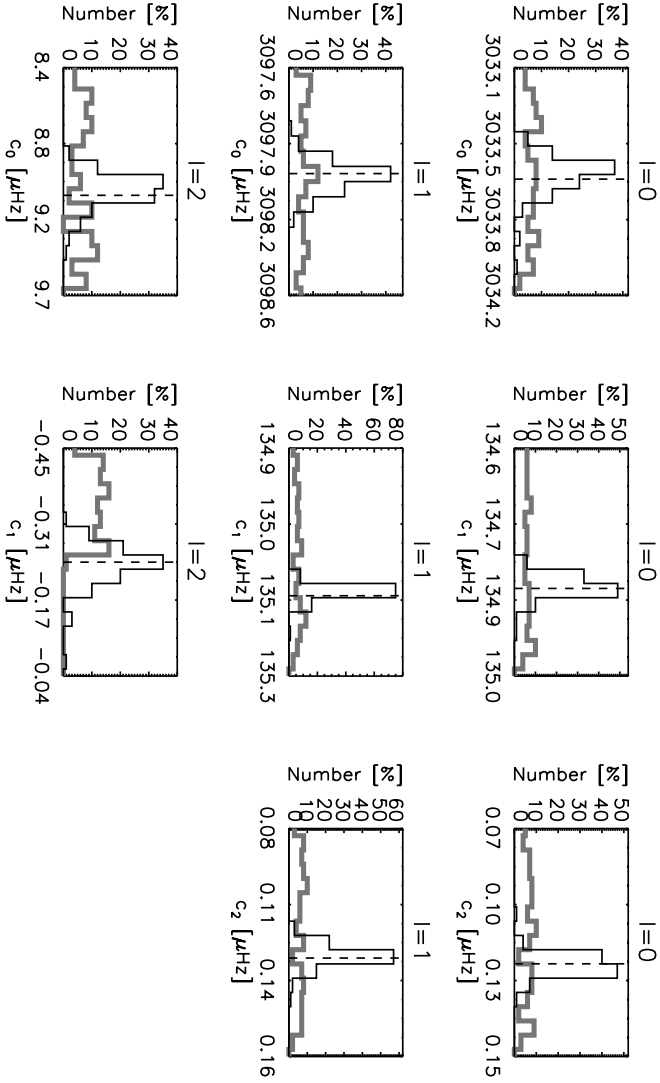
Figure 2.10: Distributions of the 100 initial guesses (*thick, grey*) and the corresponding fits (*fine, black*) of the frequency parameters for one particular block of a 120 day VIRGO time series. The fit results are determined with a global fit. In the model used in this analysis, frequencies are described in terms of 2nd-order polynomials. The distributions of these coefficients are shown in the individual panels. The row on top, in the middle, and at the bottom represent the coefficients for modes with $\ell = 0$, 1, and 2 respectively. The *vertical dashed lines* indicate the best fit.
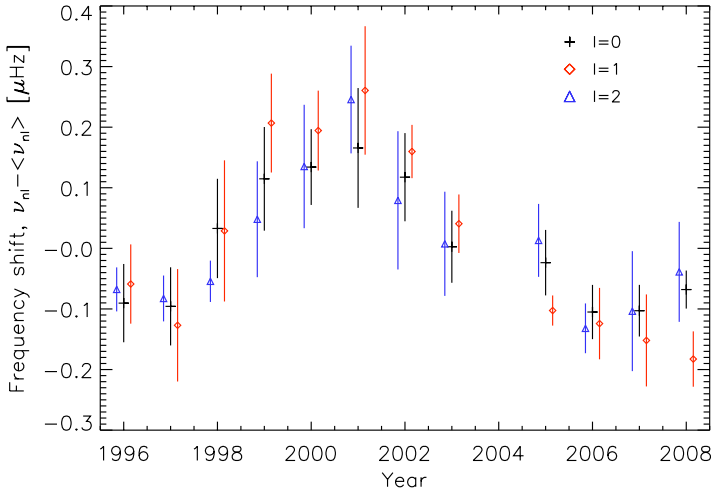
Figure 2.11: Solar cycle variation of the mode frequencies determined in this work. The VIRGO data used for this analysis covers the solar cycle 23 and the onset of solar cycle 24. The frequency shifts are defined as the difference between a particular mode frequency, $\nu_{n\ell}$, and the mean frequency, $\langle \nu_{n\ell} \rangle$, averaged over the full data set. The mode frequencies are determined with global fits of 35 blocks of 120 day time series of VIRGO data. They are averaged over one year, i.e. 2-3 blocks, and p modes with frequencies between $2500\,\mu$Hz $\leq \nu_{n\ell} \leq 3300\,\mu$Hz. Different symbols and colors correspond to different angular degrees of the modes (*black*: $\ell = 0$; *red*: $\ell = 1$; *blue*: $\ell = 2$). The size of the bar for each symbol represents the 1σ error.

responses to the spatial distribution of the magnetic field. In this context, the increase of the frequencies of the $\ell = 0$ and $\ell = 2$ modes may indicate an onset of solar cycle 24 with increasing activity at high solar latitudes. The absolute values for the frequency shift obtained in this analysis can be compared directly with Salabert et al. (2010) who also analyzed the VIRGO data during solar cycle 23. Considering the total shift of the mode frequencies, i.e. the difference between the solar minimum and the solar maximum, they found shifts of the order of $\sim 0.2\,\mu$Hz for $\ell = 0$ modes and $\sim 0.3\,\mu$Hz for the $\ell = 1$ and $\ell = 2$ modes in the green channel of VIRGO/SPM. In this work, the total frequency shift is of the same order of magnitude. The frequency shift of the $\ell = 1$ modes seems to be slightly higher during maximum solar activity (1999-2002) than the $\ell = 0$ modes. I note that the error estimates of Salabert et al. (2010) are much smaller than the error bars in this analysis. This may be attributed to the length of the time series that are analyzed in both studies. In this work, I analyzed 4-month time series while Salabert et al. analyzed time series with a total length of one year.

Table 2.2: Mode frequencies, $\nu_{n\ell}$, determined with a global fit of 35 blocks of 4 month time series of VIRGO data. The results given here correspond to the central frequency of the $m = 0$ components. The mode frequencies correspond to the mean of the measurements of the 35 blocks. The uncertainties are 1σ error bars for a 4 month observation (see text in Section 2.3.1 for details on the derivation of the uncertainty estimates).

| | Mode frequency $\nu_{n\ell}$ [μHz] | | |
n	$\ell = 0$	$\ell = 1$	$\ell = 2$
14			2218.07 ± 0.16
15	2228.94 ± 0.11	2291.90 ± 0.13	2351.88 ± 0.13
16	2362.45 ± 0.08	2425.63 ± 0.09	2485.94 ± 0.10
17	2496.20 ± 0.07	2559.62 ± 0.07	2620.22 ± 0.07
18	2630.20 ± 0.06	2693.86 ± 0.06	2754.77 ± 0.06
19	2764.45 ± 0.06	2828.37 ± 0.06	2889.56 ± 0.06
20	2898.95 ± 0.06	2963.12 ± 0.07	3024.60 ± 0.06
21	3033.70 ± 0.07	3098.14 ± 0.07	3159.89 ± 0.07
22	3168.70 ± 0.07	3233.41 ± 0.06	3295.43 ± 0.09
23	3303.94 ± 0.08	3368.94 ± 0.06	3431.21 ± 0.12
24	3439.43 ± 0.11	3504.72 ± 0.08	3567.25 ± 0.15
25	3575.17 ± 0.14	3640.76 ± 0.11	3703.53 ± 0.20
26	3711.15 ± 0.18	3777.06 ± 0.15	3840.06 ± 0.25
27	3847.39 ± 0.22	3913.62 ± 0.21	3976.83 ± 0.31
28	3983.87 ± 0.28	4050.43 ± 0.29	

Table 2.2 lists the central frequencies of the modes determined with the global fit in this work. The measured frequencies correspond to the mean derived from the frequency estimates of the 35 blocks of VIRGO data. The uncertainty estimates correspond to 1σ error bars of a 4 month observation. To derive these uncertainties, the standard deviations from frequency measurements during one year, i.e. 2-3 blocks of VIRGO data, are averaged over the full time span of the observation. Here it is assumed that the mode frequencies do not change much within one year of observation. The results of the fit of the mode frequencies is also illustrated in Figure 2.12. In this figure, the results of my global fit are directly compared with the mode frequencies of Broomhall et al. (2009). The Broomhall frequencies are determined from 23 years of observation with BiSON. Due to the length of the data set, the uncertainties of the Broomhall frequencies are small compared to the uncertainties determined in this work. This is particularly true at low frequencies $\nu \lesssim 3700\,\mu$Hz where the mode linewidth is small. At higher frequencies the uncertainties are comparable. I note that only ~ 40% of all frequency estimates match the Broomhall frequencies within 1σ and only ~ 60% within 3σ. The deviations may be attributed to the simplicity of the 2nd-order polynomial that is used here to describe the mode frequencies. As described in Section 1.4, sharp features in the sound speed profile cause variations of seismic observables, in particular the mode frequencies. These *acous-*
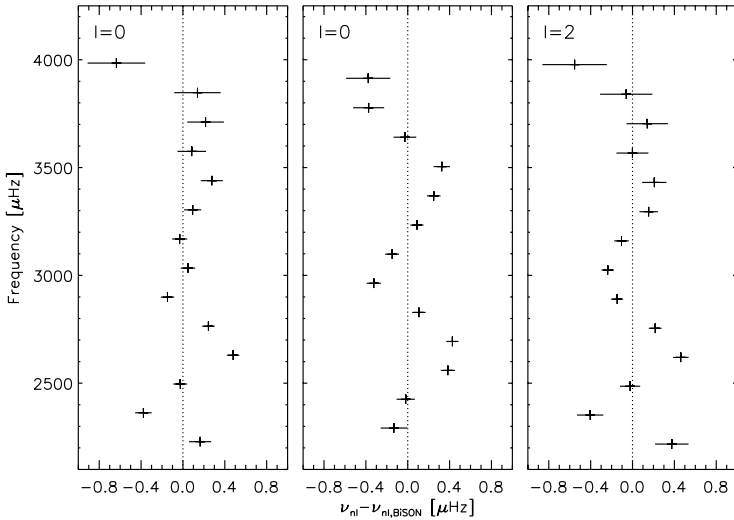
Figure 2.12: Frequencies of solar p modes determined with a global fit of 35 blocks of 120 day time series of VIRGO data. The measured frequencies, $\nu_{n\ell}$, are plotted versus the difference of $\nu_{n\ell}$ and the corresponding mode frequency from Broomhall et al. (2009), $\nu_{n\ell,\text{BiSON}}$. The width of the symbols in horizontal direction corresponds to the 1σ error of a 4 month observation derived in this work. The measured frequencies are ordered by their angular degree ℓ (*left:* $\ell = 0$; *middle:* $\ell = 1$; *right:* $\ell = 2$;) and by their radial order (increasing from bottom to top of each panel). The Broomhall frequencies are derived from 23 years of BiSON data. The uncertainties for frequencies $\nu \lesssim 3700\,\mu\text{Hz}$ are small compared to the error estimates determined in this work. At higher frequencies, they are comparable to the uncertainties determined in this work. The difference between the frequencies obtained with the global fit in this work and the BiSON frequencies can be attributed to the parabolic dependence of the mode frequency with radial order that was applied to parameterize the mode frequencies in this work.

tic glitches can be related for example to the bottom of the convection zone or at the He II ionization zone near the surface (e.g. Gough 1990, Monteiro et al. 2000, Basu et al. 2004, Ballot et al. 2004). These departures from the regular frequency pattern cannot be recovered by the 2nd-order polynomial. This is also illustrated in Figure 2.13 where the large separation of the radial modes, $\Delta\nu_0$, is plotted as a function of frequency. The frequency dependence of the large separation is shown for the frequency measurements of this analysis as well as for the BiSON frequencies of Broomhall et al. It is obvious that the global fit allows us to measure the global frequency dependence of the large separation, i.e. the
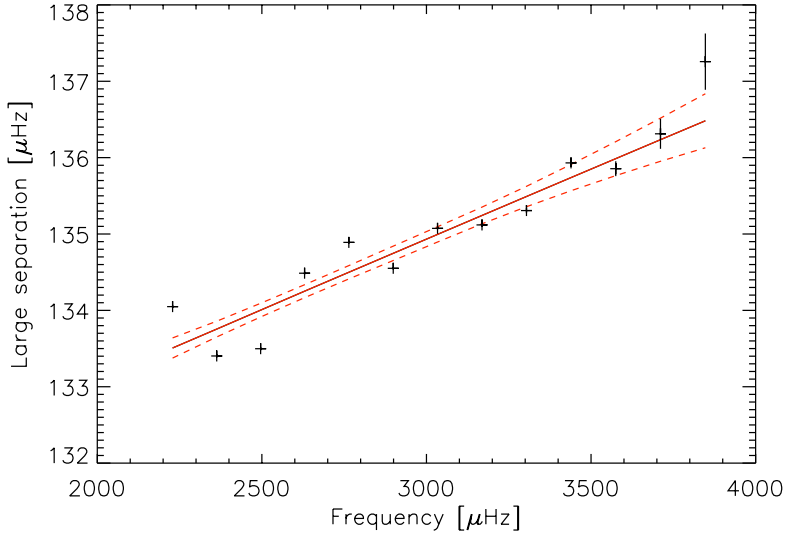
Figure 2.13: Large separation $\Delta\nu$ of the solar radial modes ($\ell = 0$) as a function of frequency. The *solid red line* shows the large separation deduced from the mode frequencies from Table 2.2, i.e. the results of this work. The *dashed red lines* represent the 1σ error. The *symbols* show the large separation determined from 23 years of BiSON observations (Broomhall et al. 2009). For frequencies $\nu > 3500\,\mu$Hz the symbol size represents the 1σ uncertainty of $\Delta\nu$, at lower frequencies the error is smaller than the symbol size.

overall increase of the large separation with frequency, but not the point-to-point variation that is visible in the BiSON frequencies.

Based on the frequency estimates determined in this work (Table 2.2), the mean large and small separation may be calculated. The solar large separation, $\Delta\nu_\odot$, depends on the frequency, i.e. it increases with frequency (Figure 2.13). Therefore I calculate the mean solar large separation according to

$$\langle\Delta\nu_\odot\rangle = \langle\nu_{n+1,\ell} - \nu_{n\ell}\rangle_{n\ell} \qquad \text{with } 20 \leq n \leq 22, \ \ell \leq 2. \qquad (2.17)$$

Here, $\langle\Delta\nu_\odot\rangle$ is a weighted average over the three radial orders with the highest signal-to-noise ratio (see Table 2.4) and degree $\ell \leq 2$. Thus, I obtain a mean large separation of the Sun: $\langle\Delta\nu_\odot\rangle = (135.01 \pm 0.05)\,\mu$Hz.

Using the same arguments as for the large separation, I calculate a mean small separation of the Sun according to

$$\langle\delta\nu_\odot\rangle = \langle\nu_{n0} - \nu_{n-1,2}\rangle_n \qquad \text{with } 20 \leq n \leq 22, \qquad (2.18)$$

i.e. again a weighted average over the three radial orders with the highest signal-to-noise-ratio. Thus I obtain: $\langle\delta\nu_\odot\rangle = (9.13 \pm 0.05)\,\mu$Hz.
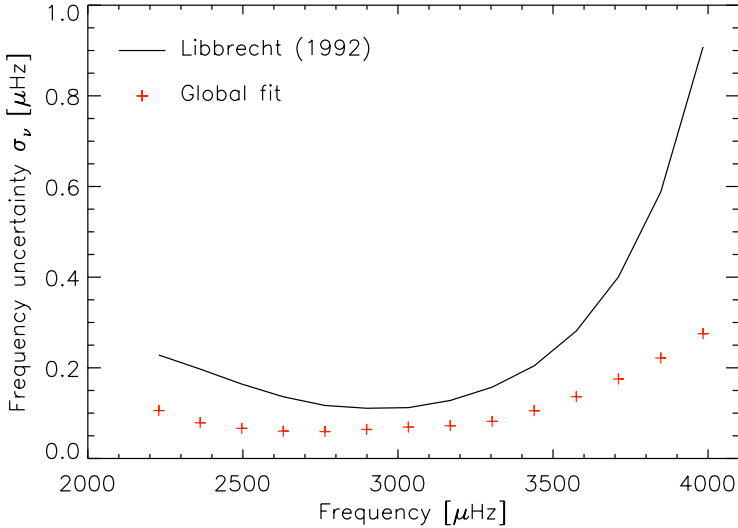
Figure 2.14: Uncertainties of the mode frequencies of the radial modes ($\ell = 0$). The *red symbols* represent the uncertainty of the global fit of 35 blocks of 120 day time series of VIRGO data (cf. Table 2.2). The *solid line* corresponds to theoretical uncertainties of an individual mode of oscillation according to (Libbrecht 1992).

The estimates of the frequency uncertainty listed in Table 2.2 correspond to 1σ error bars of a 4 month observation. To assess the order of magnitude of these uncertainty estimates, they may be compared to a theoretical estimate according to Libbrecht (1992). Libbrecht derived a relation for the frequency uncertainty σ_ν of an individual mode of solar-like oscillation as a function of the signal-to-noise ratio $H/\mathcal{B}$, the total length T of the observation, and the mode linewidth Γ:

$$\sigma_\nu^2 = f(\beta)\frac{\Gamma}{4\pi T} \qquad \text{with:} \quad f(\beta) = (1+\beta)^{1/2}[(1+\beta)^{1/2} + \beta^{1/2}]^3. \qquad (2.19)$$

Here, β is the inverse signal-to-noise ratio, $\mathcal{B}/H$, where H is the height of the mode in the power spectrum, and $\mathcal{B}$ is the background noise at the location of the mode. Theoretical estimates of the frequency uncertainty according to Equation (2.19) are calculated using the results of this work for the mode linewidth Γ, the mode height H, and the background noise $\mathcal{B}$ (see Section 2.2.1). Estimates on the mode linewidth Γ and the signal-to-noise ratio $H/\mathcal{B}$ are listed in Table 2.4 and will be discussed in detail in Sections 2.3.2 and 2.3.3 respectively. Figure 2.14 compares the measured frequency uncertainties of the radial modes ($\ell = 0$) with the theoretical expected estimates. The frequency uncertainty determined in this work is of a reasonable order of magnitude. However, compared with
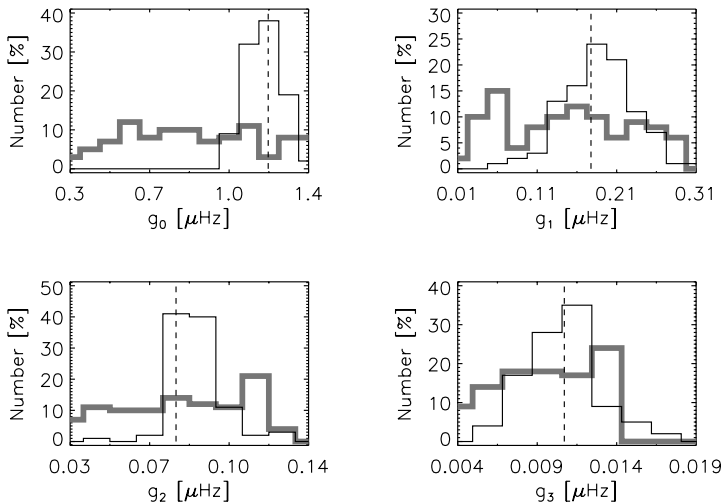
Figure 2.15: Distribution of 100 initial guesses (*thick, grey*) for the linewidth parameters and the corresponding results of the global fit (*fine, black*) for one particular block of a 120 day VIRGO time series. The individual panels correspond to the coefficients g_i ($i = 0, 1, 2, 3$) of a 3-order polynomial according to Equation (2.12). The *vertical dashed lines* in each panel denote the best fit.

the uncertainty estimates according to Libbrecht's formula, they are smaller by a factor of about two to three. The differences are particularly evident at low and high frequencies, i.e. for modes with a small signal-to-noise ratio. This may again be attributed to the simple 2nd-order polynomial that is used to model the mode frequencies. Obviously the mode frequencies at low signal-to-noise ratio are mainly constrained by the fit of the modes with high signal-to-noise. Furthermore I emphasize that the Libbrecht formula gives the frequency uncertainty of a single mode of oscillation. Thus, they cannot be compared directly with the frequency uncertainties derived from the global fit which is performed here.

2.3.2   Mode linewidths

The mode linewidth of the radial modes, Γ_{n0}, is parameterized by a 3rd order polynomial of the radial order n [cf. Section 2.2.3, Equation (2.12)]. Figure 2.15 shows the distributions of the 100 initial guesses of the linewidth parameters, g_i ($i = 0, 1, 2, 3$), and the corresponding results of the global fit for one block of a 120 day VIRGO time series.
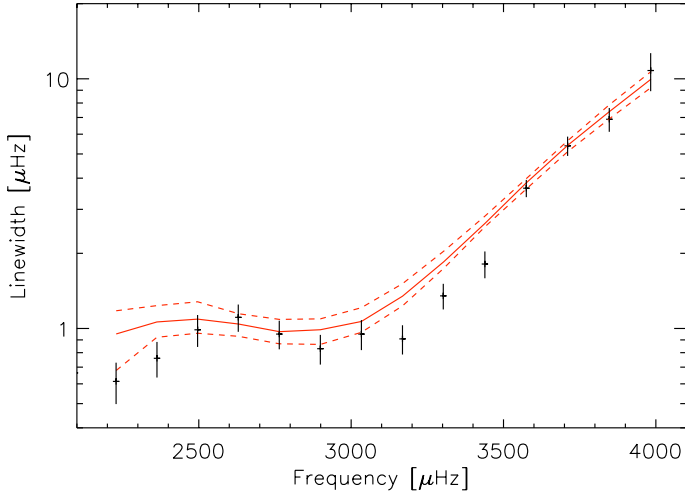
Figure 2.16: Mode linewidth, Γ_{n0}, of the radial modes ($\ell = 0$) as a function of the corresponding mode frequency, ν_{n0}. The linewidth is determined with a global fit of 35 blocks of 120 day VIRGO time series. The *solid red line* indicates the result obtained in this analysis including the 1σ error bar (*dashed red line*, see text for details). The *black symbols* represent the mode linewidth of the radial modes according to Chaplin et al. (1998).

While the initial guesses for all linewidth parameters are uniformly distributed, the distributions of the fit show a single peak. The best fit for any of the parameters is located close to the maximum of theses distributions. Even though the distributions of the fits are not quite symmetric, they suggest that a potential bias of the individual coefficients g_i is rather small. Thus, the fit of mode linewidth is stable and overall reliable.

The estimates of the coefficients g_i obtained for each of the 35 blocks of VIRGO data allow one to determine the mode linewidth $\Gamma_{n\ell}$ according to Equations (2.12)-(2.13). I found that the mode linewidth does not depend significantly on the sunspot cycle. Thus, I define the result of the global fit as the median of all 35 blocks. I define the 1σ error such that the uncertainty interval covers 68% of the results of all blocks. For the radial modes ($\ell = 0$) the results are shown in Table 2.4 and Figure 2.16. In Figure 2.16 the mode linewidth, Γ_{n0}, is plotted versus the corresponding mode frequency. For comparison, the BiSON linewidths according to Chaplin et al. (1998) are presented, too. The mode linewidths determined in this analysis reflect the overall frequency dependence quite well. The overall increase of the linewidth with frequency, the plateau in the range $2500\ \mu\text{Hz} \lesssim \nu \lesssim 3000\ \mu\text{Hz}$ including a small dip, and the steep increase at higher frequencies are well recovered. Compared to the BiSON linewidths however, the dip of the mode linewidth which is expected around $\nu \sim 3000\ \mu\text{Hz}$ is less pronounced and slightly shifted to smaller frequencies. Here, the steep increase of the mode frequencies

Table 2.3: Results of the global fit of the amplitude envelope of solar p modes. The parameters are determined with global fits of 35 blocks of 120 day VIRGO time series. The table lists the mean and the 1σ error of the individual parameters of the amplitude envelope. In order to consider amplitude variations over the solar cycle, the 1σ error corresponds to the mean of yearly uncertainty estimates, i.e. the standard deviation of 2-3 blocks of VIRGO data is averaged over the full time span of the observation.

Parameters of the amplitudes envelope	
Center of the envelope:	$\nu_0 = 3067 \pm 26\,\mu\text{Hz}$
Width of the envelope:	$\widetilde{\sigma_1} = 564 \pm 36\,\mu\text{Hz}$
	$\widetilde{\sigma_2} = 678 \pm 28\,\mu\text{Hz}$
Maximum of the envelope:	$\mathcal{A}_0 = 4.64 \pm 0.13\,\text{ppm}$
	$\mathcal{A}_1 = 6.08 \pm 0.15\,\text{ppm}$
	$\mathcal{A}_2 = 3.69 \pm 0.11\,\text{ppm}$

starts already at $\nu \approx 3000\,\mu\text{Hz}$. Thus, the linewidths for modes with $n = 22 - 24$ or $3100\,\mu\text{Hz} \leq \nu \leq 3500\,\mu\text{Hz}$ are slightly overestimated compared to the corresponding Bi-SON linewidths. However, even those linewidths match the BiSON measurements within a 3σ uncertainty range. The slight mismatch may be attributed to the simplified parameterization by a 3rd-order polynomial, that is used here to describe the mode linewidth over the full frequency range of the fit. Furthermore, the measurement of the mode linewidth of the low-degree solar p modes is often based on much longer data sets than the ones used in this analysis. The BiSON linewidths shown as a reference here are obtained from an analysis of a 32 month solar power spectrum so that the results of the global fit concerning the mode linewidth are still satisfying.

2.3.3 Oscillation amplitudes

The mode amplitudes and the corresponding mode heights are parameterized by an envelope function according to Equations (2.14)-(2.16). This envelope allows one to describe the p-mode amplitudes with angular degree $\ell \leq 2$ in the full oscillation power spectrum using only six free parameters. Three parameters describe the center, ν_0, and the width, $\widetilde{\sigma}_i$ ($i = 1, 2$), of the envelope, the other three parameters, $\mathcal{A}_\ell$ (with $\ell = 0, 1, 2$), are the maxima of the amplitude envelope for the corresponding angular degree ℓ. Figure 2.17 shows the distributions of the 100 initial guesses and the corresponding results of the global fit of these parameters for one block of a 120 day VIRGO time series. Comparing the uniform distribution of the initial guesses with the fit results, it is obvious that the global fit allows a reliable estimation of the parameters of the amplitude envelopes. The distributions of the fit results show a well defined single peak. The best fit is close the maximum of any of the distributions.

The maxima of the amplitude envelope, $\mathcal{A}_\ell$, and thus the mode amplitudes in the individual blocks of VIRGO data show a significant variation during the solar cycle, i.e. mode amplitudes are smaller during the solar maximum and higher during the solar minimum. In order to derive an uncertainty estimate for the amplitudes according to a 4 month time

Table 2.4: Mode parameters of the radial modes ($\ell = 0$) of the Sun obtained in this work. The parameters are the result of a global fits of 35 blocks of 120 day VIRGO time series. The error intervals correspond to a 4 month observation. The fit ranges over 14 consecutive radial orders (*column 1*). The mode frequencies ν_{n0} (*column 2*) correspond to Table 2.2 (see also Section 2.3.1). *Column 3* lists the mode linewidth, Γ_{n0}. The values for the linewidth correspond to the median of the results of the 35 blocks. The 1σ error intervals are defined such that 68% of all fits fall within the bounds set by the subscripts/exponents (i.e. 34% of the fits below/above the median). *Column 4* shows the mode amplitudes, $A_{n0} = \sqrt{\pi H_{n0} \Gamma_{n0}}$. The values are the mean amplitudes of all 35 blocks of VIRGO data. To take amplitude variations over a solar cycle into account, the 1σ error corresponds to the mean of yearly uncertainty estimates, i.e the standard deviation of the amplitudes of 2-3 blocks of VIRGO data is averaged over the full 14 years of data. *Column 5* lists the signal-to-noise ratio of the oscillation modes. It is defined as the ratio of the mode height, H_{n0}, and the background noise at the frequency of the corresponding mode, $\mathcal{B}(\nu_{n0})$.

| n	ν_{n0} [μHz]	Γ_{n0} [μHz]	A_{n0} [ppm]	$H_{n0}/\mathcal{B}(\nu_{n0})$
15	2228.94 ± 0.11	$0.95^{+0.23}_{-0.27}$	1.44 ± 0.08	2.7
16	2362.45 ± 0.08	$1.06^{+0.17}_{-0.14}$	1.81 ± 0.09	4.2
17	2496.20 ± 0.07	$1.09^{+0.19}_{-0.13}$	2.29 ± 0.09	7.7
18	2630.20 ± 0.06	$1.04^{+0.10}_{-0.11}$	2.90 ± 0.09	14.9
19	2764.45 ± 0.06	$0.97^{+0.12}_{-0.10}$	3.60 ± 0.11	28.2
20	2898.95 ± 0.06	$0.99^{+0.10}_{-0.13}$	4.27 ± 0.12	45.9
21	3033.70 ± 0.07	$1.07^{+0.14}_{-0.10}$	4.62 ± 0.13	56.0
22	3168.70 ± 0.07	$1.35^{+0.16}_{-0.12}$	4.54 ± 0.13	49.2
23	3303.94 ± 0.08	$1.85^{+0.19}_{-0.11}$	4.13 ± 0.12	34.1
24	3439.43 ± 0.11	$2.64^{+0.18}_{-0.08}$	3.56 ± 0.10	20.2
25	3575.17 ± 0.14	$3.84^{+0.15}_{-0.21}$	2.97 ± 0.08	11.2
26	3711.15 ± 0.18	$5.42^{+0.24}_{-0.31}$	2.43 ± 0.07	6.1
27	3847.39 ± 0.22	$7.39^{+0.48}_{-0.47}$	2.00 ± 0.06	3.4
28	3983.87 ± 0.28	$9.96^{+0.73}_{-0.73}$	1.64 ± 0.05	1.9
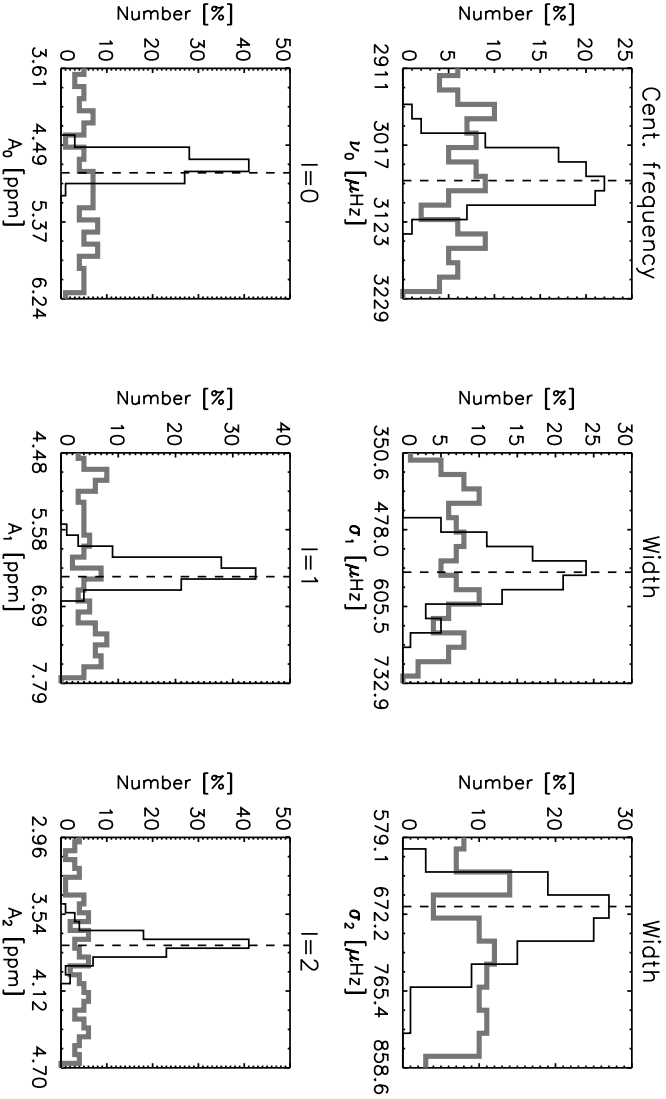
Figure 2.17: Distribution of the 100 initial guesses (*thick, grey*) and the corresponding results of the global fit (*fine, black*) of the amplitude parameters for one particular block of a 120 day VIRGO time series. The individual panels correspond to the central frequency ν_0 (*top left*), the width $\widetilde{\sigma}_i$ ($i = 1, 2$; *top middle/right*) and the maximum of the amplitude envelope $\mathcal{A}_\ell$ ($\ell = 0, 1, 2$; *bottom row*) according to Equations (2.14)–(2.15). The *vertical dashed line* in each panel denotes the best fit.
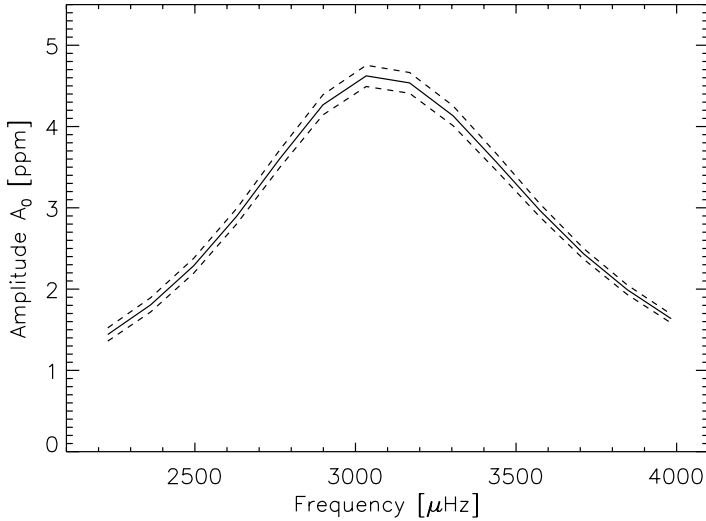
Figure 2.18: Mode amplitudes, A_0, of the radial modes ($\ell = 0$) as a function of the mode frequency, ν_{n0}. The amplitudes are determined from global fits of 35 blocks of 120 day VIRGO time series. The amplitudes are computed according to Equations (2.14)-(2.16). The *solid line* represents the mean amplitudes, the *dashed lines* correspond to 1σ error bars.

series, I adopt the same approach as for the mode frequencies. The amplitude parameters are averaged over the 35 blocks of VIRGO data, i.e. over 14 years. The 1σ error estimates are defined as the mean of yearly uncertainties. That implies the standard deviations of the individual parameters from within 1 year, i.e. 2-3 blocks of VIRGO data, are averaged over the full time span. Table 2.3 shows the mean and the 1σ error estimates on the individual parameters of the amplitude envelope. The center of the amplitude envelope is at $\nu_0 = 3067 \pm 26$ μHz confirming the maximum power of low-degree solar p modes at ~ 3 mHz. For the radial modes, I derive a maximum amplitude of $\mathcal{A}_0 = 4.64 \pm 0.13$ ppm. This result matches former measurements of the luminosity amplitude of low-degree solar p modes reasonably well. For instance, Kjeldsen and Bedding (1995) measured a luminosity variation of $(\delta L/L)_{550} = 4.7 \pm 0.3$ ppm where the index refers to a luminosity variation at a wavelength of $\lambda = 550$ nm. This value is determined from velocity measurements of low-degree solar p modes using a scaling relation derived in the same paper. Kjeldsen and Bedding (1995) relate the bolometric luminosity variation and the variation at a particular wavelength λ via

$$\left(\frac{\delta L}{L}\right)_{\text{bol}} = \left(\frac{\delta L}{L}\right)_{\lambda} \frac{\lambda}{623\text{nm}} \frac{T_{\text{eff}}}{5777\text{K}}. \tag{2.20}$$

Using this scaling relation, the amplitudes of the radial modes determined in this analysis at $\lambda = 500$ nm can be converted to a reference wavelength of $\lambda = 550\,\mu$Hz. Thus, I obtain a luminosity variation of $(\delta L/L)_{550} = 4.22 \pm 0.12$ ppm. Kjeldsen and Bedding also rescaled former measurements from Woodard and Hudson (1983), Jimenez et al. (1990), and Toutain and Froehlich (1992) and converted them to a reference of $\lambda = 550$ nm. Those studies were based on solar intensity measurements and led to a luminosity variation of 3.6 ppm $\leq (\delta L/L)_{550} \leq 6.5$ ppm which matches the results obtained in this analysis very well.

The estimates of the amplitude parameters allow us to calculate the mode heights, $H_{n\ell m}$, and the mode amplitudes, $A_{n\ell m}$, according to Equations (2.14)-(2.16). The mode amplitudes and their corresponding 1σ error bar is calculated in the same way as for the amplitude parameters above. I note that the mode amplitudes for modes with $\ell = 1, 2$ follow the same functional form and are only shifted by a factor of $\mathcal{A}_1/\mathcal{A}_0 \approx 1.3$ and $\mathcal{A}_2/\mathcal{A}_0 \approx 0.8$. The amplitudes A_{n0} of the radial modes and their corresponding uncertainty are shown in Figure 2.18 and listed in Table 2.4. The table also shows the signal-to-noise ratio $H_{n0}/\mathcal{B}(\nu_{n0})$ for the radial oscillations. It is defined as the ratio of the mode height H_{n0} to the background noise $\mathcal{B}(\nu_{n0})$ at the frequency of the corresponding mode, ν_{n0}. The modes included in this analysis have a signal-to-noise ratio of $2 \lesssim H_{n0}/\mathcal{B}(\nu_{n0}) \lesssim 60$.

2.3.4 Solar rotation and the inclination of the rotation axis

The solar rotation and the inclination of the rotation axis can in principle be measured from the splitting of the azimuthal components of the non-radial modes ($\ell \geq 1$) and their mode height ratio respectively (for details, see Gizon and Solanki 2003). In this analysis I assumed the splitting to be independent of the azimuthal order m and the radial order n, i.e. rigid body rotation.

Figure 2.19 shows the solar power spectrum and expectation value for a 120 day block of VIRGO data for modes with angular degree $\ell \leq 2$ averaged over 12 radial orders (cf. Figure 2.9). In this particular example, I obtained a rotational splitting $\Omega/2\pi = 0.40\,\mu$Hz and an inclination angle $i = 76°$. Due to the solar mode linewidth of $\Gamma \gtrsim 1\,\mu$Hz and thus $2\pi\Gamma/\Omega > 2$, the azimuthal components of the non-radial modes are not resolved. However, the average line profile of the non-radial modes is broader than the average line profile of the radial $\ell = 0$ modes. This broadening can be attributed to the contribution of the $|m| > 0$ components to the overall line profile. I conclude that the global fit allows us to detect the signature of rotation in the oscillation power spectrum of a slowly rotating star like the Sun. Finally, Figure 2.20 demonstrates the overall good performance of the global fit. The figure shows the ratio of the observed power spectrum and the expectation value determined with the global fit, i.e. the ratio of the black and the red lines in Figure 2.19. This ratio is distributed around one and does not show a significant bias.

The estimates for $\Omega/2\pi$ and i for the particular 120 day block of VIRGO data discussed above are derived from a global fit with 100 random initial guesses. The distribution of these guesses and the corresponding fits are shown in Figure 2.21. The best fit of the rotational splitting, $\Omega/2\pi = 0.40\,\mu$Hz, seems to be slightly underestimated considering the distribution of the fit results. For the inclination angle, i, the distribution of the fit results does not even show a clear peak. On the other hand, the distribution of the pro-

Table 2.5: Results of the global fit for the solar rotational splitting, $\Omega/2\pi$, the inclination angle of the rotation axis, i, and the projected splitting, $\Omega/2\pi \sin i$. The numbers in the *second column* correspond to the median and the 1σ error of global fits of 35 blocks of 120 day VIRGO time series. The 1σ error is defined such that 68% of all fits fall within the interval given by the subscripts/exponents. For reference some approximate intervals for the expected parameters are listed in the *third column*. The rotational splitting corresponds to surface rotation rates between latitudes $0° \leq \lambda \leq 60°$. The inclination of the solar rotation axis is inclined from the normal to the ecliptic plane by $\sim 7°$. The given interval considers that the actual inclination during a particular observation block depends on the ephemerides of the Sun.

Parameters for the Sun	Global fit (this work)	Reference solar values
Rotational splitting $\Omega/2\pi$ [μHz]	$0.52^{+0.12}_{-0.08}$	$\in [0.37, 0.45]$
Inclination i [°]	56 ± 11	$\in [83, 90]$
$\sin i$	$0.82^{+0.09}_{-0.12}$	$\in [0.993, 1]$
$\Omega/2\pi \sin i$ [μHz]	$0.424^{+0.038}_{-0.036}$	$\in [0.37, 0.45]$

jected splitting, $\Omega/2\pi \sin i$, shows a distinct peak with the best fit being very close to the center of this distribution. This confirms the results of Ballot et al. (2006, 2008): it is very difficult to measure the rotation and the inclination of the rotation axis reliably for slowly rotating stars. However, the projected splitting, $\Omega/2\pi \sin i$, can be measured precisely and unbiased.

The results for the rotational splitting $\Omega/2\pi$, the inclination i, and $\Omega/2\pi \sin i$ obtained from global fits of all 35 blocks of VIRGO data are summarized in Table 2.5. The numbers correspond to the median and the 1σ error of all 35 blocks. The table gives also reference values for the individual parameters. The reference interval for $\Omega/2\pi$ corresponds to a surface rotation rate at latitudes $0° \leq \theta \leq 60°$. The reference interval for the inclination considers that the solar rotation axis is inclined with respect to the normal of the ecliptic by $\sim 7°$ (Carrington 1863). The actual inclination for a particular block of VIRGO data depends on the ephemerides of the Sun. The estimates on $\Omega/2\pi$ and i obtained in this analysis are significantly biased with respect to the reference values, i.e. the rotational splitting, $\Omega/2\pi = 0.52^{+0.12}_{-0.08} \,\mu$Hz, is overestimated and the inclination angle, $i = 56° \pm 11°$, is underestimated. On the other hand, the projected splitting, $\Omega/2\pi \sin i = 0.424^{+0.038}_{-0.036} \,\mu$Hz, is in very good agreement with the expected solar reference value.

Figure 2.22 shows the estimates on $\Omega/2\pi$ and $\sin i$ for all 35 blocks of VIRGO data. Both parameters are correlated and equally distributed around a constant $\Omega/2\pi \sin i$. The color map represents the shape of the joint PDF (or the log-likelihood function) in the $\Omega/2\pi$-$\sin i$ plane. The colors correspond to the value of the joint PDF function obtained from global fits for various pairs of variates, ($\Omega/2\pi$, $\sin i$). For each point, the value of the joint PDF is averaged over all 35 blocks of VIRGO data. The estimates for $\Omega/2\pi$ and i for all 35 blocks are located around the maximum of the joint PDF. The joint PDF is very flat around its maximum (see bottom panel of Figure 2.22). So, it is very difficult
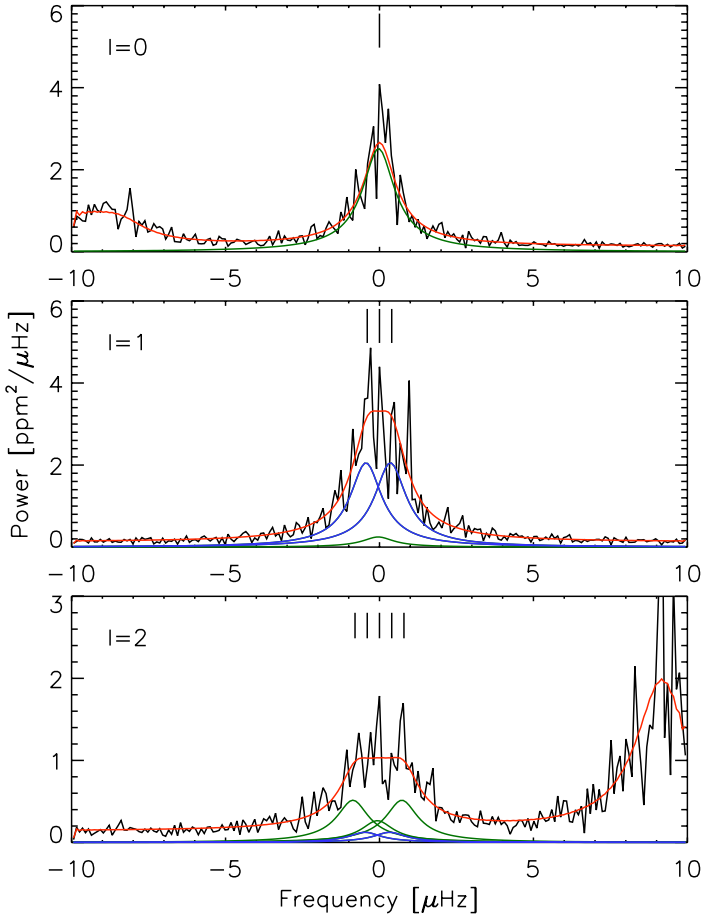
Figure 2.19: Solar power spectrum and the corresponding global fit for modes with angular degree $\ell \leq 2$ averaged over 12 radial orders for one 120 day block of VIRGO data (cf. Figure 2.9). The observed power is shown in *black*, the expectation value of the power in *red*. The vertical tick marks indicate the central frequencies of the azimuthal components which are separated by the rotational splitting $\Omega/2\pi$. The rotational splitting is assumed to be independent of the radial order and the azimuthal order. The *blue and green profiles* at the bottom of each panel show the individual odd and even azimuthal components of the corresponding averaged line profile.
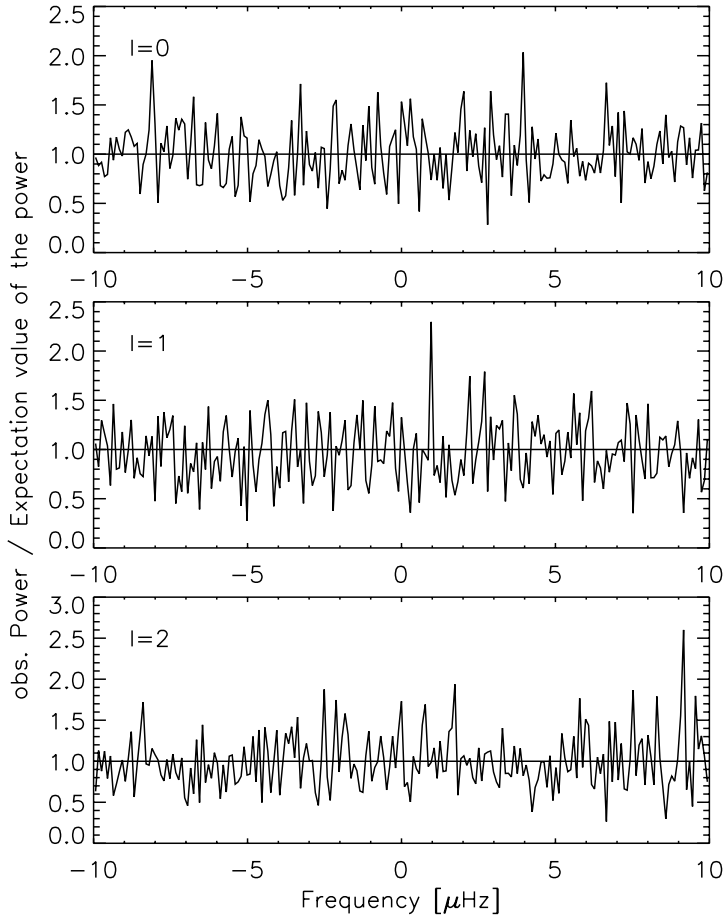
Figure 2.20: Ratio of the observed solar power spectrum and the expectation value of the power from Figure 2.19 for modes with $\ell \leq 2$. The observed power and the fit are averaged over 12 radial orders. Note that there is no systematic bias for any of the three cases indicating the reliability of the global fit.
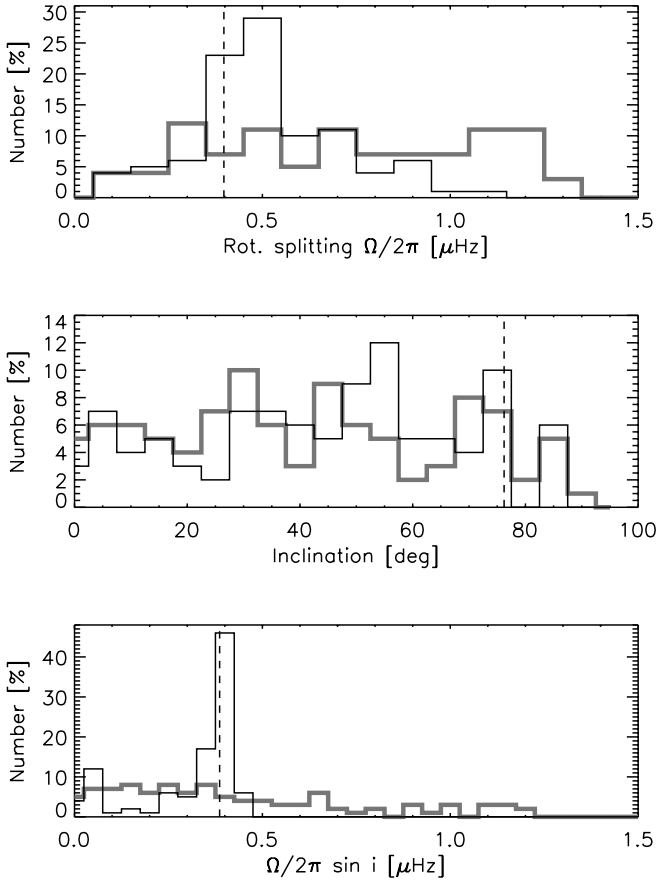
Figure 2.21: Distribution of 100 initial guesses (*thick, grey*) and the corresponding fits (*fine, black*) of the rotational splitting $\Omega/2\pi$ (*top*) and the inclination angle i of the rotation axis (*middle*) for one 120 day block of VIRGO data. The *bottom panel* shows the projected splitting, $\Omega/2\pi \sin i$, composed of the distributions in the panels above. The *vertical dashed lines* indicate the parameters of the best fit.

to give a reliable estimate of $\Omega/2\pi$ and i. Finally, the shape of the joint PDF allows us to give the following statement concerning the purely asteroseismic measurement of the solar rotation and the inclination of the rotation axis: within a 3σ error interval I find that the rotational splitting can be constrained between $0.30\,\mu$Hz $\leq \Omega/2\pi \leq 1.05\,\mu$Hz corresponding to a rotation period of 11 days$\leq P_{\text{rot}} \leq$39 days. The inclination angle of the rotation axis can be constrained between $0.4 \leq \sin i \leq 1.0$ (or $24° \leq i \leq 90°$). The two parameters are correlated and their product is $\Omega/2\pi \sin i = 0.424^{+0.038}_{-0.036}\,\mu$Hz within a 1σ error bar.

Given the reliable estimate of $\Omega/2\pi \sin i$ from the analysis of the time series, the individual estimates on $\Omega/2\pi$ and i may be further constrained when complementary measurements are taken into account. Figure 2.23 shows a 120 day VIRGO time series and the corresponding power spectrum at low frequencies (data courtesy of C. Fröhlich). There are two peaks at $\nu = 0.40\ \mu$Hz and $\nu = 0.59\ \mu$Hz. These peaks may be attributed to active regions dragged by solar rotation with a period of $P_{\text{rot}} = 29$ days and $P_{\text{rot}} = 20$ days respectively. There are also two possible harmonics at $\sim 1\ \mu$Hz and $\sim 1.4\ \mu$Hz. I emphasize that this is just one example. For various blocks of data, the exact position of the features in the low frequency power spectrum may vary slightly. Combining the estimate on the solar surface rotation with the seismic estimate on $\Omega/2\pi \sin i$ allows us to constrain the inclination angle of the solar rotation axis (see intersection of the corresponding lines in Figure 2.22). Thus, I obtain $0.66 \leq \sin i \leq 1.0$ or ($41° \leq i \leq 90°$). Note that in this case the uncertainty on the inclination angle of the rotation axis is dominated by the precision of the rotation measurement, i.e. a more precise constraint on the solar rotation allows one to estimate of the inclination angle more precisely.

2.4   Discussion: Is the global fit good enough for asteroseismology?

In this chapter I implemented a global fit of stellar oscillation power spectra. The global fit was tested using 4 month blocks of Sun-as-a-star observations from SoHO/VIRGO which cover a total time span of about 14 years. The parameterization of the expectation value of the power spectrum takes into account the regular pattern of the global p-mode spectrum in terms of smooth functions of the radial order n and the frequency ν. With the global fit I am able to measure the oscillation parameters of the solar p modes as accurate as expected for a 4 month observation. The large and small frequency variations are measured without bias over the radial orders $15 \leq n \leq 28$. Variations of the p-mode parameters over the course of the solar cycle are recovered. Since the Sun is a slowly rotating star, only $\Omega \sin i$ could be measured accurately. The independent estimates on Ω and i are biased. The simplified parameterization of the expectation value of the global oscillation power spectrum reduces the number of free parameters for the global fit significantly. In this analysis, the global fit includes 14 radial orders and modes with $\ell \leq 2$ and contains 20 free parameters. A fit with independent parameters for frequencies, linewidths, and amplitudes contains 128 free parameters. The reduction of the number of free parameters reduces the computation time significantly and minimize the risk of premature convergence of the fit. However, due to the simplified model some information is lost, e.g. the details of the variation of the large separation with frequency.

The global fit can be applied to time series of distant stars. However, the time series and the star itself have to fulfill several requirements. Time series of distant stars have a significantly higher noise level than observations of the Sun. The observed star has to be bright enough so that the oscillation signal is above the noise background. Furthermore, the data have to be continuous and long enough so that modes with particular radial order n and angular degree ℓ are resolved in the power spectrum. To adopt a simple parameterization of the expectation value of the oscillation power spectrum, the mode parameters of stellar oscillations have to vary smoothly with radial order. Thus, stars that are very Sun-like seem to be particularly suited. The stars must provide an oscillation spectrum that allows one an unambiguous identification of the angular degree ℓ of the modes. For instance, HD 49933 (Appourchaux et al. 2008) is an F5 dwarf which shows a clear oscillation power spectrum of solar-like p modes but the mode linewidth is comparable to the small separation such that an unambiguous mode identification is not possible.

Furthermore, the star must not be too evolved. When a solar-like star evolves from the main sequence towards its subgiant phase it may exhibit so-called mixed modes which have the characteristics of p modes near the surface and g modes near the stellar core. These modes show a clear deviation from the regular frequency spacing of modes with subsequent radial orders. In such a case, the mode frequencies cannot be described with a simple smooth function. HD 49385 (Deheuvels et al. 2010) is an evolved solar-like star which is in the transition from the main sequence to the post-main sequence phase. It exhibits mixed modes which show a clear deviation from the regular frequency spacing.

In the next chapter I will present the analysis of the time series of the Sun-like star HD 52265 which was observed with CoRoT for 4 months. HD 52265 delivers an excellent solar-like power spectrum that fulfills all requirements discussed above and allows one to adopt the global fit.
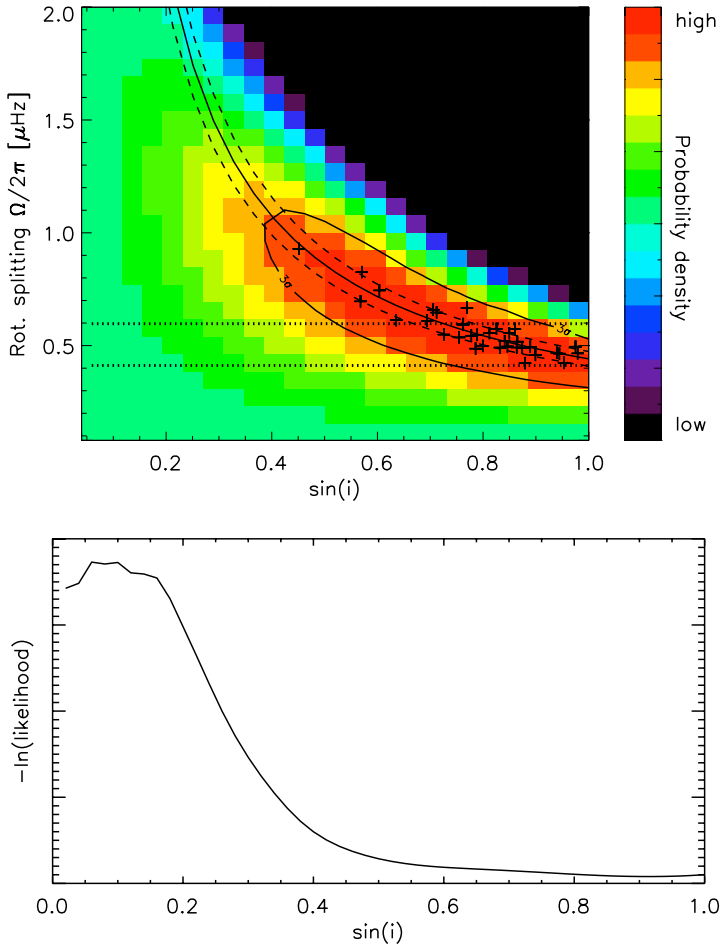
Figure 2.22: Map of the joint PDF in the $\Omega/2\pi$-$\sin i$ plane (*top panel*). The colors represent the value of the joint PDF for a pair of parameters, ($\Omega/2\pi$, $\sin i$), determined with global fits of 35 blocks of 120 day VIRGO time series. The *symbols* show the results for $\Omega/2\pi$ and i of the global fits of the 35 blocks of VIRGO data. The *solid and dashed black lines* represent the fit result of $\Omega/2\pi \sin i = 0.424^{+0.038}_{-0.036} \, \mu$Hz. The *horizontal dotted lines* mark the position of the two peaks in the low frequency power spectrum in Figure 2.23 and are attributed to solar surface rotation. The *contour line* shows the 3σ error of $\Omega/2\pi \sin i$ around the minimum of the likelihood function. *Bottom panel:* Cut through the log-likelihood function at constant $\Omega/2\pi \sin i = 0.424 \, \mu$Hz, i.e. a cut along the solid black line in the upper panel.
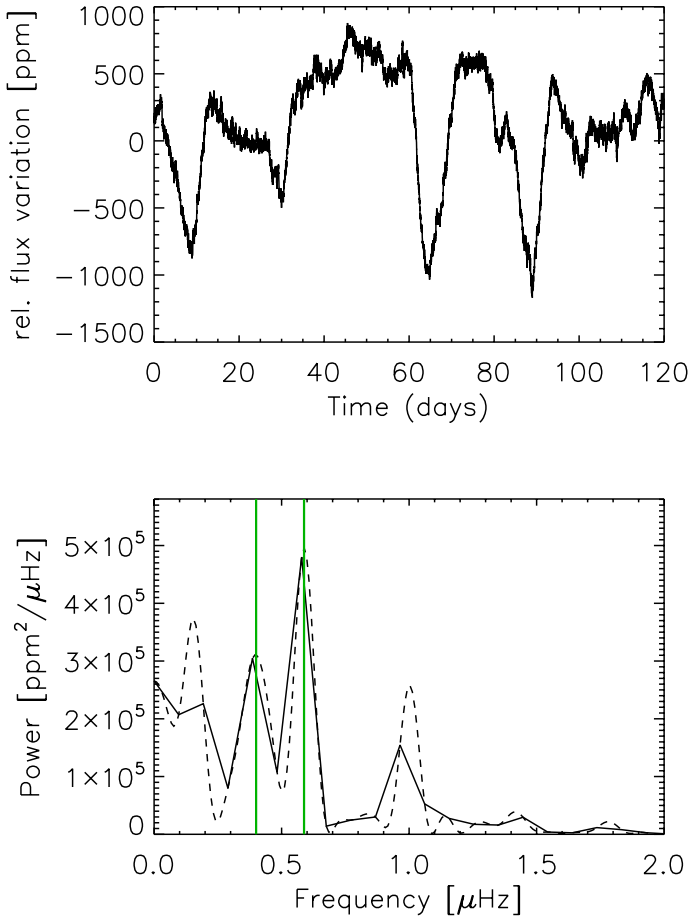
Figure 2.23: Solar surface rotation determined from the low-frequency power spectrum. The *top panel* shows a 120 day VIRGO time series. The *bottom panel* displays the corresponding power spectrum at low frequencies. The *dashed line* shows the power spectrum oversampled by a factor of 10. The *vertical green lines* mark two peaks which are attributed to the surface rotation of the Sun. The peaks are at $\nu = 0.40\ \mu$Hz and at $\nu = 0.59\ \mu$Hz corresponding to a rotation period of $T = 29$ days and $T = 20$ days respectively.

3 Asteroseismic analysis of the solar-like star HD 52265

In this chapter, I analyze the solar-like star HD 52265 which was observed continuously for about four months with the CNES-ESA space telescope CoRoT. HD 52265 was proposed as a possible CoRoT target by L. Gizon in 2005 and selected as a primary target for a CoRoT long-run thanks to the efforts of the CoRoT Scientific Committee (LRa2, November 2008 to March 2009). The analysis of the data presented in this thesis is original. In parallel, the HD 52265 data are being analyzed independently by several members of the CoRoT Data Analysis Team (DAT), led by J. Ballot. The CoRoT observations are supplemented by spectroscopic follow-ups with the Narval[1] spectropolarimeter installed on the Bernard Lyot Telescope at the Pic du Midi Observatory (France), led by C. Catala and H. Bruntt. My results were presented as a poster at the 2010 HELAS IV International Conference (Gizon et al. 2010a) and will be submitted for publication shortly. They were compared to the other results from the DAT in the poster by Ballot et al. (2010), which has resulted in another publication since then (Ballot et al. 2011).

The star HD 52265 is particularly interesting as it is very similar to the Sun with respect to its fundamental parameters and it is the only solar-like star which was known to host a planet before the launch of CoRoT. The known properties of both the central star and its companion are summarized in Section 3.1. The photometric observations with CoRoT are presented in Section 3.2. In Section 3.3, I will present the HD 52265 power spectrum. The determination of the stellar background is presented in Section 3.4. In Section 3.5 and 3.6, I describe the parameterization of the power spectrum model, the estimation of errors using Monte Carlo simulations, and the global fit itself. The results of the global fit are presented in Section 3.7.

3.1 The solar-like star HD 52265

HD 52265 (CoRoT 1426, HIP 33719) is a Sun-like star of spectral type G0 V with magnitude m_V = 6.29 (Perryman et al. 1997). In the past, HD 52265 was a target of various spectroscopic surveys which provided us with numerous measurements of its stellar parameters. For details on particular measurements see Gonzalez et al. (2001), Santos et al. (2004), Takeda et al. (2005), Valenti and Fischer (2005), Gillon and Magain (2006). In addition to the CoRoT observation of HD 52265, spectroscopic follow-ups with Narval@Bernard Lyot were carried out in December 2008 and January 2009 (Ballot et al.

---

[1]http://www.ast.obs-mip.fr/projets/narval/v1/
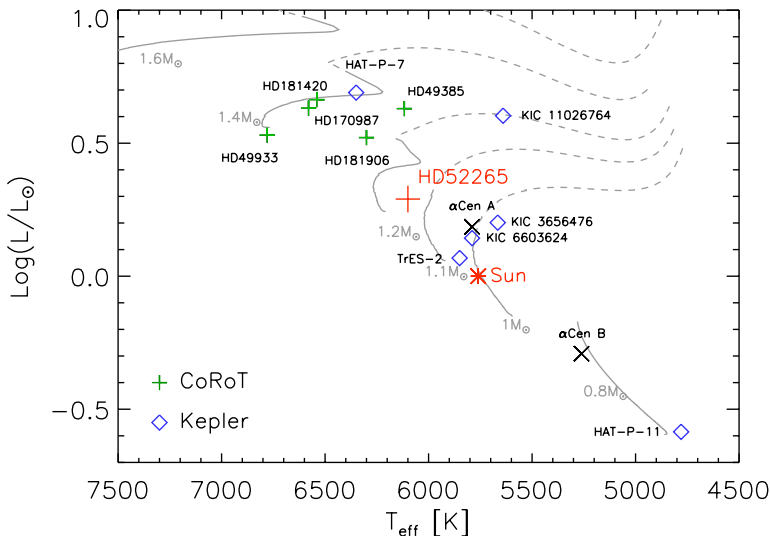
Figure 3.1: Location of HD 52265 (*red cross*) in the Hertzsprung-Russell diagram (HRD). The size of the symbol represents the uncertainties on the effective temperature and the luminosity. The other symbols show solar-like stars observed with CoRoT (*green crosses*) and Kepler (*blue diamonds*) as well as the Sun (*red asterisk*) and α Cen A,B (*black crosses*). Stellar evolutionary tracks are taken from Marques et al. (2008). They correspond to evolutionary tracks of stars with solar metal abundances and masses between $0.8 \leq M/M_\odot \leq 1.6$. The *solid sector* of each track represents the evolution on the main sequence, the *dashed sector* the post-main sequence evolution.

2011). Overall, the stellar parameters of the individual studies match fairly well, the most important differences are discussed below. Some important stellar parameters of HD 52265 are summarized in Table 3.1.

The luminosity of HD 52265 can be derived from the *Hipparcos* parallax (Perryman et al. 1997, van Leeuwen 2007), its magnitude, the bolometric correction, and the solar bolometric magnitude of the Sun. It is determined to be $\log(L/L_\odot) = 0.29 \pm 0.05$ (Valenti and Fischer 2005). Combined with an effective temperature of $T_{\text{eff}} = 6100 \pm 60$ K (Ballot et al. 2011), HD 52265 is located close to the Sun in the Hertzsprung-Russell diagram (HRD) as shown in Figure 3.1. In fact, among all solar-like stars observed with CoRoT so far (see Michel et al. 2008, Appourchaux et al. 2008, Barban et al. 2009, García et al. 2009, Deheuvels et al. 2010, Mathur et al. 2010), HD 52265 is the most Sun-like star in the HRD. The figure also shows the first solar-like stars observed with Kepler (Christensen-Dalsgaard et al. 2010, Chaplin et al. 2010). The stellar evolutionary tracks shown in the HRD are taken from Marques et al. (2008, Model Grid A) and show the evolution of stars

Table 3.1: Parameters of the Sun-like star HD 52265 determined from non-seismic measurements and their respective references. Parameters from Ballot et al. (2011) are based on ground-based follow-ups during the HD 52265 CoRoT observation.

Non-seismic parameter	Value	Reference
Distance d [pc]	28.95 ± 0.34	van Leeuwen (2007)
Temperature T_{eff} [K]	6100 ± 60	Ballot et al. (2011)
Surface gravity $\log g$ [cm/s^2]	4.35 ± 0.09	Ballot et al. (2011)
Luminosity $\log(L/L_\odot)$	0.287 ± 0.048	Valenti and Fischer (2005)
Metallicity [Fe/H]	0.19 ± 0.05	Ballot et al. (2011)
Mass $M/M_\odot$	1.05 ± 0.15	Valenti and Fischer (2005)
Mass $M/M_\odot$	$[1.19, 1.22]$	various authors*
Radius $R/R_\odot$	1.255 ± 0.033	Valenti and Fischer (2005)
$v \sin i$ [km/s]	$3.6^{+0.3}_{-1.0}$	Ballot et al. (2011)
Age [Gyr]	$2.7^{+0.7}_{-1.5}$	Valenti and Fischer (2005)
Chromospheric emission $\log R'(HK)$	-5.02	Wright et al. (2004)

* Mass estimates obtained from isochrone fits (Gonzalez et al. 2001, Santos et al. 2004, Takeda et al. 2005, Valenti and Fischer 2005); typical uncertainties are of the order of $\sigma_M = 0.02$-$0.05\,M_\odot$.

with solar initial chemical composition and masses between $0.8 \leq M/M_\odot \leq 1.6$. Note that the evolutionary tracks are not representative for HD 52265 because this star is metal-rich. Its metallicity was determined in the range of [Fe/H] = 0.19 ± 0.05 (Valenti and Fischer 2005) and [Fe/H] = 0.25 ± 0.06 (Santos et al. 2004). Tables with abundances of individual elements can be found, for example, in Gonzalez et al. (2001) and Valenti and Fischer (2005).

The most controversial parameter that was measured spectroscopically for HD 52265 is the $v \sin i$. Valenti and Fischer (2005) and Gillon and Magain (2006) measured relatively high values of $v \sin i = 4.7 \pm 0.5$ km/s and $v \sin i = 5.0 \pm 1.3$ km/s respectively. However, Valenti and Fischer admit that their result may be systematically overestimated for metal-rich stars with temperatures larger than 5800 K. The most recent study with Narval@Bernard Lyot led to a smaller value of $v \sin i = 3.6^{+0.3}_{-1.0}$ km/s (Ballot et al. 2011).

From spectroscopic measurements, fundamental parameters like the stellar mass and radius can be derived. For instance, the stellar radius was estimated from the luminosity and the effective temperature to be $R = 1.255 \pm 0.033$ R$_\odot$ (Valenti and Fischer 2005). They also measured a mass of $M = 1.05 \pm 0.15$ M$_\odot$ using spectroscopic constraints. Note that this value is at the lower end of the mass estimates for HD 52265. Other authors derived masses based on isochrones that are centered around $M \approx 1.2$ M$_\odot$ (e.g. Gonzalez et al. 2001, Santos et al. 2004, Valenti and Fischer 2005).

Table 3.2: Spectroscopic constraints on the planet HD 52265b and its orbit around HD 52265 according to the most recent study of Butler et al. (2006).

Parameter	Value
$M_p \sin i_p$ [M_{Jup}]	1.09 ± 0.11
Period [days]	119.290 ± 0.086
Semi major axis a [AU]	0.504 ± 0.029
Eccentricity e	0.325 ± 0.065
Amplitude K [m/s]	42.1 ± 3.1

Isochrones were also used to estimate the age of HD 52265. Gonzalez et al. (2001) and Valenti and Fischer (2005) determined an age of $\tau = 2.1 \pm 0.3$ Gyr and $\tau = 2.7^{+0.7}_{-1.5}$ Gyr respectively. Gonzalez et al. also deduced the stellar age from the magnetic activity (Donahue 1993, Henry et al. 1996) which was measured in terms of the chromospheric emission of the Ca II-lines, $\log R'_{HK}$. This way, they found a higher age of $\tau = 4$ Gyr. In this context, note that the magnetic activity is fairly close to the solar value implying that HD 52265 is expected to be magnetically quiet (e.g. Wright et al. 2004).

The asteroseismic analysis of the CoRoT observation of HD 52265 is expected to provide more precise constraints on the fundamental parameters such as mass, radius and age. For details, see the discussion in Section 6.2.

3.1.1 The planet HD 52265b

The discovery of a companion orbiting HD 52265 was reported independently by Butler et al. (2000) and Naef et al. (2001). The planet HD 52265 b was discovered spectroscopically by the radial velocity method. Its parameters and its orbit were revised by Butler et al. (2006). The parameters determined in these studies agree well within their corresponding error bars. According to the recent measurement of Butler et al. (2006), HD 52265 b is a planet with a projected mass of $M_p \sin i_p = 1.09 \pm 0.11 \, M_{Jup}$ in a long-period and fairly eccentric orbit. The respective parameters are listed in Table 3.2.

Based on Hipparcos intermediate astrometric data, Han et al. (2001) determined the inclination angle, i_p, of the normal to the orbital plane of HD 52265b with respect to the line of sight. They determined $i = 178.5°$ implying that the system is observed nearly pole-on. Thus, the mass of the HD 52265b would be $M_p \sim 42 \, M_{Jup}$, i.e. clearly above the most conservative brown dwarf mass limit of $M_{BD} > 13 \, M_{Jup}$ which is defined by the minimum mass for deuterium burning (for a review, see e.g. Burrows et al. 2001). However, Pourbaix (2001) suggested that the results of Han et al. are systematically biased due to the adopted data reduction procedure. I will discuss the perspective of constraining the mass of the companion HD 52265b by means of the asteroseismic analysis of its host star in Section 6.3.

3.2 Observation of HD 52265 with CoRoT

CoRoT is a CNES-ESA space telescope which performs high precision photometry (see e.g. Baglin et al. 2006). The mission comprises two simultaneous science objectives, a planet finding program and a stellar seismology program. The latter part of the mission includes so-called long runs and short runs, where a limited number of target stars (~50 objects) are observed continuously for up to ~150 days and ~20 days respectively. The continuity of the long photometric observations is ensured by the polar orbit of the satellite which allows one the observation of a particular field of stars for ~180 days. Then, the satellite is turned by 180° from the field of view in the galactic centre to the anticentre and vice versa.

HD 52265 was a primary target of the second long run directed at the galactic anti-centre (LRa2) from 11/13/2008 to 3/11/2009. During that time, it was observed for about 117 days. Standard data reduction and correction for instrumental effects as described in Samadi et al. (2007a) was applied to the raw data to generate a N2-level time series. The N2-level data provide the stellar flux (in electrons/s) on a regular temporal grid in the heliocentric reference frame with a sampling of $\Delta t = 32$ s. The duty cycle of the N2-level data of HD 52265 is 94.6%. The N2-level data contain a very strong noise component for a few minutes of each orbit when the telescope crosses the South Atlantic Anomaly (SAA). The data during these times cannot be used and are removed. Thus, the duty cycle becomes 90.2%. Removing bad data points during the crossing of the SAA also produces an observation window with very short but regular gaps. Thus, the window function exhibits a lot of peaks due to the satellite orbit and its harmonics as well as daily aliases. However, since the gaps are very short, they can be interpolated effectively using an inpainting algorithm (Sato et al. 2010). This reduces the window effects in the power spectrum significantly (see Figure 3.2). There remains a long-term trend in the raw lightcurve, i.e. the electron flux decreases slowly over the observation run. Such trends are visible in the N2-level data of many objects and are thus attributed to instrumental effects. In the case of HD 52265 this trend was removed by a fit of a 3rd-order polynomial. The lightcurve after applying all corrections is shown in Figure 3.2.

3.3 The power spectrum of HD 52265

From the lightcurve of the 117 day CoRoT observation of HD 52265 in Figure 3.2, I computed a power spectrum using the Fast Fourier Transform algorithm (FFT). The power spectrum in the frequency range between $\nu = 0.1$ μHz and the Nyquist frequency $1/(2\Delta t) = 15.6$ mHz is also shown in Figure 3.2. The power spectrum of HD 52265 shows the typical characteristics of a Sun-like star, in particular including an excess of power due to solar-like low-degree p modes around $\nu \sim 2000$ μHz. For frequencies $\nu \leq 2000$ μHz, the background power increases due to stellar convection. For frequencies $\nu \geq 3000$ μHz, the background is rather flat and dominated by photon noise. The properties of the stellar background will be discussed in detail in Section 3.4. There are two peaks at very low frequency around $\nu \sim 1$ μHz which are interpreted as signatures of stellar surface rotation (see Section 3.3.2). Despite all efforts to interpolate the gaps in the time series of HD 52265, there remain some signatures of the satellite orbit in the
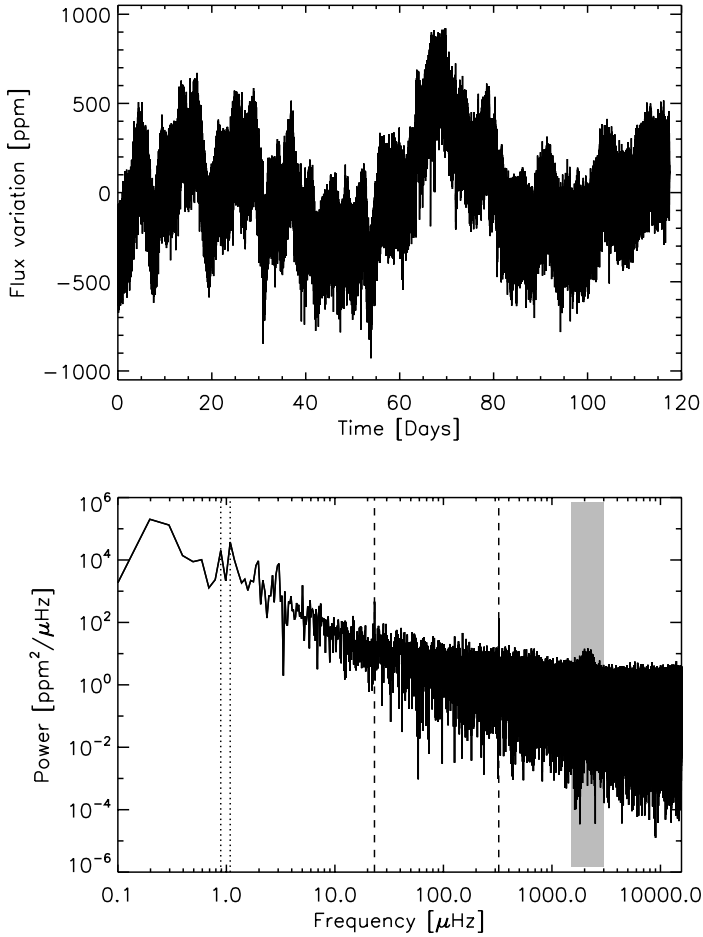
Figure 3.2: Lightcurve of the 117 day CoRoT observation of the Sun-like star HD 52265 after applying all steps of data reduction and interpolation as described in Section 3.2 (*top panel*). The *bottom panel* shows the corresponding power spectrum in the frequency range between $\nu = 0.1\ \mu$Hz and the Nyquist frequency at 15.6 mHz. The vertical *dashed lines* at $\nu = 23.2\ \mu$Hz and $\nu = 323.3\ \mu$Hz correspond to the first harmonics of the daily alias and the satellite orbit respectively. The two *dotted lines* at $\nu \sim 1\ \mu$Hz can be interpreted as surface rotation of the star (see Section 3.3.2). The grey shaded region at $\nu \sim 2000\ \mu$Hz represents the frequency range of the low-degree p-modes.
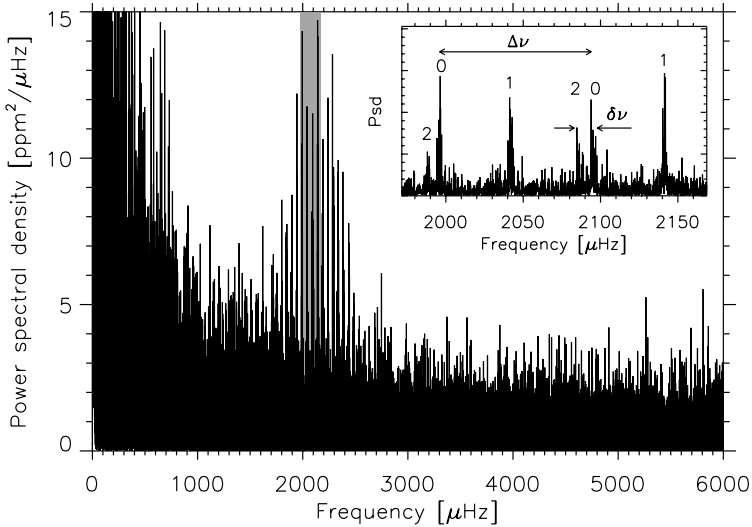
Figure 3.3: Oscillation power spectrum of HD 52265. The comb-like structure of the solar-like low-degree p modes is clearly visible in the frequency range between 1600 μHz $\lesssim \nu \lesssim$ 2600 μHz. The inset shows a zoom into the *grey shaded* frequency region which spans about two radial orders. Low-degree p modes with $\ell \leq 2$ are iden- tified as indicated by the numbers. The horizontal arrows show the large separation, $\Delta\nu$, and the small separation, $\delta\nu$.

power spectrum. Even though the daily alias at $\nu = 11.6$ μHz and the satellite orbit at $\nu = 161.7$ μHz (according to an orbit period of $\sim$ 103 minutes) are suppressed, their corresponding first harmonics are still visible. However, the relative amplitudes of these peaks are smaller than 1% compared to the central peak of the window function so that they are not expected to affect the data analysis significantly.

Figure 3.3 shows the oscillation power spectrum of HD 52265. The power spectrum in the frequency range 1600 μHz $\lesssim \nu \lesssim$ 2600 μHz shows the comb-like structure which is typical for solar-like low-degree p modes. The oscillation peaks in the power spectrum appear in regular series: a pair of peaks close together and a separated third peak (see inset of Figure 3.3). Those peaks can be identified unambiguously as modes with $\ell \leq 2$ (see Section 3.3.1). From the oscillation power spectrum, some rough estimates for the large and small separation can be determined by eye: the large separation is of the order of $\Delta\nu \sim 100$ μHz, and the small separation between modes with $\ell = 0$ and 2 is $\delta\nu_{02} \sim 8$ μHz. The maximum of the power distribution of the low-degree p modes is at $\nu \sim 2200$ μHz corresponding to a period of $T \sim 7.5$ minutes.
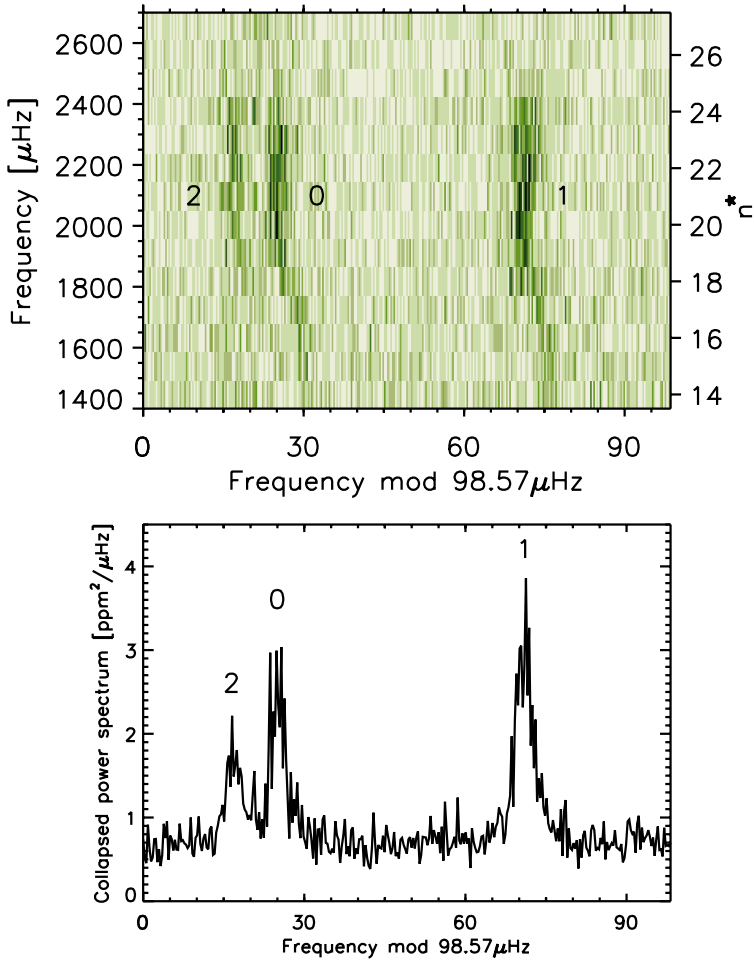
Figure 3.4: Echelle spectrum of the 117 day CoRoT observation of HD 52265 (*top panel*). The folding frequency is $\widetilde{\Delta \nu} = 98.57$ μHz. For clarity, the frequency resolution in any $\widetilde{\Delta \nu}$-wide interval is reduced by a factor of three by rebinning. The ordinate on the right hand side, $n^\star$, is a running number which labels the $n^\star$'s interval of length $\widetilde{\Delta \nu}$. There are three distinct ridges corresponding to modes with angular degrees $\ell = 0, 1,$ and 2. The *bottom panel* shows a collapsed power spectrum, i.e. the $\widetilde{\Delta \nu}$-wide intervals averaged between $17 \le n^\star \le 24$. There is no evidence for modes with $\ell = 3$, neither in the echelle spectrum nor in the collapsed power spectrum.

54
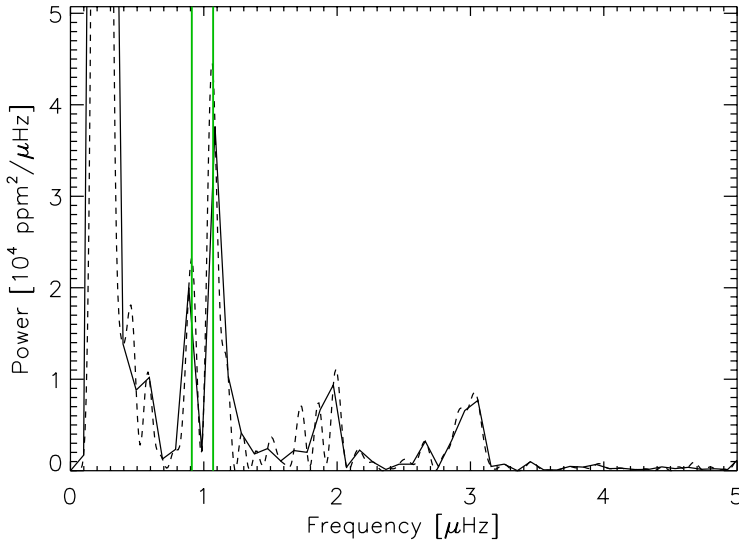
Figure 3.5: Power spectrum of the 117 day CoRoT time series of HD 52265 at low frequencies. The *solid line* shows the original power spectrum, the *dashed lines* is oversampled by a factor of 10. The two *green lines* represent the assumed signatures of the surface rotation at $\Omega/2\pi = 0.91\,\mu$Hz and $\Omega/2\pi = 1.07\,\mu$Hz corresponding to a rotation period of $P_{\rm rot} = 12.7$ days and $P_{\rm rot} = 10.8$ days respectively.

3.3.1 Echelle spectrum

I construct an echelle spectrum with the folding frequency $\widetilde{\Delta\nu} = 98.57\,\mu$Hz. The echelle spectrum in Figure 3.4 shows three clearly distinct ridges. The particular structure with three distinct ridges allows us a direct identification of the $\ell = 0, 1$, and 2 ridges by comparison with the Sun (cf. Figure 2.3). The two ridges which are close together are identified as $\ell = 0$ and $\ell = 2$ while the single ridge is identified as $\ell = 1$. The echelle spectrum does not show any evidence for modes of higher ℓ, in particular no $\ell = 3$ modes which would be expected to be close to the $\ell = 1$-ridge.

To further demonstrate the existence of modes with $\ell \leq 2$, I also construct a collapsed power spectrum, i.e. a power spectrum where the $\widetilde{\Delta\nu}$-wide intervals in the frequency region of the p modes are averaged. The collapsed power spectrum is also shown in Figure 3.4. It confirms the existence of three distinct peaks corresponding to modes with $\ell \leq 2$. There is again no evidence for $\ell = 3$ modes. However, if there is power caused by $\ell = 3$ modes, it may be washed-out in the collapsed power spectrum due to the curvature of the corresponding ridge in the echelle spectrum. Based on the analysis of the echelle spectrum so far, I will only include modes with angular degree $\ell \leq 2$ in the global fit.

Table 3.3: Parameters of the least-square fit to the power spectrum of HD 52265 using the model according to Equations (2.3), (2.5), (2.6), and (3.1). The error estimates correspond to 1σ standard deviation returned by the fitting algorithm (gradient expansion algorithm).

Harvey models	$A_1 = (45.3^{+5.6}_{-5.0})\,\mathrm{ppm^2\,\mu Hz^{-1}}$
	$A_2 = (2.3 \pm 0.3)\,\mathrm{ppm^2\,\mu Hz^{-1}}$
	$\tau_1 = (40900^{+4700}_{-4200})\,\mathrm{s}$
	$\tau_2 = (1800^{+270}_{-230})\,\mathrm{s}$
Photon noise	$P_{\mathrm{WN}} = (0.476 \pm 0.010)\,\mathrm{ppm^2\,\mu Hz^{-1}}$
P-mode signal	$P_{\mathrm{S}} = (0.276^{+0.080}_{-0.062})\mathrm{ppm^2\,\mu Hz^{-1}}$
	$\nu_c = (2320^{+190}_{-180})\,\mathrm{\mu Hz}$
	$\sigma_1 = (960^{+800}_{-440})\,\mathrm{\mu Hz}$
	$\sigma_2 = (310^{+440}_{-180})\,\mathrm{\mu Hz}$

3.3.2   Power at low frequencies: signature of stellar rotation

The analysis of the lightcurve may allow one to derive an estimate on the surface rotation of the star. The signature of rotation in the lightcurve arise from starspots which are dragged by the rotating stellar surface. This leads to a modulation of the lightcurve and a power excess in the low-frequency part of the power spectrum. The study of the low-frequency part of the power spectrum may lead to useful constraints on the stellar rotation as shown by e.g. Appourchaux et al. (2008). In other cases the lightcurves of solar-like stars did not show any signatures of stellar activity (e.g. Deheuvels et al. 2010). The HD 52265 lightcurve in Figure 3.2 looks similar to a solar time series in the sense that it is affected by stellar activity.

Figure 3.5 shows the power spectrum of the HD 52265 lightcurve in the low-frequency range. There are two distinct peaks at $\Omega/2\pi = 0.91\,\mu\mathrm{Hz}$ and at $\Omega/2\pi = 1.07\,\mu\mathrm{Hz}$. This corresponds to a rotation period of $P_{\mathrm{rot}} = 12.7$ days and $P_{\mathrm{rot}} = 10.8$ days respectively ($2.1 \leq \Omega/\Omega_\odot \leq 2.5$). There are also first and second harmonics of these peaks at $\nu \approx 2\,\mu\mathrm{Hz}$ and $\nu \approx 3\,\mu\mathrm{Hz}$. In fact, the HD 52265 lightcurve shows a modulation with a period of $T \sim 10$ days. The continuity of this modulation is confirmed by a wavelet analysis (Mathur et al. 2010, Ballot et al. 2011). The existence of two distinct peaks in the low-frequency power spectrum and the asymmetric shape of the peak at $1.07\,\mu\mathrm{Hz}$ may well indicate differential rotation effects. However, I did not investigate this possibility any further. For now, I point out that there is clear evidence of surface rotation of approximately $\Omega/2\pi \sim 1\,\mu\mathrm{Hz}$ or $T \sim 11$ days. This constraint provides a useful reference point for the measurement of the stellar rotation by means of the asteroseismic analysis.

Finally, the strong peak between $0.1\,\mu\mathrm{Hz} < \nu < 0.6\,\mu\mathrm{Hz}$ is attributed to the long-term trend in the raw-lightcurve of HD 52265 (see Section 3.2). Such a trend was measured in many stars of the CoRoT LRa2 and is thus interpreted as an instrumental effect.
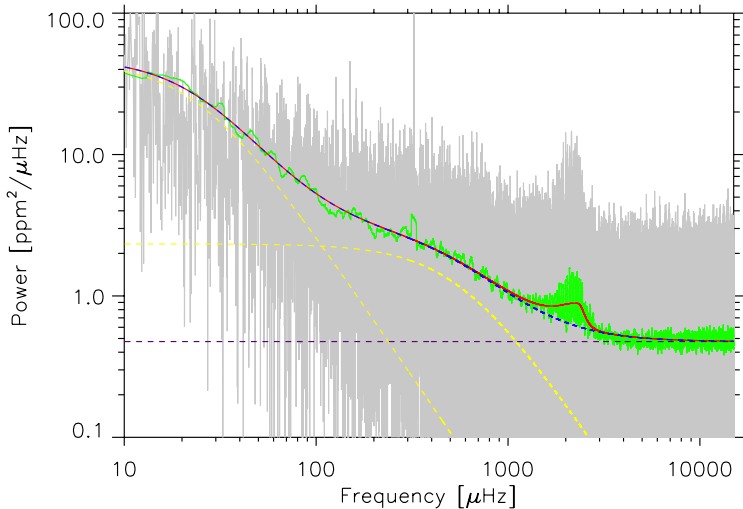
Figure 3.6: Fit to the power spectrum of the 117 day CoRoT observation of HD 52265. The observed power is shown in *grey*, the *green spectrum* is smoothed with a 20 μHz-boxcar. The *solid red line* is the fit to the smoothed power spectrum according to Equations (2.3), (2.5), (2.6), and (3.1). The *dashed blue line* represents the noise background composed of two Harvey models (*dashed yellow lines*) and a flat photon noise component (*dashed purple line*). The prominent peak at $\nu \sim 220\,\mu$Hz corresponds to the first harmonic of the satellite orbit (see Section 3.3).

3.4   Determination of the stellar background noise

For the analysis of the HD 52265 data I adopt the same strategy that was used for the analysis of the VIRGO data of the Sun in the previous chapter. Accordingly, the first step includes a least-square fit of the smoothed power spectrum to determine the background noise. For the determination of the p-mode parameters (second step), the functional form of the background noise is fixed (see Section 2.2.1).

According to Equation (2.3), the smoothed power spectrum is modeled by a term which describes the power excess caused by the p modes, $P_{\mathrm{osc}}(\nu)$, and term $N(\nu)$ which describes the background noise: $\overline{P}_{\mathrm{smooth}}(\nu) = P_{\mathrm{osc}}(\nu) + N(\nu)$. For the first term, I adopt Equations (2.5) and (2.6). The background noise, $N(\nu)$, is slightly modified and is given by

$$N(\nu) = \sum_{i=1}^{2} \frac{A_i}{1 + (\tau_i \nu)^2} + P_{WN}, \qquad (3.1)$$

where P_{WN} is the photon noise and the first two terms are standard Harvey models (Harvey 1985) to describe the stellar background caused by convection. For HD 52265, it turned out that a standard Harvey model with an exponent of two works better than a model with exponent four which was used for the analysis of the solar data.

Figure 3.6 shows the least-square fit to the smoothed power spectrum of HD 52265. The results of the fit for the individual parameters are listed in Table 3.3. The frequency range for the fit is chosen between $0.01\,\mathrm{mHz} \le \nu \le 15\,\mathrm{mHz}$. The lower frequency boundary is chosen to exclude long-period instrumental effects, the upper frequency limit is set by the Nyquist frequency.

Overall, the model fits the smoothed power spectrum reasonably well. One has to be careful with the interpretation of the first Harvey model parameterized by (A_1, τ_1). Due to the steep increase of the background at frequencies $\nu < 100\,\mu\mathrm{Hz}$, the fitted amplitude A_1 and its time scale τ_1 depend significantly on the choice of the lower frequency boundary. The second convection term which is parameterized by (A_2, τ_2) is rather independent on the frequency range of the fit and may be interpreted as stellar convection. Thus, the time scale of convection for HD 52265 is $\tau_2 \sim 30\,\mathrm{min}$, i.e. about six times longer than the granulation time scale of the Sun (see Section 2.2.1).

According to the fit of the smoothed power spectrum, the maximum power of the p modes is at $\nu \sim 2300\,\mu\mathrm{Hz}$ corresponding to a period of $T \sim 7\,\mathrm{min}$. The distribution of the power seems to be more asymmetric than for the Sun as indicated by the significantly different values for σ_1 and σ_2. However, this hypothesis has to be confirmed by the detailed analysis of the p-mode spectrum.

3.5 Modifications to the parameterization of the oscillation power spectrum

In Section 2.2, I gave a detailed description of the parameterization of the expectation value of the solar oscillation power spectrum. In general, I adopt this model for the analysis of the HD 52265 data with some minor modifications which I describe below.

Mode frequencies: In the solar echelle spectrum (Figure 2.3), the ridges for modes with $\ell \le 2$ at frequencies $2200\,\mu\mathrm{Hz} \le \nu \le 4100\,\mu\mathrm{Hz}$ have a *C-shape*. This shape motivates the parameterization by a 2$^{\mathrm{nd}}$-order polynomial [Equation (2.8)]. The ridges in the echelle spectrum of HD 52265 rather have an *S-shape* which indicates that the frequency dependence of the large separation is not monotone. Therefore, I parameterize the $\ell = 0$ and $\ell = 1$ mode frequencies of HD 52265 by a 3$^{\mathrm{rd}}$ order polynomial:

$$\nu_{n\ell} = \sum_{i=0}^{3} c_i^{(\ell)} (n - n_0)^i \qquad \ell = 0, 1. \qquad (3.2)$$

Here, n_0 is defined as in Section 2.2.2. In this analysis, I use $n_0 = 21$ for $\ell = 0$ and $n_0 = 20$ for $\ell = 1$. The central frequencies of the $\ell = 2$ modes are modeled as described in

Section 2.2.2, i.e. the small separation, δ_{02}, is parameterized by a linear function [cf. Equations (2.9) and (2.10)].

I assume the rotational splitting of the non-radial modes to be constant in the frequency range of the global fit, i.e. $\delta v_{n\ell m}^{(\text{rot})} = m\Omega/2\pi$ [cf. Equation (2.11)].

Mode linewidths: For the parameterization of the mode linewidth as a function of n or v, I applied two different models. Since there is no a-priori information about the mode linewidths of HD 52265 I started with a simple power law according to

$$\Gamma(v) = \Gamma_{2100} \left(\frac{v}{2100\,\mu\text{Hz}} \right)^{\gamma}. \tag{3.3}$$

There are two free parameters, Γ_{2100} and γ. The first one, Γ_{2100} (measured in μHz), can be interpreted as the mode linewidth at a frequency of $v = 2100\,\mu$Hz, the second one, γ, is the slope of the power law. The scaling of the power law to $v = 2100\,\mu$Hz corresponds to the center of the frequency region of the global fit and has only practical reasons. It was shown that a power law is appropriate to describe the solar p-mode linewidth in particular frequency intervals (e.g. Chaplin et al. 1997). I will use this model to describe the linewidth in the frequency range of the global fit. I refer to this parameterization of the mode linewidth as *Fit A*.

For the Sun, the mode linewidths are well known such that I could justify to model them by a 3rd order polynomial of the radial order n (see Section 2.2.3). Even though there is no information on the frequency dependence of the mode linewidths of HD 52265, I also perform a global fit using this more complex model according to Equations (2.12) and (2.13). I refer to this parameterization as *Fit B*.

Mode amplitudes: The model of the mode amplitudes remains unchanged as described in Section 2.2.4.

3.6 Extraction of p-mode parameters and estimation of errors

I derive maximum likelihood estimates (MLE, see Section 1.5) for the parameters of the expectation value of the oscillation power spectrum (Section 2.2 and 3.5). I perform a global fit for 500 uniformly distributed initial guesses. The high number of initial guesses improves the chances of finding the global minimum of the log-likelihood function and allows one the investigation of the reliability of the fit by comparing the distribution of the initial guesses and the corresponding fits.

Estimates on the uncertainty of the individual oscillation parameters are determined from Monte Carlo simulations. For that purpose, I generated 200 realizations of 117 day long Fourier spectra with an expectation value of the power equal to the expectation value of the best fit, $\overline{P}_{\text{bestfit}}$:

$$y(v) = \sqrt{\overline{P}_{\text{bestfit}}(v)} \cdot \eta(v). \tag{3.4}$$

Here, $y(\nu)$ is the complex Fourier amplitude at frequency ν, and η is a centered complex Gaussian random variable with unit variance and independent real and imaginary parts. The square of the magnitude of y is the power spectrum of a particular realization, i.e. $P(\nu) = |y(\nu)|^2$. MLEs using the global oscillation model are derived for all 200 realizations using 50 random initial guesses for each realization. The estimates on the uncertainty of the individual oscillation parameters is then deduced from the distribution of the individual parameters.

3.7 Global fit of the p-mode oscillation spectrum

In this section, I present the results of the global fit of the oscillation power spectrum of HD 52265. The fit spans the frequency range between $1600\,\mu\text{Hz} \leq \nu \leq 2600\,\mu\text{Hz}$. Thus, the global fit includes 9 consecutive radial orders for modes with $\ell = 0$ and $\ell = 2$, and 10 consecutive radial orders for modes with $\ell = 1$. In this analysis, I only include modes which are visible by eye in the power spectrum (Figure 3.3 and 3.4), i.e. modes which are clearly above the noise level. Note that some other groups of the DAT chose more extended frequency ranges for their respective analyses.

Figure 3.7 illustrates the result of the global fit. The figure shows the observed power spectrum of HD 52265 and the expectation value of the power computed from the fit results. By eye, the fit describes the observed power reasonably well over the full frequency range. This first impression is confirmed by a more detailed representation of the fit results in Figure 3.8. The figure shows $20\,\mu\text{Hz}$-wide sections of the observed power spectrum and the corresponding fit. The individual sections are centered around the fitted mode frequency, $\nu_{n\ell 0}$. The modes are ordered by the angular degree, ℓ, for 9 consecutive radial orders, n. A quantitative discussion on the results of the mode parameter, i.e. mode frequencies, linewidths, and amplitudes, will follow below. Figure 3.8 also shows the line profile averaged over all 9 radial orders for modes with $\ell \leq 2$ together with an averaged expectation value of the power. A first look at the averaged line profiles reveals that the azimuthal components of the non-radial modes ($\ell = 1, 2$) are not resolved. This situation is comparable with the Sun (see Section 2.3 and Section 2.3.4). This is a first indication that the p-mode linewidths in HD 52265 are at least of the order of the rotational splitting, i.e. $2\pi\Gamma/\Omega \gtrsim 1$. However, a closer look shows that the averaged line profile of the non-radial modes is slightly broader than the averaged line profile of the radial $\ell = 0$ modes. This suggests that even though the azimuthal components are not resolved, the rotational splitting is still apparent in the power spectrum and the rotation of HD 52265 may still be constrained by the asteroseismic analysis. I will discuss this issue in detail in Section 3.7.4.

3.7.1 Mode frequencies

For the global fit, the mode frequencies of HD 52265 are parameterized by a 3rd-order polynomial (Section 2.2 and 3.5). Figure 3.9 and 3.10 present the distributions of the 500 initial guesses and the corresponding fits for the 10 free parameters describing the mode frequencies, $\nu_{n\ell 0}$. The distributions presented here correspond to the global fit using Fit A. I note that the distributions for Fit B look very similar. Evidently, the parameter

distributions of the fit results are symmetric and show a well pronounced peak compared to the uniformly distributed initial guesses. For all individual parameters, $c_i^{(\ell)}$, the best fit is located near the maximum of the corresponding distribution. Thus, I conclude that the fit of the mode frequency lead to reliable results: the fit is stable and not biased.

The mode frequencies, $\nu_{n\ell 0}$, can be determined by applying the best fit parameters for $c_i^{(\ell)}$ to Equations (3.2), (2.9), and (2.10). Table 3.4 and Table 3.5 list the mode frequencies for all modes included in the global fit for Fit A and Fit B respectively. The error bars given in both tables correspond to the 1σ uncertainty derived from Monte Carlo simulations (Section 3.6). Comparing the results of the two models, it is evident that the mode frequencies match very well. All mode frequencies of Fit B fall within the error bars of the frequencies of Fit A and vice versa. Thus, I conclude that the choice of the parameterization of the mode linewidths does not affect the fit of the mode frequencies in the two cases studied here. As indicated by the symbols in the two frequency tables, there is an overall good agreement between the results obtained in this work and the results of the other 10 teams of the DAT (Ballot et al. 2010). For 13 of the 28 modes/multiplets (46%) which are included in my fit, all teams find a result that falls within the 1σ error bar of this work. For 23 of the 28 multiplets (82%) at least 8 of 10 teams determined frequencies which match the results of this work. Finally, for only 5 of 28 multiplets (17%) included in this work, five or more teams determined frequencies which do not match the corresponding results of this work (within 1σ). The mismatch of the fit for some modes may be attributed to the simplified parameterization of the mode frequencies in this work. The 3rd-order polynomial allows us to consider smooth deviations from a regular frequency pattern, e.g. the overall trend of $\Delta\nu$. However, oscillations in the frequency pattern cannot be recovered. I discussed a similar situation in the case of the analysis of the solar data in Section 2.3.1.

Figure 3.11 visualizes the estimates on the mode frequencies determined from the global fit. It shows the central mode frequencies, $\nu_{n\ell}$, obtained with Fit A (Table 3.4) in an echelle format. Note that an equivalent figure with frequencies from Fit B (Table 3.5) looks almost identical. The error bars correspond to 3σ errors. The frequency ridges determined in this work follow the general trend of the observed echelle spectrum quite well. This qualitatively supports the good performance of the global fit.

The estimates on the frequency uncertainty given in Table 3.4 and 3.5 are determined from Monte Carlo simulations. According to Libbrecht (1992) the frequency uncertainty, σ_ν, of solar-like p modes depend on the length T of the observation, the mode linewidth, Γ, and the signal-to-noise ratio, $H(\nu_{n\ell})/\mathcal{B}(\nu)$, i.e. the ratio of the mode height and the local background noise [cf. Equation (2.19)]. In Figure 3.12, I compare the frequency uncertainty of the radial modes determined in this work with the expected uncertainties according to the Libbrecht formula. To compute the frequency uncertainty with Libbrecht's formula, I used the estimates for the mode linewidths and the signal-to-noise ratios from Table 3.6 and Table 3.7, i.e. the results of this analysis. The total length of the observation is $T = 117$ days. In both cases of Fit A and Fit B, the measured frequency uncertainties follow the trend expected by the Libbrecht formula. The frequency uncertainties determined in this work are slightly smaller than the expected values according to the Libbrecht formula. This may be attributed to the fact that I perform a global fit, i.e. the individual mode frequencies are mutually dependent on each other. On the other hand, the Libbrecht formula gives the expected uncertainty of one isolated mode of oscillation. Thus, it is
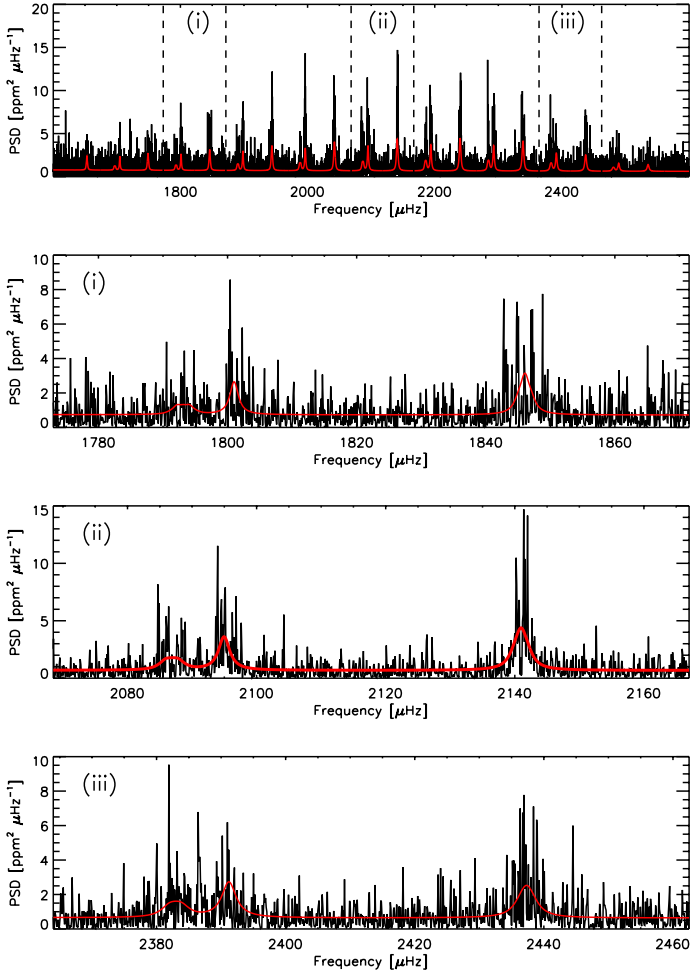
Figure 3.7: *Top panel:* Global fit of the oscillation power spectrum of HD 52265. The *black line* shows the observed power spectrum of the 117 day observation with CoRoT. The *red line* represents the expectation value of the power obtained with the global fit described in this chapter. The global fit is performed in the frequency range $1600\,\mu\text{Hz} \leq \nu \leq 2600\,\mu\text{Hz}$. The *panels (i)-(iii)* show zooms in three different frequency regions as indicated in the *top panel*. The *panels (i)-(iii)* show $\widetilde{\Delta\nu}$-wide intervals with one mode of degree $\ell = 2$, $\ell = 0$, and $\ell = 1$ each (folding frequency $\widetilde{\Delta\nu} = 98.6\,\mu\text{Hz}$).
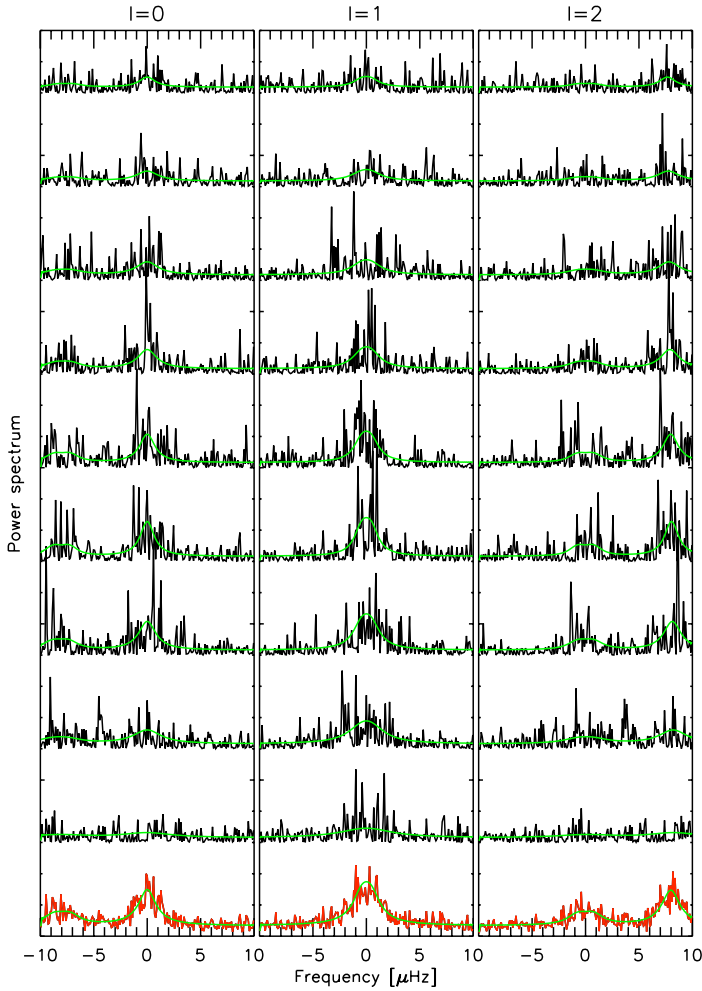
Figure 3.8: Global fit of the solar-like p modes of HD 52265. The observed power spectrum of the 117 day observation with CoRoT is shown in *black*, the *green line* is the expectation value of the power determined by the global fit. The figure shows small sections of the power spectrum centered around their respective mode frequencies obtained by the global fit. The small sections of the power spectrum are sorted by the angular degree ℓ. For each ℓ, nine consecutive radial orders are shown (n increasing from top to bottom). The *red line* at the bottom of each column represents an average of the sections above. Here, the *green line* shows an average of the fits above.
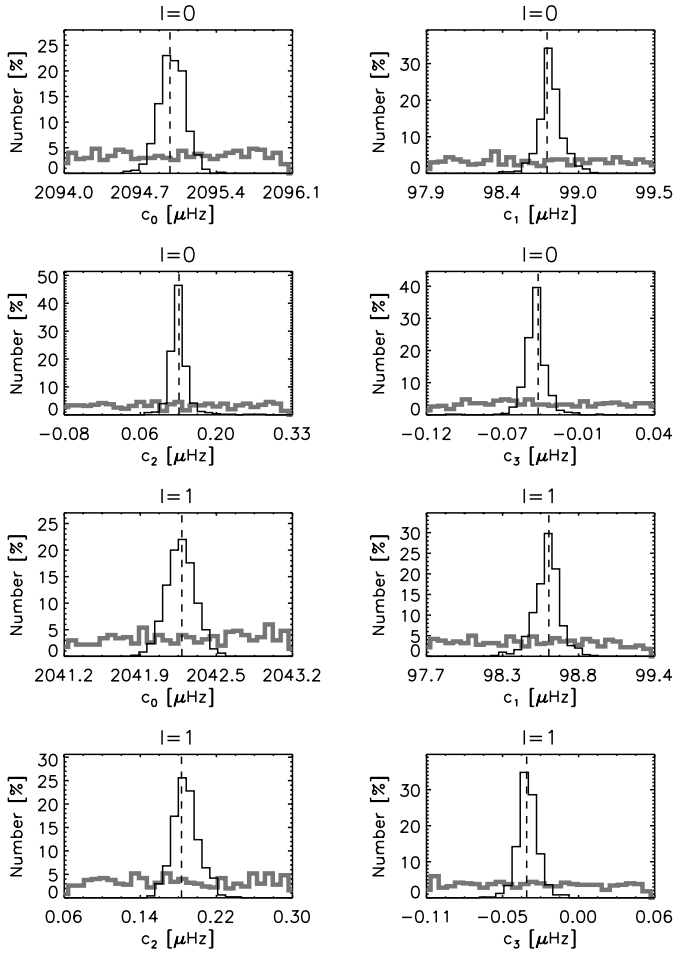
Figure 3.9: Distribution of the frequency parameters for the global fit of the 117 day CoRoT observation of HD 52265. The distribution of the 500 initial guesses is shown in *grey*, the fit results in *black*. The *vertical dashed line* marks the best fit for each parameter. The *top four panels* show the four parameters c_i ($i = 0, 1, 2, 3$) for modes with $\ell = 0$ [cf. Equation(3.2)]. The *bottom four panels* show the respective parameters for modes with $\ell = 1$. The single peaked distributions of the fit results compared to the uniformly distributed initial guesses indicate a successful fit of the mode frequencies.
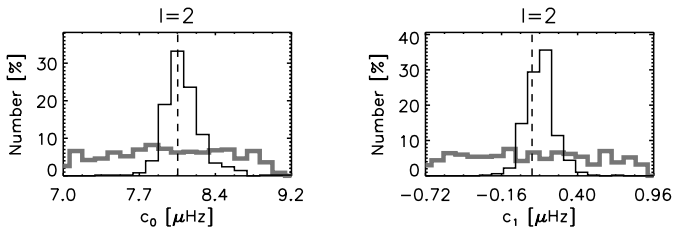
Figure 3.10: Distribution of the frequency parameters for the global fit of the 117 day CoRoT observation of HD 52265. Other than Figure 3.9 the two parameters c_i ($i = 0, 1$) for modes with $\ell = 2$ are shown here [cf. Equation (2.9)]. The distribution of the 500 initial guesses is shown in *grey*, the fit results in *black*. The *vertical dashed line* marks the best fit for each parameter.

difficult to compare the two estimates directly. In any case, the frequency uncertainties measured in this work are of the same order of magnitude as the values according to the Libbrecht formula. Therefore, I conclude that the Monte Carlo simulations lead to overall realistic estimates on the uncertainty of the p-mode frequencies.

The large frequency separation, $\Delta\nu$, is a parameter of particular interest. It is proportional to the square root of the mean stellar density and thus directly related to the fundamental stellar parameters, mass and radius (see Section 1.3 and 1.4). Based on the mode frequencies determined in this work, I calculate the mean large separation of HD 52265 according to

$$\langle\Delta\nu\rangle = \langle\nu_{n+1\,\ell} - \nu_{n\ell}\rangle_{n\ell} \qquad \text{with } 21 \leq n \leq 23,\ \ell \leq 2. \qquad (3.5)$$

Here, $\langle\Delta\nu\rangle$ is a weighted average over the three radial orders with the highest signal-to-noise ratio (see Table 3.6 and 3.7) and modes with $\ell \leq 2$. This approach takes into account that the large separation is not necessarily constant over many radial orders. Thus, I obtain the following large separation for HD 52265:

$$\begin{aligned}
\text{Fit A:} \qquad \langle\Delta\nu\rangle &= 98.84 \pm 0.12\,\mu\text{Hz},\\
\text{Fit B:} \qquad \langle\Delta\nu\rangle &= 98.36 \pm 0.07\,\mu\text{Hz}.
\end{aligned}$$

An alternative estimate of the mean large separation of solar-like oscillations can be derived from the autocorrelation of the time series. Roxburgh and Vorontsov (2006) proposed to calculate the autocorrelation as the Fourier Transform of the windowed power spectrum. The first peak of the envelope autocorrelation function (EACF), i.e. the square module of the autocorrelation, can be interpreted as half of the large separation, $\langle\Delta\nu\rangle/2$. Mosser and Appourchaux (2009) optimized this method and determined its reliability. The autocorrelation method is particularly useful for the asteroseismic analysis of noisy data since it allows one to measure the mean large separation even if the mode parameters of individual modes cannot be measured. For HD 52265, I determined the EACF using

Table 3.4: Mode frequencies of solar-like p modes in HD 52265. The frequencies are determined with a global fit of the power spectrum of HD 52265 using Fit A, i.e. a power law to describe the mode linewidths as a function of frequency (see Section 3.5). The listed frequencies are the central frequencies of the $m = 0$ components of the corresponding multiplet, $\nu_{n\ell 0}$. The 1σ error bars are determined from Monte Carlo simulations. The frequencies of Fit A are in agreement with the frequencies determined by Fit B (see Table 3.5). Symbols mark modes for which one or more of the 11 groups of the DAT fitted frequencies that do not match the result of this work. Modes marked with (†) indicate that one or two groups from the DAT find different results. Modes marked with (△) indicate that five or more groups find a different result.

Fit A: Mode frequencies $\nu_{n\ell 0}$ [μHz]			
n	$\ell = 0$	$\ell = 1$	$\ell = 2$
16		1653.01 ± 0.38	$1696.89 \pm 0.64^{\dagger}$
17	1704.71 ± 0.36	$1749.05 \pm 0.20^{\triangle}$	$1793.13 \pm 0.46^{\dagger}$
18	1801.01 ± 0.18	1846.07 ± 0.19	$1890.37 \pm 0.37^{\dagger}$
19	$1898.32 \pm 0.18^{\dagger}$	$1943.86 \pm 0.18^{\dagger}$	1988.37 ± 0.29
20	1996.39 ± 0.16	$2042.23 \pm 0.17^{\triangle}$	2086.88 ± 0.26
21	$2094.96 \pm 0.16^{\dagger}$	$2140.97 \pm 0.18^{\dagger}$	$2185.64 \pm 0.28^{\triangle}$
22	2193.79 ± 0.19	$2239.87 \pm 0.19^{\triangle}$	2284.41 ± 0.33
23	2292.62 ± 0.20	$2338.72 \pm 0.19^{\triangle}$	$2382.93 \pm 0.40^{\dagger}$
24	$2391.21 \pm 0.24^{\dagger}$	2437.32 ± 0.28	2480.96 ± 0.64
25	2489.30 ± 0.51	$2535.46 \pm 0.62^{\dagger}$	

a cosine filter with FWHM=500 μHz centered at $\nu = 2000\,\mu$Hz. Thus, the filtered power spectrum covers the frequency region of the global fit performed in this work. In that way I determine a mean large separation of $\langle \Delta \nu \rangle = 98.40 \pm 0.06\,\mu$Hz. The agreement of the large separations determined from the global fit and the EACF is acceptable, but particularly close to Fit B.

The large separation is a function of frequency, $\Delta \nu(\nu)$. As already expected from the S-shape of the frequency ridges in the echelle spectrum (Figure 3.4), the large separation increases at low frequencies $\nu \lesssim 2100\,\mu$Hz and decreases again for $\nu \gtrsim 2100\,\mu$Hz as illustrated in Figure 3.13. The figure shows the large separation, $\nu_{n+1,\ell} - \nu_{n\ell}$, for modes with degree $\ell = 0$ and $\ell = 1$ based on the frequencies from Table 3.4. For comparison, I also display the large separation as a function of frequency determined from the autocorrelation. For this purpose the autocorrelation power was calculated using a narrow filter as described in Roxburgh (2009) and Mosser and Appourchaux (2009). In this case, I applied a cosine filter with a FWHM = 200 μHz, i.e. a filter width of $\sim 2\Delta \nu$, centered at frequencies between $1550\,\mu$Hz $\leq \nu \leq 2650\,\mu$Hz in steps of 50 μHz. Overall, the frequency dependency of the large separation determined with these two methods match reasonably well. However, the large separation determined from the autocorrelation has two dips around $\nu \approx 1900\,\mu$Hz and $\nu \approx 2350\,\mu$Hz. These dips are not present in the

Table 3.5: Mode frequencies of solar-like p modes in HD 52265. The frequencies are determined with a global fit of the power spectrum of HD 52265 using the Fit B, i.e. a $3^{\rm rd}$-order polynomial to describe the dependence of the mode linewidths on the radial order n (see Section 3.5). The listed frequencies are the central frequencies of the $m = 0$ components of the corresponding multiplet, $\nu_{n\ell 0}$. The 1σ error bars are determined from Monte Carlo simulations. Symbols mark modes for which one or more of the 11 groups of the DAT fitted frequencies that do not match the result of this work. Modes marked with ($\dagger$) indicate that one or two groups from the DAT find different results. Modes marked with ($\triangle$) indicate that five or more groups find a differing result.

Fit B: Mode frequencies $\nu_{n\ell 0}$ [μHz]			
n	$\ell = 0$	$\ell = 1$	$\ell = 2$
16		1653.01 ± 0.44	$1697.10 \pm 0.62^{\dagger}$
17	1704.76 ± 0.40	$1749.01 \pm 0.24^{\triangle}$	$1793.19 \pm 0.46^{\dagger}$
18	1800.94 ± 0.23	1846.03 ± 0.21	$1890.41 \pm 0.39^{\dagger}$
19	$1898.23 \pm 0.23^{\dagger}$	$1943.85 \pm 0.18^{\dagger}$	1988.44 ± 0.31
20	1996.33 ± 0.19	$2042.25 \pm 0.14^{\triangle}$	2086.99 ± 0.24
21	$2094.96 \pm 0.14^{\dagger}$	$2141.01 \pm 0.14^{\dagger}$	$2185.76 \pm 0.23^{\triangle}$
22	2193.81 ± 0.14	$2239.91 \pm 0.16^{\triangle}$	2284.46 ± 0.27
23	2292.58 ± 0.17	$2338.74 \pm 0.20^{\triangle}$	$2382.78 \pm 0.40^{\dagger}$
24	$2390.98 \pm 0.29^{\dagger}$	2437.29 ± 0.40	2480.42 ± 0.73
25	2488.70 ± 0.65	$2535.32 \pm 0.86^{\dagger}$	

large separation determined from the global fit. This is again due to the very simplified parameterization of the mode frequencies. For future studies, it may be interesting to investigate rapid variations of the large separation in more detail since they are related to sharp features in the sound speed profile as discussed in Section 1.4.

I also determine a mean small separation, $\langle \delta \nu \rangle$, between adjacent modes with $\ell = 0$ and $\ell = 2$ according to [see also Equation (1.6)]

$$\langle \delta \nu \rangle = \langle \nu_{n0} - \nu_{n-1,2} \rangle_n \qquad \text{with } 21 \leq n \leq 23. \qquad (3.6)$$

Using the same arguments as for the large separation, I calculate a weighted average using the modes of the three radial orders with the highest signal-to-noise ratio according to Table 3.6 and 3.7.

Thus, I obtain:

$$\begin{aligned} \text{Fit A:} \quad & \langle \delta \nu \rangle \;=\; 8.14 \pm 0.20 \, \mu\text{Hz}, \\ \text{Fit B:} \quad & \langle \delta \nu \rangle \;=\; 7.99 \pm 0.13 \, \mu\text{Hz}. \end{aligned}$$

Finally, I investigate the potential evidence of p modes with angular degree $\ell = 3$ in the power spectrum of HD 52265. For this purpose, I calculate the ratio of the observed
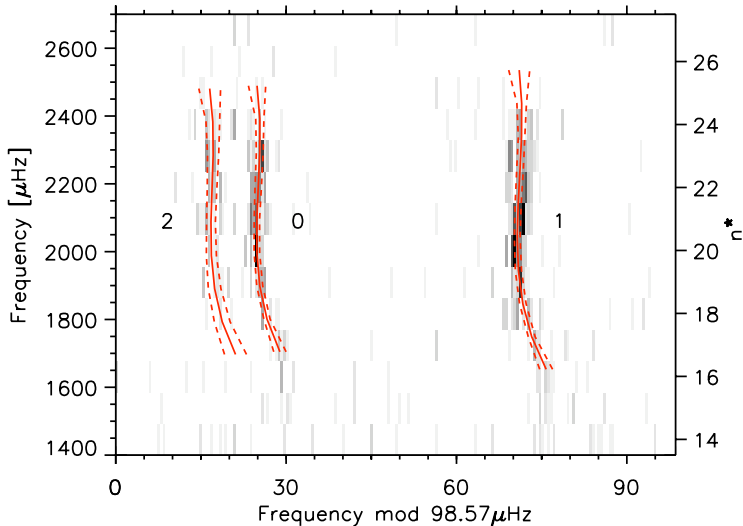
Figure 3.11: Mode frequencies determined with a global fit of the 117 day CoRoT observation of HD 52265. The mode frequencies are shown in an echelle format with a folding frequency of $\widetilde{\Delta\nu} = 98.57\,\mu$Hz. The three *solid red lines* represent the ridges of the mode frequencies, $\nu_{n\ell}$, for modes with $\ell \leq 2$. The *dashed red lines* show the corresponding 3σ error bars derived from Monte Carlo simulations. The *grey-scaled background* shows the echelle spectrum of the 117 day CoRoT observation of HD 52265 (cf. Figure 3.4). For accentuation of the observed frequency ridges, the $\Delta\nu$-wide intervals in the observed echelle spectrum are rebinned by a factor of 5. Furthermore, only frequency bins with a power value of $P \geq 0.8\,P_{max}$ are shown, where P_{max} is the maximum power in the shown frequency range.

power spectrum (cf. Figure 3.7, black line) divided by the expectation value of the power determined with the global fit (red line). Figure 3.14 presents this ratio in echelle format and as a collapsed spectrum (see Section 3.3.1). First, I would like to emphasize that there is no significant excess of power remaining at the former position of the ridges of modes with $\ell \leq 2$. The ratio of the observed power and the expectation value in the collapsed power spectrum is well centered around one. This is a further confirmation that the performance of the global fit good. The echelle spectrum and the collapsed spectrum do not show any significant excess that may be interpreted as being due to modes with $\ell = 3$. Thus, I conclude that based on my analysis there is no evidence for solar-like p modes with $\ell = 3$.
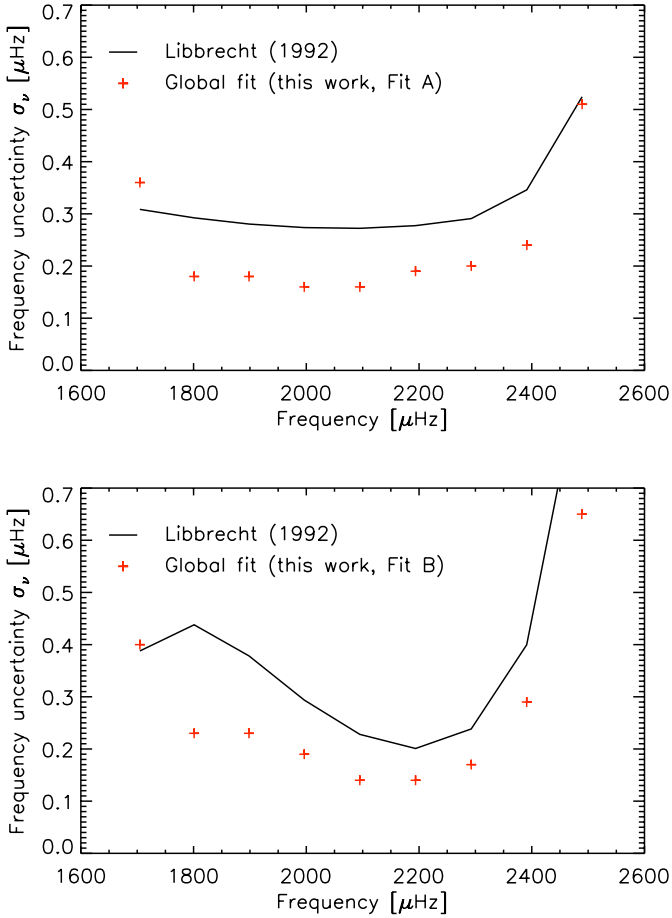
Figure 3.12: Uncertainties, σ_ν, of the mode frequencies, ν_{n0}, of the radial modes. The two panels compare the frequency uncertainty measured in this work (*red symbols*) with the expected frequency uncertainty according to Libbrecht (1992, *solid black line*). The *top panel* shows the frequency uncertainties determined for Fit A (cf. Table 3.4), and the *bottom panel* shows the frequency uncertainties obtained using Fit B (cf. Table 3.5). The expected frequency uncertainties are calculated using Equation (2.19). The mode linewidths and the signal-to-noise ratios are listed in Table 3.6 and Table 3.7. The total length of the observation is $T = 117$ days.
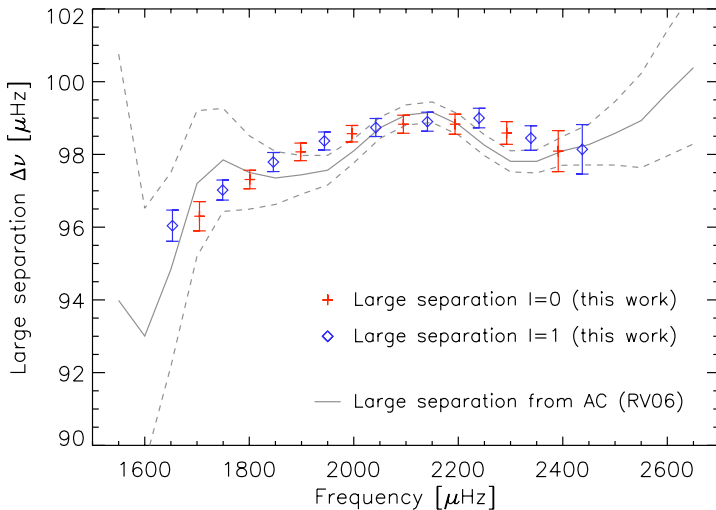
Figure 3.13: Large separation, $\Delta\nu$, of HD 52265 as a function of frequency. The *symbols* represent the large separation, $\Delta\nu_{n\ell} = \nu_{n\ell} - \nu_{n-1\,\ell}$, derived from the results of the global fit (Fit A, Table 3.4). The *red crosses* show the large separation of modes with $\ell = 0$, the *blue diamonds* show the large separation of modes with $\ell = 1$. For comparison, the *solid grey line* shows the large separation determined from the frequency-windowed autocorrelation of the HD 52265 time series (Roxburgh and Vorontsov 2006, Roxburgh 2009). The 1σ error bar (*dashed grey line*) is computed according to Mosser and Appourchaux (2009).

3.7.2 Mode linewidths

The frequency dependence of the mode linewidths of HD 52265 is parameterized using a simple power law [Fit A, Equation (3.3)] and a 3$^{\text{rd}}$-order polynomial of radial order n [Fit B, Equation (2.12), (2.13)]. Thus, the mode linewidths ranging over 10 radial orders are parameterized by two and four free parameters respectively. Figure 3.15 and Figure 3.16 show the distributions of the linewidth parameters for the two fits. The distributions of the 500 initial guesses and the corresponding fits are compared. For both models, the distributions of the fits show a single, well defined peak in contrast to the uniformly distributed guesses. Furthermore, the best fit for any parameter is located near the maximum of the corresponding distribution. Thus, I conclude that the global fit of the mode linewidths is stable and returns reliable results for both fits.

According to Equations (3.3) and (2.12) the mode linewidths, $\Gamma_{n\ell}$, can be determined from the best-fit estimates for Γ_{2100} and γ for Fit A, and from the best-fit estimates for g_i ($i = 1, 2, 3, 4$) for Fit B. The mode linewidths of the radial modes, Γ_{n0}, are listed in
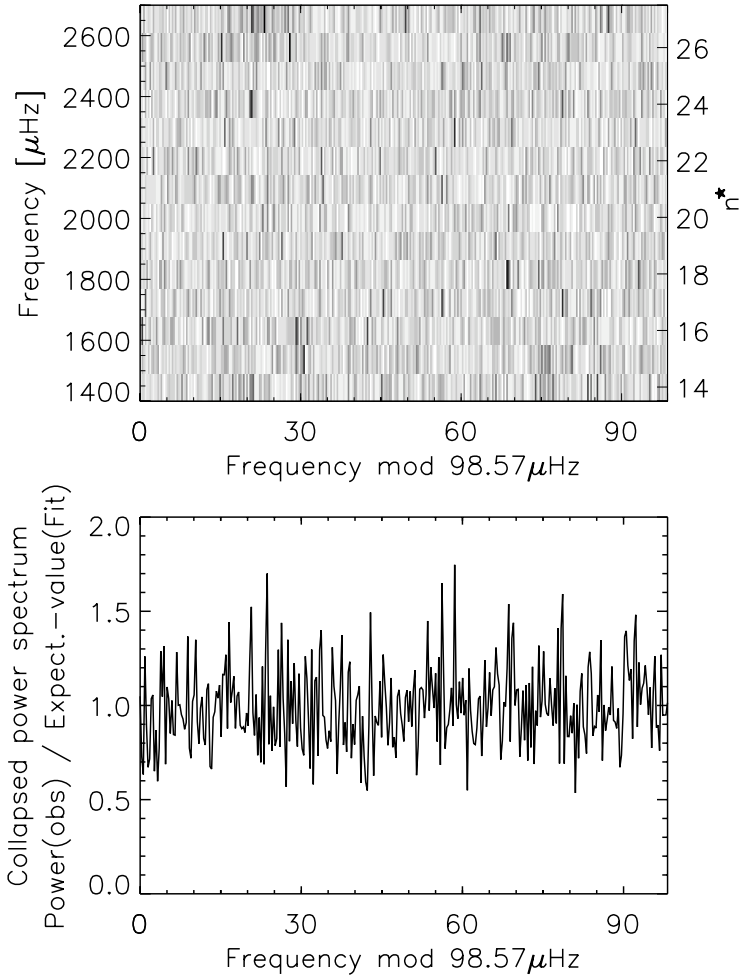
Figure 3.14: Investigation of the potential evidence of $\ell = 3$ modes. The *top panel* shows a residual power spectrum of HD 52265 in echelle format. For that purpose, the observed CoRoT power spectrum of HD 52265 is divided by the expectation value of the power determined with a global fit in this work. The folding frequency is $\widetilde{\Delta \nu} = 98.57\,\mu$Hz (cf. Figure 3.4). For clarity, the power in the $\widetilde{\Delta \nu}$-wide intervals is rebinned by a factor of three. The *bottom panel* shows a collapsed power spectrum, i.e. an average of the $\widetilde{\Delta \nu}$-wide sections between $n^{\star} = 17 - 24$. Compared to the original echelle spectrum in Figure 3.4, I note that the power in the ridges corresponding to modes with $\ell \leq 2$ is well fitted. There is no significant power left in the residual power spectrum. There is also no evidence for residual power that may be interpreted as p modes with $\ell = 3$.

71
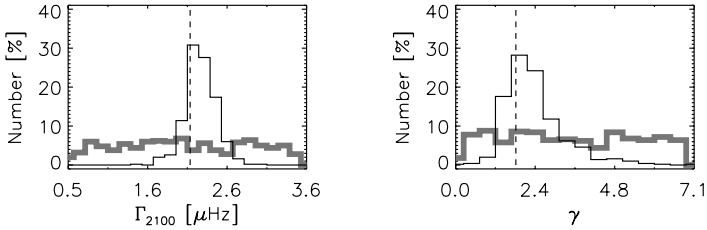
Figure 3.15: Distribution of the linewidth parameters (Fit A) for the global fit of the 117 day CoRoT observation of HD 52265. In Fit A, the mode linewidth is described in terms of a power law with two free parameters according to Equation (3.3), i.e. the linewidth Γ_{2100} at $\nu = 2100 \, \mu$Hz (*left panel*) and the slope of the power law, γ (*right panel*). In both panels, the distribution of the 500 initial guesses (*grey*) and the results of the global fit (*black*) are compared. The *vertical dashed lines* represent the respective values of the best-fit.
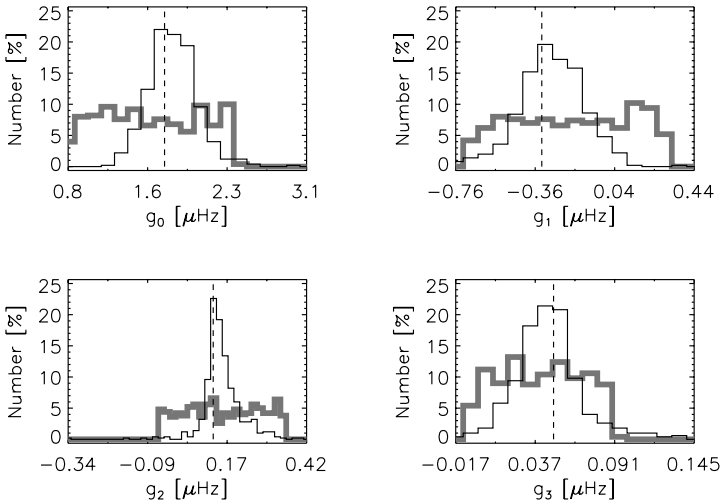
Figure 3.16: Distribution of the linewidth parameter (Fit B) for the global fit of the 117 day CoRoT observation of HD 52265. In Fit B, the mode linewidth is described as a 3rd-order polynomial with four free parameters, g_i ($i = 0, 1, 2, 3$), according to Equation (2.12). In all four panels, the distribution of the 500 initial guesses (*grey*) and the results of the global fit (*black*) are compared. The *vertical dashed line* in each panel represents the value of the best-fit.
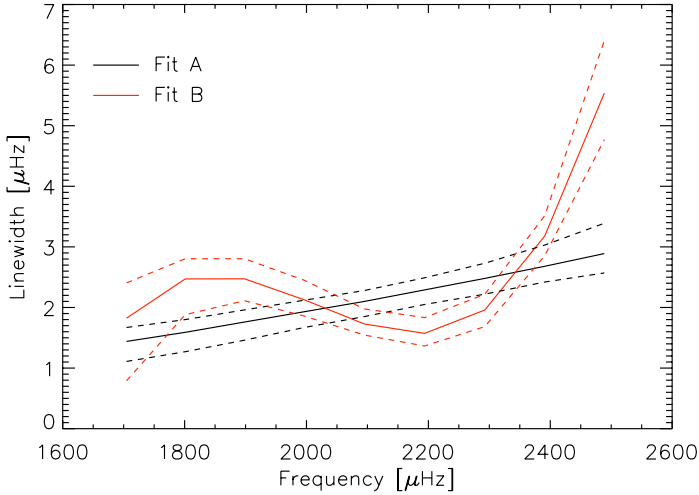
Figure 3.17: Mode linewidth, Γ_{n0}, of the radial modes of HD 52265 as a function of the mode frequency, ν_{n0}. The results for the two fits are shown in different colors. The *solid black line* represents the linewidth determined with Fit A, i.e. a power law according to Equation (3.3). The *solid red line* shows the linewidth determined with Fit B, i.e. a 3rd-order polynomial of the radial order according to Equation (2.12). The *dashed lines* represent 1σ error bars which are derived from Monte Carlo simulations. The mode linewidths and the corresponding mode frequencies are listed in Table 3.6 and Table 3.7.

Table 3.6 for Fit A and in Table 3.7 for Fit B. The 1σ error bars are deduced from Monte Carlo simulations (see Section 3.6). They are defined such that 68% of the fits fall within the given bounds (34% of the fits above the best fit estimate and 34% below). This definition takes into account that the parameter distributions of the Monte Carlo simulations are not necessarily symmetric and it is robust with respect to outliers.

Figure 3.17 shows the linewidth as a function of the mode frequency for both fits. In Fit A, the mode linewidths follow a power law with a slope of $\gamma = 1.84^{+0.50}_{-0.03}$. The linewidths are determined to be $1.4\,\mu\text{Hz} < \Gamma < 3\,\mu\text{Hz}$ in the frequency range between $1700\,\mu\text{Hz} < \nu < 2500\,\mu\text{Hz}$. The slope of the power law is slightly steeper than for the Sun. By fitting a power law in the frequency range $2200\,\mu\text{Hz} \leq \nu \leq 3500\,\mu\text{Hz}$ to the solar mode linewidths given by Chaplin et al. (1998), I obtain a slope of $\gamma \sim 1.6$. This frequency range corresponds to the low-degree p modes with the highest signal-to-noise ratio. Note that for the Sun the frequency dependence of the mode linewidth is significantly steeper at lower and higher frequencies (e.g. Chaplin et al. 1997).

The 3rd-order polynomial of Fit B leads to mode linewidths which are of the order of $\Gamma \sim 2\,\mu\text{Hz}$ in the frequency range $1400\,\mu\text{Hz} \lesssim \nu \lesssim 2300\,\mu\text{Hz}$. At higher frequencies they

Table 3.6: Mode parameters of the radial p modes ($\ell = 0$) of HD 52265. The parameters are determined from a global fit of the 117 day CoRoT power spectrum of HD 52265. The parameters listed in this table correspond to the results of Fit A, i.e. the mode linewidths are parameterized as a power law according to Equation (3.3). The global fit ranges over 9 consecutive radial orders n (*column 1*). The mode frequencies in *column 2* are taken from Table 3.4. *Column 3* lists the mode linewidths, Γ_{n0}. The amplitudes (in ppm) of the radial modes, $A_{n0} = \sqrt{\pi\Gamma_{n0}H_{n0}}$, where H_{n0} is the peak height (in ppm^2/μHz), are shown in *column 4*. Finally, *column 5* gives an estimate on the signal-to-noise ratio, i.e. the ratio of the peak height of a particular mode and the stellar background noise, $\mathcal{B}(\nu_{n0})$, at frequency ν_{n0} (see Section 3.5). The error bars are determined from Monte Carlo simulation (200 realizations). For the mode frequencies, ν_{n0}, they correspond to the 1σ standard deviation. For the linewidths, amplitudes, and signal-to-noise ratios, they are defined such that 68% of all fits of the Monte Carlo simulation fall within the range denoted by the exponents/subscripts.

	Fit A: p-mode parameters of the radial modes of HD 52265			
n	ν_{n0} [μHz]	Γ_{n0} [μHz]	A_{n0} [ppm]	$H_{n0}/\mathcal{B}(\nu_{n0})$
17	1704.71 ± 0.36	$1.44^{+0.23}_{-0.33}$	$2.69^{+0.20}_{-0.21}$	$2.1^{+0.6}_{-0.5}$
18	1801.01 ± 0.18	$1.59^{+0.21}_{-0.32}$	$3.09^{+0.19}_{-0.19}$	$2.6^{+0.6}_{-0.5}$
19	1898.32 ± 0.18	$1.76^{+0.20}_{-0.30}$	$3.53^{+0.17}_{-0.17}$	$3.2^{+0.6}_{-0.5}$
20	1996.39 ± 0.16	$1.93^{+0.19}_{-0.26}$	$3.97^{+0.19}_{-0.17}$	$3.8^{+0.7}_{-0.4}$
21	2094.96 ± 0.16	$2.10^{+0.18}_{-0.25}$	$4.38^{+0.21}_{-0.18}$	$4.3^{+0.6}_{-0.5}$
22	2193.79 ± 0.19	$2.29^{+0.20}_{-0.24}$	$4.67^{+0.22}_{-0.20}$	$4.6^{+0.5}_{-0.6}$
23	2292.62 ± 0.20	$2.48^{+0.25}_{-0.26}$	$4.78^{+0.18}_{-0.26}$	$4.5^{+0.5}_{-0.6}$
24	2391.21 ± 0.24	$2.68^{+0.35}_{-0.26}$	$4.16^{+0.19}_{-0.28}$	$3.2^{+0.6}_{-0.5}$
25	2489.30 ± 0.51	$2.89^{+0.50}_{-0.32}$	$2.88^{+0.26}_{-0.23}$	$1.5^{+0.3}_{-0.3}$

Table 3.7: Mode parameters of the radial p modes ($\ell = 0$) of HD 52265. The parameters are determined from a global fit of the 117 day CoRoT power spectrum of HD 52265. The parameters listed in this table correspond to the result of Fit B, i.e. the mode linewidths are parameterized as a 3$^{\text{rd}}$-order polynomial according to Equation (2.12). The global fit ranges over 9 consecutive radial orders n (*column 1*). The mode frequencies in *column 2* are taken from Table 3.5. *Column 3* lists the mode linewidths, Γ_{n0}. The amplitudes (in ppm) of the radial modes, $A_{n0} = \sqrt{\pi \Gamma_{n0} H_{n0}}$, where H_{n0} is the peak height (in ppm$^2/\mu$Hz), are shown in *column 4*. Finally, *column 5* gives an estimate on the signal-to-noise ratio, i.e. the ratio of the peak height of a particular mode and the stellar background noise, $\mathcal{B}(\nu_{n0})$, at frequency ν_{n0} (see Section 3.5). The error bars are determined from Monte Carlo simulation (200 realizations). For the mode frequencies, ν_{n0}, they correspond to the 1σ standard deviation. For the linewidths, amplitudes, and signal-to-noise ratios, they are defined such that 68% of all fits of the Monte Carlo simulation fall within the range denoted by the exponents/subscripts.

	Fit B: p-mode parameters of the radial modes of HD 52265			
n	ν_{n0} [μHz]	Γ_{n0} [μHz]	A_{n0} [ppm]	$H_{n0}/\mathcal{B}(\nu_{n0})$
17	1704.76 ± 0.40	$1.82^{+0.58}_{-1.03}$	$2.72^{+0.17}_{-0.22}$	$1.7^{+1.8}_{-0.6}$
18	1800.94 ± 0.23	$2.47^{+0.33}_{-0.59}$	$3.14^{+0.16}_{-0.18}$	$1.8^{+0.4}_{-0.3}$
19	1898.23 ± 0.26	$2.47^{+0.33}_{-0.36}$	$3.60^{+0.18}_{-0.17}$	$2.4^{+0.5}_{-0.3}$
20	1996.33 ± 0.19	$2.13^{+0.32}_{-0.27}$	$4.06^{+0.20}_{-0.14}$	$3.6^{+0.7}_{-0.5}$
21	2094.96 ± 0.14	$1.73^{+0.25}_{-0.18}$	$4.45^{+0.23}_{-0.16}$	$5.4^{+1.1}_{-0.9}$
22	2193.81 ± 0.14	$1.57^{+0.26}_{-0.21}$	$4.71^{+0.21}_{-0.23}$	$6.9^{+1.4}_{-1.3}$
23	2292.58 ± 0.17	$1.96^{+0.26}_{-0.27}$	$4.77^{+0.14}_{-0.31}$	$5.7^{+1.1}_{-0.8}$
24	2390.98 ± 0.29	$3.18^{+0.35}_{-0.33}$	$4.20^{+0.17}_{-0.24}$	$2.8^{+0.4}_{-0.3}$
25	2488.70 ± 0.65	$5.54^{+0.87}_{-0.77}$	$3.27^{+0.31}_{-0.14}$	$1.0^{+0.2}_{-0.2}$

Table 3.8: Parameters of the amplitude envelope determined with a global fit to the 117 day power spectrum of HD 52265. The amplitude envelope according to Equation (2.14) is applied. The results of the global fit using Fit A and Fit B are listed in the *second* and *third column* respectively. For details on Fit A and B, see Section 3.5. The error bars are derived from Monte Carlo simulation (200 realizations) and are defined such that 68% of all fits fall within the bounds denoted by the exponents/subscripts.

Amplitude parameters	Fit A	Fit B
ν_0 [μHz]	2302^{+41}_{-33}	2273^{+46}_{-44}
$\widetilde{\sigma}_1$ [μHz]	677^{+90}_{-73}	654^{+96}_{-86}
$\widetilde{\sigma}_2$ [μHz]	231^{+59}_{-65}	317^{+109}_{-78}
$\mathcal{A}_0$ [ppm]	$4.79^{+0.23}_{-0.20}$	$4.78^{+0.20}_{-0.24}$
$\mathcal{A}_1$ [ppm]	$5.81^{+0.24}_{-0.24}$	$5.91^{+0.23}_{-0.24}$
$\mathcal{A}_2$ [ppm]	$3.72^{+0.20}_{-0.23}$	$3.64^{+0.18}_{-0.17}$

increase steeply up to $\Gamma \sim 5\,\mu$Hz at $\nu \sim 2500\,\mu$Hz. At $\nu \sim 2200\,\mu$Hz there is a distinct dip of the mode linewidths. Qualitatively, the overall trend of the linewidths of HD 52265 is comparable to the Sun (see Section 2.3.2). Fit B also matches the results of the other groups of the DAT quite well (Ballot et al. 2010). The more simplified parameterization of Fit A seems to describe the overall trend of the linewidths of Fit B quite well. However, Fit A does not match the "fine structure" of Fit B, i.e. the dip of the linewidth and the following steep increase.

At maximum signal-to-noise, i.e. at $\nu \sim 2200\,\mu$Hz, the linewidths of the p modes in HD 52265 are about $\Gamma \sim 2.3\,\mu$Hz for Fit A and $\Gamma \sim 1.6\,\mu$Hz for Fit B. This corresponds to a mode lifetime, $\tau = 1/\pi\Gamma$, of $\tau \sim 1.6$ days (Fit A) and $\tau \sim 2.3$ days (Fit B) respectively. Hence, the lifetime of the p modes in HD 52265 is only about half as long as the p-mode lifetime in the Sun ($\tau \sim 4$ days for $\Gamma \sim 1\,\mu$Hz).

3.7.3 Oscillation amplitudes

For the global fit, the mode amplitudes and mode heights of the p modes in HD 52265 are parameterized by an envelope according to Equation (2.14). The amplitude envelope contains six free parameters: the center of the envelope, ν_0, the width, $\widetilde{\sigma}_i$ ($i = 1, 2$), for frequencies $\nu \leq \nu_0$ and $\nu > \nu_0$ respectively, and the envelope maxima, $\mathcal{A}_\ell$, for modes with degree $\ell \leq 2$. An additional free parameter, the inclination angle, i, of the rotation axis, gives the height ratio of the azimuthal components of the non-radial modes [cf. Equation (2.15)]. The measurement of i is discussed in Section 3.7.4. Figure 3.18 shows the distributions of the parameters of the amplitude envelope for HD 52265. The distributions of the 500 initial guesses and the fit results are compared. The distributions of the fits show overall a single peak even though it may not be very pronounced for all parameters (e.g. $\widetilde{\sigma}_2$). In general, I conclude that the global fit works. However, the best fit estimates for ν_0 and $\widetilde{\sigma}_i$ ($i = 1, 2$) seem to be slightly biased. The fit of the maxima of
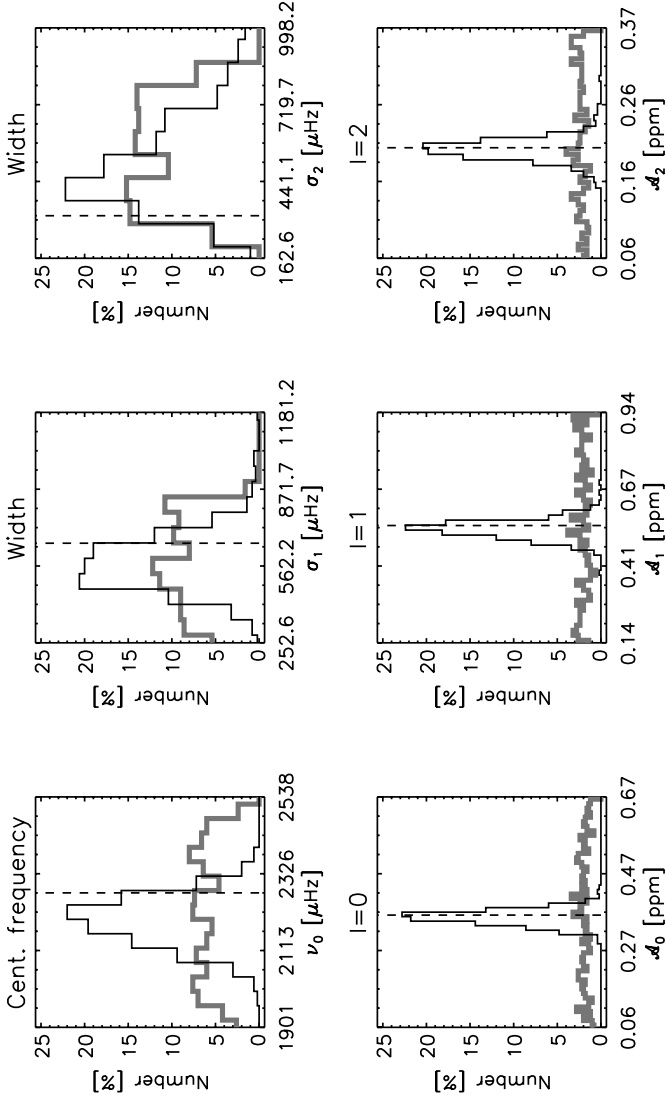
Figure 3.18: Distribution of the amplitude parameters for the global fit of the 117 day CoRoT observation of HD 52265. The distribution of the 500 initial guesses is shown in *grey*, the fit results in *black*. The *vertical dashed lines* mark the best fit for each parameter. The three panels in the *top row* show the central frequency, ν_0, and the width, $\widetilde{\sigma}_i$ ($i = 1, 2$), of the amplitude envelope. The three panels in the *bottom row* represent the maxima of the amplitude envelope for modes with $\ell \leq 2$.
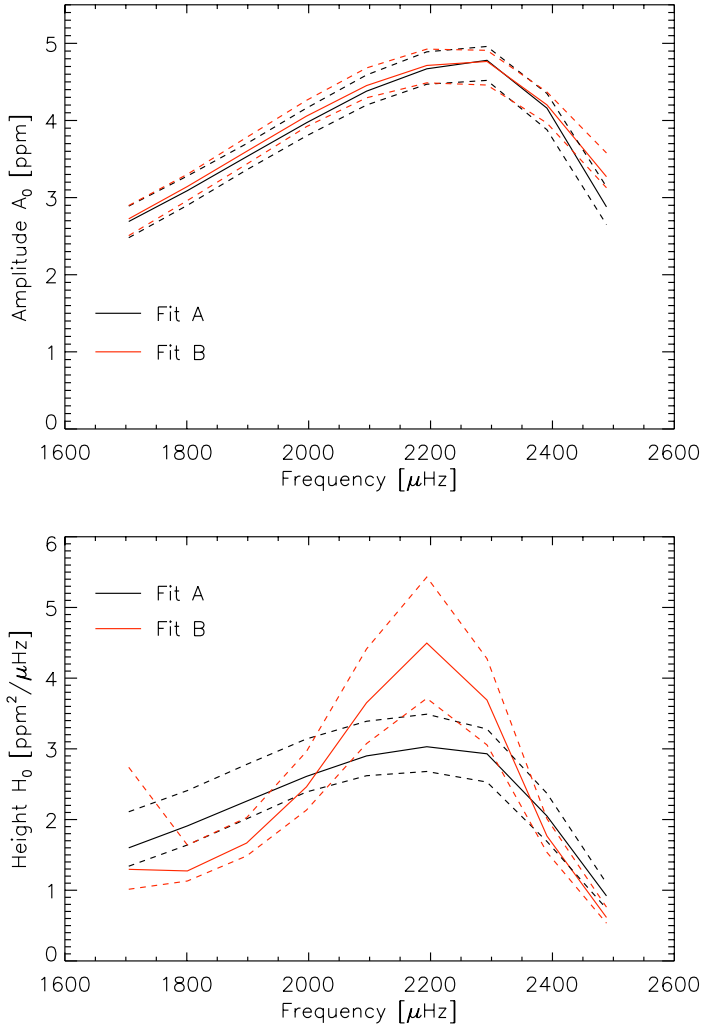
Figure 3.19: Amplitudes (*top panel*) and mode heights (*bottom panel*) of the radial modes ($\ell = 0$) determined with a global fit of the 117 day CoRoT observation of HD 52265. The mode amplitudes, A_{n0}, and mode heights, H_{n0}, are related by Equation (2.16). The result of the global fit obtained with Fit A is shown as the *solid black line*. The result obtained using Fit B is shown as the *solid red line* (see Section 3.5 for details on Fit A and Fit B). The *dashed lines* correspond to the 1σ error bars derived from Monte Carlo simulation.

the amplitude envelopes, $\mathcal{A}_\ell$ ($\ell \leq 2$), is reliable; the best fit is close to the maximum of the distribution for each ℓ.

Table 3.8 summarizes the results for the parameters of the amplitude envelope for HD 52265. The 1σ error bars are derived from Monte Carlo simulation and are defined such that 68% of the fits fall within the bounds set by the exponents and subscripts. The results obtained for Fit A and B are consistent within their respective error estimates. The center of the amplitude envelope, i.e. the maximum mode amplitude, is found at $\nu \sim 2300\,\mu$Hz. As already supposed in Section 3.4, the distribution of the mode amplitudes is asymmetric as indicated by the width of the envelope, $\widetilde{\sigma}_i$ ($i = 1, 2$). The maximum mode amplitude of the radial modes is $A \sim 4.8$ ppm. Hence, the amplitudes of HD 52265 are of the same order of magnitude as the amplitudes in the Sun.

The parameters of the amplitude envelope listed in Table 3.8 may be used to calculate the amplitudes and the heights of the p modes of HD 52265 according to Equations (2.14) and (2.16). Figure 3.19 shows the mode amplitudes, A_{n0}, and the mode heights, H_{n0}, of the radial modes obtained for Fit A and Fit B as a function of their respective mode frequency, ν_{n0}. The mode amplitudes of both fits are fully consistent. The amplitudes obtained for both fits are listed in Table 3.6 and 3.7. Since both fits return slightly different mode linewidths (see Section 3.7.2), the mode heights are also slightly different according to Equation (2.16). The amplitudes obtained in this analysis are consistent with the results of the other groups of the DAT (Ballot et al. 2010).

Table 3.6 and 3.7 also list the signal-to-noise ratio of the radial modes, $H_{n0}/\mathcal{B}(\nu_{n0})$, which I define as the ratio of the mode height and the stellar background noise at the frequency of the corresponding mode, ν_{n0}. The maximum signal-to-noise at $\nu \sim 2200\,\mu$Hz is of the order of $H/\mathcal{B} \sim 5$ for Fit A and $H/\mathcal{B} \sim 7$ for Fit B, i.e. roughly ten times smaller than the signal-to-noise ratio of the VIRGO data analyzed in Chapter 2.

3.7.4   Stellar rotation and the inclination of the rotation axis

For the global fit of the HD 52265 power spectrum, the rotational splitting of the m components of the non-radial modes is considered by one free parameter, $\Omega/2\pi$. Here, I assumed slow and uniform rotation with angular velocity $\Omega = $ const. (see Section 1.3 and 2.2.2). The inclination angle of the rotation axis, i, is determined from the mode height ratio of the m components according to Equation (2.15).

In Figure 3.20 and Figure 3.21, I show averaged line profiles for modes with $\ell \leq 2$. These line profiles are obtained by averaging sections of the power spectrum of HD 52265 which are centered around the mode frequencies, $\nu_{n\ell}$, over nine consecutive radial orders. The individual m components of the non-radial modes are not resolved since the mode linewidth is bigger than the rotational splitting, i.e. $2\pi\Gamma/\Omega \sim 2$. Here, I assumed a mode linewidth of $\Gamma \sim 2\,\mu$Hz (Section 3.7.2) and a rotational splitting according to the stellar surface rotation, $\Omega/2\pi \sim 1\,\mu$Hz (Section 3.3.2). Note that the ratio of $2\pi\Gamma/\Omega$ for HD 52265 is very close to the solar value discussed in Section 2.3.4. Even though the individual m components are not resolved, it is obvious that the averaged line profiles of the non-radial modes ($\ell \geq 1$) are broader than the averaged line profile of the radial modes. I interpret this broadening as the signature of stellar rotation. Quantitatively, the rotational splitting and the inclination angle of the rotation axis are here determined to $\Omega/2\pi = 0.98\,\mu$Hz and $i = 36°$ (Fit A) and $\Omega/2\pi = 0.53\,\mu$Hz and $i = 60°$ (Fit B). Even

Table 3.9: Seismic constraints on the rotation and the inclination angle of the rotation axis of HD 52265, derived from a global fit of the 117 day CoRoT observation. The results obtained for Fit A and Fit B are presented in the *second* and *third column* respectively. The 1σ error bars are derived from Monte Carlo simulation. They are defined such that 68% of all results fall within the bounds given by the exponents and subscripts. Note that the rotational splitting, $\Omega/2\pi$, and the inclination i were free parameters of the global fit. The other parameters, $\Omega/\Omega_\odot$, P_{rot}, $\Omega/2\pi \sin i$, are derived from those two parameters ($\Omega_\odot/2\pi = 0.4243\,\mu$Hz, corresponding to the Carrington solar rotation rate).

Seismic constraints for HD 52265	Fit A	Fit B
Rotational splitting $\Omega/2\pi$ [μHz]	$0.98^{+0.40}_{-0.44}$	$0.53^{+0.54}_{-0.05}$
Rotation $\Omega/\Omega_\odot$	$2.31^{+0.94}_{-1.04}$	$1.25^{+1.27}_{0.12}$
Rotation period P_{rot} [days]	$11.8^{+9.4}_{-3.3}$	$22.0^{+2.3}_{-11.2}$
Inclination i [deg]	36^{+39}_{-7}	60^{+8}_{-38}
$\sin i$	$0.59^{+0.37}_{-0.10}$	$0.86^{+0.06}_{-0.49}$
$\Omega/2\pi \sin i$ [μHz]	$0.58^{+0.14}_{-0.13}$	$0.47^{+0.13}_{-0.16}$

though the results for $\Omega/2\pi$ and i are different for both fits, the averaged line profiles are nearly the same. I note that the product of $\Omega/2\pi$ and $\sin i$ is very similar for both fits, i.e. $\Omega/2\pi \sin i = 0.58\,\mu$Hz (Fit A) and $\Omega/2\pi \sin i = 0.47\,\mu$Hz for (Fit B).

Figure 3.22 and Figure 3.23 show the distributions of the 500 initial guesses and the corresponding fits for $\Omega/2\pi$ and i obtained for Fit A and Fit B. It is noteworthy that for the rotational splitting the distributions of both fits show a distinct peak at $\Omega/2\pi \sim 0.5\,\mu$Hz. Only for Fit B the best-fit estimate on $\Omega/2\pi$ is close to the maximum of the distribution while the best-fit of Fit A is biased. For the inclination the situation is vice versa. The distributions of both fits show a barely pronounced peak around $i \sim 40°$. I note that the distribution of the inclination is spread over the full range between $0° \leq i \leq 90°$. However, the result of Fit A is near the maximum of the distribution while the inclination for Fit B is biased. The distribution of the product of both parameters, $\Omega/2\pi \sin i$, shows a well pronounced peak at $\Omega/2\pi \sin i \sim 0.5\,\mu$Hz, and the best-fit estimates for Fit A and Fit B are both near the maximum of the respective distribution. This confirms the studies of Gizon and Solanki (2003) and Ballot et al. (2006, 2008) and is similar to the result of the the analysis of the solar data in Chapter 2 (Section 2.3.4) of this thesis: it is very difficult to measure both the rotational splitting and the inclination angle of the rotation axis independently and without bias for a slowly rotating star. However, it is possible to measure the product, $\Omega \sin i$, precisely.

The seismic constraints on the rotation and the inclination angle of the rotation axis are summarized in Table 3.9. The 1σ error bars are derived from Monte Carlo simulation. Note that the estimates on $\Omega/2\pi$ and i for Fit A and Fit B are in agreement with respect to their error bars. The rotational splitting matches the estimate of the surface rotation

rate from Section 3.3.2 reasonably well. This is particularly true for Fit A. The estimates on $\Omega \sin i$ agree well for both fits. Furthermore, the error on $\Omega \sin i$ is quite symmetric in contrast to the error bars on $\Omega/2\pi$ and i. Note that the estimates on $\Omega \sin i$ determined in this work are consistent with an alternative measurement derived from the relation $\Omega \sin i \simeq v \sin i/R$. With a recent spectroscopic measurement of $v \sin i = 3.6^{+0.3}_{-1.0}$ km/s and a seismic radius estimate of $R = 1.34 \pm 0.02\,R_{\odot}$ (Ballot et al. 2010), one obtains $\Omega/2\pi \sin i = 0.61^{+0.06}_{-0.18}\,\mu$Hz. This value is in agreement with both estimates obtained for Fit A and Fit B in this analysis. I note that other measurements for $v \sin i$ can be found in the literature, for example $v \sin i = 4.7 \pm 0.5$ km/s (Valenti and Fischer 2005). This measurement would be less consistent with the analysis presented here. However, Valenti and Fischer (2005) also point out that their estimates on $v \sin i$ may be overestimated for metal-rich stars with temperatures larger than 5800 K.

The fit result for the stellar rotational splitting and the inclination angle of the rotation axis are illustrated in Figure 3.24 and Figure 3.25. The figures show the shape of the joint PDF in the $\Omega/2\pi$-$\sin i$ plane. This was obtained by performing global fits with fixed values for $\Omega/2\pi \in [0.05\mu\text{Hz}, 2.5\mu\text{Hz}]$ in steps of 0.05μHz and $\sin i \in [0.02, 1]$ in steps of 0.02. "Good fits" of the parameters $\Omega/2\pi$ and i are aligned along constant $\Omega \sin i$. The shape of the joint PDF in the $\Omega/2\pi$-$\sin i$ plane allows us to constrain $\Omega/2\pi$ and i solely based on the asteroseismic analysis (as indicated by the 1σ contour line): for Fit A, the rotational splitting is constrained between $0.45\,\mu\text{Hz} < \Omega/2\pi < 1.30\,\mu\text{Hz}$. The lower limit of the inclination is $i > 25°$. Rotational splitting and the inclination angle are correlated and further constrained by $\Omega/2\pi \sin i = 0.58^{+0.14}_{-0.13}\,\mu$Hz. For Fit B, I obtain $0.25\,\mu\text{Hz} < \Omega/2\pi < 1.15\,\mu\text{Hz}$ and $i > 22°$. Both parameters are further constrained by $\Omega/2\pi \sin i = 0.47^{+0.13}_{-0.16}\,\mu$Hz.

To further constrain the estimates on the inclination angle of the rotation axis, the precise asteroseismic measurement of $\Omega \sin i$ may be combined with the estimate on the stellar surface rotation from Section 3.3.2. For this purpose, the low-frequency peaks at $\Omega/2\pi = 0.91\,\mu$Hz and $\Omega/2\pi = 1.07\,\mu$Hz (Figure 3.5) are shown in Figure 3.24 and Figure 3.25. The intersection of the surface rotation features and the 1σ-contour line (or the estimate on $\Omega \sin i$ directly) allows us to constrain the inclination angle of the rotation axis of HD 52265:

$$\text{Fit A:} \qquad 0.45 \leq \sin i \leq 0.82, \qquad 27° \leq i \leq 55°,$$
$$\text{Fit B:} \qquad 0.38 \leq \sin i \leq 0.72, \qquad 22° \leq i \leq 46°.$$

The constraints on the inclination, i, are consistent for Fit A and Fit B. However, I note that only the best fit of Fit A ($\Omega/2\pi = 0.98\,\mu$Hz, $i = 36°$) falls within the intersection of the low-frequency features and the constraint on $\Omega \sin i$. The best-fit estimate for Fit B is obviously biased but it is still in agreement with the estimate on the surface rotation within its error bars.
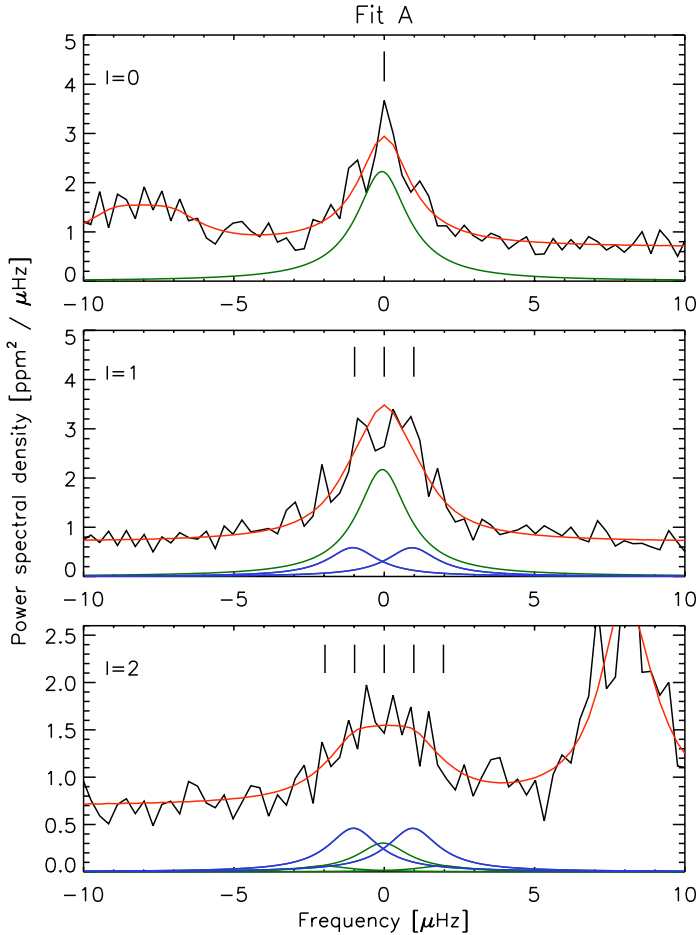
Figure 3.20: Average power spectrum of the solar-like p modes observed in HD 52265. Small sections of the power spectrum centered around the mode frequency, $\nu_{n\ell}$, are averaged over nine consecutive radial orders for modes with $\ell \leq 2$ (cf. bottom row of Figure 3.8). For clarity, the resolution is reduced by a factor of three by rebinning. The *black line* is the observed power, the *red line* is the averaged expectation value of the power (Fit A). The *green and blue lines* at the bottom of each panel represent the individual azimuthal components with even and odd m respectively. The rotational splitting of the azimuthal components is indicated by the *vertical tick marks*. Even though the m components are not resolved, the averaged line profiles of the non-radial modes ($\ell = 1, 2$) are broader than the profile of the radial modes ($\ell = 0$). In this case, rotation and the inclination angle of the rotation axis are determined to be $\Omega/2\pi = 0.98\,\mu$Hz and $i = 36°$.
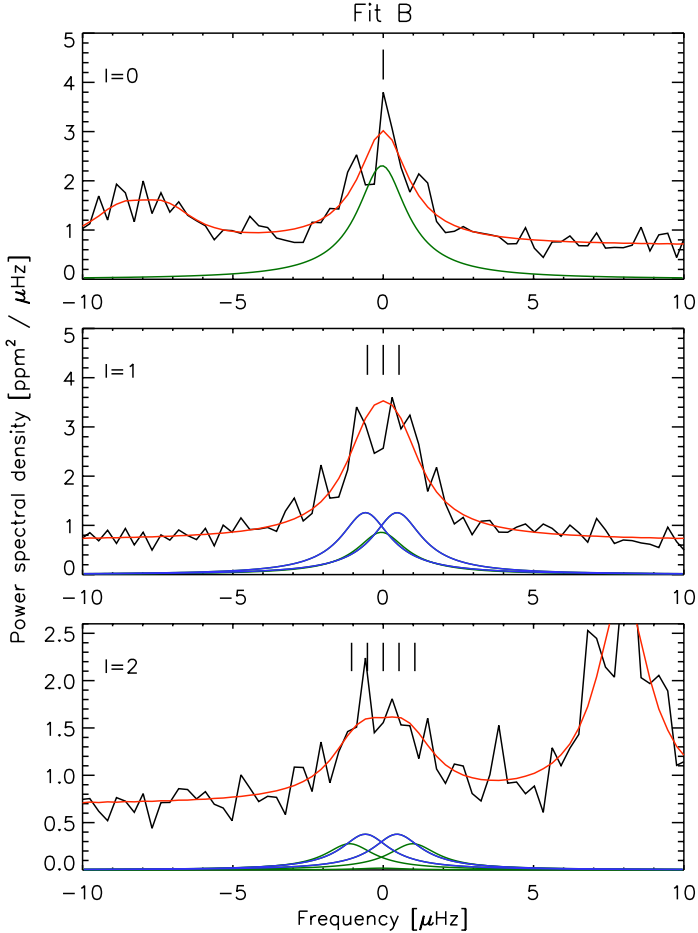
Figure 3.21: Average power spectrum of the solar-like p modes observed in HD 52265. Small sections of the power spectrum centered around the mode frequency, $\nu_{n\ell}$, are averaged over nine consecutive radial orders for modes with $\ell \leq 2$ (cf. bottom row of Figure 3.8). For clarity, the resolution is reduced by a factor of three by rebinning. The *black line* is the observed power, the *red line* is the averaged expectation value of the power (Fit B). The *green and blue lines* at the bottom of each panel represent the individual azimuthal components with even and odd m respectively. The rotational splitting of the azimuthal components is indicated by the *vertical tick marks*. Even though the m components are not resolved, the averaged line profiles of the non-radial modes ($\ell = 1, 2$) are broader than the profile of the radial modes ($\ell = 0$). In this case, rotation and the inclination angle of the rotation axis are determined to be $\Omega/2\pi = 0.54\,\mu$Hz and $i = 59°$. Despite different rotational splitting and inclination angle compared to Figure 3.20, the averaged line profiles are nearly the same.
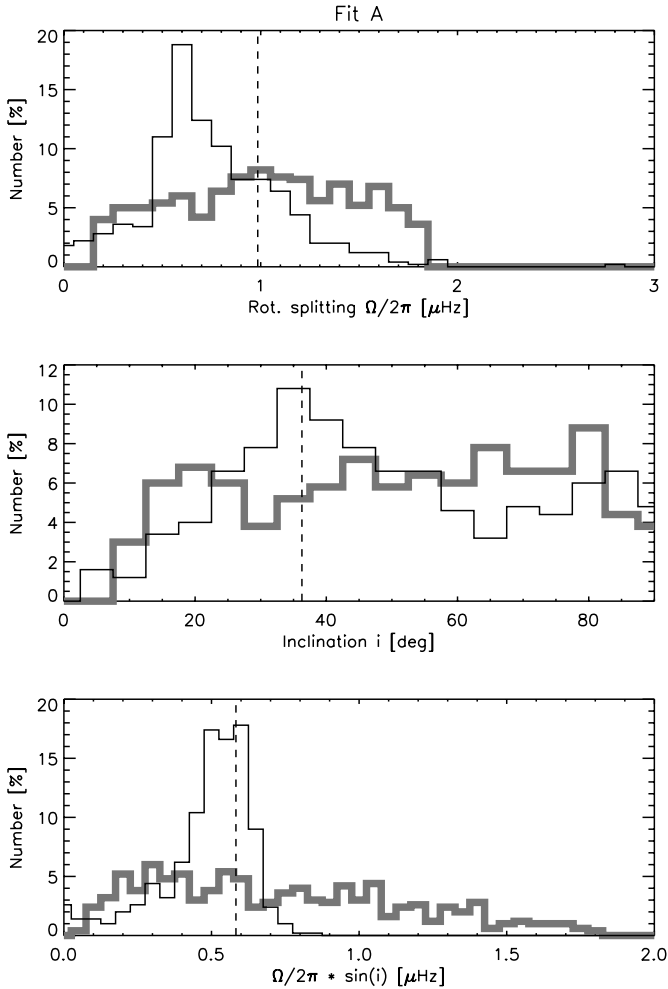
Figure 3.22: Distribution of the rotational splitting, $\Omega/2\pi$ (*top panel*), and the inclination angle of the rotation axis, i (*middle panel*), determined with a global fit of the 117 day CoRoT observation of HD 52265 (Fit A). The *grey line* represents the distribution of 500 initial guesses, the *black line* shows the distribution of the fit results. The *vertical dashed line* marks the result of the best fit. The *bottom panel* shows the distribution of $\Omega/2\pi \sin i$ which is composed of the parameters in the two panels above.
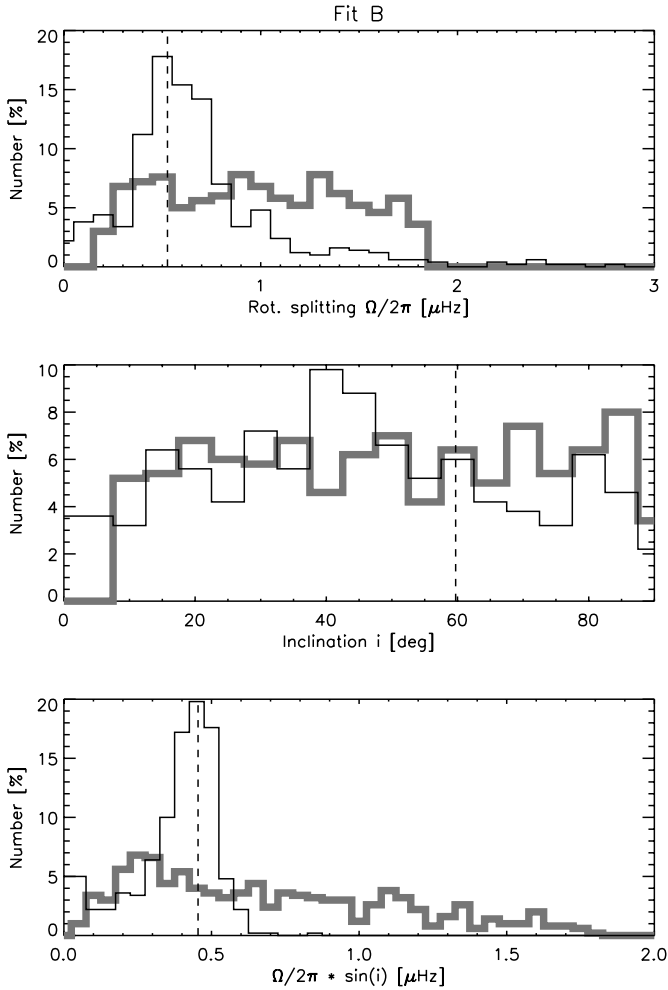
Figure 3.23: Distribution of the rotational splitting, $\Omega/2\pi$ (*top panel*), and the inclination angle of the rotation axis, *i* (*middle panel*), determined with a global fit of the 117 day CoRoT observation of HD 52265 (Fit B). The *grey line* represents the distribution of 500 initial guesses, the *black line* shows the distribution of the fit results. The *vertical dashed line* marks the result of the best fit. The *bottom panel* shows the distribution of $\Omega/2\pi \sin i$ which is composed of the parameters in the two panels above.
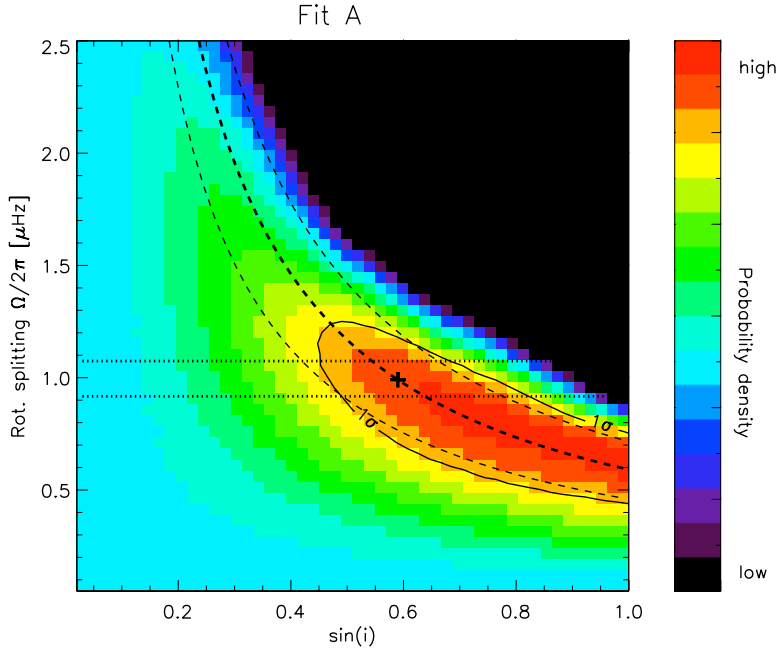
Figure 3.24: Constraints on the rotational splitting, $\Omega/2\pi$, and the inclination angle of the rotation axis, i, determined with a global fit of the 117 day CoRoT observation of HD 52265 (Fit A). The (+) symbol represents the result of the global fit, i.e. $\Omega/2\pi = 0.98\,\mu$Hz and $\sin i = 0.59$ ($i = 36°$). The color map in the background illustrates the shape of the joint PDF (or the log-likelihood function) in the $\Omega/2\pi$-$\sin i$ plane. For various sets of fixed parameters, $[\Omega/2\pi, \sin i]$, a global fit was performed. The colors represent the value of the log-likelihood function given the maximum likelihood estimates for a particular pair of $[\Omega/2\pi, \sin i]$. The *three dashed lines* represent the fit result for $\Omega/2\pi \sin i = 0.58^{+0.14}_{-0.13}\,\mu$Hz. The error estimates are derived from Monte Carlo simulation (200 realizations). The *1σ-contour line* contains 68% of the fits of $[\Omega/2\pi, \sin i]$ from the Monte Carlo simulation. The *horizontal dotted lines* at $\nu = 0.91\,\mu$Hz and $\nu = 1.07\,\mu$Hz represent the two peaks in the low-frequency power spectrum which are attributed to the stellar surface rotation of HD 52265 (cf. Section 3.3.2).
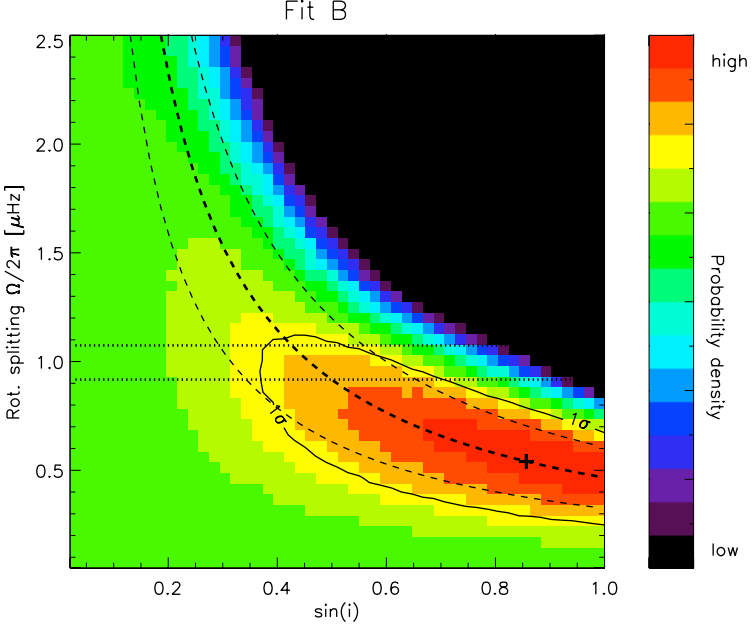
Figure 3.25: Constraints on the rotational splitting, $\Omega/2\pi$, and the inclination angle of the rotation axis, i, determined with a global fit of the 117 day CoRoT observation of HD 52265 (Fit B). The (+) symbol represents the result of the global fit, i.e. $\Omega/2\pi = 0.53\,\mu$Hz and $\sin i = 0.86$ ($i = 60°$). The color map in the background illustrates the shape of the joint PDF (or the log-likelihood function) in the $\Omega/2\pi$-$\sin i$ plane. For various sets of fixed parameters, $[\Omega/2\pi, \sin i]$, a global fit was performed. The colors represent the value of the log-likelihood function given the maximum likelihood estimates for a particular pair of $[\Omega/2\pi, \sin i]$. The *three dashed lines* represent the fit result for $\Omega/2\pi \sin i = 0.47\,^{+0.13}_{-0.16}\,\mu$Hz. The error estimates are derived from Monte Carlo simulation (200 realizations). The *1σ-contour line* contains 68% of the fits of $[\Omega/2\pi, \sin i]$ from the Monte Carlo simulation. The *horizontal dotted lines* at $\nu = 0.91\,\mu$Hz and $\nu = 1.07\,\mu$Hz represent the two peaks in the low-frequency power spectrum which are attributed to the stellar surface rotation of HD 52265 (cf. Section 3.3.2).

3.7.5   Fit A or Fit B: Which fit is better?

For the global fit, I applied two different parameterizations of the mode linewidth: a power law according to Equation (3.3) for Fit A, and a 3rd-order polynomial of the radial order n according to Equation (2.12) for Fit B. Comparing the results obtained with both fits, I point out that the mode frequencies and amplitudes are almost the same. The estimates on the rotational splitting and the inclination angle of the rotation axis are in agreement within their respective error bars. Thus, the parameterizations of the mode linewidth which are used here do not affect the fit of those parameters significantly. The linewidth estimates are slightly different for both fits which may be attributed to the simpler parameterization of Fit A compared to Fit B (see Section 3.7.2). Fit A seems to be a more cautious approach with less assumptions on the frequency dependence of the mode linewidth than Fit B. However, comparing the values of the joint PDF for Fit A and Fit B calculated for their respective maximum likelihood estimates, I find that Fit B has a slightly higher likelihood than Fit A. Finally, I note that Fit A was the initial result of my analysis and the basis for discussion of the results of the different groups of the DAT. Fit B is a further development of the analysis of the HD 52265 data.

4 Fourier analysis of gapped time series: maximum likelihood estimation

So far, the data analyzed in this thesis were continuous or the fraction of gaps in the time series was so small that the missing data could be interpolated. This allows to apply the standard maximum likelihood estimation method as described in Section 1.5. However, such uninterrupted data are only available for the Sun and a limited number of stars observed in intensity from space. There exists a large number of asteroseismic data with gaps. In this chapter, I present the implementation of maximum likelihood estimates for gapped time series. The work presented in this chapter is largely based on the paper of Stahn and Gizon (2008). The paper focuses on the effect of the duty cycle on the accuracy of the estimators of the oscillation parameters. Here, additional sections will also investigate the effect of the signal-to-noise ratio (Section 4.7.4), the mode lifetimes (Section 4.7.5), and the initial guess (Section 4.7.6) on the estimation of the oscillation parameters.

4.1 Introduction

Solar and stellar oscillations are a powerful tool to probe the interior of stars. In this paper we classify stellar oscillations into solar-like or deterministic. Solar-like oscillations are stochastically excited by turbulent convection and are present in the Sun and other main-sequence, subgiant, and giant stars (see *e.g.* Bedding and Kjeldsen, 2007 and references therein). Deterministic oscillations are seen in classical pulsators and have mode lifetimes much longer than any typical observational run; one of the best studied objects in this class is the pre-white dwarf PG1159−035 also known as GW Vir Winget et al. (1991). In practice, observations of solar-like or deterministic pulsations always have an additional stochastic component due to instrumental, atmospheric, stellar, or photon noise.

An important aspect of helioseismology and asteroseismology is the determination of the parameters of the global modes of oscillation, especially the mode frequencies. In the case of the Sun, it is known (Woodard 1984) that the measurement precision is limited by the stochastic nature of the oscillations (realization noise). Libbrecht (1992), and Toutain and Appourchaux (1994) have shown that realization noise is expected to scale like $1/\sqrt{T}$, where T is the total duration of the observation. A common practice is to extract the solar mode parameters from the power spectrum using maximum likelihood estimation (MLE, see *e.g.* Anderson et al. 1990, Schou 1992, Toutain and Appourchaux 1994, Appourchaux

et al. 1998, 2000). In its current form, however, this method of analysis is only valid for uninterrupted time-series. This is a significant limitation because gaps in the data are not uncommon (because of the day-night cycle, bad weather, or technical problems). The gaps complicate the analysis in Fourier space: The convolution of the data with the observation window leads to correlations between the different Fourier components. The goal of this paper is to extend the Fourier analysis of solar and stellar oscillations to time series with gaps, by using appropriate maximum likelihood estimators based on the correct statistics of the data.

Section 4.2 poses the problem of the analysis of gapped time series in Fourier space. In Section 4.3 we derive an expression for the joint probability density function (PDF) of the observations, taking into account the frequency correlations. Our answer is consistent with an earlier (independent) derivation by Gabriel (1994). Based on this PDF, we derive maximum likelihood estimators in Section 4.4. In Section 4.5 we recall the "old method" of maximum likelihood estimation based on the unjustified assumption that frequency bins are statistically independent. Section 4.6 explains the setup of the Monte Carlo simulations used to test the fitting methods on artificial data sets. In Section 4.7 we present the results of the Monte Carlo simulations and compare the new and old fitting methods. For the sake of simplicity, we consider only one mode of oscillation at a time (solar-like or sinusoidal). We present several cases for which our new fitting method leads to a significant improvement in the determination of oscillation parameters, and in particular the mode frequency.

4.2   Statement of the problem

4.2.1   The observed signal in Fourier space

Let us denote by $\tilde{y} = \{\tilde{y}_i\}$ the time series that we wish to analyze. It is sampled at times $t_i = i\Delta t$, where i is an integer in the range $0 \leq i \leq N - 1$, and $\Delta t = 1$ min is the sampling time. All quantities with a tilde are defined in the time domain. The total duration of the time series is $T = (N - 1)\Delta t$. By choice, all of the missing data points were assigned the value zero: This enables us to work on a regularly sampled time grid. Formally, we write

$$\tilde{y}_i = \tilde{w}_i \tilde{x}_i, \quad i = 0, 1, \ldots, N - 1, \tag{4.1}$$

where $\tilde{x}$ is the uninterrupted time series that we *would* have observed if there had been no gaps and $\tilde{w}$ is the window function defined by $\tilde{w}_i = 1$ if an observation is recorded at time t_i and $\tilde{w}_i = 0$ otherwise. The $\tilde{x}$ is drawn from a random process, whose statistical properties will be discussed later.

We define the discrete Fourier transform $\hat{y}$ of $\tilde{y}$ by

$$\hat{y}_j = \frac{1}{N} \sum_{i=0}^{N-1} \tilde{y}_i \, e^{-i2\pi\nu_j t_i} \quad \text{for } j \in \mathbb{N}, \tag{4.2}$$

where $\nu_j = j/(N\Delta t)$ is the frequency and the frequency resolution is $1/(N\Delta t)$. Note that $\hat{y}_j = \hat{y}_{N-j}^*$ and $\hat{y}_j = \hat{y}_{-j}^*$, where (∗) denotes the complex conjugate. The Fourier transform has periodicity $1/\Delta t$ or twice the Nyquist frequency.

Our intention is to fit not the complete Fourier spectrum, but a rather small interval that contains one (or a few) modes of stellar oscillation. Thus, we extract a section of the data of length M starting from a particular frequency ν_q, as shown in Figure 4.1(c). This subset of the data is represented by the vector $y = [y_0, y_1, \cdots, y_{M-1}]^T$ with components

$$y_i = \hat{y}_{q+i}, \quad i = 0, 1, \ldots, M-1. \tag{4.3}$$

By using this definition of the Fourier transform [Equation (4.2)], the vector y is given by the convolution of $\hat{x}$ with the window $\hat{w}$:

$$y_i = \sum_{j=-p}^{M+p-1} \hat{w}_{i-j} \, \hat{x}_{q+j}. \tag{4.4}$$

The integer p in Equation (4.4) refers to the cutoff frequency ν_p beyond which the observation window has no significant power. Truncating the window function at frequency ν_p is a simplification of the general problem. Our main goal, however, is, given a known window function, to study its effects on the determination of the parameters of stellar oscillations. Figure 4.1 is a schematic representation in Fourier space of the convolution of a single mode of oscillation by the window function. The observed signal is spread over some frequency range and, as we shall see later, its statistical properties are affected.

We note that, in practice, one can never completely isolate one single mode of oscillation in the power spectrum. In particular, other modes with frequencies outside of the fitting range can leak into it after convolution by the temporal window function. Hence, fitting one mode of oscillation is a simplification. But our first objective is to try to study the effects of gaps, independently from the complications associated with a badly specified model.

Equation (4.4) can be rewritten in matrix form as

$$y = Wx, \tag{4.5}$$

where the vector $x = [x_0, x_1, \ldots, x_{M+2p-1}]^T$ of length $M + 2p$ is defined by

$$x_i = \hat{x}_{q-p+i}, \quad i = 0, 1, \ldots, M+2p-1, \tag{4.6}$$

and $W = [W_{ij}]$ is the $M \times (M+2p)$ rectangular window matrix with elements $W_{ij} = \hat{w}_{i-j+p}$, where $i = 0, 1, \ldots, M-1$ and $j = 0, 1, \ldots, M+2p-1$:

$$W = \begin{bmatrix} \hat{w}_p & \cdots & \hat{w}_0 & \cdots & \hat{w}_{-p} & & & \\ & \ddots & & \ddots & & \ddots & & 0 \\ & & \hat{w}_p & \cdots & \hat{w}_0 & \cdots & \hat{w}_{-p} & \\ & 0 & & \ddots & & \ddots & & \ddots \\ & & & & \hat{w}_p & \cdots & \hat{w}_0 & \cdots & \hat{w}_{-p} \end{bmatrix}. \tag{4.7}$$

Note that $\hat{w}_i = \hat{w}_{-i}^*$ and that W is of rank M.

Equation (4.5) is the master equation. Our goal is to extract the stellar oscillation parameters (contained in x), given the incomplete information y.
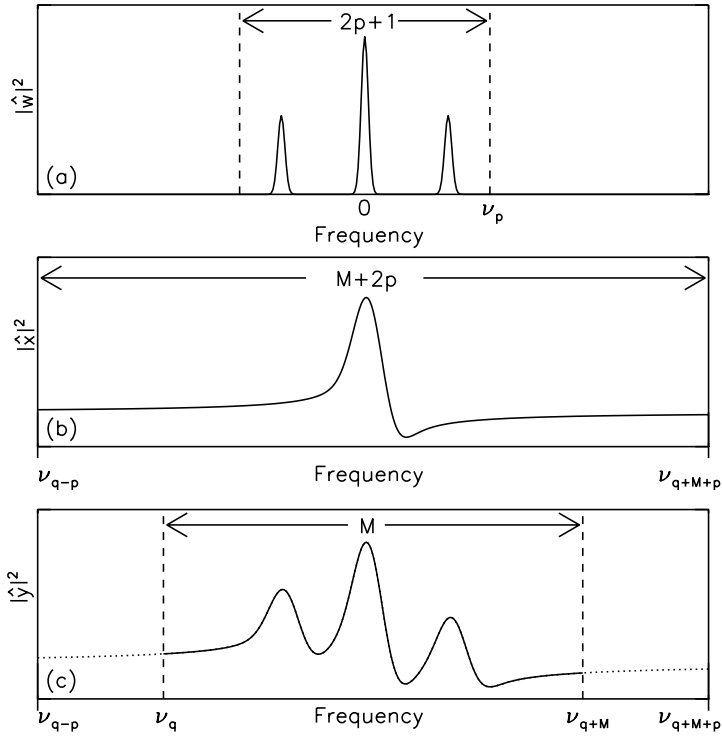
Figure 4.1: Schematic representation in Fourier space of the convolution of the signal $\hat{x}$ with the window function $\hat{w}$. For the sake of simplicity, only the power spectra of the different quantities are shown here. Panel (a) shows the window function $\hat{w}$ and its cutoff frequency ν_p, panel (b) shows the unconvolved signal $\hat{x}$, and panel (c) shows the observed signal $\hat{y}$. Note that the selected section of the observed signal, starting at frequency ν_p, is of length M, whereas the unconvolved signal is of length $(M + 2p)$.

4.2.2 Statistics of the unconvolved signal

Here we describe the basic assumptions that we make about the statistics of the data in the Fourier domain. The unconvolved signal [x] consists of a deterministic component [d] and a zero-mean stochastic component [e] such that

$$x = d + e. \qquad (4.8)$$

The deterministic component d may include deterministic stellar oscillations that are long-lived compared to the total length of the observation. The stochastic component e may

include various sources of noise (e.g. stellar convection, photon noise, atmospheric noise, etc.) and stochastically excited pulsations as observed on the Sun.

We assume that the e_i are $M+2p$ independent random variables in the Fourier domain. This is equivalent to saying that the stochastic component of the signal in the time domain is stationary. We further assume that e is a Gaussian random vector with independent real and imaginary parts and covariance matrix

$$E[e_i^* e_j] = \sigma_i^2 \delta_{ij}, \quad i, j = 0, 1, \ldots, M + 2p - 1, \tag{4.9}$$

where E denotes the expectation value and σ_i is the standard deviation of e_i at frequency ν_i. One may invoke the central limit theorem to justify the choice of Gaussian distributions. The quantity σ_i^2 is the expected power spectrum at frequency ν_i, which may include background noise and peaks corresponding to the modes of oscillations (Duvall and Harvey 1986, Appourchaux et al. 1998). In terms of a complex Gaussian random vector g with unit covariance matrix, $E[g^* g^T] = I_{M+2p}$, we can rewrite e as

$$e = S g, \tag{4.10}$$

where S is the $(M + 2p) \times (M + 2p)$ diagonal matrix

$$S = \text{diag}(\sigma_0, \sigma_1, \ldots, \sigma_{M+2p-1}). \tag{4.11}$$

We emphasize that, although the e_i are uncorrelated random variables, the y_i are correlated because of the multiplication of x by the window matrix [Equation (4.5)].

4.3   Joint PDF of the complex Fourier spectrum

In this section we derive an expression for the joint probability density function of the observed signal y. This problem had already been solved by Gabriel (1994). We reach the same conclusion, independently and with more compact notations. We start by rewriting the master equation, Equation (4.5), given by

$$y = Wd + Cg, \tag{4.12}$$

where

$$C = WS \tag{4.13}$$

is an $M \times (M + 2p)$ matrix with rank M and singular value decomposition (Horn and Johnson 1985, chapter 7.3)

$$C = U \Sigma V^H. \tag{4.14}$$

Here the superscript H denotes the Hermitian conjugate and U and V are unitary matrices of dimensions $M \times M$ and $(M + 2p) \times (M + 2p)$, respectively (i.e., $U^H U = I_M$ and $V^H V = I_{M+2p}$). The $M \times (M + 2p)$ matrix Σ can be written as

$$\Sigma = [\Lambda \,\vdots\, 0], \quad \Lambda = \text{diag}(\lambda_0, \lambda_1, \ldots, \lambda_{M-1}), \tag{4.15}$$

where $\lambda_0, \lambda_1, \ldots, \lambda_{M-1}$ are the M (positive) singular values of the matrix C. Thus, there exists a vector $\xi = V^H g$ such that

$$y = Wd + U[\Lambda \,\vdots\, 0]\xi. \tag{4.16}$$

Since g has unit covariance matrix and V is unitary, the vector ξ is a complex Gaussian random vector of size $M + 2p$ with unit covariance matrix. It is obvious from Equation (4.16) that there exists a lower rank complex Gaussian random vector of length M, $\eta = [\xi_0, \xi_1, \ldots, \xi_{M-1}]^T$, such that

$$y = Wd + U\Lambda\eta. \qquad (4.17)$$

The variables $\xi_M, \xi_{M+1}, \ldots, \xi_{M+2p-1}$ are dummy variables, which do not enter in the description of y. Equation (4.17) is an important step, as the vector y of length M is now expressed in terms of M independent complex Gaussian variables. This enables us to write the PDF of y as

$$p_y(y) = \frac{1}{J}\, p_\eta\big((U\Lambda)^{-1}(y - Wd)\big), \qquad (4.18)$$

where $p_\eta(\eta)$ denotes the PDF of η and J is the Jacobian of the linear transformation $\eta \to y$. Since η is a complex Gaussian random vector with unit covariance, $i.e.$ $E[\eta^*\eta^T] = I_M$, we have

$$p_\eta(\eta) = \frac{\exp(-\|\eta\|^2)}{\pi^M}, \qquad (4.19)$$

where we used the notation $\|\eta\|^2 = \eta^H\eta$. Since U is unitary and Λ is diagonal and real, the Jacobian of the transformation is given by

$$J = |\det(U\Lambda)|^2 = (\det\Lambda)^2 = \prod_{i=0}^{M-1} \lambda_i^2. \qquad (4.20)$$

Combining Equations (4.18), (4.19), and (4.20), we get the joint PDF of the observed vector y:

$$p_y(y) = \frac{\exp(-\|\Lambda^{-1}U^H(y - Wd)\|^2)}{\pi^M(\det\Lambda)^2}. \qquad (4.21)$$

This expression is, perhaps, more elegantly written as

$$p_y(y) = \frac{\exp(-\|C^\dagger(y - Wd)\|^2)}{\pi^M(\det\Lambda)^2} \qquad (4.22)$$

in terms of $C^\dagger$, the $(M + 2p) \times M$ Moore–Penrose generalized inverse of C (Horn and Johnson 1985, chapter 7.3),

$$C^\dagger = V\Sigma^\dagger U^H = C^H(CC^H)^{-1}, \qquad (4.23)$$

where $\Sigma^\dagger$ is the transpose of Σ in which the singular values are replaced by their inverse. One may ask, after the fact, if the quantity $(U\Lambda)^{-1}$ in Equation (4.18) is always defined. The answer would appear to be yes since the Moore-Penrose generalized inverse of C is perfectly well defined. It is not excluded, however, that some singular values λ_i could be infinitesimally small. We have not encountered any such difficulty with the test cases given in Section 4.7. Should C be ill-conditioned in other cases, a simple truncated SVD would help avoiding in a numerical problem.

Before discussing the implementation of the method in Section 4.4, we should like to draw attention to a parallel between fitting data with temporal gaps and fitting data with spatial gaps. To understand this analogy, we refer the reader to the work of (Appourchaux et al. 1998, Section 3.3.4), who discuss how to interpret the spatial leaks of non-radial oscillations that arise from the fact that only half of the solar disk can be observed from Earth. Their approach is similar to the one developed in this paper.

4.4 Maximum likelihood estimation of stellar oscillation parameters

Let us assume that the stellar oscillation model that we are trying to fit to the data depends on a set of k parameters $\mu = (\mu_0, \mu_1, \ldots, \mu_{k-1})$. These parameters may be the amplitude, the phase, the frequency, the line asymmetry, the noise level, etc. The basic idea of maximum likelihood estimation is to pick the estimate $\mu_\star$ that maximizes the likelihood function. The likelihood function is another name for the joint PDF [Equation (4.22)] evaluated for the sample data. In practice, one minimizes

$$\mathcal{L}(\mu) = -\ln p_y = \|C^\dagger(y - Wd)\|^2 + 2 \sum_{i=0}^{M-1} \ln \lambda_i + \text{constant}, \qquad (4.24)$$

rather than maximizing the likelihood function itself. In this expression, the quantities $C^\dagger$ and λ_i all depend implicitly on the model parameters μ through the covariance matrix S. The vector d also depends on the model parameters in the case of deterministic oscillations. The probability of observing the sample data is greatest if the unknown parameters are equal to their maximum likelihood estimates $\mu_\star$:

$$\mu_\star = \arg\min_\mu \mathcal{L}(\mu). \qquad (4.25)$$

The method of maximum likelihood has many good properties (Brandt 1970). In particular, in the limit of a large sample size (M large), the maximum likelihood estimator is unbiased and has minimum variance.

What is particularly new about our work is the minimization of the likelihood function given by Equation (4.24). We use the direction set method, or Powell's algorithm, to solve the minimization problem with a computer. In practice, the result of the fit depends on the initial guess and the fractional tolerance of the minimization procedure (the relative decrease of $\mathcal{L}$ in one iteration). The fitted parameters depend on the initial guess because the function $\mathcal{L}$ may have local minima in addition to the global minimum. We will address this issue in more detail in Section 4.7.

4.4.1 Solar-like oscillations

In the case of solar-like oscillations, there is no deterministic component and the log-likelihood becomes

$$\mathcal{L}(\mu) = \|C^\dagger y\|^2 + 2 \sum_{i=0}^{M-1} \ln \lambda_i + \text{constant}. \qquad (4.26)$$

4.4.2 Deterministic oscillations plus white noise

If background white noise is the only stochastic component then

$$\sigma_i = \sigma_0 = \text{constant}, \quad i = 0, 1, \ldots, M + 2p - 1. \qquad (4.27)$$

The log-likelihood function becomes

$$\mathcal{L}(\mu) = \frac{1}{\sigma_0^2} \, \|W^\dagger(y - Wd)\|^2 + M \, \ln \sigma_0^2 + \text{constant}. \tag{4.28}$$

Splitting the unknowns $\mu = (\check{\mu}, \sigma_0)$ into the parameters describing the oscillations, $\check{\mu} = (\mu_0, \mu_1, \ldots, \mu_{k-2})$, and the noise level σ_0, reduces the minimization problem to finding the most likely estimates

$$\check{\mu}_\star = \arg \min_{\check{\mu}} \, \|W^\dagger(y - Wd)\|^2, \tag{4.29}$$

where $d = d(\check{\mu})$. The noise level is explicitly given by

$$\sigma_{0\star} = M^{-1/2} \|W^\dagger[y - Wd(\check{\mu}_\star)]\|. \tag{4.30}$$

4.5 The old way: fitting the power spectrum and ignoring the correlations

Maximum likelihood estimation has been used in the past to infer solar and stellar oscillation parameters, even in the case of gapped time series. The joint PDF of the observations was assumed to be the product of the PDFs of the individual y_i, as if the frequency bins were uncorrelated. For comparison purposes, we briefly review this (unjustified) approach.

According to Equation (4.12), the PDF of y_i is a normal distribution

$$p_{y_i}(y_i) = \frac{\exp(-|y_i - \bar{y}_i|^2/v_i)}{\pi v_i} \tag{4.31}$$

with mean

$$\bar{y}_i = \sum_{j=0}^{M+2p-1} W_{ij} d_j \tag{4.32}$$

and variance

$$v_i = \sum_{j=0}^{M+2p-1} |W_{ij}|^2 \sigma_j^2. \tag{4.33}$$

Under the (wrong) assumption that the y_i are independent random variables, the joint PDF of y becomes

$$p_y^{\text{nc}}(y) = \prod_{i=0}^{M-1} p_{y_i}(y_i), \tag{4.34}$$

where the superscript "nc" stands for "no correlation". This joint PDF uses the correct mean ($\bar{y}_i$) and variance (v_i) of the data, but it ignores all the nonvanishing cross-terms $E[y_i^* y_j]$. In other words, the spread of power implied by the convolution with the window is taken care of, but not the proper statistics.

Under the same simplifying "no-correlation" assumption, the log-likelihood function is

$$\mathcal{L}^{\text{nc}}(\mu) = \sum_{i=0}^{M-1} \frac{|y_i - \bar{y}_i|^2}{v_i} + \sum_{i=0}^{M-1} \ln v_i + \text{constant}, \tag{4.35}$$

where the $\bar{y}_i$ and v_i are implicit functions of the model parameters μ.

4.5.1   Solar-like oscillations

If the signal has no deterministic component ($d = 0$), then the power spectrum [$P_i(\mu) = |y_i|^2$] has the expectation value $\overline{P}_i = E[P_i] = v_i$. Thus, in the case of purely solar-like oscillations, we recover the standard expression (Toutain and Appourchaux 1994):

$$\mathcal{L}^{\mathrm{nc}}(\mu) = \sum_{i=0}^{M-1} \left(\frac{P_i}{\overline{P}_i} + \ln \overline{P}_i \right) + \text{constant} \quad \text{when } d = 0. \tag{4.36}$$

Although this expression is perfectly valid for uninterrupted data, it is not justified when gaps are present. The parameters $\mu_\star^{\mathrm{nc}}$ that minimize $\mathcal{L}^{\mathrm{nc}}(\mu)$ are not optimal, as will be shown later by using Monte Carlo simulations.

4.5.2   Deterministic oscillations plus white noise

When $\sigma_i = \sigma_0 = \text{constant}$, the "no-correlation" log-likelihood function simplifies to

$$\mathcal{L}^{\mathrm{nc}}(\mu) = \frac{1}{\sigma_0^2} \frac{\|y - Wd\|^2}{\sum_{j=-p}^{p} |\hat{w}_j|^2} + M \, \ln \sigma_0^2 + \text{constant}. \tag{4.37}$$

The minimization problem becomes

$$\check{\mu}_\star^{\mathrm{nc}} = \arg \min_{\check{\mu}} \, \|y - Wd\|^2, \tag{4.38}$$

where $d(\check{\mu})$ depends on the oscillation parameters $\check{\mu} = (\mu_0, \mu_1, \ldots, \mu_{k-2})$. The noise level is explicitly given by

$$\sigma_{0\star}^{\mathrm{nc}} = \left(M \sum_{j=-p}^{p} |\hat{w}_j|^2 \right)^{-1/2} \|y - Wd(\check{\mu}_\star^{\mathrm{nc}})\|. \tag{4.39}$$

4.6   Simulation of artificial time series

So far we have considered a general signal, which includes a deterministic component and a stochastic component. The parametrization of each component depends on prior knowledge about the physics of the stellar oscillations. Solar-like pulsations are stochastic in nature and no deterministic component is needed in this case. However, long-lived stellar pulsations are treated as deterministic. Some stars may support both deterministic and stochastic oscillations. In this section, we model the two cases separately.

We want to test the fitting method [Equations (4.24) and (4.25)] by applying it to simulated time series with gaps. For comparison, we also want to apply the old fitting method (Section 4.5) to the same time series. We need to generate many realizations of the same random process to test the estimators for bias and precision: This is called Monte Carlo simulation. In Section 4.6.1 we discuss the generation of the synthetic window functions. We then discuss the parametrization of the solar-like oscillations (Section 4.6.2) and the deterministic oscillations (Section 4.6.3) used to simulate the unconvolved signal.
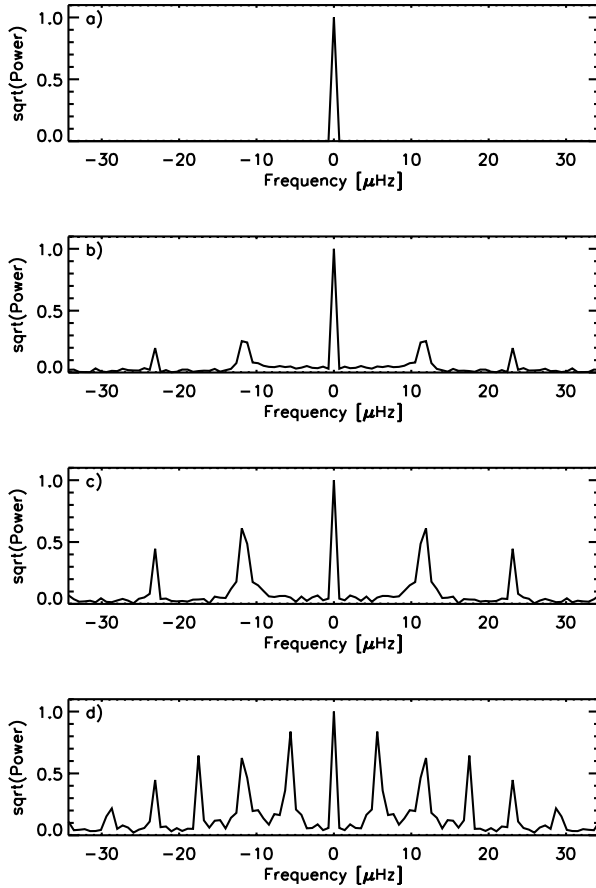
Figure 4.2: Square root of the power spectra of the synthetic window functions [$\hat{w}$] used in this paper for duty cycles of (a) 100%, (b) 66%, (c) 30%, and (d) 15%. The main periodicity of the window is 24 hours for cases (b) and (c) and 48 hours for window (d). All windows are truncated at frequency $\nu_p = 34.3\ \mu$Hz.

4.6.1   Synthetic Window Functions

We generate three different observation windows, corresponding to different duty cycles. The observation windows are first constructed in the time domain. By definition, $\tilde{w}_i$ is set to one if an observation is available and zero otherwise. The total length of all time series

is fixed at $T = 16.5$ days (frequency resolution $\Delta \nu = 0.7$ μHz). A window function is characterized by two main properties: the duty cycle (fraction of ones) and the average periodicity. A typical window function for a single ground-based site has a 24-hour periodicity. To deviate slightly from purely periodic window functions we introduce some randomness for the end time of each observation block.

Figure 4.2(b)–4.2(d) shows the power spectra of the three window functions. The first and second window functions have a main periodicity of 24 hours and duty cycles of 66% and 30%, respectively. Two side lobes occur at frequencies of 11.6 μHz and 23.1 μHz. The nonvanishing power between the side lobes is due to the deviation from a purely periodic window. The third window function has a main periodicity of 48 hours and a duty cycle of only 15%. All of these window functions are not unrealistic.

We apply a sharp low-pass filter at frequency $\nu_p = 34.3$ μHz ($p = 49$) to all window functions. The power at higher frequencies corresponds to about 5% of the total power in the windows. This truncation is needed to apply the fitting algorithm, which assumes that there exists a frequency ν_p beyond which the power in the window vanishes (*i.e.*, that the window function is band limited).

4.6.2 Solar-like oscillations

We generate the realizations of the unconvolved solar-like oscillation signal directly in the Fourier domain. We consider a purely stochastic signal ($d = 0$) and a single mode of oscillation. Since we assumed stationarity in the time domain, the Fourier spectrum of the unconvolved signal for one single mode can be written as

$$x_i = e_i = [\mathcal{S}L(\nu_i) + \mathcal{N}]^{1/2} \eta_i, \quad i = 0, 1, \ldots, M + 2p - 1, \tag{4.40}$$

where L describes the line profile of the mode in the power spectrum, $\mathcal{S}$ is the mode's maximum power, $\mathcal{N}$ is the variance of the background noise, and η_i is a centered complex Gaussian random variable with unit variance and independent real and imaginary parts. Solar-like oscillations are stochastically excited and intrinsically damped by turbulent convection (Goldreich and Keeley 1977, Stein et al. 2004). The expectation value of the power spectrum is nearly Lorentzian, except for some line asymmetry (e.g. Duvall et al. 1993). Here we use a simple asymmetric line profile:

$$L(\nu) = \frac{(1 + bX)^2 + b^2}{1 + X^2} \quad \text{with} \quad X = \frac{\nu - \nu_0}{\Gamma/2}, \tag{4.41}$$

where ν_0 is the resonant frequency, b is the asymmetry parameter of the line profile ($|b| \ll 1$), and Γ is a measure of the width of the line profile. We refer to $\mathcal{S}/\mathcal{N}$ as the signal-to-noise ratio in the power spectrum. As b tends to zero, Γ becomes the full width at half maximum (FWHM) of the power spectrum and $1/(\pi\Gamma)$ the mode lifetime. There are five model parameters, $\mu = (\nu_0, \Gamma, b, \mathcal{S}, \mathcal{N})$.

Once the unconvolved signal x has been generated in the Fourier domain, the observed signal y is obtained by multiplication with the window matrix W, as previously explained.

4.6.3   Deterministic sinusoidal oscillations plus white noise

In the time domain, we consider a purely sinusoidal function on top of white background noise:

$$\tilde{x}_i = A \sin\left(2\pi\nu_0\, t_i + \varphi\right) + \sigma_t\, \eta_i \qquad i = 0, 1, \ldots, N-1. \tag{4.42}$$

The first term describes the deterministic component of the signal, where A is the amplitude, ν_0 the mode frequency, and φ the phase of the mode. The second term is stochastic noise with standard deviation σ_t. The η_i are N normally distributed independent real random variables with zero mean and unit variance. The observed signal is obtained by multiplying $\tilde{x}_i$ by the window $\tilde{w}_i$ in the time domain. The model parameters are $\mu = (\nu_0, \varphi, A, \sigma_t)$.

We have defined the signal and the noise in the time domain, but a definition of signal-to-noise ratio in the Fourier domain is desirable. On the one hand, the variance of the noise in the Fourier domain is

$$\sigma_{\mathrm{n}}^2 = \sigma_0^2 \sum_{i=-p}^{p} |\hat{w}_i|^2 = \frac{\sigma_t^2}{N} \sum_{i=-p}^{p} |\hat{w}_i|^2, \tag{4.43}$$

where $\sum_i |\hat{w}_i|^2$ is the total power in the window. On the other hand, the maximum power of the signal in Fourier space is $P_{\mathrm{max}} = A^2 |\hat{w}_0|^2 / 4$, where $|\hat{w}_0|^2$ is the power of the window at zero frequency. Thus, by analogy with the solar-like case, it makes sense to define the signal-to-noise ratio in the Fourier domain as

$$\mathcal{S}/\mathcal{N} = \left(\frac{N |\hat{w}_0|^2}{4 \sum_i |\hat{w}_i|^2} \right) \frac{A^2}{\sigma_t^2}. \tag{4.44}$$

In practice we fix A and $\mathcal{S}/\mathcal{N}$ and deduce the corresponding noise level σ_t.

4.7   Testing and comparing the fitting methods for solar-like oscillations

Several hundreds of realizations are needed to assess the quality of a fitting method. We do not intend to test all possible combinations of mode parameters but we want to show a few cases for which the new fitting method provides a significant improvement compared to the old fitting method.

4.7.1   Window function with a 30% duty cycle

Figure 4.3 shows one realization of a simulated mode of solar-like oscillation with input parameters $\nu_0 = 3000\ \mu$Hz, $\Gamma = 3.2\ \mu$Hz, $\mathcal{S} = 0.9$, $\mathcal{N} = 0.15$, and $b = 0.1$. The signal-to-noise ratio is $\mathcal{S}/\mathcal{N} = 6$ and the window function is 30% full (see Figure 4.2c). The mode lifetime is $1/(\pi\Gamma) = 27.6$ hours. Figure 4.3(a) displays the real and imaginary parts of the Fourier transform y, together with the standard deviation of the data (nc fit in blue, new fit in red, and expectation value in green). Figure 4.3(b) shows the power spectrum and the fits. Notice the side lobes introduced by the convolution of the signal with the window
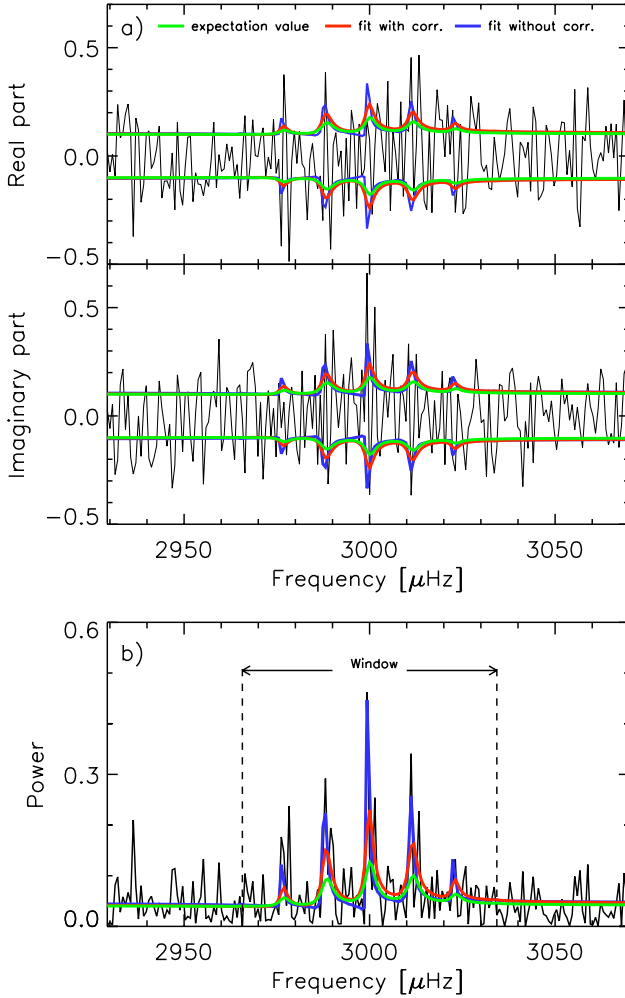
Figure 4.3: Example of a realization of one mode of a solar-like oscillation (*black line*) with input frequency $\nu_0 = 3000$ μHz, line width $\Gamma = 3.2$ μHz, and $\mathcal{S}/\mathcal{N} = 6$. The window function is 30% full. Panel (a) shows the real and imaginary parts of the Fourier spectrum. Panel (b) shows the power spectrum. The *vertical dashed lines* represent the width of the window function. Also shown are the new fit (*red*), the old fit (*blue*), and the expectation value (*green*).

functions. The "no-correlation" fit is done on the power spectrum [Equation (4.36)], whereas the new fit is performed in complex Fourier space [Equation (4.24)].

Each fit shown in Figure 4.3 corresponds in fact to the best fit out of five fits with different initial guesses. For each realization, we use the frequency guesses $3000 + (0, \pm5.5, \pm11.9)$ μHz for ν_0. The last two frequency guesses correspond to the frequencies of the two main side lobes of the window function (Figure 4.2c). For the other parameters, we choose random guesses within $\pm20\%$ of the input values. The reason for using several guesses is to ensure that the fit converges to the global maximum of the likelihood, not to a nearby local maximum, i.e. that the estimates returned by the code are the MLE estimates defined by Equation (4.25). In some cases, the global maximum coincides with a side lobe at ±11.9 μHz from the main peak. We note that the new fitting method requires a much longer computing time than the old "nc" method: typically, three hours on a single CPU core for a single realization (five guesses and five fits).

For the particular realization of Figure 4.3, the new fit is closer to the expectation value (i.e., is closer to the answer) than the old "nc" fit. No conclusions should be drawn, however, from looking at a single realization.

To test the reliability of each fitting method, we computed a total of 750 realizations with the same input parameters as in Figure 4.3 and the same window function (30% full). The quality (bias and precision) of the estimators can be studied from the distributions of the inferred parameters. As shown by the distributions of Figure 4.4 the new fitting method is superior to the old nc method. This is true for all the parameters, in particular the mode frequency ν_0. The distributions for the mode frequency (Figure 4.4a) are quite symmetric and Gaussian-like, although the old fitting method leads to a significant excess of values beyond the 2σ mark. We note that, in general, the old fitting method is more sensitive to the initial frequency guess. Also the estimates of the line width Γ and the mode power $\mathcal{S}$ are significantly more biased with the old fitting method than with the new one (Figures 4.4b and 4.4c). It is worth noting that the fits return a number of small Γ/large $\mathcal{S}$ estimates away from the main peaks of the distributions, but less so for the new fits. These values correspond to instances when the signal barely comes out of the noise background. The new fit returns the noise level [$\mathcal{N}$] with a higher precision and a lower number of underestimated outliers than the old method (where the outliers are represented by the vertical bars in Figure 4.4d). Although the estimation of the asymmetry parameter is unbiased with the new fitting method (Figure 4.4e), the uncertainty on b is so large that it probably could have been ignored in the model.

Quantitative estimates of the mean and the dispersion of the estimators are provided in Table 1. Because the distributions of the estimated parameters are not always Gaussian and may contain several outliers, we compute the median (instead of the mean) and the lower and upper bounds corresponding to $\pm34\%$ of the points on each side of the median (instead of the one-σ dispersion). This definition has the advantage of being robust with respect to the outliers. The notation 3000.0^{+b}_{-a} μHz in the first row of Table 4.1 means that the median mode frequency is 3000.0 μHz and that 68% of the fits belong to the interval $[3000.0 - a, 3000.0 + b]$ μHz. We emphasize that the subscript $-a$ and the superscript $+b$ do not refer to an uncertainty in the determination of the median: The median is known to a much higher precision because of the large number of realizations. Later we relax the language and refer to the "one-σ uncertainty" to mean the average $\sigma = (a + b)/2$.
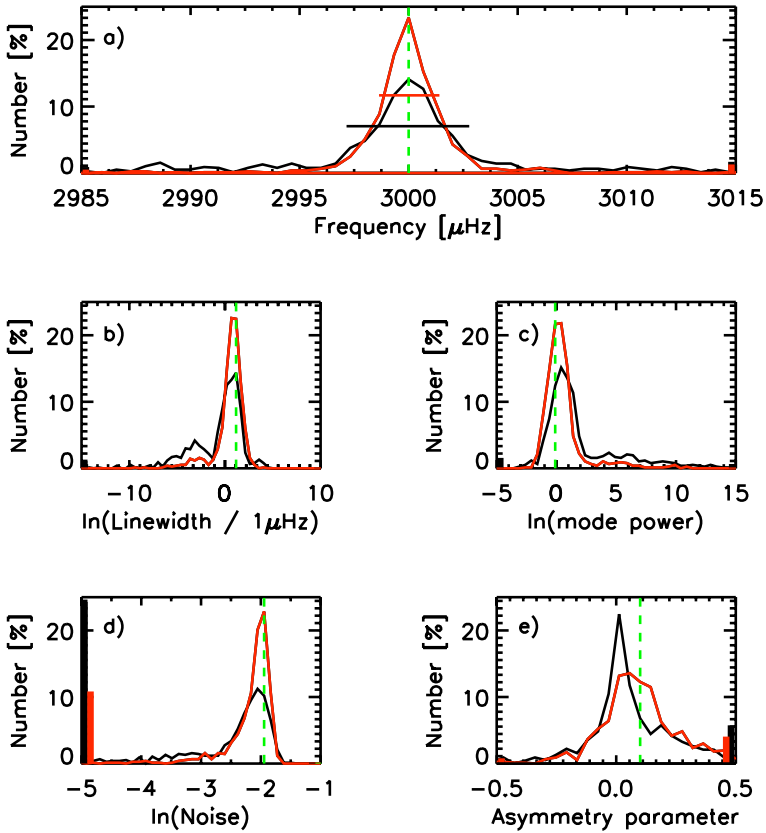
Figure 4.4: Distributions of the inferred oscillation parameters from fits to 750 realizations of a single mode of solar-like oscillations. The input parameters are given in Table 4.1 and the window function is 30% full. The five panels show the distributions of the inferred (a) mode frequency ν_0, (b) line width Γ, (c) mode power $\mathcal{S}$, (d) noise level $\mathcal{N}$, and (e) asymmetry parameter b. The *red lines* show the results obtained with the new fitting method and the *black lines* show the old "no-correlation" fits. The *vertical green dashed line* in each plot indicates the input value. The *horizontal lines* in panel (a) are intervals containing 68% of the fits for the new (*black line*) and the old (*gray line*) fitting methods. The *thick red* and *black vertical bars* give the numbers of outliers with estimates beyond the plot boundaries

Table 4.1: Medians and scatters of the distributions of the estimated parameters of solar-like oscillations (see Figure 4.4). The window function is 30% full, the input line width is 3.2 μHz, and the input signal-to-noise ratio is $S/N = 6$. The new and old MLE estimates are given in the last two columns. By definition, 68% of the fits fall within the bounds set by the subscripts and superscripts (with the notation explained in detail in the text).

Mode parameter	Input value	New fitting	Old fitting
ν_0 [μHz]	3000.0	$3000.0^{+1.4}_{-1.4}$	$3000.0^{+2.8}_{-2.8}$
$\ln(\Gamma/1\mu\text{Hz})$	1.2	$0.8^{+0.8}_{-1.0}$	$0.2^{+1.1}_{-3.7}$
$\ln S$	-0.1	$0.2^{+0.9}_{-0.9}$	$0.9^{+4.3}_{-1.2}$
$\ln N$	-1.9	$-2.1^{+0.2}_{-0.9}$	$-2.4^{+0.4}_{-6.8}$
b	0.1	$0.1^{+0.2}_{-0.1}$	$0.0^{+0.2}_{-0.1}$

Table 4.2: Medians and scatters of the mode frequency estimates (solar-like oscillations) for the window functions defined in Section 4.6.1. The input mode frequency is $\nu_0 = 3000\,\mu$Hz, the input line width is $\Gamma = 3.2\,\mu$Hz, and the signal-to-noise ratio is fixed at $S/N = 6$. The mode lifetime is 27.6 hours.

	Window function		Frequency estimate [μHz]	
Duty cycle	Main period	Average gap	New fitting	Old fitting
100%	–	–	$3000.0^{+1.1}_{-1.2}$	$3000.0^{+1.1}_{-1.2}$
66%	24 hours	7.4 hours	$3000.0^{+1.1}_{-1.3}$	$3000.1^{+1.5}_{-1.4}$
30%	24 hours	16.4 hours	$3000.0^{+1.4}_{-1.4}$	$3000.0^{+2.8}_{-2.8}$
15%	48 hours	40.7 hours	$3000.0^{+1.7}_{-1.3}$	$3000.0^{+8.3}_{-6.5}$

The numbers from the last two columns in Table 1 confirm the analysis of Figure 4.4. The mode frequency can be measured with a precision of 1.4 μHz, and so the precision of the new fitting method is exactly twice that of the old one. This gain in precision is very significant and potentially important. Since measurement uncertainty scales like $T^{-1/2}$ (Libbrecht 1992), one may equate the gain in using the proper fitting procedure to an effective increase in the total length of the time series by a factor of four. As seen in Table 1, the line width, the mode power, the background noise, and the line asymmetry parameter are all less biased and more precise with the new fitting method than the old one. Notice that the larger dispersions in the old-fit case are due in part to non-Gaussian distributions with extended tails.
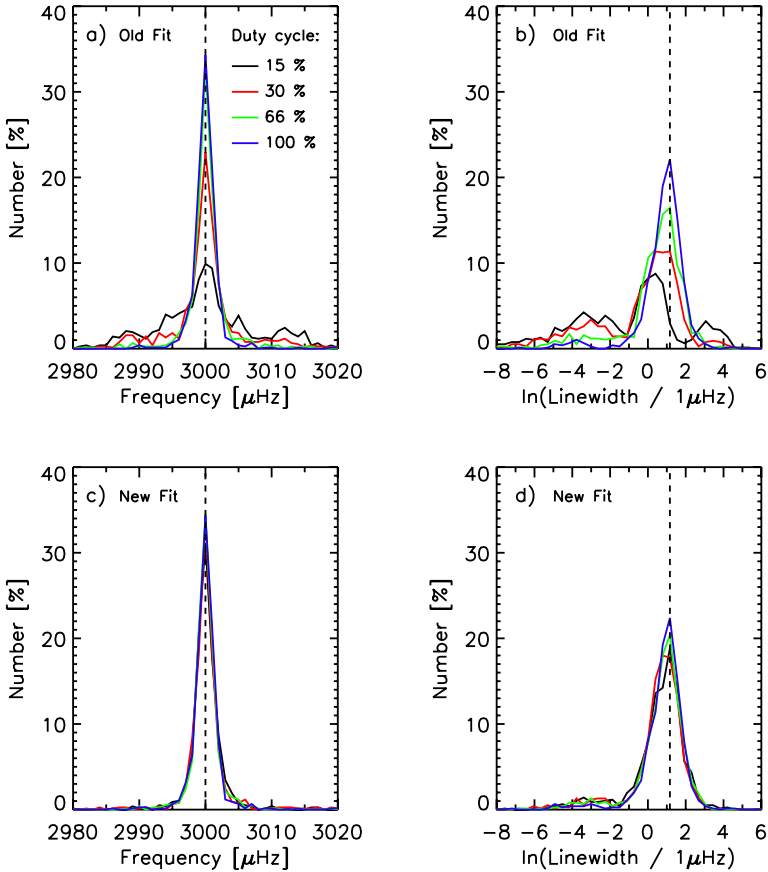
Figure 4.5: Distributions of the mode frequency and the line width for 750 realizations of solar-like oscillations, using the old fitting method (panels a and b) and the new fitting method (panels c and d). The observation windows have duty cycles of 15%, 30%, 66%, and 100%. The *vertical dashed lines* represent the input values. The input line width is $\Gamma = 3.2 \, \mu Hz$

4.7.2 Different window functions

Here we study how bias and precision change as the window function changes, in particular as the duty cycle changes. We consider the four window functions defined in Section 4.6.1 with duty cycles [α] equal to 15%, 30%, 66%, and 100%. First we consider input parameters of solar-like oscillations that are exactly the same as in the previous section: $\nu_0 = 3000 \, \mu Hz$, $\Gamma = 3.2 \, \mu Hz$, $\mathcal{S} = 0.9$, $\mathcal{S}/\mathcal{N} = 6$, and $b = 0.1$. Figure 4.5 shows the

105
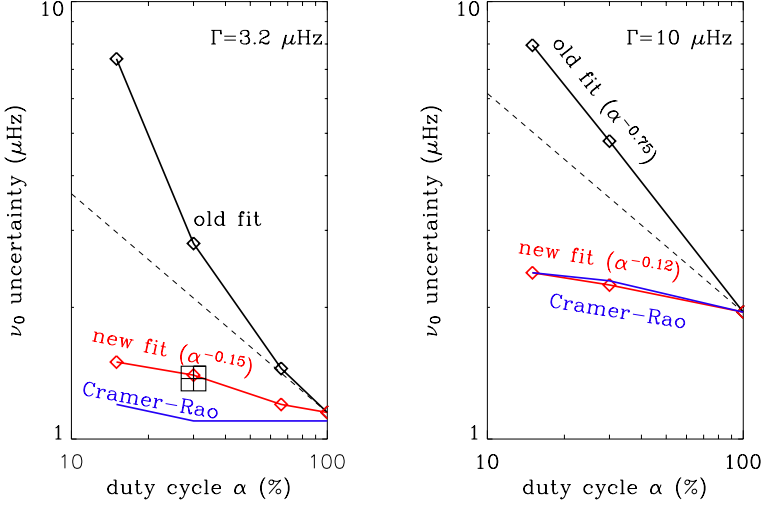
Figure 4.6: Uncertainty on estimates of the mode frequency [ν_0] as a function of the window duty cycle [α]. The window functions are as defined in Section 4.6.1. The *red curve* shows the 1-σ Monte Carlo MLE uncertainties for the new fitting method. The *black curve* shows the 1-σ Monte Carlo MLE uncertainties for the old no-correlation fitting method. The *blue curves* show the mean Cramér–Rao lower bounds (formal error bars). The *square symbol with a cross* at $\alpha = 30\%$ in the left panel is a rough estimate (see text). In the *left panel*, the input line width is $\Gamma = 3.2\,\mu$Hz (see also numbers in Table 1). In the *right panel*, the input line width is $\Gamma = 10\,\mu$Hz, with all of the other parameters being the same as in the left panel. In both panels the signal-to-noise ratio is $\mathcal{S}/\mathcal{N} = 6$. For reference, the *dashed lines* have slope $\alpha^{-1/2}$.

distributions of the inferred mode frequencies and line widths, using the old (Figures 4.5a and 4.5b) and the new (Figures 4.5c and 4.5d) fitting methods. Each fit is the best fit from five different ν_0 guesses (see Section 4.7.1). The distributions for the 100% window are identical for the two fitting methods; this is expected since the old and new fitting methods are equivalent in the absence of gaps.

The precision on ν_0 using the old "no-correlation" MLE drops fast as the duty cycle decreases (Figure 4.5a). This drop is much faster than in the case of the fits that take the frequency correlations into account (Figure 4.5c). When the duty cycle is 15%, the frequency estimate is five times better with the new method than with the old one. The difference is perhaps even more obvious for the line width. For the 15% window, it is almost impossible to retrieve Γ with the old fitting method (Figure 4.5b), whereas the new method gives estimates that are almost as precise as in the no-gap case (Figure 4.5d). The estimates of Γ are significantly less biased with the new method. Figure 4.5 confirms the importance of using the correct expression for the likelihood function.

Table 4.2 gives the medians and half-widths of the ν_0 distributions. The one-σ dispersions are plotted as a function of the duty cycle α in the left panel of Figure 4.6. The improvement in the fits is quite spectacular. For example, when $\alpha = 15\%$ the dispersion on ν_0 is reduced by nearly 80% with the new fitting method (1.5 μHz vs. 7.4 μHz).

With the old method, the uncertainty on ν_0 increases much faster than $\alpha^{-1/2}$ as the duty cycle α drops ($\sim\alpha^{-1}$ between the 30% and 15% windows). This steep dependence on α is worse than "predicted" by Libbrecht (1992). In his paper, Libbrecht suggested using the uncertainty $\sigma_{\nu_0} = \sqrt{f\Gamma/(4\pi T)}$, where $f(\beta) = (1 + \beta)^{1/2}[(1 + \beta)^{1/2} + \beta^{1/2}]^3$ and β is an "effective" noise-to-signal ratio. He suggested that the main effect of the gaps is to increase the noise-to-signal ratio $\mathcal{N}/\mathcal{S}$, presumably by a factor $\sum_i |\hat{w}_i|^2/|\hat{w}_0|^2$, itself proportional to $1/\alpha$. This leads however to a dependence of σ_{ν_0} on α, which, in our particular case, is closer to $\alpha^{-1/2}$ than α^{-1}. We suspect that the Libbrecht formula underestimates the dispersion because it ignores the frequency correlations.

The new fitting method returns a ν_0 uncertainty that is much less sensitive to the duty cycle, with a variation like $\sim\alpha^{-0.15}$ (red curve, left panel of Figure 4.6). This is quite remarkable. That the frequency uncertainty could remain nearly constant for $\alpha > 30\%$ is not really surprising since the average gap (see numbers in Table 2) is less than the mode lifetime $\tau = 1/(\pi\Gamma) = 27.6$ hours. This regime was studied by Fossat et al. (1999) using a gap-filling method: As long as the signal-to-noise ratio is large enough, the signal can be reconstructed. Why the new fit is doing such a good job for duty cycles $\alpha \leq 30\%$ is, however, puzzling (at first sight), since the average gap (40.7 hours) is larger than the mode lifetime. This can be understood as follows. For small duty cycles, the time series is effectively a collection of nearly independent blocks of data, which, for the 30% window function, are eight-hours long on average. Since MLE simulations tell us that the uncertainty on the mode frequency for an uninterrupted series of eight hours is about 5.5 μHz, we would expect for the gapped time series ($T = 16.5$ days, with 24-hour periodicity) to be able to reach the uncertainty $5.5/\sqrt{16} = 1.375$ μHz. This value, represented by the box with a cross in Figure 4.6, is found to be very close to the MLE estimate from the new fits. Hence, what matters at very low duty cycle is the number of independent blocks of continuous data. The new fitting method captures this very well, which is satisfying. By comparison, the old no-correlation fitting method does poorly (black line).

To further investigate this last point, we ran another set of simulations using a mode line width ($\Gamma = 10$ μHz) corresponding to a mode lifetime $\tau = 8.8$ hours, which is significantly smaller than the average gap lengths of the 30% and the 15% windows. The other input parameters remained the same as before. We computed and fitted 1350 realizations. The results are shown in the right panel of Figure 4.6. For the new fitting method, the dependence of the frequency uncertainty on the duty cycle is about $\alpha^{-0.12}$, which is comparable to the previous simulations with $\Gamma = 3.2$ μHz. We conclude that it is really worth solving for the correct minimization problem and that fitting for the phase information in complex Fourier space is important to get a good match between the model and the data. Of course, this can only be done properly when we have perfect knowledge of the model, which is the case with these numerical simulations but is rarely the case with real observations.
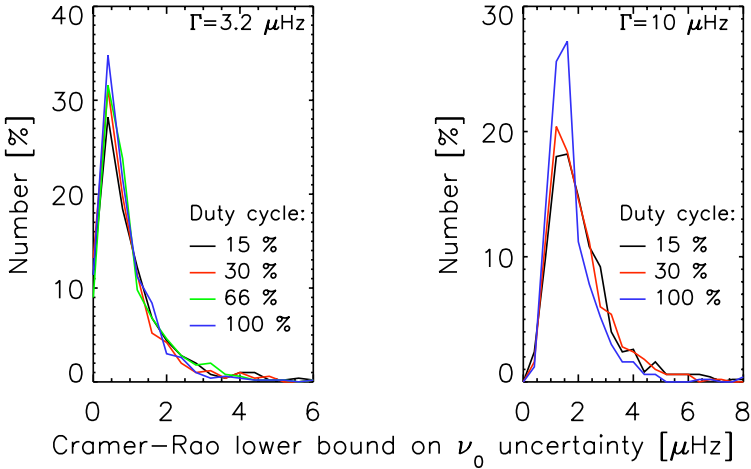
Figure 4.7: Distributions of formal errors on the mode frequency obtained by inverting the Hessian. The *left panel* is for the simulation with $\Gamma = 3.2\ \mu Hz$ (see Figure 5c) and the *right panel* is for $\Gamma = 10\ \mu Hz$. The different curves correspond to different window functions, as indicated in the legend. The means of these distributions (Cramér–Rao lower bounds) give the blue curves plotted in Figure 4.6.

4.7.3 Cramér–Rao lower bounds

Monte Carlo simulations are very useful for assessing the variance and the bias of a particular estimator. When fitting real observations, however, the variance of the estimator cannot be computed directly by Monte Carlo simulation since the input parameters are, by definition, not known. Hopefully, the fit can return a formal error from the shape of the likelihood function in the neighborhood of the global maximum.

The Cramér–Rao lower bound (Kendall and Stuart 1967) achieves minimum variance among unbiased estimators. It is obtained by expanding $\mathcal{L}$ about its minimum. The formal error σ_{μ_i} on the parameter μ_i is given by

$$\sigma_{\mu_i} = \sqrt{K_{ii}}, \qquad (4.45)$$

where K_{ii} is the i-th element on the diagonal of the inverse ($K = H^{-1}$) of the Hessian matrix with elements

$$H_{ij} = \frac{\partial^2 \mathcal{L}}{\partial \mu_i \, \partial \mu_j} \quad \text{for} \quad i, j = 0, 1, \ldots, k - 1. \qquad (4.46)$$

The Cramér–Rao formal errors have been used in helioseismology by, for example, Toutain and Appourchaux (1994), Appourchaux et al. (1998), Gizon and Solanki (2003).

We have computed the formal error on the mode frequency for many realizations and for all window functions. The resulting distributions are shown in Figure 4.7. The

Table 4.3: Medians and scatters of the distributions of the estimated parameters of one mode of solar-like oscillation (see Figure 4.10). The window function is 30% full, the input linewidth is $\Gamma = 3.2\,\mu$Hz, and the input signal-to-noise ratio is $\mathcal{S}/\mathcal{N} = 20$. The new and the old MLE estimates are given in the last two columns. By definition, 68% of the fits fall within the bounds set by the subscripts/exponents (with the notation explained in the text).

Mode parameter	Input value	New fitting	Old fitting
ν_0 [μHz]	3000.0	$3000.0^{+0.8}_{-0.8}$	$3000.0^{+1.3}_{-1.3}$
$\ln(\Gamma/1\mu\text{Hz})$	1.2	$1.1^{+0.5}_{-0.5}$	$1.0^{+0.7}_{-0.8}$
$\ln\mathcal{S}$	-0.1	$-0.1^{+0.6}_{-0.6}$	$0.1^{+0.9}_{-0.8}$
$\ln\mathcal{N}$	-3.1	$-3.2^{+0.2}_{-0.3}$	$-3.3^{+0.3}_{-2.2}$
b	0.1	$0.1^{+0.1}_{-0.1}$	$0.1^{+0.1}_{-0.1}$

mean formal error from each distribution is plotted in Figure 4.6. Overall the Cramér–Rao lower bound is remarkably close to the Monte Carlo MLE uncertainty using the new fitting method; they are even undistinguishable when $\Gamma = 10\,\mu$Hz.

This is useful information as it means that, on average, the Hessian method provides reasonable error estimates. It should be clear, however, that the distributions shown in Figure 4.7 shows a significant amount of scatter: The formal error from the Hessian may be misleading for particular realizations.

4.7.4 Different signal-to-noise ratios

In this section I present the results of Monte Carlo simulations of one mode of solar-like oscillation with various signal-to-noise ratios. We use the same mode parameters as in Section 4.7.1, i.e. $\nu_0 = 3000\,\mu$Hz, $\Gamma = 3.2\,\mu$Hz, $\mathcal{S} = 0.9$. The window duty cycle is 30% (see Figure 4.2c). For each realization we used again five different guesses for the mode frequency (ν_0, $\nu_0 \pm 5.5\,\mu$Hz, $\nu_0 \pm 11.9\,\mu$Hz) and random guesses for the other parameters (see Section 4.7.1).

Figure 4.8 shows an example of one realization of one mode of solar-like oscillation with a signal-to-noise ratio of $\mathcal{S}/\mathcal{N} = 20$. The real and the imaginary parts of this particular realization together with the standard deviation of the data (red: new fit, blue: old fit, green: expectation value) are shown in Figure 4.8a, the power spectrum is shown in Figure 4.8b. For this particular realization, both fitting method return similar results.

We computed a total of 1100 realisations with the same input parameters as in Figure 4.8 and a window function with a duty cycle of 30%. The distributions of the fitted parameters are shown in Figure 4.10. The differences between both fitting methods are less pronounced than for a signal-to-noise ratio of $\mathcal{S}/\mathcal{N} = 6$ (see Section 4.7.1, Figure 4.4). However, the new fitting method is still superior to the old fitting method. The distributions of the frequency (Figure 4.4a) are for both fitting methods again quite symmetric
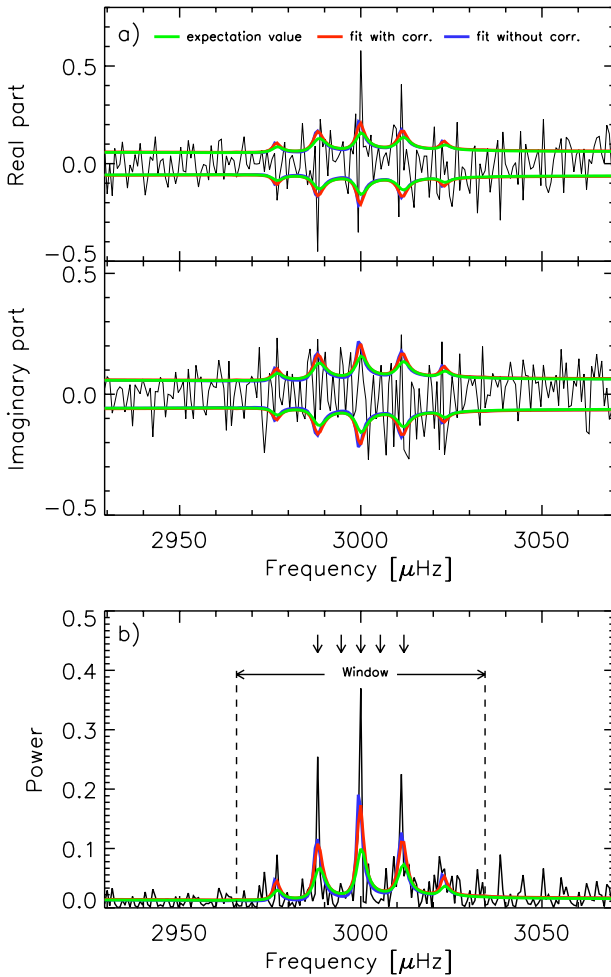
Figure 4.8: Example of a realization of one mode of a solar-like oscillation (*black line*) with input frequency $\nu_0 = 3000$ μHz, linewidth $\Gamma = 3.2$ μHz, and $\mathcal{S}/\mathcal{N} = 20$. The duty cycle of the window function is 30%. Panel (a) shows the real and imaginary parts of the Fourier spectrum. Panel (b) shows the power spectrum. The *vertical dashed lines* represent the width of the window function. Also shown are the new fit (*red*), the old fit (*blue*), and the expectation value (*green*). The small arrows in panel (b) indicate the five different frequency guesses used to fit this realization.
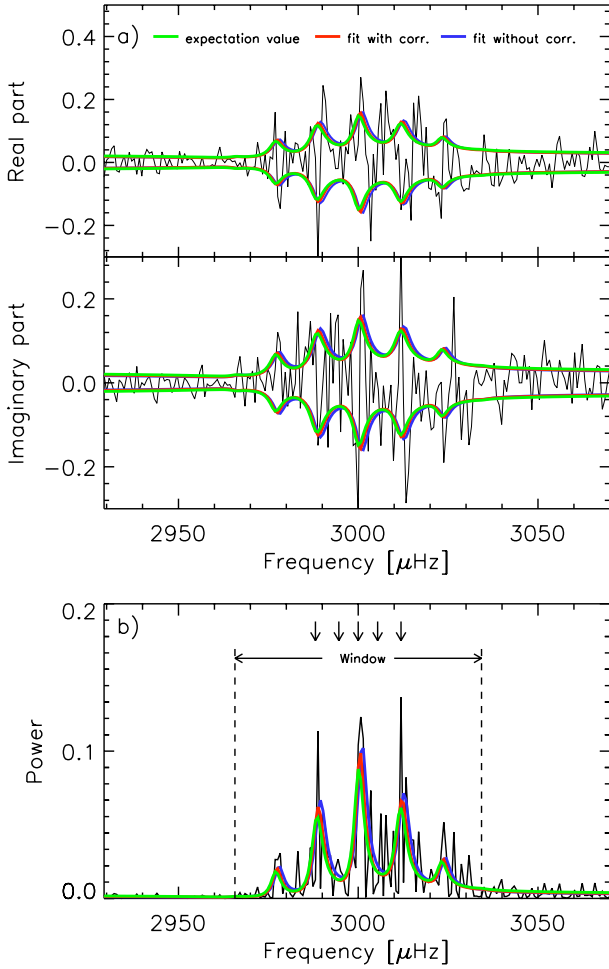
Figure 4.9: The same as in Figure 4.8 but showing a realization and the corresponding fits with an input signal-to-noise-ratio of $\mathcal{S}/\mathcal{N} = 1000$.
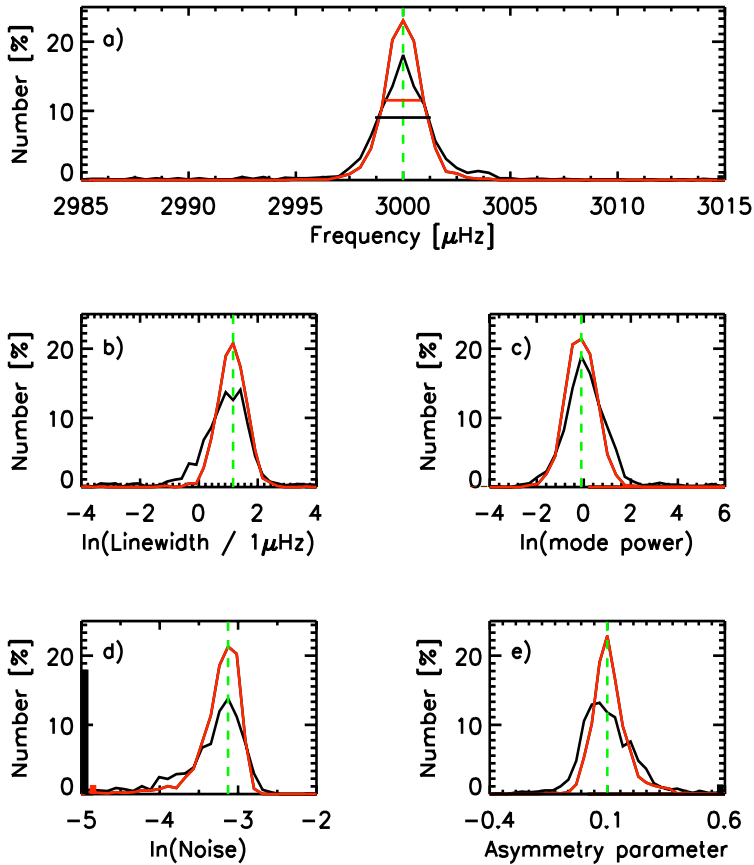
Figure 4.10: Distributions of the inferred oscillation parameters from fits to 1100 real-izations of a single mode of solar-like oscillation with $\mathcal{S}/\mathcal{N} = 20$. The input parameters are given in Table 4.3 and the window function is 30% full. The five panels show the distributions of the inferred (a) mode frequency ν_0, (b) linewidth Γ, (c) mode power $\mathcal{S}$, (d) noise level $\mathcal{N}$, and (e) asymmetry parameter b. The *red lines* show the results obtained with the new fitting method and the *black lines* show the old "no-correlation" fits. The *vertical green dashed line* in each plot indicates the input value. The horizontal lines in panel (a) are intervals containing 68% of the fits for the new (*red*) and the old (*black*) fitting methods. The *thick red* and *black vertical bars* in panels (a), (d), and (e) give the number of outliers with estimates beyond the plot boundaries.

Figure 4.11: The same as in Figure 4.10 but for 400 realizations with a signal-to-noise ratio of $\mathcal{S}/\mathcal{N} = 1000$. (Input parameters are given in Table 4.4.)
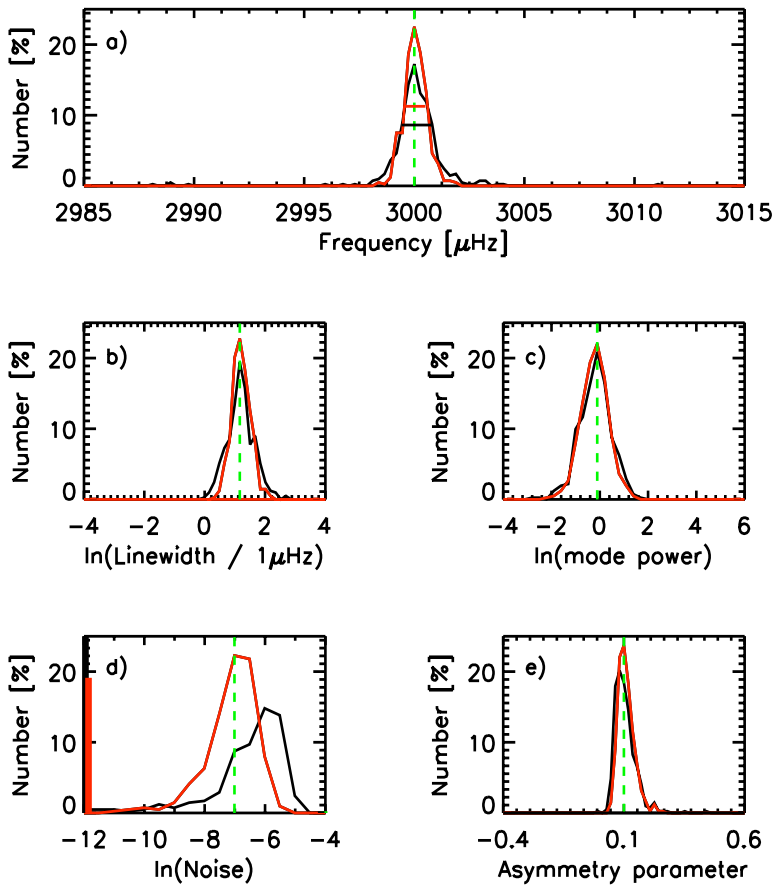
Table 4.4: Medians and scatters of the distributions of the estimated parameters of one mode of solar-like oscillation (see Figure 4.11). The window function is 30% full, the input linewidth is $\Gamma = 3.2\,\mu$Hz, and the input signal-to-noise ratio is $\mathcal{S}/\mathcal{N} = 1000$. The new and the old MLE estimates are given in the last two columns. By definition, 68% of the fits fall within the bounds set by the subscripts/exponents (with the notation explained in the text).

Mode parameter	Input value	New fitting	Old fitting
ν_0 [μHz]	3000.0	$3000.0\,^{+0.5}_{-0.5}$	$3000.1\,^{+0.7}_{-0.6}$
$\ln(\Gamma/1\mu\text{Hz})$	1.2	$1.2\,^{+0.3}_{-0.3}$	$1.2\,^{+0.5}_{-0.4}$
$\ln\mathcal{S}$	-0.1	$-0.2\,^{+0.5}_{-0.6}$	$-0.2\,^{+0.6}_{-0.7}$
$\ln\mathcal{N}$	-7.0	$-7.2\,^{+0.8}_{-25.8}$	$-7.3\,^{+1.5}_{-30.6}$
b	0.1	$0.1\,^{+0.03}_{-0.03}$	$0.1\,^{+0.04}_{-0.03}$

and Gaussian-like but the precision of the frequency estimator is still better with the new fitting method. For the old fitting method the number of fits beyond the 2-sigma mark is decreased significantly compared to the case with $S/\mathcal{N} = 6$. With respect to the distributions of the linewidth Γ (Figure 4.10b) and the mode power $\mathcal{S}$ (Figure 4.10c), note that the strong bias of the old fitting method decreased noticeably, but the estimates obtained with the new fitting method are still significantly more accurate and less biased. The fit of the noise level, $\mathcal{N}$, is still a problem with the old fitting method. The corresponding distribution (Figure 4.10d) is still significantly biased and $\sim$ 20% of all fits return extremely underestimated values for $\mathcal{N}$. The estimator of the noise level $\mathcal{N}$ obtained with the new fitting method is significantly less biased. Compared to the case with $S/\mathcal{N} = 6$ the asymmetry parameter b (Figure 4.10e) can be determined with higher precision and is almost unbiased for both fitting methods but its uncertainty is still quite big. Quantitative estimates of the median and the dispersion of the individual estimators are summarized in Table 4.3. We use the same definition for the dispersion of each estimator as described in detail in Section 4.7.1, i.e. the upper and lower bounds in Table 4.10 cover 34% of the fits on each side of the median. The new fitting method is still superior to the old method. For example, the mode frequency can be determined with an uncertainty of $\sim 0.8\,\mu$Hz and is therefore by a factor of 1.6 more accurate than the estimator obtained with the old fitting method. This is still significant but not as much as in the case of $S/\mathcal{N} = 6$ discussed in Section 4.7.1. The results of the new method for the other parameters Γ, $\mathcal{S}$, and $\mathcal{N}$ are less biased and in parts significantly more precise (e.g. the noise level $\mathcal{N}$).

We also computed a total of 400 realizations of one mode of solar-like oscillation with an even higher signal-to-noise ratio of $S/\mathcal{N} = 1000$, i.e. realizations with almost no noise. The mode parameters are kept as above, i.e. $\nu_0 = 3000\,\mu$Hz, $\Gamma = 3.2\,\mu$Hz, $\mathcal{S} = 0.9$, and $b = 0.1$. Figure 4.9 shows an example of one of these realizations together with the fits obtained with the new and the old fitting method as well as the expectation value of the power. Apparently a reasonable fit close to the expectation value is obtained
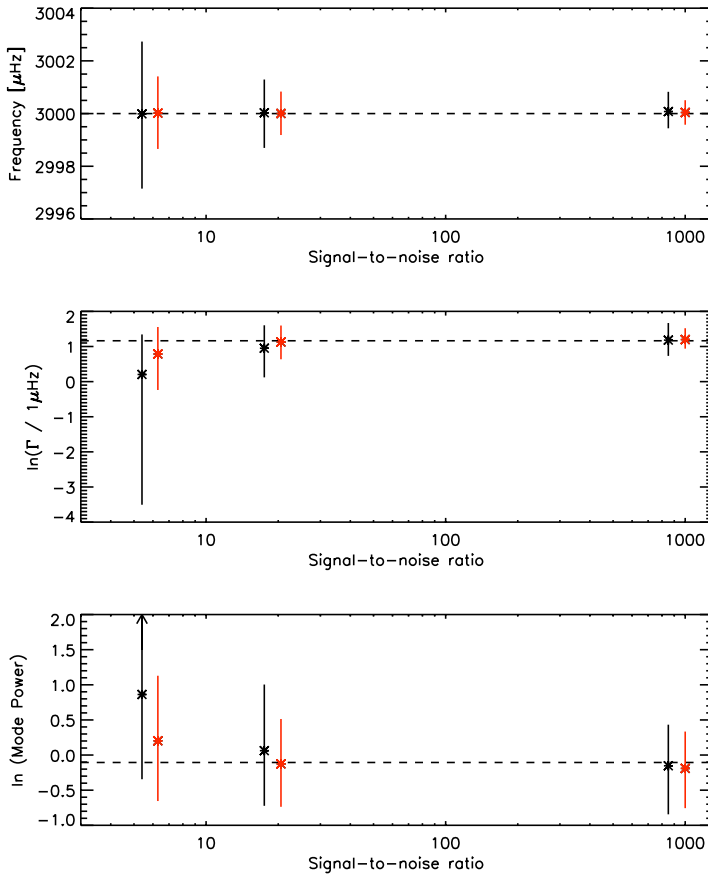
Figure 4.12: Median (cross) and scatter (vertical bar) of the mode frequency ν_0 (top), the mode linewidth Γ (middle), and the mode power $\mathcal{S}$ (bottom) for one mode of a solar-like oscillation as a function of the signal-to-noise ratio, $\mathcal{S}/\mathcal{N}$. The distributions of the individual parameters are shown in Figure 4.4, 4.10, and 4.11. The duty cycle of the observation window is 30%. The scatter is defined such that 34% of all fits on each side of the median are covered. The results obtained with the new and the old fitting methods are shown in *red* and *black* respectively. For clarity, the estimators for the old method are shifted slightly to lower $\mathcal{S}/\mathcal{N}$. Arrows indicate that the error bar of the corresponding estimate exceeds the plot boundary. The *dashed horizontal lines* indicate the respective input values for ν_0, Γ, and $\mathcal{S}$.

115

Table 4.5: Medians and scatters of the distributions of the estimated parameters of one mode of solar-like oscillation (see Figure 4.13). The window function is 30% full, the input linewidth is $\Gamma = 1$ μHz, and the input signal-to-noise ratio is $\mathcal{S}/\mathcal{N} = 6$. The new and old MLE estimates are given in the last two columns. By definition, 68% of the fits fall within the bounds set by the subscripts/exponents (with the notation explained in the text).

Mode parameter	Input value	New fitting	Old fitting
ν_0 [μHz]	3000.0	$3000.1^{+2.0}_{-1.3}$	$3000.3^{+5.7}_{-3.7}$
$\ln(\Gamma/1\mu\text{Hz})$	0.0	$-1.3^{+2.0}_{-2.6}$	$-1.9^{+2.6}_{-2.7}$
$\ln\mathcal{S}$	-0.1	$1.0^{+4.5}_{-1.8}$	$1.5^{+4.7}_{-1.8}$
$\ln\mathcal{N}$	-3.1	$-2.9^{+0.9}_{-8.3}$	$-5.1^{+3.0}_{-10.0}$
b	0.1	$0.0^{+0.3}_{-0.1}$	$0.0^{+0.3}_{-0.1}$

with both methods for this particular realization. The distributions of the parameters of all 400 realizations are shown in Figure 4.11. The distributions for the mode frequency, ν_0, the linewidth, Γ, the mode power, S, and the asymmetry parameter, b, are quite similar for both fitting methods. Furthermore, they are nearly unbiased even for the old fitting method. However, this is not true for the estimator of the noise level, $\mathcal{N}$. Both distributions show a long tail of underestimated noise fits. An unbiased estimation of the background noise seems to be impossible for either of the two fitting methods. This is confirmed by the formal error which is summarized together with the median of all fit parameters in Table 4.4. The formal error is defined as above such that it covers 68% of all fits. Note that the noise distribution obtained with the old fitting method seems to have a reasonable median. However, the distribution is composed of a peak of overestimated values and a long tail of strongly underestimated fits such that the median of all fits seems to be acceptable. For all other fit parameters except the background noise, the corresponding estimator is almost unbiased and its precision does nearly not depend on the fitting method. It is noteworthy that for a very high signal-to-noise ratio even the line asymmetry can be determined quite well. The median and the scatter of the mode frequency, ν_0, the linewidth, Γ, and the mode power, S, are shown as a function of the input signal-to-noise ratio in Figure 4.12. This figure confirms again that the new fitting method is superior to the old fitting method, in particular when the signal-to-noise ratio is low; the estimators obtained with the new fitting method are then more accurate and less biased. For an increasing signal-to-noise ratio, the differences between both fitting methods become smaller.

4.7.5   Different mode lifetimes

The power spectrum of solar-like oscillations is spread over several frequency bins due to the finite lifetime of the modes, i.e. $\tau = 1/\pi\Gamma$. The exact number of frequency bins

Table 4.6: The same as in Table 4.5 but for a mode linewidth of $\Gamma = 10\,\mu\text{Hz}$. The corresponding distributions of the parameters are shown in Figure 4.14.

Mode parameter	Input value	New fitting	Old fitting
$\nu_0\,[\mu\text{Hz}]$	3000.0	$3000.1^{+2.2}_{-2.3}$	$3000.1^{+4.8}_{-4.8}$
$\ln(\Gamma/1\mu\text{Hz})$	2.3	$2.2^{+0.5}_{-0.5}$	$1.5^{+0.7}_{-0.9}$
$\ln\mathcal{S}$	-0.1	$0.0^{+0.4}_{-0.5}$	$0.6^{+0.8}_{-0.8}$
$\ln\mathcal{N}$	-1.9	$-2.0^{+0.1}_{-0.2}$	$-2.1^{+0.3}_{-0.7}$
b	0.1	$0.1^{+0.1}_{-0.1}$	$0.1^{+0.1}_{-0.1}$

over which the power of a mode is spread depend on the length T of the observation (here, $T = 16.5\,\text{days}$). So far, we used $\Gamma = 3.2\,\mu\text{Hz}$ so that the mode is spread over roughly five frequency bins given the bin size of $1/T = 0.7\,\mu\text{Hz}$. In this section, we compare the new and the old fitting method for one mode of solar-like oscillation with various mode linewidths. In addition to the case with $\Gamma = 3.2\,\mu\text{Hz}$ (see Section 4.7.1) we computed many realizations of one mode of solar-like oscillation with mode linewidths of $\Gamma = 1\,\mu\text{Hz}$ and $\Gamma = 10\,\mu\text{Hz}$, i.e. modes which are spread over roughly 1 and 14 frequency bins respectively. The other input parameters were kept as in Section 4.7.1, i.e. the mode frequency is $\nu_0 = 3000\,\mu\text{Hz}$, the signal-to-noise ratio is $\mathcal{S}/\mathcal{N} = 6$, and the line asymmetry is $b = 0.1$. We used the window function with a duty cycle of 30% (see Figure 4.2). We computed 1650 realizations for a mode linewidth of $\Gamma = 1\,\mu\text{Hz}$ and 1350 realizations with $\Gamma = 10\,\mu\text{Hz}$.

Note that it may be misleading to compare the three simulations with different mode linewidths directly due to the definition of the signal-to-noise ratio. In this work, the signal-to-noise, $\mathcal{S}/\mathcal{N}$, is defined as the ratio of the maximum peak height, $\mathcal{S}$, and the noise level, $\mathcal{N}$ [see Equation (4.40)]. With respect to this definition there is actually more integrated power in a mode with a linewidth of $\Gamma = 10\,\mu\text{Hz}$ than in a mode with $\Gamma = 1\,\mu\text{Hz}$ when $\mathcal{S}/\mathcal{N} =$const.

The distributions of the parameters inferred from the Monte Carlo simulations with mode linewidth $\Gamma = 1\,\mu\text{Hz}$ and $\Gamma = 10\,\mu\text{Hz}$ are shown in Figure 4.13 and Figure 4.14 respectively. The median and the uncertainty of the individual estimates derived from those distributions are summarized in Table 4.5 and Table 4.6. Again, the uncertainty is defined such that 68% of all fits fall within the given error estimate. For a mode linewidth of $\Gamma = 1\,\mu\text{Hz}$ the frequency distribution shows a distinct peak for both fitting methods and long tails on both sides of the distribution. The tails are more pronounced for the old fitting method. These tails lead to rather big formal error estimates of $\sigma_\nu = 1.7\,\mu\text{Hz}$ for the new fitting method and $\sigma_\nu = 4.7\,\mu\text{Hz}$ for the old method. The central peak of the frequency distribution for the new fitting method has a FWHM of $\sim 0.7\,\mu\text{Hz}$. The relatively high number of biased frequency estimates can be explained as follows: for $\Gamma = 1\,\mu\text{Hz}$ the expectation value of the power of the mode is spread over not much more than one frequency bin. When we generate a realization of a Fourier line, the square root of the
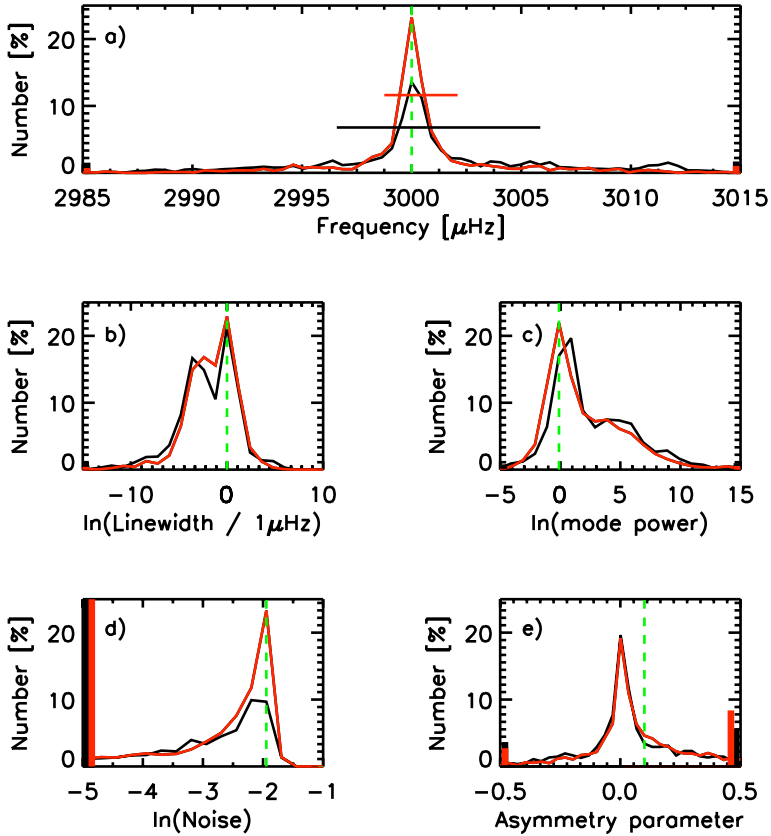
Figure 4.13: Distributions of the inferred oscillation parameters from fits of 1650 realizations of a single mode of solar-like oscillation with a mode linewidth of $\Gamma = 1$ μHz, and $\mathcal{S}/\mathcal{N} = 6$. The input parameters are given in Table 4.5. The duty cycle of the window function is 30%. The five panels show the distributions of the inferred (a) mode frequency ν_0, (b) linewidth Γ, (c) mode power $\mathcal{S}$, (d) noise level $\mathcal{N}$, and (e) asymmetry parameter b. The *red lines* show the results obtained with the new fitting method and the *black lines* show the old "no-correlation" fits. The *vertical green dashed line* in each plot indicates the input value. The horizontal lines in panel (a) are intervals containing 68% of the fits for the new (*red*) and the old (*black*) fitting methods. The *thick black* and *red vertical bars* give the number of outliers with estimates beyond the plot boundaries. In panel (d) these bars even exceed the 25%-plot boundary in y-direction. The height of these bars is 34% for the new fitting method (*red*) and 50% for the old fitting method (*black*).

Figure 4.14: The same as Figure 4.13 but for 1350 realizations with a mode linewidth of $\Gamma = 10\,\mu Hz$. (Input parameters are given in Table 4.6.)

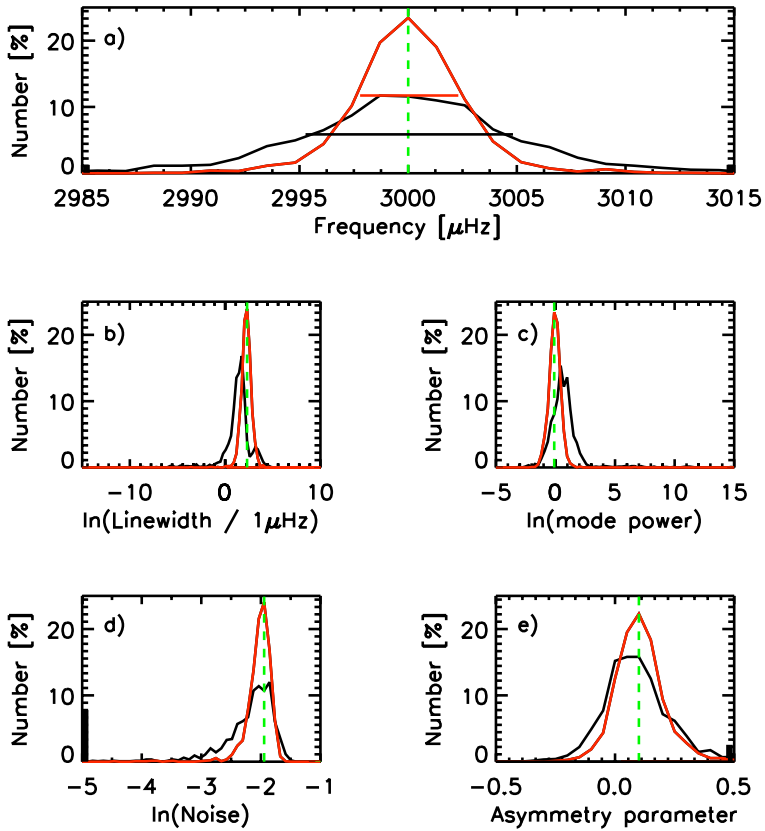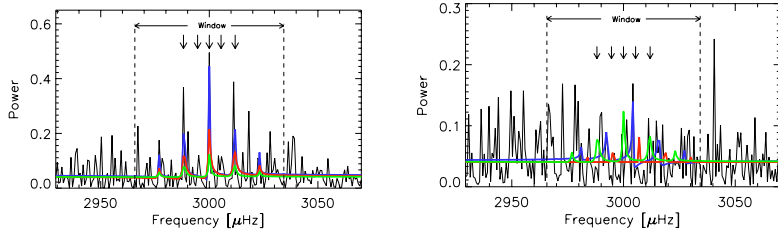Figure 4.15: Power spectra of two realizations of one mode of solar-like oscillation with input frequency $\nu_0 = 3000\mu Hz$, mode linewidth $\Gamma = 1\mu Hz$, signal-to-noise ratio $\mathcal{S}/\mathcal{N} = 6$, and mode asymmetry $b = 0.1$. The realizations are shown in black, the colored lines represent the fits with the new (*red*) and the old fitting methods (*blue*) as well as the expectation value of the power (*green*). The *vertical dashed lines* represent the width of the window function, the small arrows indicate the five different frequency guesses used to fit each realization. Even though the expectation value of the power is identical in both realizations, the example on the right does not show any significant signal above the noise level.

expectation value is multiplied with a centered complex gaussian random vector with unit variance and independent real and imaginary parts [cf. Equation(4.40)]. This may lead to realizations which show hardly any significant signal in the power spectrum around the resonant frequency ν_0. This is illustrated in Figure 4.15. It shows two realizations with identical input parameters ($\nu_0 = 3000 \mu Hz$, $\Gamma = 1 \mu Hz$, $\mathcal{S}/\mathcal{N} = 6$, $b = 0.1$). It is obvious that the realization on the left hand side exhibits a significant signal peak around $\nu = 3000 \mu Hz$ leading to a reasonable fit of the frequency for both fitting methods. However, the realization on the right hand side shows hardly any signal around $\nu = 3000 \mu Hz$. Here, both methods fit some random peak in the noise with large offsets of the frequency estimates. The distributions for the other parameters reveal a significant bias for both fitting methods. The noise estimates tend to be largely underestimated, a fit for the line asymmetry is impossible.

In the case of a mode linewidth of $\Gamma = 10 \mu Hz$ (Figure 4.14 and Table 4.6) the new fitting method provides nearly unbiased estimates for all inferred parameters. In addition the estimators are more accurate than the results obtained with the old fitting method. For example, the uncertainty of the frequency estimator of the new fitting method is less than half of the uncertainty obtained with the old method. Moreover, all estimators obtained with the old fitting method are significantly biased (except the mode frequency).

Figure 4.16 shows the median and the uncertainty for the mode frequency, ν_0, the mode linewidth, Γ, and the mode power, $\mathcal{S}$, as a function of the input mode linewidth in units of frequency bins. The frequency estimator is nearly unbiased for both fitting methods and all tested mode linewidths. The frequency uncertainty increases towards low and high mode linewidth with a minimum in between. According to Libbrecht (1992) the frequency uncertainty scales like $\sigma_\nu \propto \sqrt{\Gamma}$. This relation is only fulfilled at low Γ if the long tails in the frequency distribution are neglected and the width of the central peak is considered as the "true" uncertainty of the frequency estimator. However, this is only
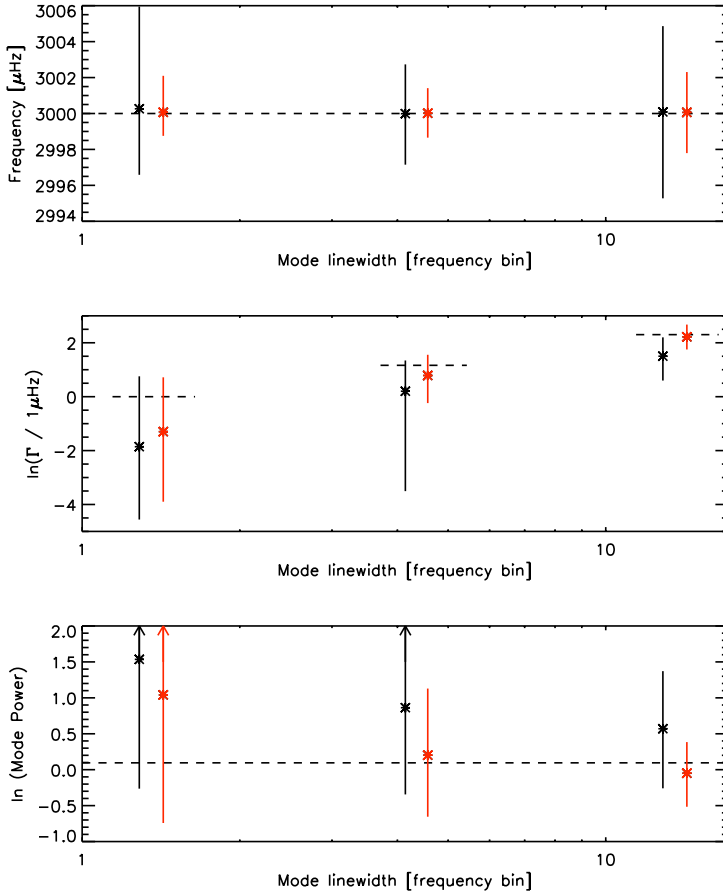
Figure 4.16: Median (cross) and scatter (vertical bar) of the mode frequency ν_0 (top), the mode linewidth Γ (middle), and the mode power $\mathcal{S}$ (bottom) of one mode of a solar-like oscillation as a function of the input mode linewidth Γ. Here, the input mode linewidth is given in units of frequency bins. One frequency bin is $1/T = 0.7$ μHz. The duty cycle of the observation window is 30%. The scatter is defined such that 34% of all fits on each side of the median are covered. The results obtained with the new and the old fitting methods are shown in *red* and *black* respectively. For clarity, the estimators for the old method are shifted slightly to the left. Arrows indicate that the error bar of the corresponding estimate exceeds the plot boundary. The *dashed horizontal lines* indicate the respective input values for ν_0, Γ and $\mathcal{S}$.

a hypothesis. With respect to the other parameters it is absolutely necessary to apply the new fitting method in order to obtain reliable estimators; by using the new fitting method the estimates are more precise and less biased than for the old fitting method. Furthermore, I note that the mode linewidth has to be spread at least over a few frequency bins in order to estimate the mode parameters unbiased. This is particularly true for the mode linewidth Γ and the mode power $\mathcal{S}$ which are strongly biased even with the new fitting method for an input mode linewidth of $\Gamma = 1\ \mu$Hz.

4.7.6   Impact of the initial guess

For the fit of each single realization, we applied a loop of 5 different frequency guesses around the input mode frequency. As initial guesses, we choose the input frequency $\nu_0 = 3000\ \mu$Hz as well as $\nu_0 \pm 5.5\mu$Hz and $\nu_0 \pm 11.9\ \mu$Hz, corresponding to the position of the sidelobes in the observation window with a duty cycle of 15% (Figure 4.2 d). The guesses for the other parameters are uniformly distributed within $\pm 20\%$ of the input values. In this section, we investigate the result of the fit with the two fitting methods depending on the initial guess.

In the previous sections we only presented the best fit for each realization, i.e. the fit which maximizes the joint PDF. Figure 4.17 shows the frequency distributions for 750 realizations obtained with the new fitting method and with the old fitting method respectively. Each colored distribution corresponds to a particular initial guess for the mode frequency. In this particular case we simulated one mode of solar-like oscillation with input parameters $\nu_0 = 3000\ \mu$Hz, $\Gamma = 3.2\ \mu$Hz, $\mathcal{S} = 0.9$, $\mathcal{N} = 0.15$, and $b = 0.1$ and used the window function with a duty cycle of 15%. It is obvious that the new fitting method depends much less on the initial guess and leads to a more accurate estimate of the mode frequency. The frequency distributions obtained with the old fitting method (Fig. 4.17b) suggest that the old fitting method basically fits the oscillation peak and the sidelobes of the window function depending on the initial guess. For the new fitting method the distributions corresponding to the guesses of $\nu = 2988.1\ \mu$Hz and $\nu = 3011.9\ \mu$Hz have a bimodal distribution with a smaller second peak around the corresponding initial guess. The smaller second peak contains about 20%–40% of all realisations. Nevertheless the best-fit distribution does not suffer from these "bad fits" and shows a well centered, un-biased distribution. In contrast, the best-fit distribution for the old fitting method shows strong tails on both sides of the maximum.

The other fit parameters, i.e. mode linewidth, mode power, line asymmetry, and noise, are less dependent on the initial guess. Figure 4.18 shows the distribution of the logarithm of the mode linewidth for 750 realisations obtained with both fitting methods. The distribution for each guess is shown in a different color. Neither for the new fitting method nor for the old method, we find a significant dependence of the fit result on the initial frequency guess. The distributions of the fits for the individual frequency guesses compare quite well with the best-fit distribution in both cases. The independence of the fit of the linewidth on the initial guess that is demonstrated in Figure 4.18 is representative for the other parameters, i.e. the mode power, the line asymmetry and the noise level.
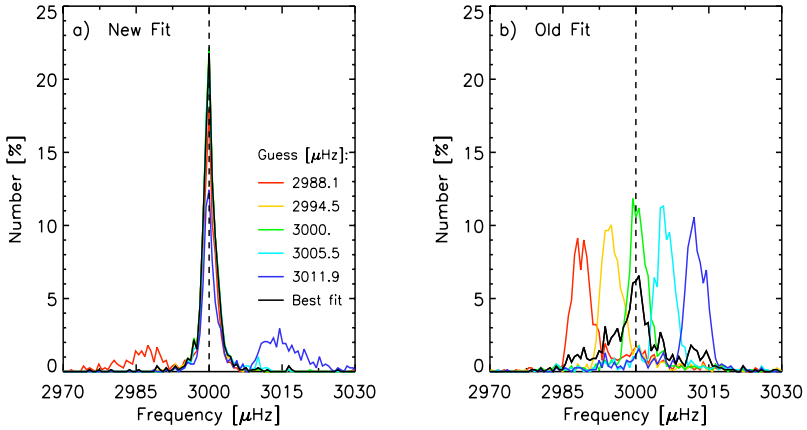
Figure 4.17: Distributions of the mode frequency, ν_0, obtained with (a) the new fitting method and (b) the old fitting method using an observation window with a duty cycle of 15% (Figure 4.2 d). Each of the 750 realizations is fitted with five different guesses of the mode frequency. Each color represents the distribution of the fits for a particular frequency guess. The black line shows the distribution of the best fits. The vertical dashed line indicates the input mode frequency, ν_0.
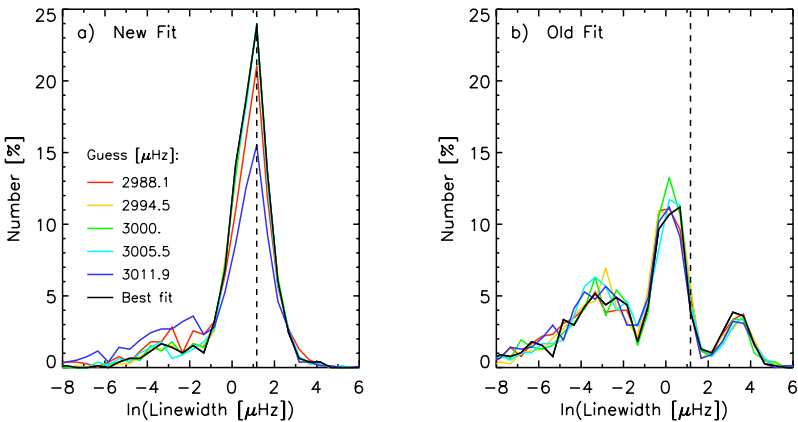
Figure 4.18: Distributions of $\ln \Gamma$ obtained with (a) the new fitting method and (b) the old fitting method using an observation window with a duty cycle of 15% (Figure 4.2 d). Each of the 750 realizations is fitted with five different guesses of the mode frequency and random guesses of the other parameters. Each color represents the distribution of the fits of $\ln \Gamma$ for a particular frequency guess. The black line shows the distribution of the best fits. The vertical dashed line indicates the input linewidth, $\ln \Gamma_0$.
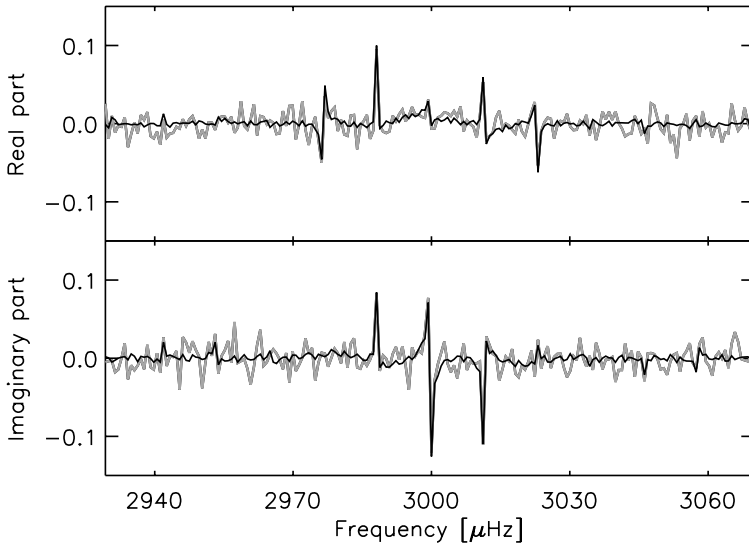
Figure 4.19: Real and imaginary parts of the Fourier transform of a simulated gapped time series containing a sinusoid on top of white background noise. The signal-to-noise ratio is $S/N = 100$. The observation window has a duty cycle of 30%. The simulated data are shown by the *thick gray line*. The *thin black line* shows the fit to the data using the new fitting method. The fit with the old method is not shown since it is almost identical.

4.8 Testing and comparing the methods for sinusoidal deterministic oscillations plus white noise

Figure 4.19 shows the Fourier spectrum of a simulated time series containing a sinusoidal mode of oscillation on top of a white noise background as described in Section 4.6.3. In this particular case the observation window with a duty cycle of 30% is used (see Figure 4.2c). The input parameters of the sinusoidal function are the mode frequency $\nu_0 = 3000 \ \mu$Hz, the amplitude $A = 1.1$, and the phase $\varphi = 60°$. The signal-to-noise ratio is $S/N = 100$. The fit shown in Figure 4.19 was obtained with the new fitting method. Since we found no significant difference between the old and the new fitting methods in this case, the old fitting method is not shown. Differences between the data and the fit are essentially due to the noise.

We computed 500 realizations of sinusoidal oscillations with the same mode parameters (frequency, amplitude, and phase) as before, the same observation window (30% full), but with a signal-to-noise ratio $S/N = 46$. The resulting distributions of the inferred parameters obtained with the two fitting methods are shown in Figure 4.20. For this simulation, the known input values were used as an initial guess to speed up the

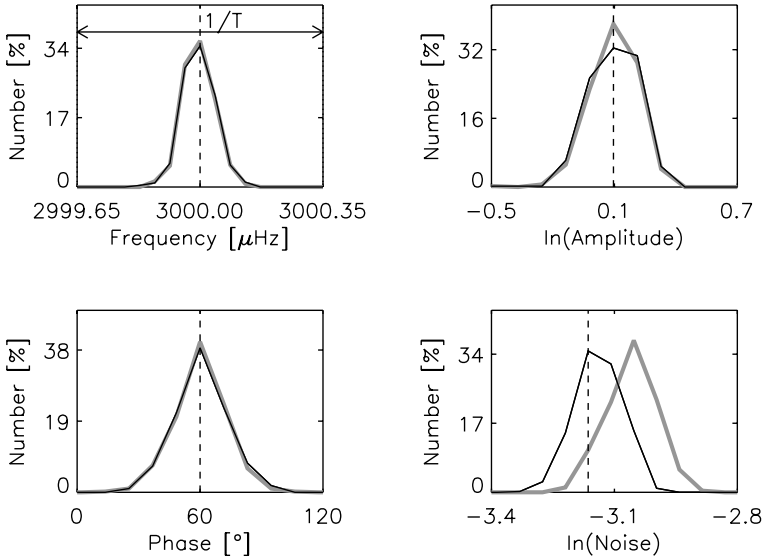Figure 4.20: Distributions of the inferred oscillation parameters for a set of 500 realizations of long-lived sinusoidal oscillations with $S/N = 46$. The window function with a duty cycle of 30% is used. The *black* and the *gray lines* are for the new and old fitting methods, respectively. The *vertical dashed line* in each plot indicates the input value. The parameters shown are (a) the mode frequency [ν_0], (b) the logarithm of the mode amplitude [$\ln A$], (c) the phase of the oscillation [ϕ], and (d) the logarithm of the noise level [$\ln \sigma_0$] (see Section 6.3). Notice that the estimate of the noise is biased when frequency correlations are ignored (old "nc" fit), although by a very small amount.

minimization; we checked on several realizations that it is acceptable to do so when the signal-to-noise ratio is large. The distributions of the inferred parameters (Figure 4.20) show that, for sinusoidal oscillations, the new fitting method does not provide any significant improvement compared to the old fitting method.

We emphasize that the fitting parameters can be determined with a very high precision when the noise level is small. In particular, we confirm that the uncertainty of the frequency estimator can be much smaller than $1/T$ (see Figure 4.20a). Figure 4.21 shows the median and the standard deviation of the mode frequency for different signal-to-noise ratios. Each symbol and its error bar in Figure 4.21 is based on the computation of 500 realizations of sinusoidal oscillations with the same mode parameters as before, the same observation window (30% full), but various signal-to-noise ratios. Since we did not find any significant difference between the two fitting methods, only the results obtained with the new fitting method are shown. Figure 4.21 illustrates that even for a relatively low signal-to-noise ratio of $S/N = 10$, the standard deviation of the inferred mode frequency
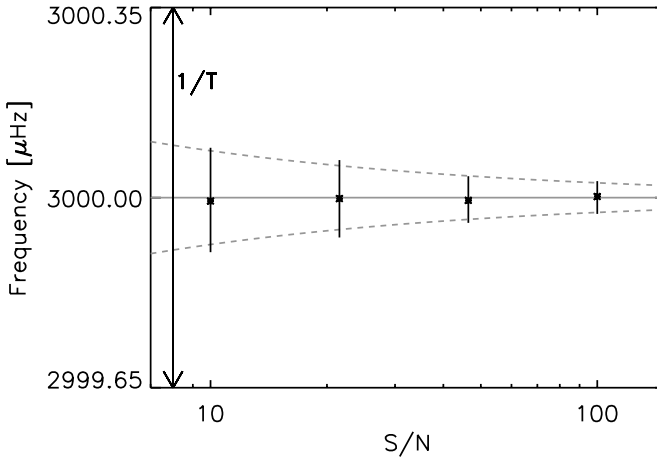
Figure 4.21: Median (*cross*) and standard deviation (*vertical bar*) of the inferred frequency of sinusoidal oscillations [ν_0] as a function of signal-to-noise ratio $\mathcal{S}/\mathcal{N}$. The duty cycle is 30 %. Only the results obtained with the new fitting method are shown. The *horizontal gray line* shows the input mode frequency. The *dashed gray lines* show the theoretical value of frequency uncertainty, σ_{ν_0}, given by Equation (4.47). The vertical axis of the plot spans the interval $\Delta\nu = 1/T = 0.7\,\mu$Hz.

is smaller than $1/T$ by a factor of four. For higher signal-to-noise ratios the precision is even more impressive: When $\mathcal{S}/\mathcal{N} = 100$, the standard deviation of the mode frequency is about $1/20$ that of $1/T$.

The theoretical value of the standard deviation of the mode frequency obtained by Cuypers (1987) can be extended to the case of gapped data (Cuypers, 2008, private communication) as follows:

$$\sigma_{\nu_0} = \frac{\sqrt{6}\,\sigma_{\mathrm{t}}}{\pi A T \sqrt{n}}, \tag{4.47}$$

where A is the amplitude of the sinusoid in the time domain, σ_{t} is the rms value of the noise, $n = \alpha N$ is the number of recorded data points, and T is the total observation length. This theoretical uncertainty is overplotted in Figure 4.21. The match with our Monte Carlo measurements is excellent. This confirms that, in this case, it is equivalent to perform the fits in the temporal and in the Fourier domains. Note that Equation (4.47) is only valid under the assumption that the noise is uncorrelated in the time domain, a condition fulfilled by our simulations. The main reason why the measurement precision is only limited by the noise-to-signal ratio is because perfect knowledge of the model is assumed.

4.9 Conclusion

In this paper we derived an expression for the joint PDF of solar or stellar oscillations in complex Fourier space, in agreement with the work of Gabriel (1994). This joint PDF explicitly takes into account frequency correlations introduced by the convolution with the window function. We implemented a maximum likelihood estimation method to retrieve the parameters of stellar oscillations. Both stochastic solar-like oscillations and deterministic sinusoidal oscillations were considered.

In the case of solar-like oscillations, we performed Monte Carlo simulations to show that the improvement provided by our fitting method can be very significant in comparison with a fitting method that ignores the frequency correlations. The results are summarized in Figure 4.6. In one particular example, by using an observation window with a duty cycle $\alpha = 30\%$ and a signal-to-noise ratio $\mathcal{S}/\mathcal{N} = 6$, the new fitting method increased the precision of the mode frequency by a factor of two and the estimates of the line width and mode power were less biased and more precise. For a window with a duty cycle $\alpha = 15\%$, the precision on the mode frequency estimate was increased by a factor of five. We also found that the Cramér–Rao lower bounds (formal errors) can provide reasonable estimates of the uncertainty on the MLE estimates of the oscillation parameters.

In the case of long-lived, purely sinusoidal oscillations, we did not find any significant improvement in using this new fitting method. Yet, we confirm that the standard deviation of the mode frequency can be measured in Fourier space with a precision much better than $1/T$ for large signal-to-noise ratios, in accordance with a previous time-domain calculation (Cuypers, 1987; Cuypers, 2008, private communication).

The analysis of time series containing many gaps can benefit from our work. Applications may include, for example, the reanalysis of solar oscillations from the early days of the BiSON network (Miller et al. 2004) or the solar-like oscillations of α Centauri observed from the ground with two telescopes (Butler et al. 2004).

5 Efficient maximization of the joint PDF: Cholesky decomposition

In the previous chapter, maximum likelihood estimators for gapped time series were implemented. The method as it is described there is computationally quite expensive due to the singular value decomposition (SVD) which is involved in the computation of the joint PDF. In this chapter, I describe a more efficient way to maximize the joint PDF. Here, the SVD is replaced by a Cholesky decomposition. I describe the Cholesky decomposition and its application to our particular problem in Section 5.1. In Section 5.2, I demonstrate that the application of the Cholesky decomposition is more efficient and show that both algorithms give essentially the same results.

5.1 The Cholesky decomposition

Equation (4.22) is the correct joint PDF of the Fourier line of a gapped time series. This equation can be used to derive maximum likelihood estimates by minimizing Equation (4.24). The minimization of Equation (4.24) becomes very time-consuming when the selected section of the data, i.e. its length M, is big and/or a high number of parameters are fitted simultaneously. Thus, the computation time may become an issue when the analyzed time series become long and/or when many modes are included in the fit.

The most time-consuming steps in the computation of Equation (4.24) are the inversion of the matrix CC^H to compute the Moore-Penrose generalized inverse of C [Equation (4.23)] and the computation of the Jacobian J [Equation (4.20)]. For example, in the case discussed in Section 4.7.1 , ~ 95% of the time to minimize Equation (4.26) is taken by the inversion of CC^H (~ 12%) and the SVD (~ 83%).

The inversion of CC^H may be speed up by replacing the standard Gaussian elimination by an LU-decomposition. The computation of the Jacobian J in Equation (4.20) requires a SVD of the $M \times (M + 2p)$ matrix C. The computation of the SVD can be avoided by rewriting Equation (4.20) as follows:

$$J = |\det(U\Lambda)|^2 = |\det(U\Lambda\Lambda U^H)| = |\det(U\Sigma V^H V\Sigma U^H)| = |\det(CC^H)|. \tag{5.1}$$

Note that the matrix V is unitary, i.e. $V^H V = I_{M+2p}$ by definition of the singular value decomposition of the Matrix C [Equation (4.14)]. The matrix CC^H is a Hermitian and positive semi-definite $M \times M$ matrix. Therefore, the matrix CC^H may be decomposed as (e.g. Higham 1990)

$$CC^H = T^H T, \tag{5.2}$$

Table 5.1: Computation time for a fit of one mode of solar-like oscillation using different algorithms to maximize the joint PDF. The numbers correspond to the median and the scatter from fits to 500 realizations (see Figure 5.1). The subscripts/exponents give the 1σ error bar which covers 68% of all computation times (34% above and below the median).

Fitting Method	Computation time [sec]
Old method	90^{+149}_{-46}
New method:	
SVD	1524^{+1702}_{-487}
Cholesky decomposition	212^{+205}_{-70}

where T is a $M \times M$ lower triangular matrix and T^H is its conjugate transpose. This is a Cholesky decomposition (e.g. Horn and Johnson 1985, chapter 7.2). Since the matrix T is a lower triangular matrix with diagonal elements $\tau_{ii} = \tau_i$, we can rewrite Equation (5.1) as

$$J = |\det(CC^H)| = |\det(T^H T)| = (\det T)^2 = \left(\prod_{i=0}^{M-1} \tau_i\right)^2 . \tag{5.3}$$

By rewriting the Jacobian in this form, we can replace the SVD of the matrix C by a Cholesky decomposition of C. Equation (4.24) then reads

$$\mathcal{L}(\mu) = \|C^\dagger(y - Wd)\|^2 + 2\sum_{i=0}^{M-1} \ln \tau_i + \text{constant.} \tag{5.4}$$

In the equation above the singular values λ_i of C are replaced by the diagonal elements τ_i of the matrix T.

The special case considering only solar-like oscillations [Section 4.4.1, Equation (4.26)] then reads

$$\mathcal{L}(\mu) = \|C^\dagger y\|^2 + 2\sum_{i=0}^{M-1} \ln \tau_i + \text{constant.} \tag{5.5}$$

5.2   Testing the Cholesky decomposition

We computed 500 realizations of one mode of solar-like oscillation with input parameters $\nu_0 = 3000~\mu Hz$, $\Gamma = 3.2~\mu Hz$, $\mathcal{S} = 0.9$, $\mathcal{N} = 0.15$, and $b = 0.1$. The window function has a duty cycle of 30% (cf. Section 4.7.1). In this example, the selected data set contains $M = 202$ elements (or frequency bins) and the window function contains $2p + 1 = 99$ elements. Each realization was fitted with the old fitting method [cf. Equation (4.36)] and the new fitting method. For the new fitting method we used both the singular value decomposition and the Cholesky decomposition [cf. Equations (4.26) and (5.5)]. In the latter case we also applied a LU-decomposition to compute the inverse $(CC^H)^{-1}$. Only one
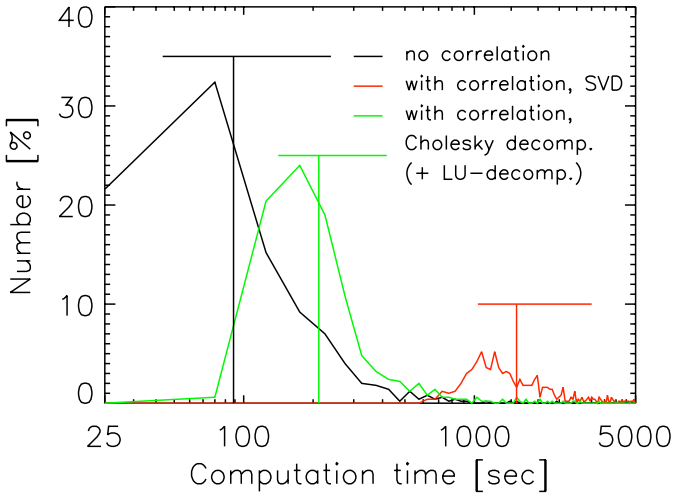
Figure 5.1: Distributions of the computation times for fits of 500 realizations of one mode of solar-like oscillation using different maximization algorithms. The *black distribution* represents the fit with the old fitting method [Equation (4.36)], the *red distribution* corresponds to the fit with the new fitting method using the SVD [Equation (4.26)], and the *green distribution* shows the fit with the new method using LU- and Cholesky decompositions [Equation (5.5)]. The *vertical bars* are the median of the corresponding distribution, the horizontal bars show the corresponding scatter. The scatter is defined such that 68% of the realizations fall within the error bars. Note that the x-axis (computation time) of the plot is on logarithmic scale.

guess for each method and each realization is applied. The initial guesses are identical for all three algorithms.

Figure 5.1 shows the distributions of the computation times for the fit of the 500 realizations of one mode of solar-like oscillation using the three different algorithms. The distribution for the old fitting method and the new fitting method using the Cholesky decomposition are well peaked while the distribution for the new method using the SVD is much more scattered. The median and the scatter of each distribution are summarized in Table 5.1. The scatter is defined such that 68% of all realizations fall within the given bounds (±34% on both sides of the median). As expected, the old fitting method is the fastest algorithm. However, the new fitting method using the Cholesky decomposition is slower by only a factor of ∼ 2. Even more important, the fit using the Cholesky decomposition is by a factor of ∼ 7 faster than the new fitting method using the SVD. With the new algorithm, the inversion of CC^H and the Cholesky decomposition take only ∼ 50% of the minimization of Equation (5.5). Here, ∼ 40% of the computation time is taken by the inversion using an LU-decomposition and only ∼ 10% are taken by the Cholesky

Table 5.2: Quantitative comparison of the fit results obtained with the new fitting method using either a SVD or a Cholesky decomposition. The *second column* lists the dispersion of $x_{SVD} - x_{Chol}$ for all fit parameters, x. The difference $x_{SVD} - x_{Chol}$ is deduced from fits of 500 realizations of one mode of solar-like oscillation (Figure 5.2). The dispersion is defined such that 68% of all fits fall within the given values. For comparison, the third column shows the uncertainty of the individual estimators deduced from Monte Carlo simulations in Section 4.7.1 (Table 4.1).

Mode parameter x	Dispersion of the difference of the two algorithms: $\sigma_{(x_{SVD} - x_{Chol})}$	Uncertainty from the MCS σ_x (cf. Section 4.7.1)
Frequency ν_0 [μHz]	$1.1 \cdot 10^{-3}$	1.4
Linewidth $\ln(\Gamma/1\mu\text{Hz})$	$1.0 \cdot 10^{-3}$	0.9
Mode power $\ln\mathcal{S}$	$1.4 \cdot 10^{-3}$	0.9
Noise $\ln\mathcal{N}$	$1.4 \cdot 10^{-3}$	0.6
Asymmetry parameter b	$4.0 \cdot 10^{-4}$	0.2

decomposition. This demonstrates impressively that the implementation of the Cholesky decomposition allows us to maximize the joint PDF of a gapped time series much more efficient than the algorithm using the SVD. We note again that the improvement in terms of computation time may also depends on the length M of the selected data set and the number of free parameters. For different setups, e.g. longer time series (bigger M) or more parameters to fit, the new fitting method using the Cholesky decomposition may be significantly slower than the old fitting method. But even then, the Cholesky decomposition is expected to be still much faster than the SVD.

For a comparison of the results obtained with the new fitting method using either the Cholesky decomposition or the SVD, we calculated the difference $x_{SVD} - x_{Chol}$ of the fit results for all fit parameters, x. The distribution of this difference of all 500 realizations is shown in Figure 5.2, For all parameters, the distributions of $x_{SVD} - x_{Chol}$ are well centered around zero and only exhibit very small scatter. The dispersion of $x_{SVD} - x_{Chol}$ deduced from these distributions is listed in the second column of Table 5.2. For comparison, the table also shows the dispersion of the estimators that were deduced from Monte Carlo simulations in Section 4.7.1 (Table 4.1). Note that overall the dispersion of $x_{SVD} - x_{Chol}$ is by a factor of ~ 1000 smaller than the uncertainty of the corresponding estimator derived from the Monte Carlo simulations (note that for the mode power, $\ln S$, the factor is "only" ~ 600). Thus, we conclude that the application of the Cholesky decomposition provides an efficient and reliable algorithm to derive maximum likelihood estimates of stellar oscillation parameters from gapped time series. The analysis of real observational data should benefit significantly from the application of the this algorithm.
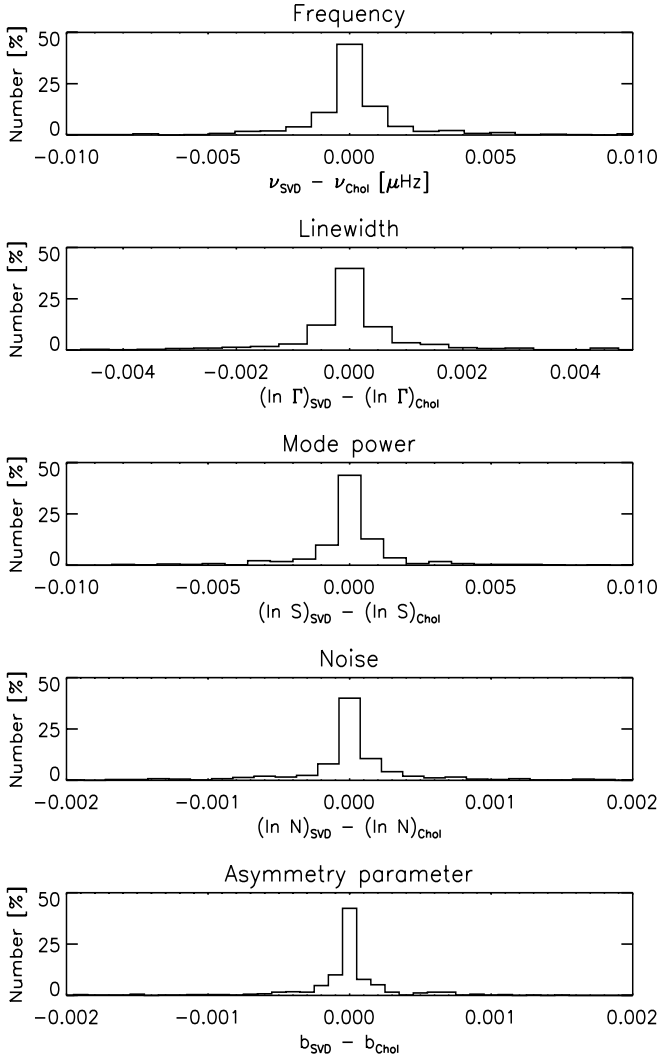
Figure 5.2: Distributions of the difference $x_{\mathrm{SVD}} - x_{\mathrm{Chol}}$ of the fit parameters, x, obtained with the new fitting method using either the SVD or the Cholesky decomposition. The distributions are deduced from fits of 500 realizations of one mode of solar-like oscillation using Equations (4.26) and (5.5) respectively. The input parameters are $\nu_0 = 3000\,\mu\mathrm{Hz}$, $\Gamma = 3.2\,\mu\mathrm{Hz}$, $\mathcal{S}/\mathcal{N}{=}6$, $b = 0.1$, and the duty cycle of the window is 30% (cf. Section 4.7.1).

6 Discussion

6.1 HD 52265: A remarkable data set for asteroseismology

The CoRoT observations of HD 52265 are very valuable for a number of reasons: i) The power spectrum of the 4-month time series of HD 52265 is of similar quality as the power spectra that were observed for the Sun at the beginning of the 1980s (Grec et al. 1980). The modes with $\ell = 0$ and $\ell = 2$ are well resolved and lead to an unambiguous mode identification. ii) Compared to many other asteroseismic targets, HD 52265 is very solar-like as illustrated by its position in the HRD. iii) The effect of stellar rotation on oscillations can be measured without a doubt. iv) HD 52265 hosts a planet.

The signal-to-noise ratio is high enough that modes with $\ell \leq 2$ spanning 9 radial orders can be observed (by eye). The high quality of the HD 52265 data allows us to measure the mode frequency with a precision of $\sim 0.15\,\mu$Hz which is expected for a 4-month observation with the given signal-to-noise. Table 6.1 lists the mean large and small separations for HD 52265 determined in this work and compares it with measurements for other solar-like stars observed with CoRoT, Kepler, and ground-based telescopes. The precision of the estimates for the large and small frequency separation, $\Delta\nu$ and $\delta\nu$, clearly ranks among the best for all Sun-like stars observed so far. Below I will discuss the implications of my work for constraining the fundamental parameters of HD 52265, constraining the mass of the orbiting planet, and for future asteroseismic projects such as PLATO and SONG.

6.2 On the determination of global stellar parameters of HD 52265

In Chapter 3, I presented the analysis of the CoRoT time series of the solar-like star HD 52265. One of the central results of this analysis is the measurement of the large and small frequency separations, $\Delta\nu = 98.84 \pm 0.12\,\mu$Hz and $\delta\nu = 8.14 \pm 0.20\,\mu$Hz (Fit A, Section 3.7.1). As described in Section 1.3 the large separation is proportional to the square root of the mean stellar density, $\Delta\nu \propto \overline{\rho}^{1/2}$. For the large separation of the Sun, I obtained $\Delta\nu_\odot = 135.01 \pm 0.05\,\mu$Hz (see Section 2.3.1). Given the large separation of the Sun and HD 52265, one can estimate the mean stellar density: $\overline{\rho} = (0.536 \pm 0.002)\,\overline{\rho}_\odot$. Hence the mean stellar density is known to a precision of 0.4%. To assess the quality of this seismic constraint, one can determine a non-seismic constraint on the mean density of HD 52265. Using the non-seismic estimates (spectroscopic) from Table 3.1, $M/M_\odot = 1.05 \pm 0.15$ and

Table 6.1: Estimated large and small separation for HD 52265 and other solar-like stars observed with CoRoT, Kepler, and ground-based telescopes. The typical length of the observations is 4-5 months for CoRoT, 6 weeks for Kepler, and 2 weeks for αCen A. When no (unambiguous) measurement of the small separation is possible, no value is given.

Object	Large separation $\Delta\nu$ [μHz]	Small separation $\delta\nu$ [μHz]	Reference
CoRoT:			
HD 52265	**98.84 ± 0.12**	**8.14 ± 0.20**	**this work (21 ≤ n ≤ 23, ℓ ≤ 2)**
HD 49933	85.9 ± 0.15	--	Appourchaux et al. (2008)
HD 181420	75.3 ± 0.1	--	Barban et al. (2009)
HD 181906	85.7 ± 2.3	--	García et al. (2009)
HD 49835	56.21 ± 0.19[1]	4.04 ± 0.26[1]	Deheuvels et al. (2010)
HD 181420	55.2 ± 0.8	--	Mathur et al. (2010)
Kepler:			
KIC 6603624	110.2 ± 0.6	4.7 ± 0.2	Chaplin et al. (2010)
KIC 3656476	94.1 ± 0.6	4.4 ± 0.2	Chaplin et al. (2010)
KIC 3656476	50.8 ± 0.3	4.3 ± 0.5	Chaplin et al. (2010)
Ground-based spectroscopy:			
αCen A	105.5 ± 0.1	5.6 ± 0.7	Bouchy and Carrier (2002)

[1] derived from individual frequency estimates given by Deheuvels et al. (2010)

$R/R_\odot = 1.255 \pm 0.033$, one obtains a mean stellar density of $\overline{\rho}_{ns} = (0.531 \pm 0.087)\overline{\rho}_\odot$. Asteroseismology improves the precision by a factor of about 40!

To illustrate the potential of the large and small frequency separations for the inference of the mass and the age of a star, Figure 6.1 shows the measurements of $\Delta\nu$ and $\delta\nu$ for the Sun and HD 52265 obtained in this work in an asteroseismic HR-diagram (cf. Section 1.3, Figure 1.2). The diagram shows stellar evolution tracks for stars with solar chemical abundance and various masses (solid lines), and lines of constant core hydrogen abundance (dotted lines). In this diagram, the measurements of $\Delta\nu$ and $\delta\nu$ for HD 52265 are consistent with a mass and an age that are known to a precision of ~ 3% and ~ 11% respectively. Since the chemical composition of HD 52265 is not the same as for the Sun, the mass and age of HD 52265 which may be extracted from Figure 6.1 are biased. Therefore, proper modeling is needed. However, similar error bars on mass and age are expected.

The modeling of HD 52265 is beyond the scope of this thesis. There exist several pipelines and codes to generate stellar models and compute their oscillation frequencies. Codes which are commonly used to compute stellar models and their oscillation frequencies are e.g. SEEK (Quirion et al. 2010), ASTEC (Christensen-Dalsgaard 2008a),
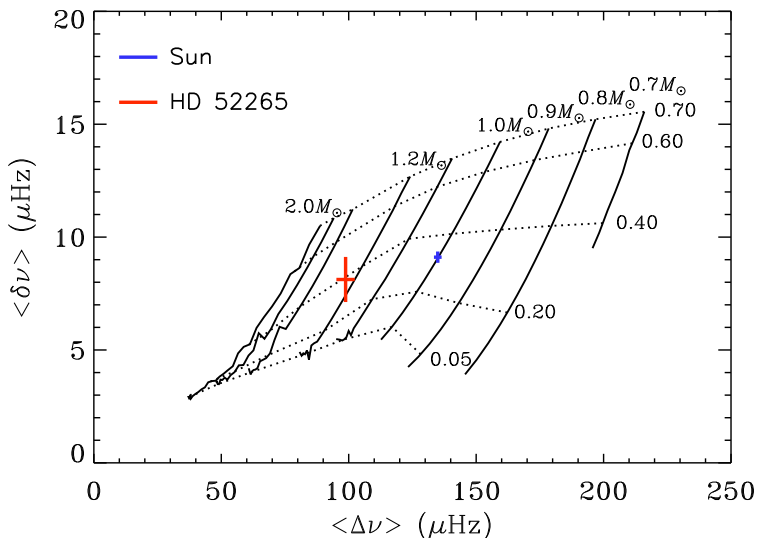
Figure 6.1: Asteroseismic HR-diagram using solar metallicity (cf. Figure 1.2) including constraints on the large and small separations for the Sun (*blue symbol*) and for HD 52265 (*red symbol*) determined in this work. The size of the symbols correspond to the measurement errors on the large separation, $\Delta\nu$ (30σ), and the small separation, $\delta\nu$ (5σ). The *solid lines* show stellar evolution tracks for stars with various masses and solar chemical composition. The *dotted lines* correspond to isopleths of constant central hydrogen abundance. The fraction of hydrogen at the star's center is indicated by the numbers at the right end of each line. HD 52265 is a overmetallic star and the stellar mass and the central hydrogen abundance cannot be inferred directly from the diagram without bias. [Asteroseismic HR-diagram courtesy of J. Christensen-Dalsgaard.]

CESAM (Morel and Lebreton 2008), TGEC (Eggenberger et al. 2008), YREC (Demarque et al. 2008), ADIPLS (Christensen-Dalsgaard 2008b), POSC (Monteiro 2008), and FILOU (Suárez and Goupil 2008). To infer fundamental stellar parameters like mass, radius, and age for an observed star from a grid of stellar models one has to find the best match of observation and model given a set of observed parameters. The set of observables includes non-seismic parameters like the effective temperature, T_{eff}, the surface gravity, $\log g$, and the metallicity, [Fe/H]. If available, the list of observables also includes seismic constraints, e.g. the large separation, $\Delta\nu$, and the small separation, $\delta\nu$.

The precision of seismic constraints on stellar fundamental parameters, e.g. mass, radius, and age, may be compared to the non-seismic constraints. Table 6.2 lists some random errors on the mass, radius, and age of HD 52265. Theses values are obtained from modeling by Quirion (private communication) and Creevey (private communica-

tion). For comparison, the table also lists the errors of the non-seismic constraints derived from the measurements in Table 3.1. With respect to the stellar age, Saffe et al. (2005) compared several classical methods to estimate the stellar age. They found that the most reliable and most precise methods, i.e. isochrones and chromospheric activity, achieve a precision of 30-50%. As shown for HD 52265, seismic age constraints provide a significant improvement by a factor of ~ 4. Concerning the mass of a star, Valenti and Fischer (2005) performed a spectroscopic analysis for 1040 F, G, and K dwarfs. They found that the relative uncertainties of the spectroscopic mass estimates and mass estimates derived from isochrones are typically of the order $10\% < \Delta M/M < 20\%$ (even though they quote an error of $\sim 4\%$ for HD 52265). In the particular case of HD 52265 the seismic mass estimate provides an improvement of a factor of ~ 5 compared to the spectroscopic mass estimate. The improvement on the radius estimate is still significant (at least given the result of Quirion), i.e. the relative error of the seismic constraints is reduced by a factor of ~ 2 compared to the spectroscopic estimate of Valenti and Fischer (2005). Precise and model-independent radius estimates are also expected from interferometry of nearby stars (e.g. Creevey et al. 2007) and in particular from GAIA astrometry (Perryman et al. 2001). As pointed out by Lebreton (2008), the precision of the luminosity of GAIA target stars at distances below 200 pc will be $\Delta L/L \leq 5.5\%$. Combined with temperatures derived from high-resolution spectroscopy ($\Delta T_{\text{eff}}/T_{\text{eff}} \sim 1\%$), stellar radii may be estimated with a precision of less than 2 %, i.e. comparable to the precision of the seismic constraint for HD 52265. In summary, Table 6.2 demonstrates that the consideration of seismic constraints for stellar modeling provides very significant improvements for the inference of stellar fundamental parameters.

The analysis of the CoRoT data of HD 52265 can be regarded as a case study demonstrating the potential of asteroseismic investigations based on high-quality space photometry. Recent studies of solar-like stars observed with CoRoT (e.g. Michel et al. 2008, Appourchaux et al. 2008, Barban et al. 2009, García et al. 2009, Deheuvels et al. 2010, Mathur et al. 2010) and first results from Kepler (Christensen-Dalsgaard et al. 2010, Chaplin et al. 2010) suggest that precise fundamental stellar parameters will be available for an increasing number of stars in the near future. The variety of different stars at different stages of their evolution will improve significantly the ability to generate realistic stellar models.

The very high quality of the CoRoT data of HD 52265 will allow one to constrain its inner structure beyond the determination of its mass, age, and radius. This may be achieved by considering individual mode frequencies instead of "only" mean large and small separations. As described in Section 1.4 sharp features in the sound-speed profile cause oscillations of the mode frequencies which can be measured for instance by means of the second difference $\Delta_2 \nu_{n\ell} = \nu_{n-1,\ell} - 2\nu_{n\ell} + \nu_{n+1,\ell}$. Such oscillations of the frequencies may allow one to measure the envelope helium abundance, the location of the helium ionization zones, and the bottom of the convection zone.

The mode frequencies of the Sun are affected by magnetic activity as it was confirmed in Section 2.3.1. Such frequency variations are non-negligible and are also expected in other solar-like stars. To search for stellar cycle effects one has to investigate if HD 52265 has a periodic cycle and in which phase of the cycle it was observed by CoRoT. Therefore it would be very useful to obtain at least one more CoRoT data set to correct the frequencies for stellar-cycle surface effects. Alternatively ground-based follow-up observations

Table 6.2: Random error on fundamental stellar parameters of HD 52265. Seismic constraints are obtained by Quirion (private communication) and Creevey (private communications). Both modelers use seismic ($\Delta\nu$, $\delta\nu$) and non-seismic observables (e.g. T_{eff}, [Fe/H]) to derive the stellar fundamental parameters. For comparison, non-seismic (spectroscopic) constraints from Table 3.1 are also listed. Note that the seismic constraints are not published yet so that only relative error estimates can be given here.

HD 52265: random errors on fundamental stellar parameters				
Parameter	seismic constraints			non-seismic constraints
	This work	Quirion*	Creevey*	from Table 3.1
Density: $\Delta\bar{\rho}/\bar{\rho}_\odot$ [%]	0.4	–	–	16
Mass: $\Delta M/M$ [%]	–	2.4	4.0	14 (4.2)†
Radius: $\Delta R/R$ [%]	–	1.5	2.7	2.6
Age: $\Delta\tau$ [Myr]	–	290	–	1100

* private communications; † from isochrone fits

of activity tracers like Ca II chromospheric emission could be used to determine the phase of the activity cycle of HD 52265. Cincunegui et al. (2007) observed Ca II and Hα activity proxies for 109 late type stars (including HD 52265) in a 7 year program at the CASLEO Argentinean Observatory. At the time of writing I do not have information as to whether this data is suited to examine HD 52265's activity. HD 52265 was not included in the Mt. Wilson survey on Ca II chromospheric emission by Henry et al. (1996).

A rough estimate on the expected period of the activity cycle of HD 52265 can be deduced from the relation of the rotation period, P_{rot}, and the period of the activity cycle, P_{cyc}, according to Noyes et al. (1984b):

$$\frac{P_{\text{cyc}}}{P_{\text{cyc},\odot}} \simeq \left(\frac{P_{\text{rot}}}{P_{\text{rot},\odot}}\frac{\tau_{c,\odot}}{\tau_c}\right)^{1.25}. \tag{6.1}$$

Here, τ_c denotes the convective turnover time over the convection zone. For HD 52265 the convective turnover time may be approximated by Equation (4) of Noyes et al. (1984a) using $(B - V) = 0.572$ (Perryman et al. 1997). Thus, I obtain $\tau_c = 11.5$ days. Using $P_{\text{rot}} = 11$ days as estimated in this work and the solar values $P_{\text{rot},\odot} = 25.4$ days and $\tau_{c,\odot} = 12.6$ days according to Noyes et al. (1984b), the expected activity cycle of HD 52265 becomes $P_{\text{cyc}} \approx 5$ years. According to this estimate ground-based follow-up observations of ~ 10 years would be required to study the activity cycle of HD 52265.

6.3 Asteroseismic constraint on the mass of the exoplanet HD 52265b

The analysis of the time series of HD 52265 presented in Chapter 3 allows us to constrain the absolute mass of its companion HD 52265b under certain assumptions. Figure 6.2 shows the asteroseismic constraints on the stellar angular velocity, Ω, versus the inclination angle, $\sin i$, of the stellar rotation axis (see Section 3.7.4). The *dark and light red regions* are deduced from the likelihood function. They contain 68% and 85% of the fits from the Monte Carlo simulation.

The seismic constraints on Ω and $\sin i$ are arranged along constant $\Omega \sin i$ and are in very good agreement with the independent estimate from spectroscopy (see Section 3.7.4). In addition, the seismic data analysis sets a limit on the angular velocity and the inclination of the rotation axis, i.e. $1.3 \leq \Omega/\Omega_\odot \leq 3.2$ and $i > 25°$. Combining the results of this work on $\Omega \sin i = 0.58^{+0.14}_{-0.13}\,\mu$Hz and the surface rotation $0.91\,\mu$Hz $\leq \Omega/2\pi \leq 1.07\,\mu$Hz, one obtains an estimate for the inclination angle of the rotation axis of $0.45 \leq \sin i \leq 0.82$ (result correspond to Fit A). Butler et al. (2006) determined a lower limit for the mass of the companion from radial velocity measurements, i.e. $M_p \sin i_p = 1.09 \pm 0.11\,\mathrm{M_{Jup}}$. Assuming that the spin axis of the star and the normal of the planetary orbit are co-aligned, i.e. $i = i_p$, one obtains an estimate on the true mass of HD 52265b:

$$1.3 \leq M_p/\mathrm{M_{Jup}} \leq 2.4 \tag{6.2}$$

I note that an analogue calculation using the estimates on $\Omega \sin i$ obtained for Fit B (see Section 3.7.4) would lead to a mass of HD 52265b of $1.4 \leq M_p/\mathrm{M_{Jup}} \leq 3.2$, i.e. consistent with the value given above. This mass constraint puts HD 52265b well below the mass limit of brown dwarfs, i.e. $M \leq 13\,\mathrm{M_{Jup}}$. A mass of $M \gtrsim 13\,\mathrm{M_{Jup}}$ is required to sustain thermonuclear processes like deuterium burning. This mass limit is the lowest limit to separate brown dwarfs and giant gas planets (see e.g. Burrows et al. 2001). Thus, the analysis of the solar-like p modes of the star HD 52265 suggests that its companion is a planet rather than a brown dwarf (see also Gizon et al. 2010a). This result contradicts the work of Han et al. (2001), who derived an inclination of $i \approx 178.5°$ based on Hipparcos intermediate astrometry. Such an inclination would correspond to a mass of $M_p \approx 42\,\mathrm{M_{Jup}}$. However, Pourbaix (2001) already pointed out that a systematic bias on the inclination angle towards small values of $\sin i$ (i.e. $i \approx 0°$ or $i \approx 180°$) is expected with Hipparcos intermediate astrometry when the spectroscopically constrained semi-major axis of the orbit, $a \sin i$, is smaller than the astrometric precision.

6.4 Other implications for the characterization of exoplanetary systems

Precise estimates of fundamental parameters of exoplanet host stars impact the characterization of the planet. From photometric planetary transits the ratio of the radii of the planet and the star can be deduced, i.e. $\Delta F/F = (R_p/R)^2$, where $\Delta F/F$ is the transit depth in the photometric signal. Here and below, the index (p) denotes the properties of the planet, quantities without index correspond to the host star. When the inclination i_p of the normal
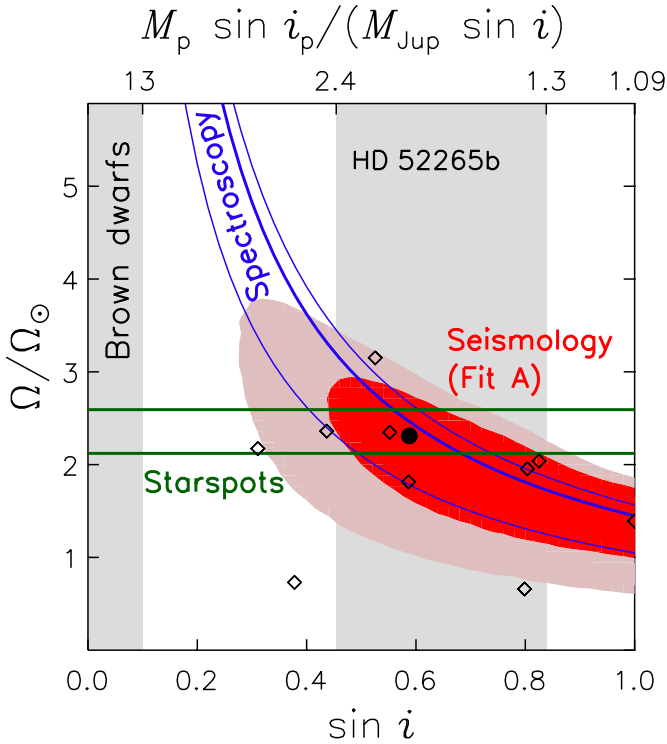
Figure 6.2: Asteroseismic constraint on the mass of the companion of HD 52265. The *filled circle* represents the estimate on the stellar angular velocity, Ω, in units of the Carrington value ($\Omega_\odot/2\pi = 0.424\,\mu$Hz) and the inclination angle, $\sin i$, of the rotation axis of HD 52265 (Fit A). These values are derived from a global fit of the HD 52265 oscillation power spectrum. The *red area* indicates the uncertainty on Ω and i deduced from the likelihood function and contains 68% (*dark-red*) and 85% (*light-red*) of all fits from the Monte Carlo simulation. The *diamonds* represent the results for Ω and i obtained by the other groups of the DAT. The *horizontal green lines* correspond to the low-frequency peaks in the power spectrum which are attributed to stellar surface rotation (see Section 3.3.2, Figure 3.5). The *blue lines* represent an alternative estimate on $\Omega \sin i \simeq v \sin i/R$, where $v \sin i$ is constrained by spectroscopy and R is derived from seismic modeling (see also Section 3.7.4). A lower limit for the mass of the companion HD 52265b was determined with radial velocity measurements, i.e. $M_{\rm p} \sin i_{\rm p} = 1.09 \pm 0.11\,{\rm M_{Jup}}$ (Butler et al. 2006). Here $i_{\rm p}$ is the inclination of the normal to the orbital plane of HD 52265b with respect to the line of sight. The mass is given in units of the Jupiter mass $M_{\rm Jup}$. Thus, the inclination angle of the rotation axis, i.e. the x-axis, may be interpreted as the mass, $M_{\rm p}$ of the HD 52265b in units of $M_{\rm Jup} \sin i/\sin i_{\rm p}$. Assuming $i = i_{\rm p}$, the upper x-axis gives the absolute mass of HD 52265b, suggesting that it is a planet and not a brown dwarf as indicated by the *grey shaded regions*.

to the orbital plane with respect to the line of sight is known from the transit measurement, spectroscopic follow-up observations allow one to solve Kepler's laws, such that the mass function, $(M_p/M)^{2/3}$, can be determined with a precision of a few percent. The two relations demonstrate that the precision of the mass and radius of the planet crucially depends on the precision of the mass and radius estimates of the host star. Furthermore, the modeling of the evolution of exoplanetary systems require precise constraints on the age of the system, i.e. the age of the host star. In Section 6.2, I showed that asteroseismology provides improved estimates on these parameters compared to classical methods, in particular considering the stellar mass and age.

The assumption of the spin-orbit alignment, $i = i_p$, to determine the mass of HD 52265b in the previous section is a very strong assumption which does not necessarily has to apply in the case of HD 52265. In fact, the measurement of the spin-orbit angle has become an important topic in the field of exoplanet research. According to the current state of the evolution of exoplanetary systems, giant gas planets are believed to form in the outer regions ($\sim$ 5 AU) of the circumstellar disc of the central star and later migrate towards it and become a "hot Jupiter". There are several scenarios describing the migration process which try to model the actual distribution of of eccentricities and semi-major axis of the orbits of hot Jupiters. The "classical" disc-migration scenario proposed by Lin et al. (1996) results in planet orbits which are co-aligned with the stellar equator. On the other hand scenarios like the Kozai cycles (Kozai 1962, Wu and Murray 2003) and planet scattering (Rasio and Ford 1996) allow for a misalignment of the stellar spin axis and the normal to the planetary orbit. The measurement of the spin-orbit angle may favor one of these scenarios and may help to constrain the theoretical modeling of the evolution of exoplanetary systems. The *true* spin-orbit angle, ψ, is given by (see e.g. Fabrycky and Winn 2009, Winn et al. 2009b)

$$\cos\psi = \cos i \cos i_p + \sin i \sin i_p \cos \lambda, \qquad (6.3)$$

where λ is the *sky-projected* spin-orbit angle. The measurement of the spin-orbit angle ψ requires an estimate of the inclination angle of the rotation axis of the host star. It was shown in this work, that the analysis of the time series of solar-like oscillations may in principle provide such an estimate on i. The inclination, i_p, of the normal to the planet's orbit and the sky-projected spin-orbit angle, λ, can be derived from planetary transits. The parameter λ can be measured with the Rossiter-McLaughlin (RM) effect (Rossiter 1924, McLaughlin 1924), i.e. the apparent shift of a spectral line while the planet transits its host star. When the planet occults a part of the star that forms, for example, the blue wing of the spectral line, this components is partially removed and the spectral line appears to be red-shifted and vice versa. For a detailed description of the measurement of λ, see for instance Gaudi and Winn (2007). In recent years, the sky-projected spin-orbit angle was measured for several systems. The first successful measurement of λ for HD 20958 suggested a fairly co-aligned system (Queloz et al. 2000, Winn et al. 2005). Recent studies reported on several transit systems which show a significant spin-orbit misalignment, e.g. HD 80606 (Moutou et al. 2009, Winn et al. 2009a), XO-3 (Hébrard et al. 2008, Winn et al. 2009c), CoRoT-3b (Triaud et al. 2009), and WASP 14b (Johnson et al. 2009). Winn et al. (2009b) even found that the planet HAT-P-7 is in a retrograde orbit around its host star, i.e. the orbital motion of the planet is opposite to the stellar rotation. Based on measurements of λ and reasonable assumptions on the distribution of the inclination angle of

the star's rotation axis, Fabrycky and Winn (2009) found that there may be two populations of planetary systems, one population where the planet orbit and the stellar equator is coplanar, and one population with a significant spin-orbit misalignment. The most recent study of Triaud et al. (2010) comprises all 26 known planetary systems where λ could be measured so far. Assuming a uniform distribution for $\cos i$, i.e. the inclination of the stellar rotation axis, they conclude that $\psi > 20°$ for 80% of the "hot Jupiters". I note again that these results are based on assumptions on the distribution of the stellar spin axis. As shown in this work, asteroseismology is in principle able to provide real measurements of the inclination of the stellar rotation axis such that true measurements of the spin-orbit angle, ψ, are feasible.

There is no transit measurement for HD 52265. Thus, a measurement of ψ for this system is not possible. However, the analysis of the CoRoT time series of HD 52265 reveals the potential of asteroseismology to supplement the characterization of planetary systems. The primary objective of the Kepler mission is the detection of planets with the transit method (e.g. Borucki et al. 2010). At the same time, the data may be used for an asteroseismic investigation of the observed stars (e.g. Christensen-Dalsgaard et al. 2008, Gilliland et al. 2010). Combined with spectroscopic follow-up observations this will improve constraints on the fundamental parameters of the observed planets, in particular their mass and age. The first seismic studies of planet host stars among the Kepler targets presented by Christensen-Dalsgaard et al. (2010) look very promising. In particular, the object HAT-P-7 provides both the planetary transit and a clear spectrum of solar-like oscillations.

The possibility of combining planetary transit measurements with asteroseismic investigations of their host stars will be taken to the next level if PLATO (e.g. Catala 2009) will be selected as an ESA M-class mission in late 2011 (the planned launch would be around 2018). The objective of PLATO is the characterization of planetary systems and the study of their evolution. For this purpose PLATO will observe 30000 cool dwarfs with $V \leq 11$ for which a detailed asteroseismic analysis will be feasible. Combining the precise results on the stellar mass and age from seismology with the information obtained from the transits and the follow-up observations (e.g. ground-based spectroscopy and GAIA astrometry), mass and radius estimates of the planets with a precision of $\sim 2\%$ and an age within a few hundred million years will become feasible.

6.5   On ground-based observations for asteroseismology

Space telescopes like CoRoT and Kepler provide long and nearly uninterrupted time series. The gaps are so short that they may be interpolated efficiently, e.g. with the inpainting method (e.g. Sato et al. 2010). However, for long-term observations from ground, gaps in the time series can hardly be avoided. Ground-based spectroscopic observations will remain irreplaceable for asteroseismology. The signal-to-noise ratio of radial velocity measurement is significantly higher than for photometry and for the foreseeable future, there will be no space-based spectrograph available. Thus, there will still be a request for proper analysis methods of gapped time series as it was presented in Chapter 4 and 5.

Interruptions in observations are particularly a problem for single-site observations where the duty cycle is typically of the order of $\lesssim$ 50%. With respect to solar-like

stars there are several examples of single- and two-site observations. Of particular interest is α Cen A which was observed several times with high resolution spectrographs like CORALIE (Bouchy and Carrier 2002), VLT/UVES and AAT/UCLES (Butler et al. 2004, Bedding et al. 2004), and HARPS (Bazot et al. 2007), as well as in photometry with the WIRE space telescope (Fletcher et al. 2006). These time series comprise observations with a length ranging from $3 - 5$ days (VLT/UVES, AAT/UCLES) up to 50 days (WIRE) and duty cycles ranging from 15% (WIRE) up to about 50% (HARPS).

Interruptions are also an issue for multi-site campaigns and global observation networks like BiSON and GONG. For instance, the solar-like star Procoyon was observed in a multi-site spectroscopic campaign including 11 ground-based telescopes (Arentoft et al. 2008, Bedding et al. 2010). Despite the high number of telescopes the three week observation still contained gaps such that a sidelobe-optimized weighting of the data had to be applied in order to extract the seismic information with the highest possible precision. Concerning observation networks, BiSON achieves a duty cycle of $\lesssim 80\%$ at best in long-term on a yearly basis (Chaplin et al. 1996). This amount of gaps must not be ignored in the data analysis. The soon to be launched SONG network (e.g. Grundahl et al. 2008) consists of eight telescope nodes installed at different longitudes. It is expected to achieve a comparable performance regarding the duty cycle of the observations. SONG will perform radial velocity measurements of selected targets over an extended period of ~ 4 months. The SONG data should benefit from the application of the Maximum Likelihood Estimation of gapped time series presented in this work.

Bibliography

Abramowitz, M., Stegun, I. A., 1965, Handbook of mathematical functions with formulas, graphs, and mathematical tables

Aerts, C., Christensen-Dalsgaard, J., Kurtz, D. W., 2010, Asteroseismology, Springer

Anderson, E. R., Duvall, Jr., T. L., Jefferies, S. M., 1990, Modeling of solar oscillation power spectra, ApJ, 364, 699

Appourchaux, T., Gizon, L., Rabello-Soares, M.-C., 1998, The art of fitting p-mode spectra. I. Maximum likelihood estimation, A&AS, 132, 107

Appourchaux, T., Chang, H.-Y., Gough, D. O., Sekii, T., 2000, On measuring low-degree p-mode frequency splitting with full-disc integrated data, MNRAS, 319, 365

Appourchaux, T., Michel, E., Auvergne, M., Baglin, A., Toutain, T., Baudin, F., Benomar, O., Chaplin, W. J., Deheuvels, S., Samadi, R., Verner, G. A., Boumier, P., García, R. A., Mosser, B., Hulot, J., Ballot, J., Barban, C., Elsworth, Y., Jiménez-Reyes, S. J., Kjeldsen, H., Régulo, C., Roxburgh, I. W., 2008, CoRoT sounds the stars: p-mode parameters of Sun-like oscillations on HD 49933, A&A, 488, 705

Appourchaux, T., Belkacem, K., Broomhall, A., Chaplin, W. J., Gough, D. O., Houdek, G., Provost, J., Baudin, F., Boumier, P., Elsworth, Y., García, R. A., Andersen, B. N., Finsterle, W., Fröhlich, C., Gabriel, A., Grec, G., Jiménez, A., Kosovichev, A., Sekii, T., Toutain, T., Turck-Chièze, S., 2010, The quest for the solar g modes, A&A Rev., 18, 197

Arentoft, T., Kjeldsen, H., Bedding, T. R., Bazot, M., Christensen-Dalsgaard, J., Dall, T. H., Karoff, C., Carrier, F., Eggenberger, P., Sosnowska, D., Wittenmyer, R. A., Endl, M., Metcalfe, T. S., Hekker, S., Reffert, S., Butler, R. P., Bruntt, H., Kiss, L. L., O'Toole, S. J., Kambe, E., Ando, H., Izumiura, H., Sato, B., Hartmann, M., Hatzes, A., Bouchy, F., Mosser, B., Appourchaux, T., Barban, C., Berthomieu, G., Garcia, R. A., Michel, E., Provost, J., Turck-Chièze, S., Martić, M., Lebrun, J., Schmitt, J., Bertaux, J., Bonanno, A., Benatti, S., Claudi, R. U., Cosentino, R., Leccia, S., Frandsen, S., Brogaard, K., Glowienka, L., Grundahl, F., Stempels, E., 2008, A Multisite Campaign to Measure Solar-like Oscillations in Procyon. I. Observations, Data Reduction, and Slow Variations, ApJ, 687, 1180

Baglin, A., Auvergne, M., Barge, P., Deleuil, M., Catala, C., Michel, E., Weiss, W., The COROT Team, 2006, Scientific Objectives for a Minisat: CoRoT, in ESA Special Publication, (Ed.) M. Fridlund, A. Baglin, J. Lochard, & L. Conroy, vol. 1306 of ESA Special Publication, pp. 33

145

Ballot, J., Turck-Chièze, S., García, R. A., 2004, Seismic extraction of the convective extent in solar-like stars. The observational point of view, A&A, 423, 1051

Ballot, J., García, R. A., Lambert, P., 2006, Rotation speed and stellar axis inclination from p modes: how CoRoT would see other suns, MNRAS, 369, 1281

Ballot, J., Appourchaux, T., Toutain, T., Guittet, M., 2008, On deriving p-mode parameters for inclined solar-like stars, A&A, 486, 867

Ballot, J., Gizon, L., Samadi, R., Vauclair, G., Benomar, O., Bruntt, H., Campante, T. L., García, R. A., Stahn, T., Verner, G. A., Appourchaux, T., Baudin, F., Chaplin, W. J., Creevey, O., Deheuvels, S., Nolez, N., Gaulme, P., Mathur, S., Michel, E., Mosser, B., Régulo, C., Salabert, D., Sato, K., Auvergne, M., Baglin, A., Bazot, M., Catala, C., Roxburgh, I. W., Vauclair, S., CoRoT Data Analysis Team, 2010, CoRoT observations of solar-like oscillations in the overmetallic cool dwarf HD52265, HELAS IV International Conference, Lanzarote, poster

Ballot, J., Gizon, L., Samadi, R., Vauclair, G., Benomar, O., Bruntt, H., Mosser, B., Stahn, T., Verner, G. A., Campante, T. L., García, R. A., Mathur, S., Salabert, D., Gaulme, P., Régulo, C., Roxburgh, I. W., Appourchaux, T., Baudin, F., Catala, C., Chaplin, W. J., Deheuvels, S., Michel, E., Bazot, M., Creevey, O., Dolez, N., Elsworth, Y., Sato, K. H., Vauclair, S., Auvergne, M., Baglin, A., 2011, Accurate p-mode measurements of the G0V metal-rich CoRoT target HD 52265, A&A, 530, A97

Barban, C., Deheuvels, S., Baudin, F., Appourchaux, T., Auvergne, M., Ballot, J., Boumier, P., Chaplin, W. J., García, R. A., Gaulme, P., Michel, E., Mosser, B., Régulo, C., Roxburgh, I. W., Verner, G., Baglin, A., Catala, C., Samadi, R., Bruntt, H., Elsworth, Y., Mathur, S., 2009, Solar-like oscillations in HD 181420: data analysis of 156 days of CoRoT data, A&A, 506, 51

Basu, S., Mazumdar, A., Antia, H. M., Demarque, P., 2004, Asteroseismic determination of helium abundance in stellar envelopes, MNRAS, 350, 277

Bazot, M., Bouchy, F., Kjeldsen, H., Charpinet, S., Laymand, M., Vauclair, S., 2007, Asteroseismology of α Centauri A. Evidence of rotational splitting, A&A, 470, 295

Bedding, T. R., Kjeldsen, H., 2007, Observations of solar-like oscillations, Communications in Asteroseismology, 150, 106

Bedding, T. R., Kjeldsen, H., Butler, R. P., McCarthy, C., Marcy, G. W., O'Toole, S. J., Tinney, C. G., Wright, J. T., 2004, Oscillation Frequencies and Mode Lifetimes in α Centauri A, ApJ, 614, 380

Bedding, T. R., Kjeldsen, H., Campante, T. L., Appourchaux, T., Bonanno, A., Chaplin, W. J., Garcia, R. A., Martić, M., Mosser, B., Butler, R. P., Bruntt, H., Kiss, L. L., O'Toole, S. J., Kambe, E., Ando, H., Izumiura, H., Sato, B., Hartmann, M., Hatzes, A., Barban, C., Berthomieu, G., Michel, E., Provost, J., Turck-Chièze, S., Lebrun, J., Schmitt, J., Bertaux, J., Benatti, S., Claudi, R. U., Cosentino, R., Leccia, S., Frandsen, S., Brogaard, K., Glowienka, L., Grundahl, F., Stempels, E., Arentoft, T., Bazot, M.,

Christensen-Dalsgaard, J., Dall, T. H., Karoff, C., Lundgreen-Nielsen, J., Carrier, F., Eggenberger, P., Sosnowska, D., Wittenmyer, R. A., Endl, M., Metcalfe, T. S., Hekker, S., Reffert, S., 2010, A Multi-Site Campaign to Measure Solar-Like Oscillations in Procyon. II. Mode Frequencies, ApJ, 713, 935

Borucki, W. J., Koch, D., Basri, G., Batalha, N., Brown, T., Caldwell, D., Caldwell, J., Christensen-Dalsgaard, J., Cochran, W. D., DeVore, E., Dunham, E. W., Dupree, A. K., Gautier, T. N., Geary, J. C., Gilliland, R., Gould, A., Howell, S. B., Jenkins, J. M., Kondo, Y., Latham, D. W., Marcy, G. W., Meibom, S., Kjeldsen, H., Lissauer, J. J., Monet, D. G., Morrison, D., Sasselov, D., Tarter, J., Boss, A., Brownlee, D., Owen, T., Buzasi, D., Charbonneau, D., Doyle, L., Fortney, J., Ford, E. B., Holman, M. J., Seager, S., Steffen, J. H., Welsh, W. F., Rowe, J., Anderson, H., Buchhave, L., Ciardi, D., Walkowicz, L., Sherry, W., Horch, E., Isaacson, H., Everett, M. E., Fischer, D., Torres, G., Johnson, J. A., Endl, M., MacQueen, P., Bryson, S. T., Dotson, J., Haas, M., Kolodziejczak, J., Van Cleve, J., Chandrasekaran, H., Twicken, J. D., Quintana, E. V., Clarke, B. D., Allen, C., Li, J., Wu, H., Tenenbaum, P., Verner, E., Bruhweiler, F., Barnes, J., Prsa, A., 2010, Kepler Planet-Detection Mission: Introduction and First Results, Science, 327, 977

Bouchy, F., Carrier, F., 2002, The acoustic spectrum of alpha Cen A, A&A, 390, 205

Brandt, S., 1970, Statistical and computational methods in data analysis, Amsterdam: North-Holland, and New York: American Elsevier Publication Co., 1970

Broomhall, A., Chaplin, W. J., Davies, G. R., Elsworth, Y., Fletcher, S. T., Hale, S. J., Miller, B., New, R., 2009, Definitive Sun-as-a-star p-mode frequencies: 23 years of BiSON observations, MNRAS, 396, L100

Burrows, A., Hubbard, W. B., Lunine, J. I., Liebert, J., 2001, The theory of brown dwarfs and extrasolar giant planets, Reviews of Modern Physics, 73, 719

Butler, R. P., Vogt, S. S., Marcy, G. W., Fischer, D. A., Henry, G. W., Apps, K., 2000, Planetary Companions to the Metal-rich Stars BD -10°3166 and HD 52265, ApJ, 545, 504

Butler, R. P., Bedding, T. R., Kjeldsen, H., McCarthy, C., O'Toole, S. J., Tinney, C. G., Marcy, G. W., Wright, J. T., 2004, Ultra-High-Precision Velocity Measurements of Oscillations in α Centauri A, ApJ, 600, L75

Butler, R. P., Wright, J. T., Marcy, G. W., Fischer, D. A., Vogt, S. S., Tinney, C. G., Jones, H. R. A., Carter, B. D., Johnson, J. A., McCarthy, C., Penny, A. J., 2006, Catalog of Nearby Exoplanets, ApJ, 646, 505

Carrier, F., Eggenberger, P., 2006, Asteroseismology of the visual binary 70 Ophiuchi, A&A, 450, 695

Carrington, R. C., 1863, Observations of the spots of the sun from november 9, 1853, to march 24, 1861, made ar redhill, london/edinburgh

Catala, C., 2009, PLATO: PLAnetary Transits and Oscillations of stars, Experimental Astronomy, 23, 329

Chaplin, W. J., Elsworth, Y., Howe, R., Isaak, G. R., McLeod, C. P., Miller, B. A., van der Raay, H. B., Wheeler, S. J., New, R., 1996, BiSON Performance, Sol. Phys., 168, 1

Chaplin, W. J., Elsworth, Y., Isaak, G. R., McLeod, C. P., Miller, B. A., New, R., 1997, Solar p-mode linewidths from recent BiSON helioseismological data, MNRAS, 288, 623

Chaplin, W. J., Elsworth, Y., Isaak, G. R., Lines, R., McLeod, C. P., Miller, B. A., New, R., 1998, Solar p-mode excitation: further insight from recent low-l BiSON helioseismological data, MNRAS, 298, L7

Chaplin, W. J., Appourchaux, T., Elsworth, Y., Isaak, G. R., New, R., 2001, The phenomenology of solar-cycle-induced acoustic eigenfrequency variations: a comparative and complementary analysis of GONG, BiSON and VIRGO/LOI data, MNRAS, 324, 910

Chaplin, W. J., Elsworth, Y., Miller, B. A., Verner, G. A., New, R., 2007, Solar p-Mode Frequencies over Three Solar Cycles, ApJ, 659, 1749

Chaplin, W. J., Appourchaux, T., Elsworth, Y., García, R. A., Houdek, G., Karoff, C., Metcalfe, T. S., Molenda-Żakowicz, J., Monteiro, M. J. P. F. G., Thompson, M. J., Brown, T. M., Christensen-Dalsgaard, J., Gilliland, R. L., Kjeldsen, H., Borucki, W. J., Koch, D., Jenkins, J. M., Ballot, J., Basu, S., Bazot, M., Bedding, T. R., Benomar, O., Bonanno, A., Brandão, I. M., Bruntt, H., Campante, T. L., Creevey, O. L., Di Mauro, M. P., Doğan, G., Dreizler, S., Eggenberger, P., Esch, L., Fletcher, S. T., Frandsen, S., Gai, N., Gaulme, P., Handberg, R., Hekker, S., Howe, R., Huber, D., Korzennik, S. G., Lebrun, J. C., Leccia, S., Martic, M., Mathur, S., Mosser, B., New, R., Quirion, P., Régulo, C., Roxburgh, I. W., Salabert, D., Schou, J., Sousa, S. G., Stello, D., Verner, G. A., Arentoft, T., Barban, C., Belkacem, K., Benatti, S., Biazzo, K., Boumier, P., Bradley, P. A., Broomhall, A., Buzasi, D. L., Claudi, R. U., Cunha, M. S., D'Antona, F., Deheuvels, S., Derekas, A., García Hernández, A., Giampapa, M. S., Goupil, M. J., Gruberbauer, M., Guzik, J. A., Hale, S. J., Ireland, M. J., Kiss, L. L., Kitiashvili, I. N., Kolenberg, K., Korhonen, H., Kosovichev, A. G., Kupka, F., Lebreton, Y., Leroy, B., Ludwig, H., Mathis, S., Michel, E., Miglio, A., Montalbán, J., Moya, A., Noels, A., Noyes, R. W., Pallé, P. L., Piau, L., Preston, H. L., Roca Cortés, T., Roth, M., Sato, K. H., Schmitt, J., Serenelli, A. M., Silva Aguirre, V., Stevens, I. R., Suárez, J. C., Suran, M. D., Trampedach, R., Turck-Chièze, S., Uytterhoeven, K., Ventura, R., Wilson, P. A., 2010, The Asteroseismic Potential of Kepler: First Results for Solar-Type Stars, ApJ, 713, L169

Christensen-Dalsgaard, J., 1984, What Will Asteroseismology Teach us, in Space Research in Stellar Activity and Variability, (Ed.) A. Mangeney & F. Praderie, pp. 11

Christensen-Dalsgaard, J., 1988, A Hertzsprung-Russell Diagram for Stellar Oscillations, in Advances in Helio- and Asteroseismology, (Ed.) J. Christensen-Dalsgaard & S. Frandsen, vol. 123 of IAU Symposium, pp. 295

Christensen-Dalsgaard, J., 1993, On the Asteroseismic HR Diagram, in GONG 1992. Seismic Investigation of the Sun and Stars, (Ed.) T. M. Brown, vol. 42 of Astronomical Society of the Pacific Conference Series, pp. 347

Christensen-Dalsgaard, J., 2002, Helioseismology, Reviews of Modern Physics, 74, 1073

Christensen-Dalsgaard, J., 2008a, ASTEC – the Aarhus STellar Evolution Code, Ap&SS, 316, 13

Christensen-Dalsgaard, J., 2008b, ADIPLS – the Aarhus adiabatic oscillation package, Ap&SS, 316, 113

Christensen-Dalsgaard, J., Dappen, W., Ajukov, S. V., Anderson, E. R., Antia, H. M., Basu, S., Baturin, V. A., Berthomieu, G., Chaboyer, B., Chitre, S. M., Cox, A. N., Demarque, P., Donatowicz, J., Dziembowski, W. A., Gabriel, M., Gough, D. O., Guenther, D. B., Guzik, J. A., Harvey, J. W., Hill, F., Houdek, G., Iglesias, C. A., Kosovichev, A. G., Leibacher, J. W., Morel, P., Proffitt, C. R., Provost, J., Reiter, J., Rhodes, Jr., E. J., Rogers, F. J., Roxburgh, I. W., Thompson, M. J., Ulrich, R. K., 1996, The Current State of Solar Modeling, Science, 272, 1286

Christensen-Dalsgaard, J., Arentoft, T., Brown, T. M., Gilliland, R. L., Kjeldsen, H., Borucki, W. J., Koch, D., 2008, The Kepler asteroseismic investigation, Journal of Physics Conference Series, 118, 012 039

Christensen-Dalsgaard, J., Kjeldsen, H., Brown, T. M., Gilliland, R. L., Arentoft, T., Frandsen, S., Quirion, P., Borucki, W. J., Koch, D., Jenkins, J. M., 2010, Asteroseismic Investigation of Known Planet Hosts in the Kepler Field, ApJ, 713, L164

Cincunegui, C., Díaz, R. F., Mauas, P. J. D., 2007, Hα and the Ca II H and K lines as activity proxies for late-type stars, A&A, 469, 309

Cox, J. P., 1980, Theory of stellar pulsation, Research supported by the National Science Foundation Princeton, NJ, Princeton University Press, 1980.

Creevey, O. L., Monteiro, M. J. P. F. G., Metcalfe, T. S., Brown, T. M., Jiménez-Reyes, S. J., Belmonte, J. A., 2007, The Complementary Roles of Interferometry and Asteroseismology in Determining the Mass of Solar-Type Stars, ApJ, 659, 616

Cuypers, J., 1987, vol. 3, p. 21, Brussel: Palais der Academien, medelingen van de koninklijke academie voor wetenschappen, letteren en schone kunsten van belgie edn.

De Ridder, J., Barban, C., Carrier, F., Mazumdar, A., Eggenberger, P., Aerts, C., Deruyter, S., Vanautgaerden, J., 2006, Discovery of solar-like oscillations in the red giant ε Ophiuchi, A&A, 448, 689

Deheuvels, S., Bruntt, H., Michel, E., Barban, C., Verner, G., Régulo, C., Mosser, B., Mathur, S., Gaulme, P., Garcia, R. A., Boumier, P., Appourchaux, T., Samadi, R., Catala, C., Baudin, F., Baglin, A., Auvergne, M., Roxburgh, I. W., Pérez Hernández, F., 2010, Seismic and spectroscopic characterization of the solar-like pulsating CoRoT target HD 49385, A&A, 515, A87

Demarque, P., Guenther, D. B., Li, L. H., Mazumdar, A., Straka, C. W., 2008, YREC: the Yale rotating stellar evolution code. Non-rotating version, seismology applications, Ap&SS, 316, 31

Donahue, R. A., 1993, Surface differential rotation in a sample of cool dwarf stars, Ph.D. thesis, New Mexico State Univ., University Park.

Duvall, Jr., T. L., Harvey, J. W., 1986, Solar Doppler shifts - Sources of continuous spectra, in NATO ASIC Proc. 169: Seismology of the Sun and the Distant Stars, (Ed.) D. O. Gough, pp. 105

Duvall, Jr., T. L., Jefferies, S. M., Harvey, J. W., Osaki, Y., Pomerantz, M. A., 1993, Asymmetries of solar oscillation line profiles, ApJ, 410, 829

Eggenberger, P., Meynet, G., Maeder, A., Hirschi, R., Charbonnel, C., Talon, S., Ekström, S., 2008, The Geneva stellar evolution code, Ap&SS, 316, 43

Fabrycky, D. C., Winn, J. N., 2009, Exoplanetary Spin-Orbit Alignment: Results from the Ensemble of Rossiter-McLaughlin Observations, ApJ, 696, 1230

Fletcher, S. T., Chaplin, W. J., Elsworth, Y., Schou, J., Buzasi, D., 2006, Frequency, splitting, linewidth and amplitude estimates of low-l p modes of α Cen A: analysis of Wide-Field Infrared Explorer photometry, MNRAS, 371, 935

Fossat, E., Kholikov, S., Gelly, B., Schmider, F. X., Fierry-Fraillon, D., Grec, G., Palle, P., Cacciani, A., Ehgamberdiev, S., Hoeksema, J. T., Lazrek, M., 1999, Full disk helioseismology: repetitive music and the question of gap filling, A&A, 343, 608

Frandsen, S., Carrier, F., Aerts, C., Stello, D., Maas, T., Burnet, M., Bruntt, H., Teixeira, T. C., de Medeiros, J. R., Bouchy, F., Kjeldsen, H., Pijpers, F., Christensen-Dalsgaard, J., 2002, Detection of Solar-like oscillations in the G7 giant star xi Hya, A&A, 394, L5

Fröhlich, C., Romero, J., Roth, H., Wehrli, C., Andersen, B. N., Appourchaux, T., Domingo, V., Telljohann, U., Berthomieu, G., Delache, P., Provost, J., Toutain, T., Crommelynck, D. A., Chevalier, A., Fichot, A., Däppen, W., Gough, D., Hoeksema, T., Jiménez, A., Gómez, M. F., Herreros, J. M., Cortés, T. R., Jones, A. R., Pap, J. M., Willson, R. C., 1995, VIRGO: Experiment for Helioseismology and Solar Irradiance Monitoring, Sol. Phys., 162, 101

Fröhlich, C., Andersen, B. N., Appourchaux, T., Berthomieu, G., Crommelynck, D. A., Domingo, V., Fichot, A., Finsterle, W., Gomez, M. F., Gough, D., Jimenez, A., Leifsen, T., Lombaerts, M., Pap, J. M., Provost, J., Cortes, T. R., Romero, J., Roth, H., Sekii, T., Telljohann, U., Toutain, T., Wehrli, C., 1997, First Results from VIRGO, the Experiment for Helioseismology and Solar Irradiance Monitoring on SOHO, Sol. Phys., 170, 1

Gabriel, A. H., Charra, J., Grec, G., Robillot, J., Roca Cortés, T., Turck-Chièze, S., Ulrich, R., Basu, S., Baudin, F., Bertello, L., Boumier, P., Charra, M., Christensen-Dalsgaard, J., Decaudin, M., Dzitko, H., Foglizzo, T., Fossat, E., García, R. A., Herreros, J. M., Lazrek, M., Pallé, P. L., Pétrou, N., Renaud, C., Régulo, C., 1997, Performance and

Early Results from the GOLF Instrument Flown on the SOHO Mission, Sol. Phys., 175, 207

Gabriel, M., 1994, The probability-density function of a Fourier line, A&A, 287, 685

García, R. A., Régulo, C., Samadi, R., Ballot, J., Barban, C., Benomar, O., Chaplin, W. J., Gaulme, P., Appourchaux, T., Mathur, S., Mosser, B., Toutain, T., Verner, G. A., Auvergne, M., Baglin, A., Baudin, F., Boumier, P., Bruntt, H., Catala, C., Deheuvels, S., Elsworth, Y., Jiménez-Reyes, S. J., Michel, E., Pérez Hernández, F., Roxburgh, I. W., Salabert, D., 2009, Solar-like oscillations with low amplitude in the CoRoT target HD 181906, A&A, 506, 41

Gaudi, B. S., Winn, J. N., 2007, Prospects for the Characterization and Confirmation of Transiting Exoplanets via the Rossiter-McLaughlin Effect, ApJ, 655, 550

Gelly, B., Lazrek, M., Grec, G., Ayad, A., Schmider, F. X., Renaud, C., Salabert, D., Fossat, E., 2002, Solar p-modes from 1979 days of the GOLF experiment, A&A, 394, 285

Gilliland, R. L., Jenkins, J. M., Borucki, W. J., Bryson, S. T., Caldwell, D. A., Clarke, B. D., Dotson, J. L., Haas, M. R., Hall, J., Klaus, T., Koch, D., McCauliff, S., Quintana, E. V., Twicken, J. D., van Cleve, J. E., 2010, Initial Characteristics of Kepler Short Cadence Data, ApJ, 713, L160

Gillon, M., Magain, P., 2006, High precision determination of the atmospheric parameters and abundances of the COROT main targets, A&A, 448, 341

Gizon, L., Birch, A. C., 2005, Local Helioseismology, Living Reviews in Solar Physics, 2, 6

Gizon, L., Solanki, S. K., 2003, Determining the Inclination of the Rotation Axis of a Sun-like Star, ApJ, 589, 1009

Gizon, L., Ballot, J., Catala, C., Stahn, T., Vauclair, G., Appourchaux, T., Auvergne, M., Baglin, A., Baudin, F., Bazot, M., Benomar, O., Bruntt, H., Campante, T. L., Chaplin, W. J., Creevey, O., Deheuvels, S., Nolez, N. García, R. A., Gaulme, P., Mathur, S., Michel, E., Mosser, B., Régulo, C., Roxburgh, I. W., Salabert, D., Samadi, R., Sato, K., Vauclair, S., Verner, G. A., Catala, C., CoRoT Data Analysis Team, 2010a, Asteroseismic constraint on the mass of the planet orbiting the CoRoT Sun-like star HD 52265, HELAS IV International Conference, Lanzarote, poster

Gizon, L., Birch, A. C., Spruit, H. C., 2010b, Local Helioseismology: Three-Dimensional Imaging of the Solar Interior, ARA&A, 48, 289

Goldreich, P., Keeley, D. A., 1977, Solar seismology. II - The stochastic excitation of the solar p-modes by turbulent convection, ApJ, 212, 243

Goldreich, P., Murray, N., Kumar, P., 1994, Excitation of solar p-modes, ApJ, 424, 466

Gonzalez, G., Laws, C., Tyagi, S., Reddy, B. E., 2001, Parent Stars of Extrasolar Planets. VI. Abundance Analyses of 20 New Systems, AJ, 121, 432

Gough, D. O., 1986, EBK Quantization of Stellar Waves, in Hydrodynamic and Magnetodynamic Problems in the Sun and Stars, (Ed.) Y. Osaki, pp. 117

Gough, D. O., 1990, Comments on Helioseismic Inference, in Progress of Seismology of the Sun and Stars, (Ed.) Y. Osaki & H. Shibahashi, vol. 367 of Lecture Notes in Physics, Berlin Springer Verlag, pp. 283

Gough, D. O., Kosovichev, A. G., Toomre, J., Anderson, E., Antia, H. M., Basu, S., Chaboyer, B., Chitre, S. M., Christensen-Dalsgaard, J., Dziembowski, W. A., Eff-Darwich, A., Elliott, J. R., Giles, P. M., Goode, P. R., Guzik, J. A., Harvey, J. W., Hill, F., Leibacher, J. W., Monteiro, M. J. P. F. G., Richard, O., Sekii, T., Shibahashi, H., Takata, M., Thompson, M. J., Vauclair, S., Vorontsov, S. V., 1996, The Seismic Structure of the Sun, Science, 272, 1296

Grec, G., Fossat, E., Pomerantz, M., 1980, Solar oscillations - Full disk observations from the geographic South Pole, Nature, 288, 541

Grec, G., Fossat, E., Pomerantz, M. A., 1983, Full-disk observations of solar oscillations from the geographic South Pole - Latest results, Sol. Phys., 82, 55

Green, E. M., Fontaine, G., Reed, M. D., Callerame, K., Seitenzahl, I. R., White, B. A., Hyde, E. A., Østensen, R., Cordes, O., Brassard, P., Falter, S., Jeffery, E. J., Dreizler, S., Schuh, S. L., Giovanni, M., Edelmann, H., Rigby, J., Bronowska, A., 2003, Discovery of A New Class of Pulsating Stars: Gravity-Mode Pulsators among Subdwarf B Stars, ApJ, 583, L31

Grundahl, F., Arentoft, T., Christensen-Dalsgaard, J., Frandsen, S., Kjeldsen, H., Rasmussen, P. K., 2008, Stellar Oscillations Network Group SONG, Journal of Physics Conference Series, 118, 012 041

Han, I., Black, D. C., Gatewood, G., 2001, Preliminary Astrometric Masses for Proposed Extrasolar Planetary Companions, ApJ, 548, L57

Hansen, C. J., Kawaler, S. D., Trimble, V., 2004, Stellar interiors : physical principles, structure, and evolution, New York: Springer-Verlag

Harvey, J., 1985, High-Resolution Helioseismology, in Future Missions in Solar, Heliospheric & Space Plasma Physics, (Ed.) E. Rolfe & B. Battrick, vol. 235 of ESA Special Publication, pp. 199

Harvey, J. W., 1988, Techniques for Observing Stellar Oscillations, in Advances in Helio- and Asteroseismology, (Ed.) J. Christensen-Dalsgaard & S. Frandsen, vol. 123 of IAU Symposium, pp. 497

Harvey, J. W., Hill, F., Hubbard, R. P., Kennedy, J. R., Leibacher, J. W., Pintar, J. A., Gilman, P. A., Noyes, R. W., Title, A. M., Toomre, J., Ulrich, R. K., Bhatnagar, A., Kennewell, J. A., Marquette, W., Patron, J., Saa, O., Yasukawa, E., 1996, The Global Oscillation Network Group (GONG) Project, Science, 272, 1284

Hébrard, G., Bouchy, F., Pont, F., Loeillet, B., Rabus, M., Bonfils, X., Moutou, C., Boisse, I., Delfosse, X., Desort, M., Eggenberger, A., Ehrenreich, D., Forveille, T., Lagrange, A., Lovis, C., Mayor, M., Pepe, F., Perrier, C., Queloz, D., Santos, N. C., Ségransan, D., Udry, S., Vidal-Madjar, A., 2008, Misaligned spin-orbit in the XO-3 planetary system?, A&A, 488, 763 `0806.0719`

Henry, T. J., Soderblom, D. R., Donahue, R. A., Baliunas, S. L., 1996, A Survey of Ca II H and K Chromospheric Emission in Southern Solar-Type Stars, AJ, 111, 439

Higham, N. J., 1990, Analysis of the Cholesky decomposition of a semi-definite maxtrix, in Reliable Numerical Computation, (Eds.) M. G. Cox, S. J. Hammarling, pp. 161

Horn, R. A., Johnson, C. R., 1985, Matrix Analysis, Cambridge University Press, New York, NY, USA, ISBN 0-521-38632-2

Houdek, G., 2006, Stochastic excitation and damping of solar-like oscillations, in Proceedings of SOHO 18/GONG 2006/HELAS I, Beyond the spherical Sun, vol. 624 of ESA Special Publication

Houdek, G., Gough, D. O., 2007, An asteroseismic signature of helium ionization, MNRAS, 375, 861

Houdek, G., Balmforth, N. J., Christensen-Dalsgaard, J., Gough, D. O., 1999, Amplitudes of stochastically excited oscillations in main-sequence stars, A&A, 351, 582

Howe, R., 2009, Solar Interior Rotation and its Variation, Living Reviews in Solar Physics, 6, 1

Howe, R., Komm, R. W., Hill, F., 2002, Localizing the Solar Cycle Frequency Shifts in Global p-Modes, ApJ, 580, 1172

Jimenez, A., Jones, A., Alvarez, M., Andersen, N. B., Domingo, V., 1990, Phase differences between luminosity and velocity measurements of the acoustic modes, Sol. Phys., 126, 1

Johnson, J. A., Winn, J. N., Albrecht, S., Howard, A. W., Marcy, G. W., Gazak, J. Z., 2009, A Third Exoplanetary System with Misaligned Orbital and Stellar Spin Axes, PASP, 121, 1104

Kallinger, T., Weiss, W. W., Barban, C., Baudin, F., Cameron, C., Carrier, F., De Ridder, J., Goupil, M., Gruberbauer, M., Hatzes, A., Hekker, S., Samadi, R., Deleuil, M., 2010, Oscillating red giants in the CoRoT exofield: asteroseismic mass and radius determination, A&A, 509, A77

Kendall, M. G., Stuart, A., 1967, The Advanced Theory of Astrophysics: Inference And Relationship, vol. 2, London: Butler & Tanner, 2 edn.

Kippenhahn, R., Weigert, A., 1990, Stellar Structure and Evolution, Springer-Verlag Berlin Heidelberg New York. Also Astronomy and Astrophysics Library

Kjeldsen, H., Bedding, T. R., 1995, Amplitudes of stellar oscillations: the implications for asteroseismology., A&A, 293, 87

Kjeldsen, H., Bedding, T. R., Baldry, I. K., Bruntt, H., Butler, R. P., Fischer, D. A., Frandsen, S., Gates, E. L., Grundahl, F., Lang, K., Marcy, G. W., Misch, A., Vogt, S. S., 2003, Confirmation of Solar-like Oscillations in η Bootis, AJ, 126, 1483

Kjeldsen, H., Bedding, T. R., Butler, R. P., Christensen-Dalsgaard, J., Kiss, L. L., Mc-Carthy, C., Marcy, G. W., Tinney, C. G., Wright, J. T., 2005, Solar-like Oscillations in α Centauri B, ApJ, 635, 1281

Komm, R. W., Howe, R., Hill, F., 2000, Width and Energy of Solar p-Modes Observed by Global Oscillation Network Group, ApJ, 543, 472

Kozai, Y., 1962, Secular perturbations of asteroids with high inclination and eccentricity, AJ, 67, 591

Lanza, A. F., 2010, Stellar magnetic cycles, in IAU Symposium, (Ed.) A. G. Kosovichev, A. H. Andrei, & J.-P. Roelot, vol. 264 of IAU Symposium, pp. 120

Lebreton, Y., 2008, Stars in the age of micro-arc-second astrometry, in IAU Symposium, (Ed.) W. J. Jin, I. Platais, & M. A. C. Perryman, vol. 248 of IAU Symposium, pp. 411

Ledoux, P., 1951, The Nonradial Oscillations of Gaseous Stars and the Problem of Beta Canis Majoris., ApJ, 114, 373

Leighton, R. B., Noyes, R. W., Simon, G. W., 1962, Velocity Fields in the Solar Atmosphere. I. Preliminary Report., ApJ, 135, 474

Libbrecht, K. G., 1988, Solar p-mode phenomenology, ApJ, 334, 510

Libbrecht, K. G., 1992, On the ultimate accuracy of solar oscillation frequency measurements, ApJ, 387, 712

Lin, D. N. C., Bodenheimer, P., Richardson, D. C., 1996, Orbital migration of the planetary companion of 51 Pegasi to its present location, Nature, 380, 606

Marques, J. P., Monteiro, M. J. P. F. G., Fernandes, J. M., 2008, Grids of stellar evolution models for asteroseismology (cesam + posc), Ap&SS, 316, 173

Mathur, S., García, R. A., Régulo, C., Creevey, O. L., Ballot, J., Salabert, D., Arentoft, T., Quirion, P., Chaplin, W. J., Kjeldsen, H., 2010, Determining global parameters of the oscillations of solar-like stars, A&A, 511, A46

McLaughlin, D. B., 1924, Some results of a spectrographic study of the Algol system., ApJ, 60, 22

Michel, E., Baglin, A., Auvergne, M., Catala, C., Samadi, R., Baudin, F., Appourchaux, T., Barban, C., Weiss, W. W., Berthomieu, G., Boumier, P., Dupret, M., Garcia, R. A., Fridlund, M., Garrido, R., Goupil, M., Kjeldsen, H., Lebreton, Y., Mosser, B., Grotsch-Noels, A., Janot-Pacheco, E., Provost, J., Roxburgh, I. W., Thoul, A., Toutain, T.,

Tiphène, D., Turck-Chieze, S., Vauclair, S. D., Vauclair, G. P., Aerts, C., Alecian, G., Ballot, J., Charpinet, S., Hubert, A., Lignières, F., Mathias, P., Monteiro, M. J. P. F. G., Neiner, C., Poretti, E., Renan de Medeiros, J., Ribas, I., Rieutord, M. L., Cortés, T. R., Zwintz, K., 2008, CoRoT Measures Solar-Like Oscillations and Granulation in Stars Hotter Than the Sun, Science, 322, 558

Michel, E., Samadi, R., Baudin, F., Barban, C., Appourchaux, T., Auvergne, M., 2009, Intrinsic photometric characterisation of stellar oscillations and granulation. Solar reference values and CoRoT response functions, A&A, 495, 979

Miller, B. A., Hale, S. J., Elsworth, Y., Chaplin, W. J., Isaak, G. R., New, R., 2004, Twenty-Eight Years of BISON Data, in SOHO 14 Helio- and Asteroseismology: Towards a Golden Future, (Ed.) D. Danesy, vol. 559 of ESA Special Publication, pp. 571

Monteiro, M. J. P. F. G., 2008, Porto Oscillation Code (posc), Ap&SS, 316, 121

Monteiro, M. J. P. F. G., Christensen-Dalsgaard, J., Thompson, M. J., 2000, Seismic study of stellar convective regions: the base of the convective envelope in low-mass stars, MNRAS, 316, 165

Monteiro, M. J. P. F. G., Christensen-Dalsgaard, J., Thompson, M. J., 2002, Asteroseismic inference for solar-type stars, in Stellar Structure and Habitable Planet Finding, (Ed.) B. Battrick, F. Favata, I. W. Roxburgh, & D. Galadi, vol. 485 of ESA Special Publication, pp. 291

Morel, P., Lebreton, Y., 2008, CESAM: a free code for stellar evolution calculations, Ap&SS, 316, 61

Mosser, B., Appourchaux, T., 2009, On detecting the large separation in the autocorrelation of stellar oscillation times series, A&A, 508, 877

Moutou, C., Pont, F., Bouchy, F., Deleuil, M., Almenara, J. M., Alonso, R., Barbieri, M., Bruntt, H., Deeg, H. J., Fridlund, M., Gandolfi, D., Gillon, M., Guenther, E., Hatzes, A., Hébrard, G., Loeillet, B., Mayor, M., Mazeh, T., Queloz, D., Rabus, M., Rouan, D., Shporer, A., Udry, S., Aigrain, S., Auvergne, M., Baglin, A., Barge, P., Benz, W., Bordé, P., Carpano, S., de La Reza, R., Dvorak, R., Erikson, A., Gondoin, P., Guillot, T., Jorda, L., Kabath, P., Lammer, H., Léger, A., Llebaria, A., Lovis, C., Magain, P., Ollivier, M., Pätzold, M., Pepe, F., Rauer, H., Schneider, J., Wuchterl, G., 2009, Planetary transit candidates in the CoRoT initial run: resolving their nature, A&A, 506, 321

Naef, D., Mayor, M., Pepe, F., Queloz, D., Santos, N. C., Udry, S., Burnet, M., 2001, The CORALIE survey for southern extrasolar planets. V. 3 new extrasolar planets, A&A, 375, 205

Nather, R. E., Winget, D. E., Clemens, J. C., Hansen, C. J., Hine, B. P., 1990, The whole earth telescope - A new astronomical instrument, ApJ, 361, 309

Noyes, R. W., Hartmann, L. W., Baliunas, S. L., Duncan, D. K., Vaughan, A. H., 1984a, Rotation, convection, and magnetic activity in lower main-sequence stars, ApJ, 279, 763

Noyes, R. W., Weiss, N. O., Vaughan, A. H., 1984b, The relation between stellar rotation rate and activity cycle periods, ApJ, 287, 769

Perryman, M. A. C., Lindegren, L., Kovalevsky, J., Hoeg, E., Bastian, U., Bernacca, P. L., Crézé, M., Donati, F., Grenon, M., van Leeuwen, F., van der Marel, H., Mignard, F., Murray, C. A., Le Poole, R. S., Schrijver, H., Turon, C., Arenou, F., Froeschlé, M., Petersen, C. S., 1997, The HIPPARCOS Catalogue, A&A, 323, L49

Perryman, M. A. C., de Boer, K. S., Gilmore, G., Høg, E., Lattanzi, M. G., Lindegren, L., Luri, X., Mignard, F., Pace, O., de Zeeuw, P. T., 2001, GAIA: Composition, formation and evolution of the Galaxy, A&A, 369, 339

Pourbaix, D., 2001, The Hipparcos observations and the mass of sub-stellar objects, A&A, 369, L22

Prantzos, N., 2009, On the chemical evolution of the Milky Way, in IAU Symposium, (Ed.) J. Andersen, J. Bland-Hawthorn, & B. Nordström, vol. 254 of IAU Symposium, pp. 381

Press, W. H., Teukolsky, S. A., Vetterling, W. T., Flannery, B. P., 1992, Numerical recipes in C. The art of scientific computing, Cambridge: University Press, |c1992, 2nd ed.

Queloz, D., Eggenberger, A., Mayor, M., Perrier, C., Beuzit, J. L., Naef, D., Sivan, J. P., Udry, S., 2000, Detection of a spectroscopic transit by the planet orbiting the star HD209458, A&A, 359, L13

Quirion, P.-O., Christensen-Dalsgaard, J., Arentoft, T., 2010, Automatic Determination of Stellar Parameters Via Asteroseismology of Stochastically Oscillating Stars: Comparison with Direct Measurements, ApJ, 725, 2176

Rasio, F. A., Ford, E. B., 1996, Dynamical instabilities and the formation of extrasolar planetary systems, Science, 274, 954

Rempel, M., 2008, Solar and stellar activity cycles, Journal of Physics Conference Series, 118, 012 032

Rossiter, R. A., 1924, On the detection of an effect of rotation during eclipse in the velocity of the brigher component of beta Lyrae, and on the constancy of velocity of this system., ApJ, 60, 15

Roxburgh, I. W., 2009, Narrow frequency-windowed autocorrelations as a diagnostic of solar-like stars, A&A, 506, 435

Roxburgh, I. W., Vorontsov, S. V., 2006, The autocorrelation function of stellar p-mode measurements and its diagnostic properties, MNRAS, 369, 1491

Saffe, C., Gómez, M., Chavero, C., 2005, On the ages of exoplanet host stars, A&A, 443, 609

Salabert, D., García, R. A., Pallé, P. L., Jiménez-Reyes, S. J., 2009, The onset of solar cycle 24. What global acoustic modes are telling us, A&A, 504, L1

Salabert, D., Garcia, R. A., Palle, P. L., Jimenez-Reyes, S. J., Jimenez, A., 2010, The extended minimum of solar cycle 23 as seen by radial velocity (GOLF, GONG) and intensity (VIRGO) helioseismic instruments, ArXiv e-prints, `1004.2869`

Samadi, R., Fialho, F., Costa, J. E. S., Drummond, R., Pinheiro Da Silva, L., Baudin, F., Boumier, P., Jorda, L., 2007a, The Corot Book: Chap. V.5/ Extraction of the photometric information : corrections, ArXiv Astrophysics e-prints, `arXiv:astro-ph/ 0703354`

Samadi, R., Georgobiani, D., Trampedach, R., Goupil, M. J., Stein, R. F., Nordlund, Å., 2007b, Excitation of solar-like oscillations across the HR diagram, A&A, 463, 297

Santos, N. C., Israelian, G., Mayor, M., 2004, Spectroscopic [Fe/H] for 98 extra-solar planet-host stars. Exploring the probability of planet formation, A&A, 415, 1153

Sato, K. H., Garcia, R. A., Pires, S., Ballot, J., Mathur, S., Mosser, B., Rodriguez, E., Starck, J. L., Uytterhoeven, K., 2010, Inpainting: A powerful interpolation technique for helio- and asteroseismic data, ArXiv e-prints, `1003.5178`

Scherrer, P. H., Bogart, R. S., Bush, R. I., Hoeksema, J. T., Kosovichev, A. G., Schou, J., Rosenberg, W., Springer, L., Tarbell, T. D., Title, A., Wolfson, C. J., Zayer, I., MDI Engineering Team, 1995, The Solar Oscillations Investigation - Michelson Doppler Imager, Sol. Phys., 162, 129

Schou, J., 1992, On the Analysis of Helioseismic Data, Ph.D. thesis, , Aarhus University, Aarhus, Denmark, (1992)

Stahn, T., Gizon, L., 2008, Fourier Analysis of Gapped Time Series: Improved Estimates of Solar and Stellar Oscillation Parameters, Sol. Phys., 251, 31

Stein, R., Georgobiani, D., Trampedach, R., Ludwig, H.-G., Nordlund, Å., 2004, Excitation of Radial P-Modes in the Sun and Stars, Sol. Phys., 220, 229

Stello, D., Kjeldsen, H., Bedding, T. R., 2007, Asteroseismology: a Powerful Tool to Complement Planet Transits, in Transiting Extrapolar Planets Workshop, (Ed.) C. Afonso, D. Weldrake, & T. Henning, vol. 366 of Astronomical Society of the Pacific Conference Series, pp. 247

Suárez, J. C., Goupil, M. J., 2008, filou oscillation code, Ap&SS, 316, 155

Takeda, Y., Ohkubo, M., Sato, B., Kambe, E., Sadakane, K., 2005, Spectroscopic Study on the Atmospheric Parameters of Nearby F–K Dwarfs and Subgiants, PASJ, 57, 27

Tassoul, M., 1980, Asymptotic approximations for stellar nonradial pulsations, ApJS, 43, 469

Thompson, M. J., Christensen-Dalsgaard, J., Miesch, M. S., Toomre, J., 2003, The Internal Rotation of the Sun, ARA&A, 41, 599

Toutain, T., Appourchaux, T., 1994, Maximum likelihood estimators: AM application to the estimation of the precision of helioseismic measurements, A&A, 289, 649

Toutain, T., Froehlich, C., 1992, Characteristics of solar p-modes - Results from the IPHIR experiment, A&A, 257, 287

Triaud, A. H. M. J., Queloz, D., Bouchy, F., Moutou, C., Cameron, A. C., Claret, A., Barge, P., Benz, W., Deleuil, M., Guillot, T., Hébrard, G., Lecavelier Des Étangs, A., Lovis, C., Mayor, M., Pepe, F., Udry, S., 2009, The Rossiter-McLaughlin effect of CoRoT-3b and HD 189733b, A&A, 506, 377

Triaud, A. H. M. J., Collier Cameron, A., Queloz, D., Anderson, D. R., Gillon, M., Hebb, L., Hellier, C., Loeillet, B., Maxted, P. F. L., Mayor, M., Pepe, F., Pollacco, D., Ségransan, D., Smalley, B., Udry, S., West, R. G., Wheatley, P. J., 2010, Spin-orbit angle measurements for six southern transiting planets. New insights into the dynamical origins of hot Jupiters, A&A, 524, A25

Unno, W., Osaki, Y., Ando, H., Saio, H., Shibahashi, H., 1989, Nonradial oscillations of stars, Nonradial oscillations of stars, Tokyo: University of Tokyo Press, 1989, 2nd ed.

Valenti, J. A., Fischer, D. A., 2005, Spectroscopic Properties of Cool Stars (SPOCS). I. 1040 F, G, and K Dwarfs from Keck, Lick, and AAT Planet Search Programs, ApJS, 159, 141

van Leeuwen, F., 2007, Validation of the new Hipparcos reduction, A&A, 474, 653

VandenBerg, D. A., Stetson, P. B., 2004, On the Old Open Clusters M67 and NGC 188: Convective Core Overshooting, Color-Temperature Relations, Distances, and Ages, PASP, 116, 997

Verner, G. A., Chaplin, W. J., Elsworth, Y., 2006, The Detectability of Signatures of Rapid Variation in Low-Degree Stellar p-Mode Oscillation Frequencies, ApJ, 638, 440

Walker, G., Matthews, J., Kuschnig, R., Johnson, R., Rucinski, S., Pazder, J., Burley, G., Walker, A., Skaret, K., Zee, R., Grocott, S., Carroll, K., Sinclair, P., Sturgeon, D., Harron, J., 2003, The MOST Asteroseismology Mission: Ultraprecise Photometry from Space, PASP, 115, 1023

Winget, D. E., Kepler, S. O., 2008, Pulsating White Dwarf Stars and Precision Asteroseismology, ARA&A, 46, 157

Winget, D. E., Nather, R. E., Clemens, J. C., Provencal, J., Kleinman, S. J., Bradley, P. A., Wood, M. A., Claver, C. F., Frueh, M. L., Grauer, A. D.and Hine, B. P., Hansen, C. J., Fontaine, G., Achilleos, N., Wickramasinghe, D. T., Marar, T. M. K., Seetha, S., Ashoka, B. N., O'Donoghue, D., Warner, B., Kurtz, D. W., Buckley, D. A., Brickhill, J., Vauclair, G., Dolez, N., Chevreton, M., Barstow, M. A., Solheim, J. E., Kanaan, A., Kepler, S. O., Henry, G. W., Kawaler, S. D., 1991, Asteroseismology of the DOV star PG 1159 - 035 with the Whole Earth Telescope, ApJ, 378, 326

Winn, J. N., Noyes, R. W., Holman, M. J., Charbonneau, D., Ohta, Y., Taruya, A., Suto, Y., Narita, N., Turner, E. L., Johnson, J. A., Marcy, G. W., Butler, R. P., Vogt, S. S., 2005, Measurement of Spin-Orbit Alignment in an Extrasolar Planetary System, ApJ, 631, 1215

Winn, J. N., Howard, A. W., Johnson, J. A., Marcy, G. W., Gazak, J. Z., Starkey, D., Ford, E. B., Colón, K. D., Reyes, F., Nortmann, L., Dreizler, S., Odewahn, S., Welsh, W. F., Kadakia, S., Vanderbei, R. J., Adams, E. R., Lockhart, M., Crossfield, I. J., Valenti, J. A., Dantowitz, R., Carter, J. A., 2009a, The Transit Ingress and the Tilted Orbit of the Extraordinarily Eccentric Exoplanet HD 80606b, ApJ, 703, 2091

Winn, J. N., Johnson, J. A., Albrecht, S., Howard, A. W., Marcy, G. W., Crossfield, I. J., Holman, M. J., 2009b, HAT-P-7: A Retrograde or Polar Orbit, and a Third Body, ApJ, 703, L99

Winn, J. N., Johnson, J. A., Fabrycky, D., Howard, A. W., Marcy, G. W., Narita, N., Crossfield, I. J., Suto, Y., Turner, E. L., Esquerdo, G., Holman, M. J., 2009c, On the Spin-Orbit Misalignment of the XO-3 Exoplanetary System, ApJ, 700, 302

Woodard, M., Hudson, H. S., 1983, Frequencies, amplitudes and linewidths of solar oscillations from total irradiance observations, Nature, 305, 589

Woodard, M. F., 1984, Short-Period Oscillations in the Total Solar Irradiance., Ph.D. thesis, AA(UNIVERSITY OF CALIFORNIA, SAN DIEGO.)

Woodard, M. F., Noyes, R. W., 1985, Change of solar oscillation eigenfrequencies with the solar cycle, Nature, 318, 449

Wright, J. T., Marcy, G. W., Butler, R. P., Vogt, S. S., 2004, Chromospheric Ca II emission in nearby stars (Wright+, 2004), VizieR Online Data Catalog, 215, 20 261

Wu, Y., Murray, N., 2003, Planet Migration and Binary Companions: The Case of HD 80606b, ApJ, 589, 605

Publications

Refereed publications:

Gizon, L., Schunker, H., Baldner, C. S., Basu, S., Birch, A. C., Bogart, R. S., Braun, D. C., Cameron, R., Duvall, T. L., Hanasoge, S. M., Jackiewicz, J., Roth, M., **Stahn, T.**, Thompson, M. J. Zharkov, S., 2009, *Helioseismology of Sunspots: A Case Study of NOAA Region 9787*, Space Science Reviews, 144, 249

Lutz, R., Schuh, S., Silvotti, R., Bernabei, S., Dreizler, S., **Stahn, T.**, Hügelmeyer, S. D., 2009, *The planet-hosting subdwarf B star V 391 Pegasi is a hybrid pulsator*, A&A, 496, 469

Nagel, T., Schuh, S., Kusterer, D., **Stahn, T.**, Hügelmeyer, S. D., Dreizler, S., Gänsicke, B. T., Schreiber, M. R., 2006, *SDSS J212531.92-010745.9 - the first definite PG 1159 close binary system*, A&A, 448, 25

Schuh, S., Silvotti, R., Lutz, R., Loeptien, B., Green, E. M., Østensen, R. H., Leccia, S., Kim, S., Fontaine, G., Charpinet, S., Francœur, M., Randall, S., Rodríguez-López, C., van Grootel, V., Odell, A. P., Paparó, M., Bognár, Z., Pápics, P., Nagel, T., Beeck, B., Hundertmark, M., **Stahn, T.**, Dreizler, S., Hessman, F. V., Dall'Ora, M., Mancini, D., Cortecchia, F., Benatti, S., Claudi, R., Janulis, R., 2010, *EXOTIME: searching for planets around pulsating subdwarf B stars*, A&SS, 130

Stahn, T., Gizon, L., 2008, *Fourier Analysis of Gapped Time Series: Improved Estimates of Solar and Stellar Oscillation Parameters*, SoPh, 251, 31

Conference contributions:

Dreizler, S., Werner, K., **Stahn, T.**, 2005, *Investigation of the Spectral Variability of PG 1159-035*, in 14th European Workshop on White Dwarfs, (Ed.) D. Koester & S. Moehler, vol. 334 of Astronomical Society of the Pacific Conference Series, pp. 512

Gizon, L., Cameron, R., Jackiewicz, J., Roth, M., Schunker, H., **Stahn, T.**, 2007, *Helioseismology at MPS*, in Modern solar facilities - advanced solar science, (Ed.) F. Kneer, K. G. Puschmann, & A. D. Wittmann, pp. 89

Lutz, R., Schuh, S., Silvotti, R., Dreizler, S., Green, E. M., Fontaine, G., **Stahn, T.**, Hügelmeyer, S. D., Husser, T., 2008, *Light Curve Analysis of the Hybrid SdB Pulsators HS 0702+6043 and HS 2201+2610*, in Hot Subdwarf Stars and Related Objects, (Ed.) U. Heber, C. S. Jeffery, & R. Napiwotzki, vol. 392 of Astronomical Society of the Pacific Conference Series, pp. 339

Schuh, S., Huber, J., Dreizler, S., Green, E. M., **Stahn, T.**, Randall, S., Husser, T., Heber, U., O'Toole, S., Fontaine, G., 2006, *Exciting new features in the frequency spectrum of the EC 14026 star HS 0702+6043. Simultaneous g-modes and p-modes in a sdB pulsator*, Memorie della Societĺ Astronomica Italiana, 77, 480

Schuh, S., Dreizler, S., Heber, U., Jeffery, C. S., O'Toole, S. J., Cordes, O., **Stahn, T.**, Lutz, R., Tillich, A., the Wet and MSST Collaborations, 2008, *Multi-wavelength photometric variation of PG 1605+072*, CoAst, 157, 35

Stahn, T., Gizon, L., 2008, *Fourier analysis of gapped time-series*, CoAst, 157, 369

Stahn, T., Dreizler, S., Werner, K., 2005, *The Spectral Variability of Pulsating Stars: PG 1159-035*, in 14th European Workshop on White Dwarfs, (Ed.) D. Koester & S. Moehler, vol. 334 of Astronomical Society of the Pacific Conference Series, pp. 545

Acknowledgment

Lebenslauf

Thorsten Stahn
Mittelbergstraße 17
37130 Gleichen

Geburtstag:	9. April 1980
Geburtsort:	Göttingen
Staatsangehörigkeit:	deutsch

---

02. 2006 – 10. 2010	Promotionsstudium Physik and der Universität Göttingen; Promotionsstipendium an der IMPRS des Max-Planck-Instituts für Sonnensystemforschung, Katlenburg-Lindau
27. 01. 2006	Diplom im Studiengang Physik (Universität Göttingen)
18. 10. 2002	Vordiplom im Studiengang Physik (Universität Göttingen)
10. 2000 – 01. 2006	Physikstudium an der Universität Göttingen
07. 1999 – 01. 2001	Wehrdienst
29. 06. 1999	Abitur
09. 1992 – 06. 1999	Grotefend-Gymnasium Münden, Hann. Münden
08. 1990 – 07. 1992	Orientierungsstufe II, Hann. Münden
07. 1986 – 06. 1990	Grundschule Gimte